annual report 04

institut laue-langevin

NEUTRONS FOR SCIENCE

annual report

The Institut Laue-Langevin

The Institut Laue-Langevin (ILL) is an international research centre where neutrons are used to probe the microscopic structure and dynamics of a broad range of materials from the molecular, atomic and nuclear point of view. The ILL is owned and operated by three founding countries - France, Germany and the United Kingdom - whose grants to the Institut's budget of approximately 70 million euros per year are enhanced by Scientific Membership contributions from Austria, the Czech Republic, Italy, Russia, Spain, Switzerland and most recently, in 2005, Sweden.

The ILL was founded to provide scientific communities in its member countries with a unique flow of neutrons and a matching suite of experimental facilities (some 40 instruments) for use in fields as varied as solid-state physics, materials science, chemistry, the biosciences and the earth sciences as well as nuclear physics and engineering. The Institut has ever since been an exceptional centre of excellence and a fine example of successful cooperation in Europe, a prototype of the European Research Area. It operates the most intense neutron source in the world. Over 2000 visiting scientists, performing a total of 750 experiments each year and the output in high impact journals, bear witness to the scientific success of the facility.

The ILL was founded to provide scientific communities in its member countries with a unique flow of neutrons and a matching suite of experimental facilities

We thank everyone who contributed to the production of this report.

In particular we gratefully acknowledge the help of:
H. Börner, A. Hewat, M. Johnson, J. Kulda, H. Schober and P. Timmins

annual report

Editors: Giovanna Cicognani and Christian Vettier
Design and Typesetting: Lignes droites communication - info@lignesdroites.com
Photography by Serge Claisse (ILL) and Artechnique - artechnique@wanadoo.fr
Printing: Imprimerie du Pont de Claix - May 2005

Further copies can be obtained from:
Institut Laue-Langevin
Scientific Coordination Office (SCO)
BP 156 - F-38042 Grenoble Cedex 9 (France)
Tel: +33 (0)4 76 20 72 40 - Fax: +33 (0)4 76 48 39 06
email: kjenkins@ill.fr or sco@ill.fr
Web: www.ill.fr

annualreport contents

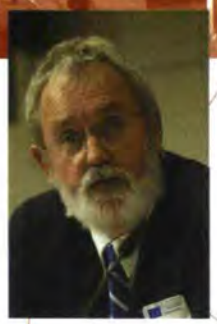

Director's introduction

As another year turns we are again visited by tragedy, this time on a colossal scale. The number of people killed as a result of the earthquake in Indonesia is so large as to numb the comprehension of such an event on the human scale.

At the same time we are brutally reminded of the untamed forces of nature and how far beyond our control they remain. However, to begin to harness the forces of nature it is first necessary to understand them. In its own small way that is the business of the ILL and its multitude of dedicated researchers, supported by our skilled engineers and technicians, who make use of our instrument suite and which is fed by our superbly reliable neutron source second to none. Underpinning their work is the infrastructure staff – administrative, secretarial, safety, medical, operational and maintenance – whose role is often unsung but nevertheless crucial.

Understanding the forces of nature, within the wide energy and spatial windows accessible to beams of neutrons, is our raison d'être and the same can be said for our six European partner laboratories within EIROforum, each in their own way.

Powerful, destructive earthquakes have a particular echo at the ILL and the event ten days ago and seemingly far away has in fact a ring much closer to home. The ILL's seismic refit programme, now moving into its third and most significant year, is designed to safeguard our facilities from very low probability but nevertheless serious events and to protect the environment and the surrounding population. This reinforcement and modernisation programme, which will secure the future of ILL, is going extremely well and will be completed in just over one year's time, when we shall resume normal operations.

However, the 2010 deadline for Europe to achieve the ambitious goals of the Lisbon agenda fast approaches and it is not yet clear whether there is the political will to redirect the necessary resources to fulfill this vision. The admirable aim for Europe to become the world's leading knowledge-based economy is not simply a question of economic competitiveness – we owe it to the hundreds of thousands who lie dead to continue to strive to understand the forces of nature and to hope that one day we may learn to harness them. This requires fine words to be urgently translated into effective actions and tangible achievements.

Colin Carlile
5 January 2005

What is the ILL?

Formally, the ILL is a non profit-making French company under civil law, which is governed by an International Convention signed at Foreign Ministry level by three countries - France, Germany and the United Kingdom. Our Associates - the CNRS and the CEA representing France, the FZ Jülich representing Germany and the CCLRC representing the United Kingdom - own and administer the Institut. They are also responsible for all liabilities and eventual decommissioning costs. With the signing of the Fourth Avenant of the ILL Intergovernmental Convention on 4th December 2002, the ILL's life was formally extended until at least 31st December 2013.

Our community of users enriches the scientific life of the Institut and has been increasing of late thanks to the improved instrumentation

Although ILL is an international organisation, its staff are not paid tax-free salaries, but instead they are enveloped within the French tax, employment and social security systems which has marked advantages but also marked disadvantages from whichever point of view you look at it. The Institut is answerable to French legal bodies and to French security authorities. We exist and operate within the French "loi de travail". Our staff representative bodies are those laid down by French law and are a significant presence in the ILL's daily life. We have strong links to the Mairie of Grenoble and surrounding communities, to the Préfecture of the Isère and to the Council of the Rhône-Alpes Region.

Whilst our Associates own the facility and contribute the largest amount to 70 M€ annual operating costs, the ILL also benefits from the scientific partnerships of seven other nations - Austria, the Czech Republic, Italy, Spain, Switzerland, Russia and most recently, in 2005, Sweden – who together contribute ~15% of the operational costs of the Institut. All ten partner countries in addition can and do contribute to capital projects at the Institut, within the Institut's priorities but according to their own priorities also.

Our governing body is the Steering Committee which meets twice-yearly and is made up of representatives of the Associates and the Scientific Partners together with Directors and Staff Representatives. Within the framework of the International Convention, the Steering Committee has the ultimate responsibility for determining operational and investment strategies for the Institut.

The Institut has a Director and two Associate Directors, one from each of the Associate countries, appointed on short-term contracts normally of 5 years. The Director's rôle is in general taken alternately by the German and British appointee. The two Associate Directors are also responsible respectively for the Science Division and the Projects and Techniques Division. The Head of the Administration Division is also appointed on a short-term contract, whereas the Head of the Reactor Division is a permanent ILL employee. These five people together constitute the Management Board of the Institut and are responsible for its day-to-day operation.

The scientific life of the Institut is guided by the Science Policy Board, with input from the ILL's nine scientific colleges. A Scientific Council, comprising 17 external scientists from the member countries, advises the Directors on scientific directions for the Institut, on the evolution of the instrument suite and technical infrastructure to best meet the needs of the user research programme, and to assess the scientific output of the Institut. It is helped in this process by the Instrument Sub-Committee and by the Chairmen of the 8 Scientific Sub-Committees who twice-yearly peer review the experiment proposals.

Scientists from non-partner nations also have access to our facilities making our community of users world-wide. This use enriches the scientific life of the Institut and has been increasing of late thanks to the improved instrumentation. From 2003 onwards, this non-partner use is limited to 10%. Our interactions with our user community have been enhanced in the past four years in order to be better informed of their needs and to be more responsive to emerging demands. The Millennium Symposium in April 2001 was a major event in this process, but our informal series of User Forums at which researchers on site on a given day are invited to a meeting with Directors and ILL group leaders have also been important. We are transforming our interactions to electronic means – proposals are now 100% electronic as are feedback forms. Much of our communication with users is now electronic although the Annual Report will remain in printed form for some time yet.

The ILL is composed of four Divisions,

each with its distinct role and, it is true to say, its own culture. Efforts have been made to bring those cultures closer together whilst recognising the need for differences. The Science Division staffs the instruments and delivers the science; the Projects and Techniques Division designs and builds new instruments, develops new concepts and maintains beamlines and instruments operational; the Reactor Division delivers the neutrons, operates and mans the reactor 24 hours per day every day of the year and has responsibility for all aspects of security; the Administration Division deals with Personnel matters particularly being responsible for interactions with staff representative bodies, with Purchasing, Finance, and Site and Building maintenance; and the Director's Services deal with Radiological safety, with conventional safety and with Health and Working Practices.

The ILL's neutron source is the finest in the world, being based on a single element 58.3 MW nuclear reactor designed for high brightness. The main moderator is the ambient D_2O coolant surrounding the core which delivers intense beams of thermal neutrons to 11 beamlines and to four neutron guides. A graphite hot source operating at 2400 K delivers hot neutrons – energies up to 1 eV and wavelengths down to 0.3 Å – to 3 beamlines. A renewal project has resulted in the installation of a new hot source and beam tubes during 2003. Two liquid deuterium cold sources at 25 K deliver cold neutrons – energies down to 200 meV and wavelengths beyond 20 Å – to 9 neutron guides. An ultra-cold neutron source fed from the top of one of the cold sources delivers neutrons vertically through the reactor pool to 5 instruments on the operational floor of the reactor. In all there are more than 50 measuring stations, 25 of which have full public access.

The ILL monitors the papers published as a result of the use of our facilities. The average number of papers published per year is about 600. With an annual budget of ~ 70 M€, the cost per paper is around 120 k€. We pay particular attention to papers published in high impact journals. Data indicate ~ 80 such papers per year are published from data taken on ILL instruments which, interestingly, is equivalent to the output of ESRF, and a factor of two higher than the second most productive neutron source in the world.

Beam days delivered for science equals 5103 for 2004. The cost per beam day of science therefore stands at a very cost effective 13,7 k€ per day.

The ILL is composed of four Divisions, each with its distinct role and, it is true to say, its own culture

Why Neutrons?

Neutron beams have the power, when used as a probe of small samples of materials, to reveal what is invisible using other radiations. Neutrons can appear to behave either as particles or as waves or as microscopic magnetic dipoles and it is these specific properties which enable them to uncover information which is often impossible to access using other techniques.

Electrically Neutral - Neutrons are non-destructive and can penetrate deep into matter making them an ideal probe for biological materials and samples under extreme conditions of pressure, temperature, magnetic field or within chemical reaction vessels.

Microscopically Magnetic - They possess a magnetic dipole moment which makes them sensitive to magnetic fields generated by unpaired electrons in materials. Precise details of the magnetic behaviour of materials at the atomic level can be investigated. In addition, the scattering power of a neutron by an atomic nucleus depends on the orientation of the neutron's spin and the spin of the atomic nuclei in a sample thereby providing a powerful tool to detect the nuclear spin order.

Wavelengths of Ångstroms - their wavelengths range from 0.1 Å to 1000 Å making them an ideal probe of atomic and molecular structures ranging from those consisting of single atomic species to complex biopolymers.

Energies of millielectronvolts - Their energies are of the same magnitude as the diffusive motions in solids and liquids, the coherent waves in single crystals (phonons and magnons) and the vibrational modes in molecules. An energy exchange between the incoming neutron and the sample of between 1μeV (even 1 neV with spin-echo) and 1eV can readily be detected.

Randomly sensitive - The variation of scattering power from nucleus to nucleus in a sample varies in a quasi-random manner. This means that light atoms are visible in the presence of heavy atoms and neighbouring atoms may be distinguished from each other. In addition, isotopic substitution (for example D for H, or one nickel isotope for another) can allow contrast to be varied in certain samples thereby highlighting specific structural features. The neutron is particularly sensitive to hydrogen atoms and therefore is a powerful probe of hydrogen storage materials, organic molecular materials, and biomolecular samples or polymers.

The French Science Festival (9-11 October 2004)

Once again the ILL was very active at the annual French Science Festival. This is a very unique occasion for ILL's scientists and engineers to meet the public and demonstrate the delights of physics! More than 10 000 visitors, including large numbers of children, crowded onto our stand over three days.

Among the events were superconducting magnetic levitation, a hexapod to manipulate, a game to guess the number of cosmic neutrons arriving on the stand ...

All over Europe everyone is concerned by the lack of interest of young people for scientific studies. But even if they do not choose a scientific career, we know from experience that 21st century kids still enjoy physics... at least those who visited our stand!

scientific**highlights**

Why has the ILL engaged in an ambitious rejuvenation programme, the Millennium Progamme? To offer the best instruments and neutron beams to scientists and engineers worldwide. Why do scientists and engineers need neutrons? Because of the unique properties of neutrons: neutrons are non-destructive, highly penetrating and sensitive to magnetic moments, they probe thermal and sub-thermal excitation spectra in materials and they can be considered as a probe themselves for fundamental physics studies. The ILL has been the most powerful neutron scattering facility in the world for more than 30 years and intends to remain in that position, at the forefront of neutron research worldwide. Today the ILL offers advanced neutron instruments and highly developed facilities around neutron beams where scientists can perform their top class science.

The ILL intends to remain at the forefront of neutron research worldwide

This present period is critical for the ILL. Tight compromises for operation have been imposed by the retrofitting of infrastructure which includes the replacement of major neutron beam tubes; as a result, the amount of beam time made available to users has been reduced but still remains significant at 150 days per year. However, instruments have benefitted from upgrades through the Millennium Programme and ILL scientists have optimised the availability of their instruments. The ILL has initiated a development programme of methods and facilities which complement the neutron methods: "more than simply neutrons". Facilities such as FaME38, the Deuteration Laboratory and the Computing Laboratory have paved the way to new partnerships such as the Partnership for Structural Biology which will enhance the scientific activity on the ILL site. Amidst all this renovation the year 2004 has been yet another highly productive and successful period for the ILL.

Instruments have benefitted from upgrades through the Millennium Programme

The high quality of science produced at the ILL is illustrated by the remarkable range of highlights presented in the following pages of the 2004 Annual Report. Indeed, the scientific programme carried out at the ILL embraces scientific applications ranging from particle physics to chemistry and life sciences, taking in material sciences and basic condensed matter physics as well as engineering. The summaries by Colleges emphasise further the multiple facets of methods which make neutrons so useful to explore properties of matter. The study of magnetism and magnetic materials with neutron methods has always been fertile and has evolved to complement parallel theoretical and technological developments. Neutron reflectometry, small angle scattering and neutron spin echo methods are key tools for the study of complex systems and soft matter. Finally, numerical modelling combined with neutron experiments is found to contribute greatly to a better understanding of the properties of condensed matter.

The ILL has been striving for scientific excellence and does not intend to stand still

The ILL has been striving for scientific excellence and does not intend to stand still: the ILL is now elaborating strategies to create a campus spirit on its own site, together with ESRF and EMBL, in order to attract more scientists and to offer them the best research facilities they can dream of!

Christian Vettier

Magnetic personalities

Better, stronger and faster! Ross Stewart is very proud of the new D7.

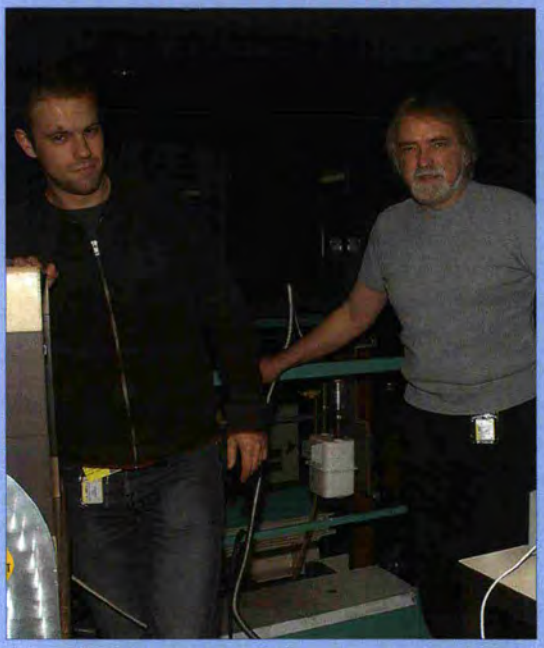

Marc "Potty" Pottinger and Bob Cywinski, from the University of Leeds.

Béatrice Grenier (D23 responsible) with Hadrien Mayaffre (left) and Arnaud Comment (right), CNRS, Grenoble.

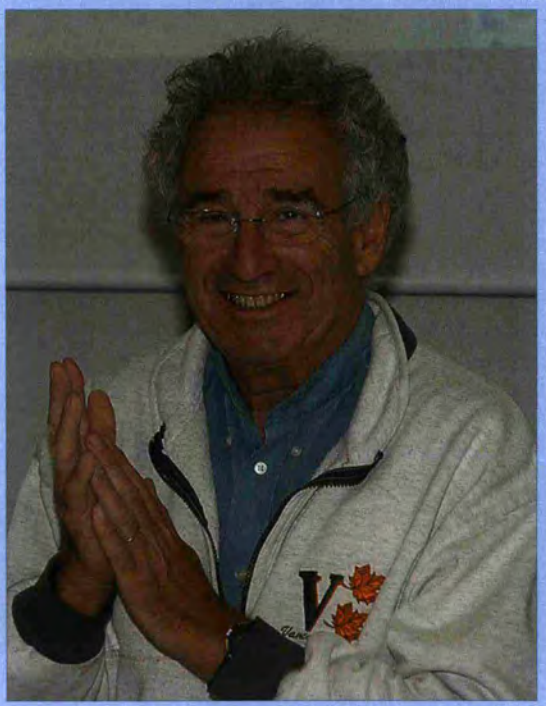

Jacques Schweitzer - CEA Grenoble - has worked as college 5B chairman for two years.

magnetism

Nolwenn Kernavanois, College 5B secretary – http://www.ill.fr/Colleges/C5B
Anne Stunault, College 4 secretary – http://www.ill.fr/Colleges/C4

During the past two decades, condensed-matter physicists have had to adjust to a climate of discovery in which many of the long-accepted rules of solid-state physics are boldly challenged by materials with unexpected properties. The field of magnetism is particularly rich in "emergent properties": different states of electronic correlations and pairing are observed in new materials exhibiting high-temperature superconductivity, unconventional superconductivity or giant magneto-resistance. While in conventional superconductivity, electrons are bound into Cooper pairs by phonons, the binding mechanism of unconventional superconductivity involves magnetic spin fluctuations. Anisotropy of the Fermi surface, magnetic densities and magnetic fluctuations play a key role, and high temperature superconductors and related compounds still attract a lot of interest, with properties apparently incompatible with conventional metal physics, and many questions still un-answered. Neutron scattering then constitutes a unique probe of such materials on microscopic scale, through the direct interaction between the neutron spin and the spin and angular momenta of atoms. Developments in neutron instrumentation, with increased neutron flux, or improved polarisation, in parallel with progress in crystal chemistry are allowing a better understanding of these exotic behaviours, in particular in cuprates.

The field of magnetism is particularly rich in "emergent properties"

One actually learns a lot from the study of fluctuations by inelastic neutron scattering. Hinkov et al. show the 2-dimensional character of magnetic fluctuations in $YBa_2Cu_3O_{6+x}$, with rings of spin-excitations in reciprocal space, in opposition to theories predicting a more rigid, one-dimensional array of stripes. In the structurally related compound Sr_2RuO_4, one of the best characterised unconventional superconductors, Braden et al. concentrate on the anisotropy of the fluctuations and evidence their antiferromagnetic rather than ferromagnetic character. Progress in that field is also gained from the study of quantum spin systems, like the spin-dimer sytem $Cs_3Cr_2Br_9$, where field induced magnetic ordering is viewed as an experimental realisation of Bose-Einstein condensation (Grenier et al.).

More understanding is also gained from structural studies of high-temperature superconductor cuprates. In particular, with small-angle neutron scattering (combined with μSR), Drew et al. show the random pinning of vortices by impurities in an applied magnetic field, to reach an exotic state of "vortex glass".

We note the leading role played by polarised neutrons in the study of complex magnetic systems

Unconventional superconductivity, also occurs in heavy Fermion systems, in the vicinity of a quantum critical point. In $CePd_2Si_2$, a typical example of an ordered Kondo lattice with strong spin fluctuations, Kernavanois et al., show a modification of the Cerium valence when passing through the quantum critical point, indicating that a spin fluctuation approach solely is not sufficient to describe the underlying physics of this system: a modification of the Fermi surface must also be considered.

Finally, we note the leading role played by polarised neutrons in the study of complex magnetic systems, from the discrimination of spin excitations (Braden), to the study of magnetic distributions (Kernavanois). With the development of a ^{3}He spin filter, these studies are not restricted to dedicated instruments any more, as shown by Wills et al., who demonstrate the feasibility of the measurement of magnetic distributions in powders using this technique.

magnetism

The in-plane geometry of spin excitations in the high-T_c superconductor $YBa_2Cu_3O_{6+x}$

V. Hinkov, A. Kulakov, C.T. Lin, D.P. Chen, C. Bernhard and B. Keimer *(MPI, Stuttgart)*

S. Pailhès, P. Bourges and Y. Sidis *(CEA Saclay)*

A. Ivanov *(ILL)*

The physics of high-temperature cuprate superconductors exhibits a two-dimensional (2D) character due to the layered structure. A well-respected theory predicts a further reduction of dimensionality: in the CuO_2-layers charge and spin are supposed to separate spontaneously forming one-dimensional (1D) stripes of antiferromagnetically ordered spins separated by charge rivers. Using inelastic neutron scattering we demonstrate, that the spin-excitations are 2D and form a ring in reciprocal space, thus excluding simple, 1D arrangements of stripes [1]. As amplitude and width are modulated along the ring and the modulation is strongly energy dependent, configurations of stripes are possible with strong orientation fluctuations, which can be quantified by our data.

The CuO_2-layers (a^*/b^*-plane) in most cuprates consist of rectangular Cu_4O_4 plaquettes. Almost all neutron experiments so far have been carried out on "twinned" crystals with equal proportions of micrometer-size twin domains, in which the rectangular plaquettes are rotated by 90° with respect to one another. Scattering from such crystals consists of equal contributions from both perpendicular twin domains, so even perfectly 1D spin excitations would generate a 2D pattern. Attempts to detwin an $YBa_2Cu_3O_{6+x}$ crystal large enough (several 100mm^3) for inelastic neutron scattering resulted in only partially detwinned crystals with twin domain population ratios of ~2:1. An experiment on such a crystal indicated that spin excitations exhibit an anisotropy between both principal directions in the CuO_2-planes, but the exact geometry remained unclear [2].

We took another approach by working with mosaics of many, fully detwinned, small crystals (figure 1). In a previous experiment at LLB we investigated a mosaic of nearly optimally doped $YBa_2Cu_3O_{6.85}$ with a total crystal volume of ~200 mm^3, where we performed different scans in the a/b-plane at a fixed energy of 35 meV (figure 2a), obtaining the geometry of spin excitations depicted in figure 2c. Elastic scans through the (200) and (020) Bragg reflections show a twin domain population ratio of 95:5 (figure 2b).

Figure 1: A sample plate showing that crystals are fixed by Al-screws to avoid incoherent hydrogen scattering from organic glue. The complete assembly is shown below.

The experiment we report here was performed on the triple axis spectrometer IN8. In contrast to [2], where the magnetic response at a single energy is investigated using an only partially detwinned crystal, we studied in detail the energy dependence of the amplitude and width modulation along the ring shown in figure 2c. For this we used an array of underdoped $YBa_2Cu_3O_{6.6}$ with a transition temperature of 61 K, a total volume of ~300 mm^3 and a domain population ratio 94:6. We performed scans along a^* and b^* – the ones depicted with "a" and "k" in figure 2a – at different energies and show them in figure 3. First of all, both along a^* and b^* there exist well defined incommensurate peaks which disperse towards the commensurate "resonance-peak" at 37 meV, so that the basic character is two-dimensional at all observed energies. However, we see a difference in the amplitude and width between scans along a^* and b^*, which becomes increasingly pronounced at lower energies. Which models can describe this anisotropy?

Theories based on a one-dimensional, rigid array of stripes predict the absence of

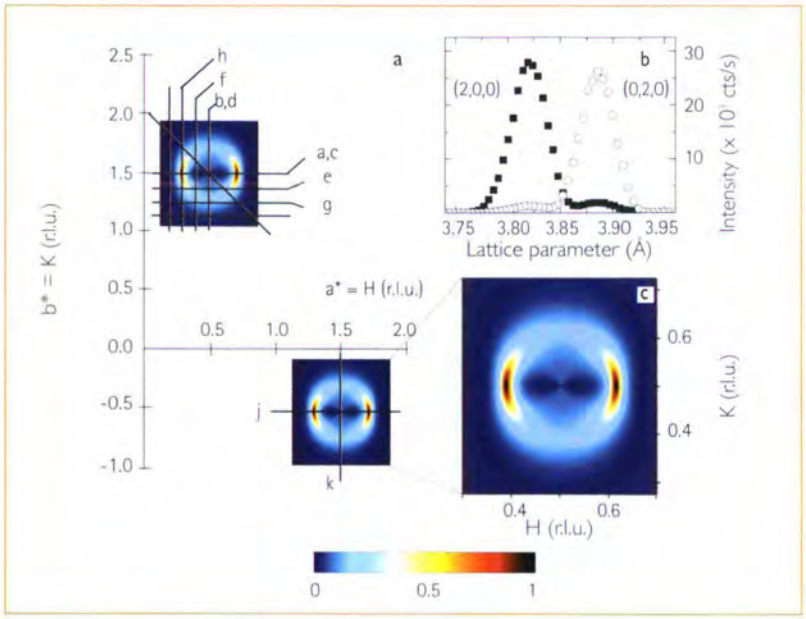

Figure 2: Layout of the reciprocal lattice indicating the trajectories of the scans, (a) we performed around the antiferromagnetic wave vector $\mathbf{Q}_{AF}$ to map the magnetic spectral weight shown in (c). In (b) scans through the crystallographic Bragg reflections demonstrate a twin domain population ratio of ~95:5 in the nearly optimally doped $YBa_2Cu_3O_{6.85}$ sample.

intensity along one direction [3], what we don't observe. However, an arrangement of only partially oriented stripes showing strong orientation fluctuations, analogous to a classical, nematic liquid crystal close to the nematic-to-smectic critical point, may be in agreement with our data: a preferential alignment of stripes along b^* would enhance the spectral weight along a^*.

Another scenario is based on a Fermi-liquid theory. Such theories have, for now, neglected the possible contribution of CuO-chains lying between the CuO_2-layers. Indeed, from our measurements we can exclude a *direct* contribution from the CuO-chains to the signal, however they may have an *indirect* effect by influencing the spin dynamics in the CuO_2-planes, as suggested by quadrupole resonance and X-ray scattering measurements. A further, appealing scenario is suggested by a theory predicting that the Fermi surface is intrinsically unstable [4], so that already a small disturbance, induced by the slight difference between the lattice constants a^* and b^* or by CuO-chain contributions, may deform the Fermi surface dramatically. So different this scenario may sound from the stripe-scenario, they have something important in common: in both cases an intrinsic instability is important.

Our data put stringent, quantitative constraints on stripe theories of high-T_c superconductivity. They rule out a large class of theories according to which the superconducting state coexists with a rigid array of stripes, over a wide range of hole concentrations encompassing the 60 and 90 K superconducting phases of $YBa_2Cu_3O_{6+x}$. If interpreted as evidence of the theoretically predicted liquid-crystalline stripe phases, they quantify the orientation stripe fluctuations.

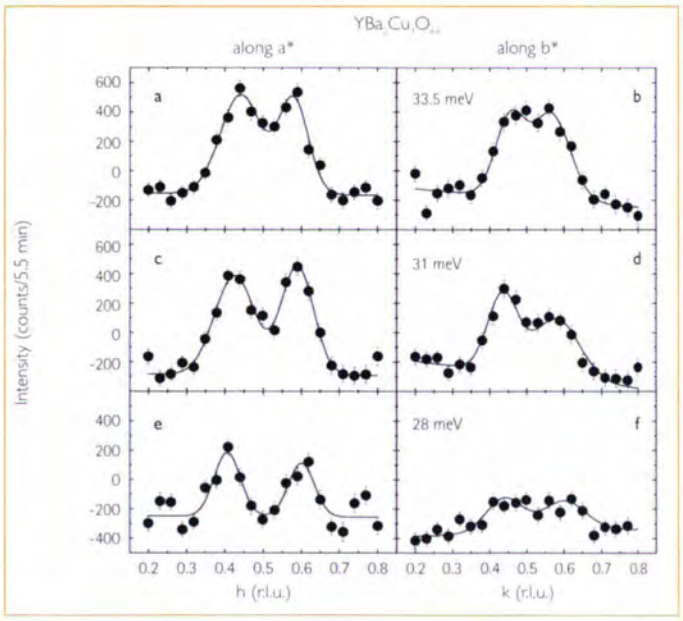

Figure 3: Scans through the $\mathbf{Q}_{AF}$ along a* (left) and b* (right) at different energies as measured on IN8 in the underdoped $YBa_2Cu_3O_{6.6}$ sample. The resolution conditions were identical along both directions, so that the scans are directly comparable. The response along the two directions becomes increasingly different at lower energies.

References: [1] V. Hinkov et al., Nature 430 (2004) 650
[2] H. Mook et al., Nature 404 (2000) 729
[3] F. Krüger et al., Phys. Rev. B 67 (2003) 134512
[4] H. Yamase et al., J. Phys. Soc. Jpn. 69 (2000) 332

magnetism

Anisotropy of the incommensurate spin fluctuations in Sr_2RuO_4

M. Braden and P. Steffens *(University of Cologne)*
Y. Sidis and P. Bourges *(LLB Saclay)*
J. Kulda *(ILL)*
S. Hayden *(University of Bristol)*
N. Kikugawa and Y. Maeno *(University of Kyoto)*

The magnetic fluctuations and their anisotropy are studied by polarised inelastic neutron scattering in the spin-triplet superconductor Sr_2RuO_4. The incommensurate nesting fluctuations are found enhanced perpendicular to the planes. In addition, there is clear evidence for broad magnetic excitations near the Brillouin-zone centre.

Initially, the layered superconductor Sr_2RuO_4 attracted interest due to its structural similarity with the high-temperature cuprate superconductors [1]. However, rapidly it turned out that the superconductivity in this material is very unconventional. Electrons appear to be paired in triplets with a p-wave order parameter symmetry. By now, Sr_2RuO_4 is one of the best characterised unconventional superconductors [2].

In contrast to the growing understanding of the character of the superconductivity in Sr_2RuO_4, the pairing mechanism remains still unsolved. A mechanism based on a coupling with magnetic fluctuations is quite promising in view of the unconventional character of the superconductivity and of the fact that correlations are less important in Sr_2RuO_4, which exhibits Fermi-liquid behaviour at low temperatures. A straightforward explanation of triplet pairing can be given by an interaction mediated by ferromagnetic fluctuations as early proposed by Rice and Sigrist [3]. Note that ferromagnetism splits the up- and down-spin bands and thereby favours pairing of parallel spins. Our first inelastic neutron scattering study, however, found dominating incommensurate fluctuations at a q-value of (0.3,0.3,0) arising from Fermi-surface nesting. The character of these nesting fluctuations is closer to antiferromagnetism than to ferromagnetism [4]. Hence, till today there persists a discrepancy between the observations of the order parameter symmetry and the character of the strongest magnetic fluctuations in Sr_2RuO_4 [5].

A solution to this problem was proposed more recently by Kuwabara et al. [6], who concluded that the observed incommensurate fluctuations at q=(0.3,0.3,0) still can lead to a triplet pairing, if they exhibit a strong anisotropy. Using longitudinal polarisation analysis on IN20 we have determined this anisotropy directly [7]. Figure 1 a) shows the sum of the scan data across the incommensurate position in the spin-flip channel. The peak confirms the magnetic character of the incommensurate fluctuations, as it was previously deduced from its Q- and temperature dependencies. No signal was found in the non-spin-flip channel. The spin-flip scattering for three different orientations of the neutron polarisation (see figure 1 b) measures different linear combinations of the components of the generalised susceptibilities. Therefore, one can calculate the in-plane and the out-of plane components of the generalised susceptibility (figure 1c), without any knowledge about the Ru-form factor in Sr_2RuO_4. The incommensurate signal exhibits a clear anisotropy. The out-of-plane susceptibility χ''_{zz} at an energy of 8 meV is about twice as large as the in-plane susceptibility χ''_{ab}. This result is confirmed by an independent experiment on IN22 [10].

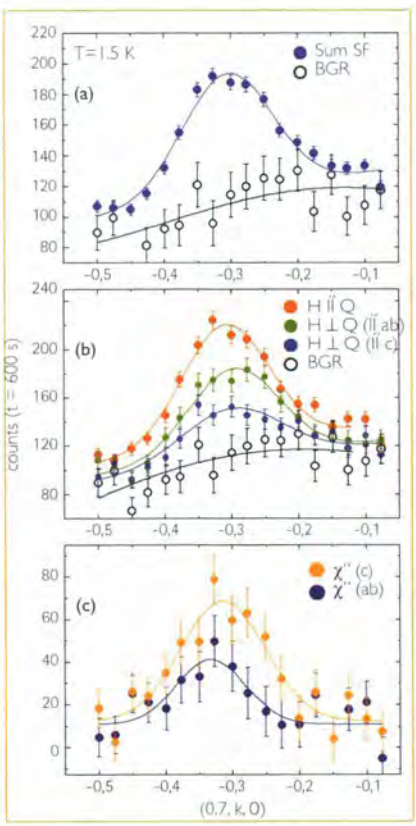

Figure 1: Results of the scans across the incommensurate position for an energy transfer of 8 meV at T = 1.5 K. (a) Total sum of the spin-flip scattering and the corresponding spin-flip background. (b) Spin-flip scattering for the different orientations of the neutron polarisation including the spin-flip background. In part (c) we show the out-of-plane and in-plane susceptibilities.

The anisotropy of the magnetic fluctuations in Sr_2RuO_4 arises from the spin-orbit coupling which is stronger than in the 3d-transition metal compounds. The sign of the anisotropy, $\chi''_{zz} > \chi''_{ab}$, agrees with the expectation for spin-orbit coupling since the octahedrons in Sr_2RuO_4 are elongated along the c-direction. Figure 2 shows the energy dependence of the anisotropy ratio χ''_{zz}/χ''_{ab}, which rapidly decreases with increasing energy. Furthermore, the anisotropy decreases upon heating, see reference [7]. Both effects appear to be related to the neighbourhood of the magnetic ordering; in a RPA theory one may explain that the anisotropy gets enhanced close to a magnetic transition. Also the spin-orbital coupling will become smeared out thermally at high temperature. The observation of sizeable anisotropy in the magnetic fluctuations of a transition metal oxide close to magnetic ordering [9] is of general interest in view of quantum criticality. Any magnetic divergence should occur only in one single component of the susceptibility, and, therefore, scaling concepts should take account of an anisotropy.

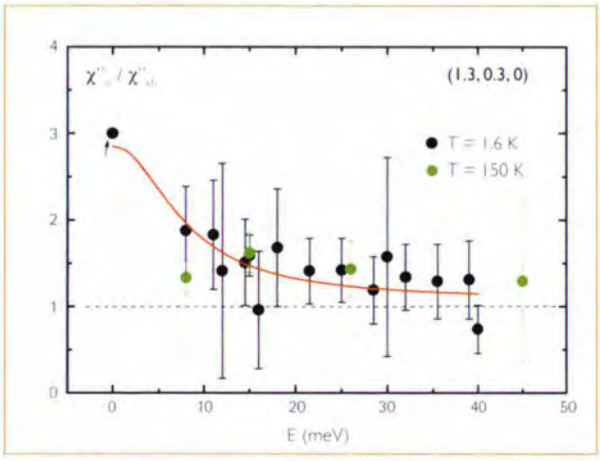

Figure 2: Energy dependence of the anisotropy ratio χ''_{zz}/χ''_{ab} of the incommensurate fluctuations; the NMR result by Ishida et al. [8] is included.

Although the anisotropy of the spin fluctuations is sizeable, it is still too small to explain a triplet pairing in Sr_2RuO_4 based on the theory of Kuwabara et al. [6]. The analysis of the incommensurate scattering in Sr_2RuO_4 in absolute units shows that at the intermediate energy at least an anisotropy of a factor 6 would be required. The question of the superconducting pairing mechanism therefore remains open.

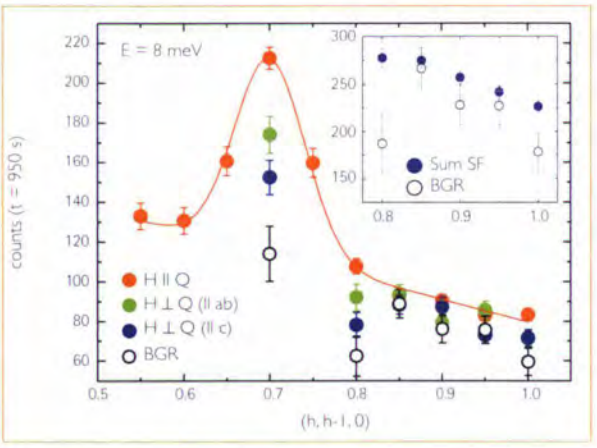

Figure 3: Spin flip signal in a scan across the incommensurate and across the ferromagnetic q-values for different orientation of the neutron polarisation. Weak magnetic scattering is found also away from the incommensurate position.

Furthermore, the polarised neutron experiments give information about the relevance of magnetic fluctuations with a quasi-ferromagnetic character. The macroscopic susceptibility is enhanced by a factor of 5 compared to the bare susceptibility obtained by LDA calculations. Also, the NMR experiments yield some temperature independent signal which cannot be explained by the nesting signal alone.

Analyses of the quasi-ferromagnetic scattering in Sr_2RuO_4 by unpolarised inelastic neutron scattering yield evidence for broad magnetic fluctuations around the Brillouin-zone centre, but can not precisely separate it from the background [11]. With the polarised experiment we obtain a significant progress. The scan in figure 3, which crosses the incommensurate and the ferromagnetic q-values, demonstrates that magnetic scattering indeed extends to the ferromagnetic zone-centre. In a second experiment we have focused on this quasi-ferromagnetic scattering; it is much less temperature dependent in analogy with the macroscopic susceptibility. Future experiments should quantify the characteristics of the quasi-ferromagnetic scattering in order to establish the full spectrum of magnetic scattering in Sr_2RuO_4, which will help to solve the superconducting pairing in this material.

References:
[1] Y. Maeno et al., Nature 372 (1994) 532
[2] Y. Maeno and A.P. Mackenzie, Rev. of Mod. Phys. 75, 657 (2003)
[3] T.M. Rice and M. Sigrist, J. Phys. Cond. Matt. 7, L643 (1995)
[4] Y. Sidis et al., Phys. Rev. Lett. 83 (1999) 3320
[5] I. Mazin and D. Singh, Phys. Rev. Lett. 82 (1999) 4324
[6] T. Kuwabara and M. Ogata, Phys. Rev. Lett. 85 (2000) 4586
[7] M. Braden et al., Phys. Rev. Lett. 92, 097402 (2004)
[8] K. Ishida et al., Phys. Rev. B 64, 100501 (2001)
[9] M. Braden et al., Phys. Rev. Lett. 88, 197002 (2002)
[10] B. Fak et al., cond-mat/0308558
[11] M. Braden et al., Phys. Rev. B 66, 064522 (2002)

magnetism

The field-induced magnetic phase of the spin $\frac{3}{2}$-dimer system $Cs_3Cr_2Br_9$

B. Grenier and L.P. Regnault
(CEA-Grenoble)
Y. Inagaki and Y. Ajiro
(Universities of Kobe and Tokyo)
J.P. Boucher *(CNRS Grenoble)*
A. Wildes and T. Ziman *(ILL)*

The field-induced magnetic phase occurring above H_{c1} = 1.5 T in $Cs_3Cr_2Br_9$ has been investigated by means of elastic and inelastic neutron scattering, on D23 and IN12, respectively. The magnetic structure was determined at 6 T and its field-dependence study shows new behaviours. The spin dynamics study reveals that the lowest excitation remains gapped above the critical field H_{c1}. A theoretical description of our results was derived, pointing out the crucial role played by single-ion anisotropy and frustration.

$Cs_3Cr_2Br_9$ (CCB) provides an interesting example of an interacting spin-dimer system. In zero field, such a system (as well as Haldane and alternating chains, ladders) shows a gap E_G between the $S = 0$ state and the first excited triplet state. In a magnetic field H, because of the Zeeman splitting of the $S = 1$ state, a phase transition occurs at low temperature at a critical field H_{c1} ($g\,\mu_B\,H_{c1} \sim E_G$), when the lowest gap closes. Above H_{c1}, the field-induced magnetic ordering (FIMO) is due to the inter-dimer couplings and concerns the spin components perpendicular to H (*transverse ordering*), while a Bose-Einstein transition might also occur [1].

The antiferromagnetic (AF) couplings of CCB (see figure 1) are: $J = 1.03$ meV (intra-dimer), $J_b = 0.054$ and $J_c = 0.039$ meV (in-plane and out-of-plane inter-dimer, respectively) [2]. $Cs_3Cr_2Br_9$ differs from the previously studied spin-dimer systems (*e.g.* $TlCuCl_3$ [3]) both by the large spin value ($S = 3/2$ Cr^{3+}) and by the hexagonal arrangement of the dimers. These two features are expected to favor *local anisotropies* and *frustration*, respectively, and should have important consequences on the properties of the FIMO. This motivated the present study of the magnetic ordering and spin excitations in the FIMO phase of CCB [4]. The experiments were performed on D23 and IN12 using a 350 mm^3 single-crystal mounted in a 6 T vertical cryomagnet (with dilution insert) with **H // a–b**.

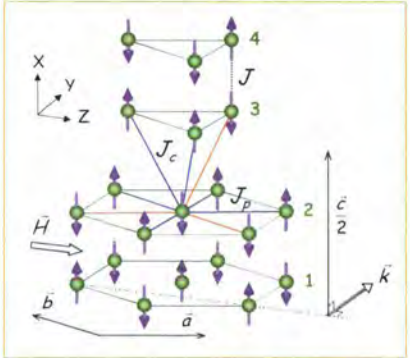

Figure 1: Transverse (AF) spin ordering of the Cr^{3+} ions in the commensurate + + - - magnetic phase of $Cs_3Cr_2Br_9$ for **H // a – b**. **k** is the corresponding propagation vector. The atoms labeled 1, 2, 3, 4 point out one unit cell. The ferromagnetic and AF inter-dimer correlations are represented, in red and blue, respectively.

Magnetic ordering

The magnetic structure was determined at $H = 6$ T. It is described by the commensurate propagation vector **k** = (1/4, 1/4, 0) and the magnetic refinement of 123 magnetic reflections gives the + + - - collinear structure depicted in figure 1: the moments (// *c*-axis) are perpendicular to H, as expected for a FIMO, and the AF transverse moment is $M_x = 1.60(1)\ \mu_B/Cr^{3+}$. Note that this ordering yields frustration in the inter-dimer couplings J_c and J_b (one out of three is ferromagnetic). In addition, a magnetisation parallel to H arises and was determined from the ferromagnetic contribution appearing on top of the weak nuclear peak (1, 1, 4): $M_z = 0.37(3)\ \mu_B/Cr^{3+}$. The field dependence of both the propagation wave vector and the average transverse moment M_x were studied up to 6 T by scanning the strongest magnetic peak, (1-*k*, 1-*k*, 2) with $k \sim 0.25$, along the (110)

Figure 2: (a) Field dependence of the propagation wave-vector component k and (b) that of the parallel (M_z) and the average ordered transverse (M_x) magnetisations. Inset: Scans at 2.9 T in the (110) direction across the (1-k, 1-k, 2) peak, with k ~ 0.25, for increasing and decreasing field.

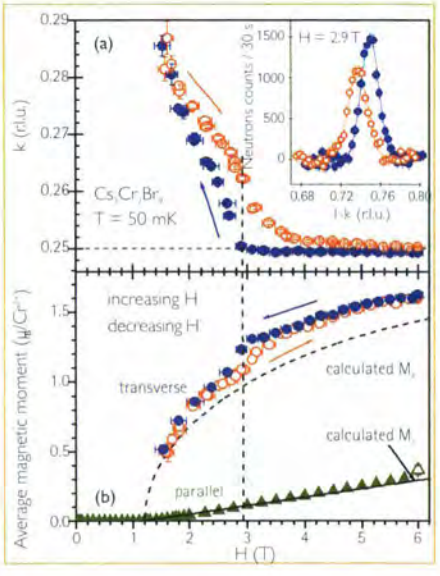

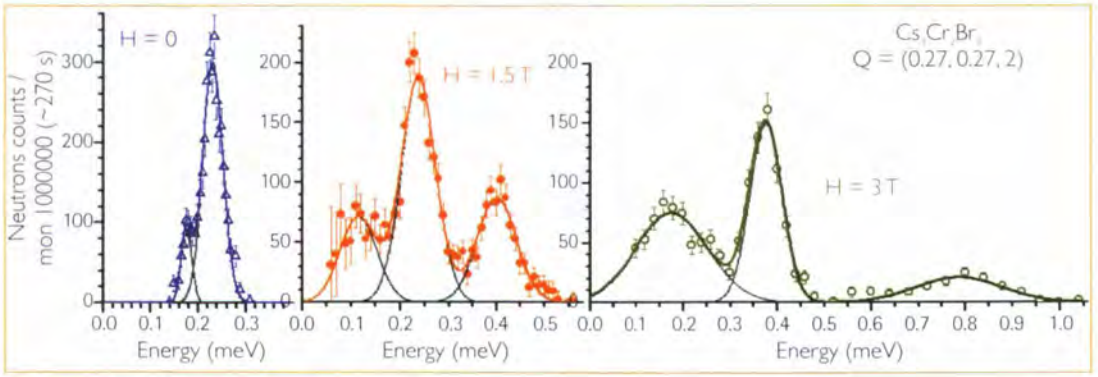

Figure 3: Q-constant energy scans measured at the minimum of the dispersion curve, Q = (0.27, 0.27, 2), for different magnetic field values: the Zeeman splitting is clearly seen below $H_{c1} \sim 1.5$ T and surprisingly, the lowest mode is still gapped for $H > H_{c1}$.

direction, for increasing and decreasing H (see figure 2). This peak could be detected down to 1.5 T, suggesting a critical field H_{c1} slightly lower than this value, in good agreement with the $M_z(H)$ curve measured on a SQUID magnetometer (closed green triangles). Interestingly, incommensurabilities and field hysteresis occur, between 1.7 and 5.4 T. To our knowledge, this represents the first observation of such behaviour in a FIMO and should result from interplay of quantum fluctuations and frustration.

Magnetic excitations

The complete dispersion curves of the three $S = 1$ modes have been obtained between 0 and 6 T [4] from Q-constant energy scans such as those plotted in figure 3. A splitting, *not detected previously* [2], is clearly observed at $H = 0$ (see figure 3). It is accounted for by a single-ion anisotropy term $D(S^z)^2$ ($X = c$) at each Cr^{3+} site with $D = -0.01$ meV, explaining the ordered moment orientation found in the FIMO. Surprisingly, the minimum of each dispersion curve was found to remain centered at $Q_h = Q_k = 0.275(5)$ from 0 to 5 T, contrary to k which shifts slowly from 0.29 to 0.25.

We focus here on the field dependence of the minimum energies of the three dispersion curves (see figure 4). Below H_{c1}, the Zeeman splitting is clearly observed and can be well reproduced using $D = -0.01$ meV. In the FIMO, the middle and upper gaps behave roughly as $g\mu_B H$ and $2g\mu_B H$, respectively.

More important is the observation of a gap in the lower branch, on the entire field range: the gap does not vanish around H_{c1} (it amounts ~ 0.11 meV) and then slowly increases with H up to 0.25 meV at 6 T. These results clearly demonstrate that there is no massless Goldstone mode, and thus no Bose Einstein condensation, in the FIMO phase of CCB.

Analysis of our results

A FIMO develops each time a crossing occurs between two states of the isolated dimers:

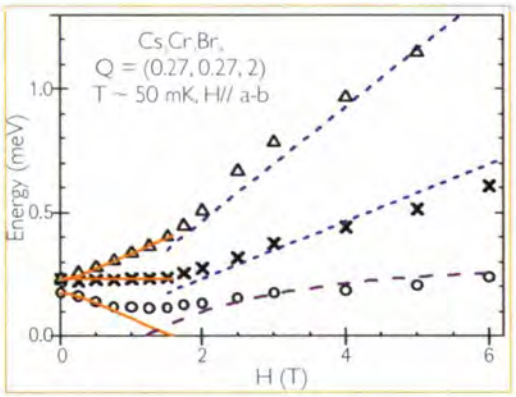

Figure 4: Field dependence of the energy gaps. The orange lines describe the Zeeman splitting below H_{c1}, with single-ion anisotropy (see text). Above H_{c1}, the blue lines are $g\mu_B H$ and $2g\mu_B H$, the purple line describes the lowest gap E_{c1} (calculated in ref. [4]).

the singlet ground-state |0> and the lowest split state |1,-1> of the initial triplet state |1>, near H_{c1}. By projecting the initial Hamiltonian onto these elementary states (simple FIMO) an effective $\sigma = 1/2$ pseudo-spin Hamiltonian can be derived for the FIMO phase. Within a mean-field approximation for the + + - - structure described above, we obtain the theoretical prediction shown in figure 2b (dashed lines). Good agreements are obtained for the critical field H_{c1}, and also for the field dependence of both the longitudinal (M_z) and transverse (M_x) magnetisations. The residual discrepancy (15% for M_x) is to be attributed to additional contributions from higher states [5]. Taking into account the small anisotropy D, the same approach predicts the presence of a gap above H_{c1}. Its field dependence is given by the dashed line in figure 4, in good agreement with the data, but an appreciable renormalisation had to be applied: it comes, as above, from the additional mixing of higher states (extended FIMO) [5]. As a general conclusion, we here establish that a very small anisotropy combined with frustration effects may open a relatively large gap in a FIMO phase.

Conclusion

We have observed new and peculiar features at the onset of field-induced magnetic order in $Cs_3Cr_2Br_9$. They should stimulate new developments concerning simple versus extended FIMO, incommensurability, and hysteretic behaviour.

References: [1] I. Affleck, Phys. Rev. B 43 (1991) 3215
[2] B. Leuenberger et al., Phys. Rev. B 30 (1984) 6300 & 31 (1985) 597
[3] T. Nikuni et al., Phys. Rev. Lett. 84 (2000) 5868, Ch. Rüegg et al., Nature (London) 423 (2003) 62
[4] B. Grenier et al., Phys. Rev. Lett. 92 (2004) 177202
[5] T. Ziman et al., unpublished

magnetism

Magnetisation distribution under pressure in the pressure induced superconductor $CePd_2Si_2$

N. Kernavanois *(ILL)*
R. Sadykov *(Institute for High Pressure Physics, Troitsk)*
E. Ressouche, S. Raymond and J. Flouquet *(CEA, Grenoble)*
P. Lejay *(CNRS-CRTBT, Grenoble)*

We report measurements performed up to ~ 30 kbar in the pressure-induced heavy fermion superconductor $CePd_2Si_2$ using polarised neutrons. Such measurements allow to microscopically probe the magnetic properties of $CePd_2Si_2$ at its quantum critical point (~ 28 kbar). A direct comparison of results obtained at zero-pressure and under ~ 30 kbar shows both a strong reduction of the induced magnetisation and a change in the global shape of the magnetic form factor. Such a change of the magnetic form factor shape could be associated to a modification of the cerium valence. Moreover, this measurement is the first one combining polarised neutrons, high magnetic field (10 T), low temperature (1.4 K) and high pressure (30 kbar). It opens up new possibilities for neutron diffraction studies under extreme conditions.

Figure 1: Photographs of the 30 kbar non-magnetic clamp cell designed at the Institute for High Pressure Physics and used in the 10 T cryomagnet on the polarised neutron diffractometer D3.

Superconductivity occurring in the vicinity of a Quantum Critical Point (QCP) has been observed for a large variety of heavy fermion (HF) systems. The QCP corresponds to the (quantum) phase transition from a magnetically ordered state to a disordered state at T = 0 K as a function of pressure, magnetic field, or chemical doping. In the vicinity of the QCP, the conventional Fermi liquid ground state disappears and so-called non Fermi liquid behaviour occurs. The nature of the excitations giving rise to this state and their relevance for superconductivity is still in debate. Microscopic probes are thus of outmost importance to characterise the magnetic properties at the QCP. While several precise NQR and inelastic neutron scattering studies performed on several compounds deal with this point, only a few detailed neutron diffraction investigations are available. The present neutron diffraction study performed under pressure on the HF compound $CePd_2Si_2$ is aiming at microscopically characterise the building up of magnetism at a QCP.

$CePd_2Si_2$ ($\gamma = 250$ mJ/molK^2) is an exemplary material showing all the subtleties involved in formation of a wide range of physical states. It orders antiferromagnetically at $T_N = 10$ K with an ordered moment of $\approx$ 0.65 μ_B/f.u. which is smaller than that predicted by the crystal field calculations [1], suggesting a partial Kondo screening. The fact that the Néel and Kondo temperatures are nearly the same ($T_K \approx 10$ K) together with the strong pressure dependence of the Néel temperature implies that $CePd_2Si_2$ is near a magnetic instability [2]. In addition, a QCP occurs under the critical pressure, $p_c \approx 28$ kbar. At p_c, magnetism is suppressed and a superconducting phase is stabilised at low temperature [3]. The strong spin fluctuations occurring at such a QCP are believed to be responsible for the superconductivity.

The combination of pressure and form factor measurement is a powerful technique to access any evolution of the *4f* magnetic properties with pressure, when passing through a QCP.

The measurements have been performed on the D3 diffractometer using a clamp-type pressure cell (see figure 1) designed at the Institute for High Pressure Physics compatible with the D3-10 T cryomagnet and the polarised neutron technique. This pressure cell, made of NiCrAl and TiZr alloys, is non-magnetic and can be loaded up to 7.5 tons, which corresponds to 30 kbar in the sample chamber (using fluorinert as pressure transmitting medium). Its reduced size (34 mm in diameter and 104 mm in height) is well adapted to most of the standard sample environment equipment. Measurements with and without pressure were done using the same $CePd_2Si_2$ single crystal (3 mm in diameter and 10 mm in height) with the

same orientation in an external magnetic field of 9.5 T.

Figure 2 shows a comparison of the magnetic form factors measured in $CePd_2Si_2$ at two different pressures (ambient pressure and ≈ 30 kbar). In both cases, the measurements have been performed in the paramagnetic state: at T = 12 K (that is above the Néel temperature of 10 K) for p = 0 kbar and at 1.4 K (the lowest accessible temperature in the cryomagnet) for p ≈ 30 kbar. At the latter pressure, we checked that no antiferromagnetic contributions were visible, which confirms that the crystal was in the paramagnetic phase, near the QCP or just above. Attempts to determine the pressure were made using a NaCl single crystal. The large uncertainty in the pressure determination, p = 39 ± 12 kbar, is due to the poor resolution of the Heusler monochromator, and to the low intensities of the NaCl Bragg peaks at large $\sin\theta/\lambda$. It should be noticed that at such a pressure, the salt strongly suffers from the non-perfectly hydrostatic pressure conditions and is characterised by a very large mosaicity.

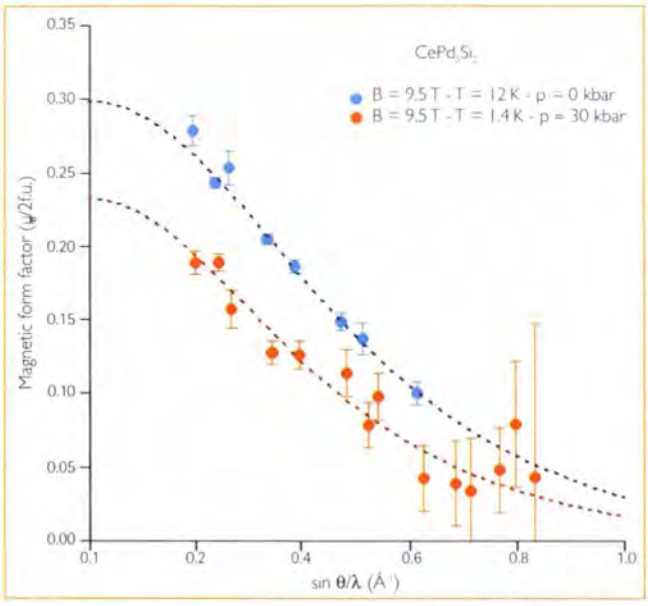

Figure 2: Magnetic form factors measured in the $CePd_2Si_2$ paramagnetic states: above 10 K at p = 0 kbar (blue circles) and at the lowest accessible temperature (1.4 K) at p ≈ 30 kbar (red circles). Preliminary refinements within the dipolar approximation are shown as dotted lines.

Two main features appear from this comparison: *i)* a reduction by a factor 1.3 of the induced magnetisation (0.30(1) and 0.23(1) μ_B/2f.u. (formula unit) at p = 0 and 30 kbar, respectively); *ii)* a change in the global shape of the magnetic form factor. A preliminary least-squares refinement within the dipolar approximation has been performed. Within this scheme, just the isotropic term in the development of the form factor is considered and the Ce^{3+} form factor is written $f^{Ce}(h, k, l) = \langle j_0 \rangle + C_2 \langle j_2 \rangle$ with $\langle j_0 \rangle$ and $\langle j_2 \rangle$ the radial integrals tabulated in reference [4]. The refined values of C_2 are 1.64(11) and 1.25(20) at p = 0 and 30 kbar, respectively. The zero-pressure value of C_2 is in perfect agreement with the calculated one of 1.6 for a Ce^{3+} valence state [5]. The decrease of C_2 with pressure could then be associated to a valence change of the cerium atoms from Ce^{3+} to $Ce^{(3+\delta)+}$. This appearance of an intermediate-valence regime can be interpreted as a wipe out of the crystal field by the strong local fluctuations as pointed out by resistivity measurements [6] which show that the Kondo energy scale and the crystal field splitting are equal at around 30 kbar. The underlying concept is that the collapse of a long range antiferromagnetic ordering cannot be described only by a spin fluctuation approach, a modification of the Fermi surface when passing through the QCP must also be considered [7]. This decrease of C_2 with pressure indicates that the form factor is less extended towards high $\sin\theta/\lambda$ values in reciprocal space, which implies an expansion of the *4f* wavefunctions in direct space when approaching the QCP. The final analysis of the data is ongoing. Nevertheless, these preliminary results already seem to evidence a modification of the magnetic properties of the *4f* Ce electrons with the pressure.

Besides the scientific aspects, the present measurements form already a first step towards the development of user-friendly experiments under pressure on the D3 spin polarised hot neutron diffractometer. It should also be noticed that the combination of polarised neutrons, high magnetic field (9.5 T), low temperature (1.4 K) and high pressure (30 kbar) achieved for this experiment can also be of interest for other measurements on other instruments.

References: [1] R.A. Steeman et al., Solid State Commun. 66 (1988) 103
[2] V. Murgai et al., Valence Instabilities, ed. P. Wachter and H. Boppart (North-Holland, Amsterdam, 1982) 537
[3] N.D. Mathur et al., Nature 394 (1998) 39
[4] E. Balcar and S.W. Lovesey, Theory of Magnetic Neutron and Photon Scattering (Oxford: Oxford University Press, 1989) ch 2
[5] J.X. Boucherle, D. Givord and J. Schweizer, Journal de Physique C7 (1982) 199
[6] A. Demuer et al., J. Phys.: Condens. Matter (2002) L529
[7] J. Flouquet, Prog. Low Temp. Physics (Elsevier ed., A.W. Halperin), to be published

magnetism

Magnetisation distribution measurements from powders using a ^{3}He spin filter

A.S. Wills *(UCL and The Royal Institution of Great Britain, London)*
A. Sella *(UCL, London)*
E. Lelièvre-Berna and F. Tasset *(ILL)*
F.G. Cloke *(University of Sussex, Brighton)*
P.L. Arnold *(University of Nottingham)*
J. Schweizer *(CEA, Grenoble)*
R. Ballou *(CNRS, Grenoble)*

The measurement of polarised neutron-dependent cross-sections is an extremely powerful technique that provides information on the distribution of magnetisation in materials with unpaired electrons. High quality data can even be used to determine the tensorial nature of the local magnetisation and so provide direct information about the electronic configurations of the valence shells. At present, the employment of the technique only at single crystal diffractometers (e.g. D3 at ILL) means that its application is limited to subjects where the single crystals are available. The development of this technique for the study of powder and polycrystalline samples could open the door to new fields of science. Years ago, measurements on powders demonstrated the great potential of the technique, but they remain isolated studies that did not explore either the technical issues associated with powdered samples or the application to weakly magnetic samples, as would be important to chemistry and biochemistry.

The well-known powder diffractometer D1B has been modified for the collection of polarisation-dependent cross-section data using a ^{3}He spin filter. The standard collimator located in between the monochromator shielding and the sample table has been replaced by the magneto-static cavity Cryopol [1] and a new collimator containing guide-fields ensuring the adiabatic transportation of the polarisation to the sample located in a 5 T cryomagnet (figure 1). Great care was taken over the effects of depolarisation and absorption of the neutron beam by the powder. The first of these effects was explicitly measured in our experiments using a Cu_2MnAl Heusler crystal that was glued to the side of the vanadium sample can. The data collected from the [111] reflection of the Heusler positioned in front and behind the sample characterised the depolarisation. The absorption was measured with a monitor positioned before and after the sample. In order to take into account the effects of ^{3}He polarisation relaxation, data were collected using a repeated (+−−+) neutron polarisation sequence.

Figure 1: The experimental team on D1B. From the left: Francis Tasset, Andrew Wills, Eddy Lelièvre-Berna and Nolwenn Kernavanois.

In the case of powder samples better quality information can be derived from the difference data $I_+ - I_-$ as contamination from the cryomagnet and sample can is then cancelled, within statistics, and only magnetic data are left. The difference spectra are related to M and N according to $I_+ - I_- = 4 K P_i D N M$ where K is a scale factor that contains the Lorentz factor, the multiplicity and the absorption coefficient for each reflection, P_i is the incident polarisation, D is the depolarisation of the beam, N and M are the nuclear and magnetic structure factors respectively (the flipper efficiency of Cryopol is 99.9%).

In order to determine the sensitivity of the technique, we have measured the difference spectra of the weak ferromagnet YNi_3 below T_c = 30 K. Previous workers had already determined the magnetisation density distribution from single crystal data [2]. The successful observation of the small saturation moment (0.04 μ_B per Ni atom) after a 15-hour data collection attests the high sensitivity. Indeed, the flux at the sample position was only 5×10^5 n cm s^{-1} at 2.52 Å on D1B and a much better statistics could be obtained in one hour on D20.

Prussian Blue, $Fe_4^{III}[Fe^{II}(CN)_6]_3 \bullet xD_2O$, is an archetypal mixed-valent molecular ferromagnet. It displays ferromagnetic ordering of the Fe(III) spins below T_c = 5.5 K. As the magnetic Fe(III) ions are well separated, it is believed that central to the magnetism is a contribution from what would naïvely be expected to be low-spin diamagnetic Fe(II) ions. Arguments based on the charge transfer transition in the optical absorption

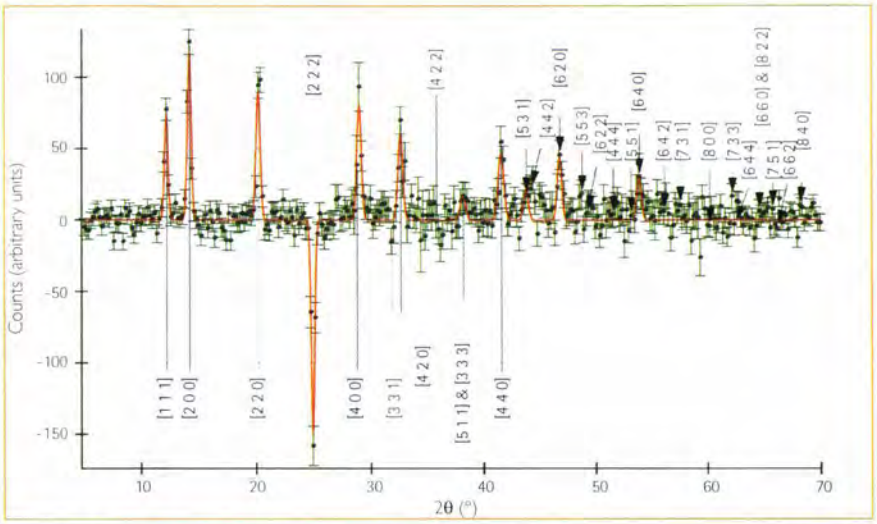

Figure 2: The Prussian Blue difference spectra collected in 10 hours with neutrons of 1.28 Å after correction for the time-dependent relaxation of the ^{3}He spin filter. Fits of Gaussian functions to the individual reflections are shown.

spectrum at 14100 cm^{-1} that leads to its well known intense blue colour, led Day and co-workers [3] to search for spin transfer from the high-spin Fe(III) to the diamagnetic Fe(II) using flipping-ratio measurements. As Prussian Blue is only known in powder form, their measurements on the polarised neutron single-crystal diffractometer D5 at the ILL demonstrated well the restrictions associated with the study of powders. In their study only 3 reflections could be resolved allowing them to deduce a maximum amount of transferred spin as $0.003 \pm 0.026\ \mu_B$.

In our measurements a total of 11 reflections were clearly discernible in the difference spectrum collected for 10 hours (figure 2). Nuclear structure factors were taken from data collected in the paramagnetic phase at 20 K in zero applied field, and used to calculate the magnetic structure factors. Determination of the magnetisation distribution was carried out using the Maximum Entropy software MEMSYS 3 and PRIMA. The major features of the magnetisation maps generated by both codes are the same (figure 3): unpaired spin density is largely localised at the Fe(III) position but a significant component at the Fe(II) position is also observed. Initial refinement suggests values for the spontaneous magnetisation of 3.0 ± 0.1 and $0.3 \pm 0.1\ \mu_B$ per atom respectively.

This experiment demonstrated the ease with which a powder diffractometer may be adapted for use with polarised neutrons with the help of large area neutron polarisers (^{3}He filters). Such devices can be included in the design of any new instruments. The high intrinsic sensitivity of the technique (measurement of NxM instead of $N^2 + M^2$) is evidenced by the observation of magnetic scattering from 0.04 μ_B per Ni in YNi_3. It encourages the study of the magnetisation distributions in chemical, physical and biological powder samples. This technique can apply successfully to relatively weak ferromagnetic systems without strong anisotropy but will not compete with the determination of the magnetisation distribution in single crystals.

Figure 3: MaxEnt reconstruction of the magnetisation map in Prussian Blue. The high density corresponds to Fe(III) and the low density to the ferromagnetic component present at the Fe(II) ion.

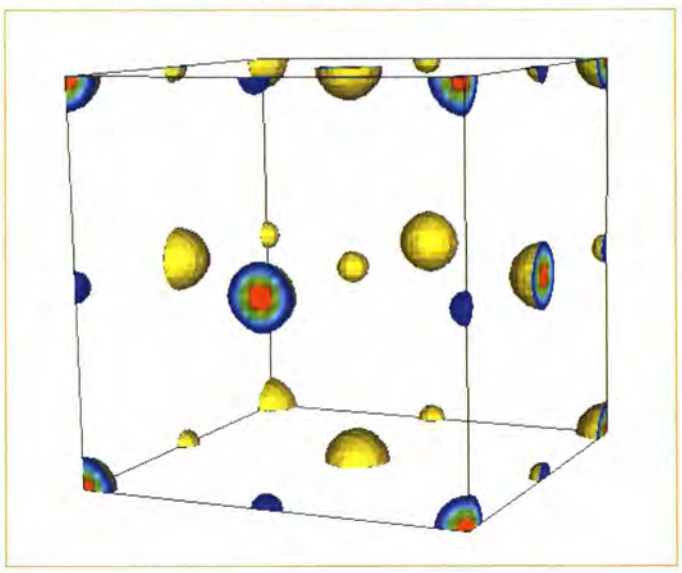

References: [1] J. Dreyer, L.P. Regnault et al., Nucl. Instr. and Meth. in Phys. Res. A 449, (2000) 638-648
[2] D. Gignoux, R. Lemaire et al., J. Magn. Magn. Mater. 21 (1980) 307
[3] P. Day, F. Herren, A. Ludi et al., Helvetica Chimica Acta 63 (1980) 148

magnetism

Direct observation of the flux-line vortex glass phase in $La_{1.9}Sr_{0.1}CuO_4$

A.J. Drew, S.L. Lee and U. Divakar *(University of St. Andrews)*
R. Gilardi and J. Mesot *(LNS, ETH Zurich and PSI Villigen)*
F.Y. Ogrin *(University of Exeter)*
D. Charalambous and E.M. Forgan *(University of Birmingham)*
G.I. Menon *(Institute of Mathematical Sciences, Chennai)*
N. Momono and M. Oda *(Hokkaido University)*
C.D. Dewhurst *(ILL)*
C. Baines *(LMSS PSI Villigen)*

The magnetic phase diagram of high-temperature superconductors can contain many exotic vortex phases not observed in conventional superconducting materials. For example, the familiar vortex lattice may melt at high temperatures into a vortex liquid. The influence of defects, which pin the vortices, is of particular interest from both a theoretical and an experimental point of view. We have used a combination of small angle neutron scattering and muon-spin rotation to probe the order of the vortex system on a microscopic scale. As a function of applied magnetic field we observe a transition from an ordered vortex state to a vortex glass phase that results from the presence of random pinning.

In conventional type II superconducting materials there exist two distinct magnetic phases. In the Meissner phase superconducting screening currents exclude externally applied magnetic fields from the bulk, while in the mixed state obtained at higher fields the magnetic field is allowed to thread the sample in the form of quantized rods of flux. These interact to form a flux line lattice (FLL), usually of hexagonal symmetry. In high-Tc cuprates the combination of extreme material parameters and high temperatures gives rise to a zoo of exotic vortex phases. In recent years there has been particular interest in the effects of random point pinning on the long range order of the vortex system. Pinning sites attract vortex cores, and these forces compete with the elastic (electromagnetic) interactions between vortices. The current theoretical perspective is that weak disorder should give a 'Bragg glass' (BG), which retains the topological order of the flux line lattice (FLL) but gives broadened diffraction peaks [1]. The BG concept accounts for the observation of an apparently ordered FLL in many systems (e.g. [2,3,4]). Strong disorder should result in the topologically disordered 'vortex glass' (VG) [1]. A transition from a BG to a VG is predicted to occur as the applied magnetic field is increased. Microscopic evidence for a field driven transition to a disordered vortex phase has previously been observed in the extremely anisotropic cuprate superconductor $Bi_2Sr_2CaCu_2O_{8+\delta}$ (BSCCO) [2,5]. In that system, however, the vortices are quasi-two dimensional, and are quite different from the rigid rods of flux found in conventional superconductors. The novelty of the vortex system presented here, in $La_{1.9}Sr_{0.1}CuO_4$ (LSCO), is that the vortices are fairly rigid vortex lines that are nonetheless highly susceptible to transverse fluctuations due to thermal effects or the presence of point disorder. As well as presenting a simple system to relate to theoretical treatments of the BG-VG transitions, it also makes it easier to trace the evolution of the disorder into the high field region of the phase diagram.

We have used a combination of small angle neutron scattering (SANS) (on D22, ILL) and muon-spin rotation (μSR) (GPS on the πM3 beam line at PSI). These are two highly complementary techniques, since μSR measures the probability distribution of the internal fields arising from the vortex lattice, and can continue to give clear information on the local order in the system even when the disorder is such that SANS measurements become extremely difficult. Even in the well-ordered BG phase, SANS on this system is rather challenging compared to many other superconducting systems. This is due to the rather long superconducting penetration depth (λ_{00}) that determines the magnetic contrast inside the sample, yielding a scattering cross-section that is $\propto \lambda_{00}^{-4}$.

Figure 1 is an example of the SANS data from the vortices at an applied field of

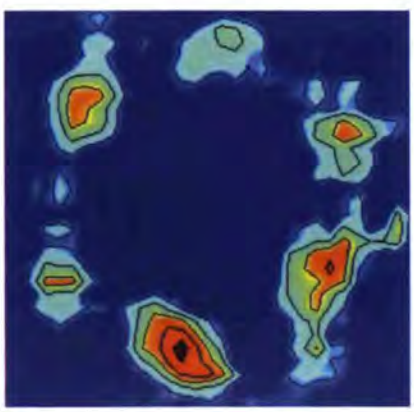

Figure 1: Diffraction pattern from the vortex system obtained on D22 at an applied field of 150 Oe and a temperature of 6.2 K, below the Bragg glass to vortex glass transition.

150 Oe [6]. The intrinsic weakness of the scattering and the low scattering angles for this large inter-vortex distance means that long counting times are required to obtain such images. It is also necessary to account for the much larger scattering from material defects, by subtracting off a background measured in the normal (non-superconducting) state. As the field is increased there is a rapid fall in the scattering intensity and an increase in the radial width of the Bragg spots due to a reduction in the transverse correlation length [7,8].

The transition to the VG phase can be mapped out in the B-T plane most efficiently using μSR. The shape of the probability distribution for internal fields $p(B)$ is very sensitive to changes in the local vortex arrangement. Using Monte Carlo simulations it is possible to extract the structure factor $S(q)$ related to the local two-body vortex correlations [9], which may be compared with measurements of the same quantity via SANS [8]. A simple measurement of the width of $p(B)$, denoted $\sigma(H,T)$, can illustrate the dramatic changes in vortex order close to the transition (figure 2). Disorder in a system composed of vortex lines will always lead to an increase in $\sigma(H,T)$ [10], and we observe a dramatic increase in this parameter around the transition to the VG phase. Interestingly, the BG-VG transition is marked by a minimum in $\sigma(H,T)$, as illustrated in figure 2. This arises since at low fields the vortices are more dilute and interact less strongly, so initially the increasing field works to pack them into a more ordered arrangement. However, above the transition there is a rapid fall in the transverse correlation length, leading to a sudden increase in $\sigma(H,T)$.

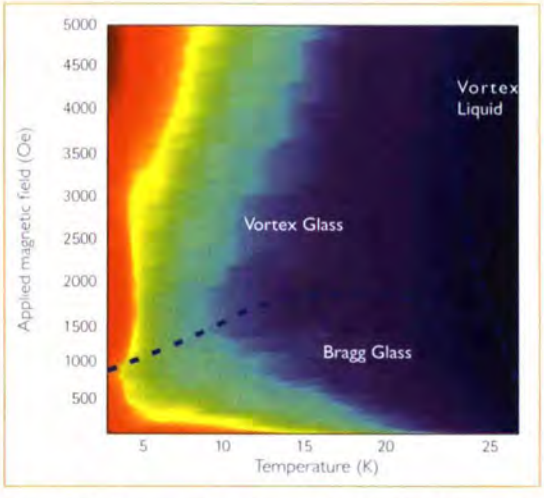

Figure 2: The variation of the width $\sigma(H,T)$ of the probability distribution of internal fields, determined by muon-spin rotation measurements. The valley in $\sigma(H,T)$, schematically traced by one of the dashed lines, locates the boundary of the Bragg glass to vortex glass transition. The other line indicates the vicinity of the vortex lattice melting line, which is close to the macroscopic irreversibility line of figure 3.

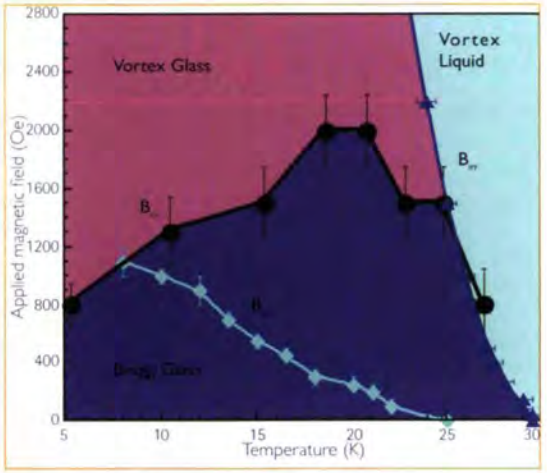

Figure 3: A summary of the phase diagram derived from our published data on neutron, muon and magnetisation measurements [6]. $B_\sigma(T)$ follows the minima in the isotherms of $\sigma(H)$. $B_{cr}(T)$ indicates a peak in the magnetisation data often associated with the BG-VG transition. $B_{irr}(T)$ marks the onset of hysteretic behaviour in magnetisation measurements, sometimes identified with the vortex lattice melting transition.

A summary of some of the combined findings of published SANS, μSR and magnetisation measurements is given in the phase diagram of figure 3. The power of using microscopic techniques is particularly apparent upon contrasting the lines $B_\sigma(T)$, reflecting the change in local order, with $B_{cr}(T)$, a signature in the bulk magnetisation frequently associated with the transition. The lines are clearly very different, reflecting the different conditions and parameters that are measured in each case. The neutron and muon experiments probe the system in a field-cooled state, while the magnetisation measurements determine the macroscopic properties of a system possessing strong flux gradients, and reflect the changing dynamic response of the vortices. The SANS and μSR results are clearly more directly comparable with theoretical descriptions of the equilibrium statistical physics of the system. It is worth noting that the upward trend of $B_\sigma(T)$ with increasing temperature is reminiscent of theoretical predictions for the BG-VG transition due to the reduced effectiveness of pinning at higher temperature [1,11]. Further details of this work can be found in reference [6]. Current work is focusing on a determination of the correlation function of vortices inside the vortex glass phase, using both SANS and μSR.

References:
[1] T. Giamarchi and P. Le Doussal, Phys. Rev. Lett. 72 (1994) 1530
T. Giamarchi and P. Le Doussal, Phys. Rev. B52 (1995) 1242
[2] R. Cubitt et al., Nature 365 (1993) 407-411
[3] R. Gilardi et al., Phys. Rev. Lett. 88 (21) (2002) 217003
[4] T. Klein et al., Nature 413 (2001) 404
[5] S.L. Lee et al., Phys. Rev. Lett. 71 (1993) 3862
[6] U. Divakar et al., Phys. Rev. Lett. 92 (23) (2004) 237004
[7] ILL Experimental Report 5-42-107 (2004)
[8] A.J. Drew et al., in preparation
[9] G.I. Menon et al., in preparation
[10] G.I. Menon et al., Phys. Rev. B 60 (1999) 7607
[11] Denis Ertas and David R. Nelson, Physica C 272 (1996) 79

P.M. Bentley and R. Cywinski
(University of Leeds)
J.R. Stewart *(ILL)*

magnetism

A magnetic emulsion

An anomalous Q^{-5} dependence of the magnetic small angle neutron scattering from compounds just beyond the percolation threshold for ferromagnetism has been observed in the $Y(MnFe)_2$ Laves phase system. This scattering, seen for the first time in a magnetic system, is attributed to Kirste-Porod-like higher order surface scattering from unusually sharply defined but very highly convoluted interfaces between the ferromagnetic percolation clusters and the residual antiferromagnetically correlated spin fluctuation matrix, an unusual morphology analogous to that of a bicontinuous emulsion.

Over the last three decades small angle neutron scattering (SANS) has proved extremely useful in mapping the evolution of spin correlations in the vicinity of the critical concentration for long range ferromagnetic order in percolating alloy systems. In most cases the $Q(=4\pi\sin\theta/\lambda)$-dependence of the magnetic intensity can be represented either by a simple Lorentzian function, representing Ornstein-Zernicke-like critical scattering, or by a combination of Lorentzian plus squared Lorentzian scattering, with the latter term accounting for the effects of random magnetic exchange or anisotropy [1]. It is therefore expected that the SANS cross section from such disordered magnetic systems will show a gradual progression from a Q^{-2}-like dependence at high temperatures to a Q^{-4}-like dependence at low temperatures.

In this context our recent D11 SANS studies of spin correlations in $Y(Mn_{1-x}Fe_x)_2$ have yielded highly anomalous results: for alloys just beyond the critical concentration for ferromagnetism ($x\sim0.3$), the magnetic SANS intensity follows a $Q^{-\alpha}$ dependence with α increasing from 2 at high temperatures to 6 at low temperatures. Scattering powers greater than $\alpha=4$ are relatively uncommon in SANS and to our knowledge such a high power has never been observed for a magnetic system.

To find an explanation for the observed Q-dependence we have had to look beyond existing models of SANS from disordered magnets, and have turned instead to scattering processes associated not with the spin correlations themselves but with the surfaces of the magnetic percolation clusters resulting from those spin correlations.

For any two phase medium in which the interface between the two phases is sharp and well defined on length scales shorter than $2\pi Q^{-1}$, the associated SANS scattering function follows the familiar Q^{-4} Porod form [2]. Occasionally even more pronounced Q dependences, $Q^{-(4+\beta)}$, are observed and attributed variously to "fuzzy" Porod scattering, associated with less well defined interfaces, or to scattering from fractal surfaces, for which $\beta=(2-D)$ where D is the fractal dimensionality. However for both situations β is always found to be less than 2, both experimentally and theoretically.

Teubner [3], on the other hand, has provided a rigorous and concise derivation of Porod surface scattering, and its related second order component, generally known as Kirste-Porod scattering [4], for systems such as bicontinuous microemulsions in which the interface surfaces are extremely thin but smooth. Teubner found

$$I(Q)\propto\left[\frac{1}{Q^4}+\frac{1}{Q^6}\left(\frac{3}{2}\langle H^2\rangle-\frac{1}{2}\langle K\rangle\right)\right]$$

where the magnitude of the Q^{-6} term depends upon the relative Gaussian (K), and mean (H) curvatures at the scattering surface. For extreme Gaussian curvature, ie for extremely convoluted surfaces, it is clear that the Q^{-6} Kirste-Porod contribution can be significant. Moreover, within this model the coefficient of the Q^{-6} component can be interpreted as a measure of the

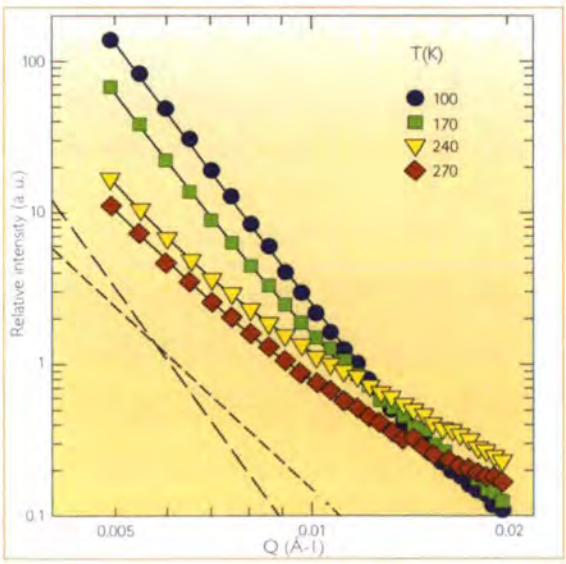

Figure 1: The Q-dependence of the SANS intensity from $Y(Mn_{0.8}Fe_{0.6})_2$ at several temperatures. Note the cross-over from Q^{-4} to Q^{-6} scattering with decreasing temperature. The Curie temperature for this sample is 260K.

The small-angle scattering instrument D11.

'non-sphericity' of the scattering surfaces within the Porod regime.

In the case of $Y(Mn_{1-x}Fe_x)_2$ we believe the magnetic surfaces responsible for the highly unusual Kirste-Porod-like Q^{-6} scattering are those associated with extremely sharply defined, non-spherical and highly convoluted interfaces between "ferromagnetic droplets", *i.e.* the percolation clusters, and the surrounding matrix.

Clues to the origin of the unusual cluster morphologies within $Y(Mn_{1-x}Fe_x)_2$ may be found in the magnetic phase diagram. The substitution of only 2.5 at % Fe for Mn in the itinerant electron helical antiferromagnet YMn_2 results in a marked decrease of the volume of the unit cell and an associated collapse of both magnetic order and the Mn moment itself [5], leaving a Pauli paramagnetic state dominated by massive antiferromagnetically correlated longitudinal spin fluctuations. With further additions of Fe the transition metal moments appear to re-localise giving rise first to a spin glass state and ultimately to extremely inhomogeneous ferromagnetic order beyond a percolation threshold of approximately $x_c \sim 0.3$. The resulting sharply defined but highly convoluted ferromagnetic clusters are embedded within a residual spin fluctuating, but antiferromagnetically correlated, matrix – effectively a magnetic emulsion.

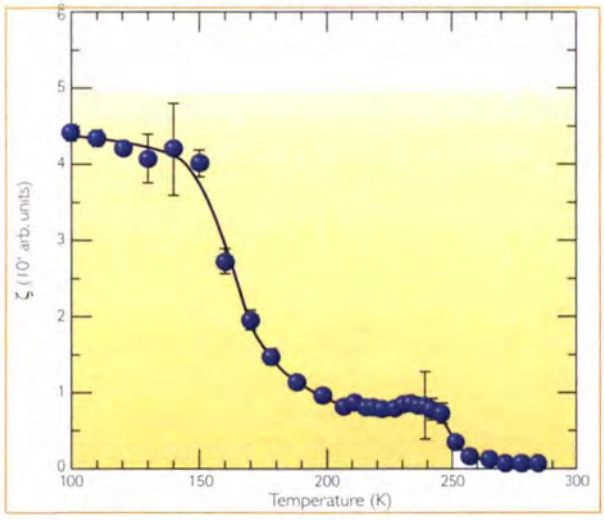

Figure 2: The temperature dependence of the relative non-sphericity parameter for $Y(Mn_{0.4}Fe_{0.6})_2$ derived from Teubner's generalised Kirste-Porod law.

Figure 3: A schematic model of the $Y(MnFe)_2$ "magnetic emulsion" containing magnetic percolation clusters with sharply defined but highly convoluted non-spherical surfaces with extreme Gaussian curvature.

eferences: [1] A Aharony and E. Pytte, Phys. Rev. B 27 (1983) 5872
[2] G. Porod, Kolloid Z. 124 (1951) 83
[3] M. Teubner, J. Chem. Phys. 92 (1990) 4501
[4] R. Kirste and G. Porod, Kolloid Z. Z. Polym. 184 (1962) 1
[5] R. Cywinski, S.H Kilcoyne and C. Ritter, Appl. Phys. A 74 (2002) S865

Personal chemistry

Natalia Skryabina - CNRS, Grenoble – performing an experiment on D1A.

Matthias Elender, instrument technician on IN16.

Isabelle Grillo is now responsible for the ILL chemistry and biochemistry laboratory.

Andrew Harrison (Univ. of Edinburgh) is the new chairman of college 5B (magnetic structures).

chemistry and structure

Paul Henry, College 5A secretary

Whatever family of materials you are interested in, an intimate knowledge of structure is pre-requisite to understanding and controlling physical properties. The neutron is an ideal probe for condensed matter and the advantages of neutron diffraction over, and complementarities to, X-ray diffraction are well documented and need not be repeated here. In the modern world of bigger, better, faster and more, the ILL is at the forefront of providing new and improved instrumentation to satisfy the needs of the scientific community, briefly summarised below.

Instrument/sample environment news - In powder diffraction, the D20 high take-off angle setting, was frequently exploited by users during 2004 and is well represented for experiments scheduled during 2005. Many highlights using this set-up will be presented in the Chemistry and Structure and Magnetism sections of next year's annual report. Also, 2005 will see the installation and commissioning of a radial oscillating collimator on D20. Data collection and refinement on a 30-mg sample of CeO_2 showed the power of the new super-D2B detector. The strain imager SALSA (for engineering applications) collected its first neutrons during 2004 after more than three years of development work, which means that D1A returns to a full-time diffraction instrument in 2005. In single crystal diffraction, the upgrades to the D19 detector array have continued and the new banana detector will be installed and commissioned during 2005. The original blue Fuji image plates on VIVALDI were replaced during 2004 by white Fuji image plates that contain a proportion of Gd_2O_3 giving a three-fold improvement in detection efficiency for thermal neutrons. Separately, a major sample environment project over the last few years has been the development of a new Paris-Edinburgh press (to 10 GPa) compatible with low and variable temperature and its associated cryogenic device (down to 4 K). Commissioning experiments have been performed with this press, which will impact positively on all the major scientific communities (structure, chemistry magnetism, geophysics, etc). With the upgrades to D2B and D20, the long-term future of D1A will be reviewed in 2005, as will the needs of the community in the future for new diffraction instrumentation. One such proposition, DRACULA, is optimised for small samples and extreme conditions comprising a D19-type banana detector and a neutron flux and resolution comparable to the high take-off angle setting of D20. Interesting times lie ahead!

In the modern world of bigger, better, faster and more, the ILL is at the forefront

The number of proposal applications has continued to increase and the subcommittee round in autumn was another record for College 5A (crystallography). It is clear that the number of groups applying for time at the ILL is increasing, and the recent decision by the ILL to award up to 10% of total beamtime allocated to non-member or affiliate countries should further increase this userbase. In order to meet this increased demand, a determined effort has been made to make available as much time as possible to the user community for invited experiments and to further optimise beam use.

It is clear that the number of groups applying for time at the ILL is increasing

The choice of highlights is extremely restricted and only a small part of the science performed at the ILL can be presented here. During the year, two structural studies on spinel based battery electrode materials using D1A by the groups of C. Bellitto et al. and R. Alcántara et al., illustrated the high interest and activity within this technologically important field. A texture analysis of alumina ceramics by D. Chateigner et al. using D1B utilises of Rietveld analysis to provide a basis for the correlation of texture, microstructural parameters and anisotropic properties. Finally an in-situ investigation of the crystallisation of isopropanol simultaneously with measurement of dielectric spectroscopy by M. Jiménez-Ruiz et al., also using D1B, demonstrates that the breakage of the hydrogen-bond network is a precursor step for the crystallisation of isopropanol.

chemistry and structure

Changes in the local structure of $LiMg_yNi_{0.5-y}Mn_{1.5}O_4$ electrode materials during Lithium extraction

R. Alcántara, P. Lavela, and J. L. Tirado *(Universidad de Córdoba, Córdoba)*

E. Zhecheva and R. Stoyanova *(Bulgarian Academy of Sciences, Sofia)*

The effect of composition and preparation temperature on the structure of $LiMg_yNi_{0.5-y}Mn_{1.5}O_4$ compounds were studied. For $y \geq 0.25$, cation ordering in a $P4_332$ superstructure takes place on increasing the annealing temperature from 450 to 750°C. In contrast, a loss of ordering is found for $LiNi_{0.5}Mn_{1.5}O_4$ when the preparation temperature increases from 700 to 800°C. From EPR spectra it is shown that the apparent g-factor is more sensitive towards the magnetic dilution of the Ni^{2+} sublattice by Mg^{2+} or Mg^{2+}/Ni^{2+}, while the line width undergoes little change. Electrochemical lithium extraction in the 5-V region was hindered by the presence of large amounts non-electroactive Mg^{2+} ions. Lithium extraction from $LiNi_{0.5}Mn_{1.5}O_4$ leads to a loss of intensity in the EPR signal as a consequence of the oxidation of paramagnetic Ni^{2+} to diamagnetic Ni^{4+} without significant changes in local environment of Mn^{4+}. For fully delithiated $Li_{1-x}Ni_{0.5}Mn_{1.5}O_4$ oxide, the EPR spectrum from localised Mn^{4+} ions is observed, indicating an exhaustion of paramagnetic Ni^{2+} ions in the vicinity of Mn^{4+} ions. Microstructural and electro-chemical properties of $LiCo_xFe_yMn_{2-(x+y)}O_4$ compounds are also discussed.

Manganese-containing spinels are used as high voltage-electrodes in lithium-ion batteries [1-5]. Structural information based on X-ray and neutron diffraction has revealed cation ordering in the spinel structure. This effect leads to the appearance of a superstructure, which can be indexed in the $P4_332$ space group and is dependent on the magnesium content and the preparation temperature. Thus, on decreasing the Ni/Mg ratio and on increasing the annealing temperature from 450 to 750°C for $LiMg_{0.5}Mn_{1.5}O_4$, low-intensity superstructure lines become visible. The XRD pattern of $LiNi_{0.5}Mn_{1.5}O_4$ and $LiMg_{0.25}Ni_{0.25}Mn_{1.5}O_4$ samples could be indexed in Fd3m corresponding to a high purity spinel phase. In the cubic spinel notation, the lattice constant increases with the Mg amount in $LiMg_yNi_{0.5-y}Mn_{1.5}O_4$ compositions: a= 8.153 Å; a = 8.180 Å, and a= 8.193 Å for y = 0, 0.25, and 1.0, respectively. For $LiMg_{0.5}Mn_{1.5}O_4$, new reflections occur, which are ascribable to a $P4_332$ lattice derived from Mg and Mn ordering in 16d sites of the initial Fd3m structure. The extent of metal ordering in the end members was also examined as a function of preparation temperature. For $LiMg_{0.5}Mn_{1.5}O_4$, significant changes are visible in the X-ray diffraction patterns obtained for samples annealed between 400 and 800°C. On increasing preparation temperature up to 750°C, an increase in the intensity of the superstructure lines is observed, while the changes are less obvious from 750 to 800°C. To overcome the difficulties related to the similar X-ray scattering factors of Mn and Ni, neutron diffraction was used to study $LiNi_{0.5}Mn_{1.5}O_4$. In this sample, a decrease in the intensity and increase in line broadening is observed on increasing preparation temperature. Thus, temperature and annealing time, as well as the presence of other elements such as Ti [1] and Co [2], condition the development of ordering in these systems. Neutron diffraction patterns (D1A instrument) for $LiNi_{0.5}Mn_{1.5}O_4$ obtained at 700 and 800°C showed loss of ordering when the temper-

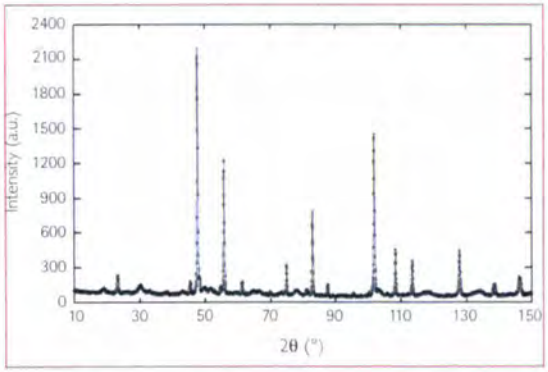

Figure 1: Neutron diffraction patterns of $LiNi_{0.5}Mn_{1.5}O_4$ obtained at 800°C.

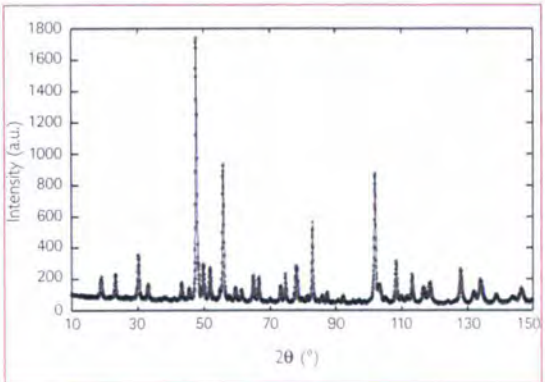

Figure 2: Neutron diffraction pattern of $LiNi_{0.5}Mn_{1.5}O_4$ obtained at 700°C showing additional lines due to a $P4_332$ superstructure.

ature of synthesis was higher (figures 1 and 2). From the well-resolved FTIR spectra, the Ni and Mg cation distribution could be concluded [3].

Electrochemical lithium de-intercalation from $LiNi_{0.5}Mn_{1.5}O_4$ takes place through a two-phase mechanism at ca. 4.7 V, involving the Ni^{2+}/Ni^{4+} redox couple and showing a reversible specific capacity of about 130 mAh/g. The extension of the 4.7 V region decreases with increasing Mg-content. Nevertheless, cycling in the 3 V region, which implies lithium insertion in octahedral sites (16d) along with Mn^{4+} reduction to Mn^{3+}, leads to an extended plateau in which capacity increased with annealing temperature for $LiMg_{0.5}Mn_{1.5}O_4$ samples (figure 3).

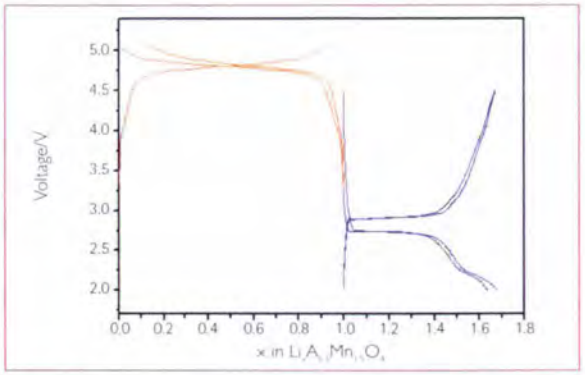

Figure 3: Typical voltage-curves for $Li_xMg_{0.5}Mn_{1.5}O_4$ (blue line) and $LiNi_{0.5}Mn_{1.5}O_4$ (red line).

The $LiNi_{0.5}Mn_{1.5}O_4$ compound shows a ferrimagnetic order in the spinel structure below T_N= 130 K. Above the magnetic ordering temperature, some residual antiferromagnetic Ni^{2+}-O^{2-}-Mn^{4+} interactions are preserved, culminating at $T > 450$ K in the paramagnetic state. The EPR spectrum of $LiNi_{0.5}Mn_{1.5}O_4$, recorded in the 140-410 K range consists of resonance absorption characterised by a Lorentzian line shape. On cooling, there is a strong resonance shift, with the apparent g-factor changing from 2.022 to 1.946. In the same temperature range, line narrowing takes place [3]. The signal disappears below 150 K. Thus, the EPR response from $LiNi_{0.5}Mn_{1.5}O_4$ can be associated with the residual antiferromagnetic correlations between Ni^{2+} and Mn^{4+} ions. The EPR spectra of Ni-Mg-Mn spinel oxides show significant changes in resonance shift when diamagnetic Mg^{2+} ions substitute paramagnetic Ni^{2+} ions in the spinel framework [3]. The changes in line-width are less abrupt. The EPR behavior of $LiMg_{0.5}Mn_{1.5}O_4$ is determined from localized Mn^{4+} ions. The extraction of lithium from $LiNi_{0.5}Mn_{1.5}O_4$ samples leads to EPR signal intensity loss as a consequence of the oxidation of paramagnetic Ni^{2+} by diamagnetic Ni^{4+} without significant changes in local environment. The fully delithiated oxide shows a different spectrum exclusively caused by Mn^{4+} ions but different to that of $LiMg_{0.5}Mn_{1.5}O_4$ samples also ascribed to this ion. The predominance of superexchange ferromagnetic interactions in the latter would justify the different profiles. Li reinsertion in $LiNi_{0.5}Mn_{1.5}O_4$ shows a good recovery of the initial properties, making evident the notorious reversibility of this cathode material.

Rietveld refinement of neutron diffraction patterns of $LiCo_{0.2}Fe_{0.2}Mn_{1.6}O_4$ (Fd3m s. g.) shows that best fitting is obtained when 8a site occupancy is restricted to lithium ions [2]. The refinement shows the complete occupancy of 16d sites by cobalt, iron, and manganese ions in stoichiometric ratios. For $LiCo_xFe_yMn_{2-(x+y)}O_4$ compounds the incorporation of iron and cobalt in the manganese spinel changes the shape of the voltage vs capacity curves in both the charge and discharge branches. Thus, for a manganese substitution lower than one manganese per formula ($x + y < 1$) an extended pseudo-plateau at ca.4 V is observed, which corresponds to oxidation from Mn^{3+} to Mn^{4+} [2]. A maximum reversible capacity of ca. 130 m Ah/g is achieved for $LiCo_{0.2}Fe_{0.2}Mn_{1.6}O_4$ in the complete potential range, including 4- and 5-V pseudo-plateaux. However, the progressive substitution of manganese (up to $x + y = 1$) results in a reduction of the 4-V region and an increase of the extension of a 5-V pseudo-plateau. For $LiCo_{0.8}Fe_{0.2}MnO_4$, ^{57}Fe Mössbauer spectra reveal high-spin Fe^{3+} ions in octahedral coordination in the pristine sample, which are oxidized to tetravalent iron ions upon electrochemical lithium extraction near 5 V and through a single cubic phase mechanism [2, 5].

References: [1] R. Alcántara, M. Jaraba, P. Lavela, J. L. Tirado, Ph. Biensan, A. de Guibert, C. Jordy and J. P. Peres, Chem. Mater. 15 (2003) 2376
[2] R. Alcántara, M. Jaraba, P. Lavela and J. L. Tirado, Chem. Mater. 15 (2003) 1210
[3] R. Alcántara, M. Jaraba, P. Lavela, J. L. Tirado, E. Zhecheva and R. Stoyanova, Chem. Mater. 16 (2004) 1573
[4] P. Strobel, A. Ibarra-Palos, M. Anne, C. Poinsignon, and A. Crisci, Solid State Sci. 5 (2003) 1009
[5] R. Alcántara, M. Jaraba, P. Lavela, J. L. Tirado, J.C. Jumas and J. Olivier-Fourcade, J. Power Sources 135 (2004) 281

chemistry and structure

Effect of doping $LiMn_2O_4$ spinel on its use as cathodes in Li-ion batteries

C. Bellitto, E.M. Bauer and G. Righini *(Istituto di Struttura della Materia del CNR, Roma)*

M.A. Green and W.R. Branford *(The Royal Institution of Great Britain, London)*

A. Antonini and M. Pasquali *(Università degli Studi "La Sapienza" di Roma, Roma)*

$LiMn_2O_4$ spinel is a promising cathode material for Li-ion batteries, and doping it with small amounts of other metal ions has a remarkable effect on its electrochemical properties. In order to elucidate the relationship between structure and the electrochemical performance of doped compounds, with the general formula $Li_{1+y}Mn_{2-x}M'_xO_4$ ($x \leq 0.1$; $y \leq 0.02$, M'=dopant metal ion), powder neutron diffraction experiments have been coupled with electrochemical data. Whereas the capacity of the spinels doped with trivalent metal ions is much greater, cyclic fading properties are much enhanced with the use of divalent metal ions. It is suggested that the occupancy of the tetrahedral sites is critical to the improved structural stability on Li insertion/extraction, but that this ultimately hinders the movement of Li.

The lithium rechargeable battery based on $LiCoO_2$ as a cathode, is today enjoying a great deal of commercial success as an energy storage device, particularly in the field of high performance portable electronics [1]. However, the search for enhanced cost-performance cathode materials represents an important goal, as $LiCoO_2$ is relatively expensive and produces some environmental issues. In this respect, $LiMn_2O_4$ has attracted considerable interest. Even though the performance of $LiMn_2O_4$ based batteries remains inferior to other systems, they offer benefits in cost/performance characteristics. $LiMn_2O_4$ crystallises in a cubic spinel structure, *Fd-3m* space group, where the lithium and manganese occupy the tetrahedral (*8a*) and the octahedral sites (*16d*), respectively, and the oxygen ions are located to the (*32e*) sites. Recent research has showed that the substitution of various trivalent ion dopants into the $LiMn_2O_4$ framework makes significant improvements to the electrochemical performance [2-4].

In order to correlate the reduction of capacity on de/re-intercalation (cyclic fading profile) and structural parameters, we have studied a series of doped compounds of formula $Li_{1+y}Mn_{2-x}M'_xO_4$ ($x \leq 0.1$; $y \leq 0.02$) by a combination of neutron diffraction measurements and electrochemical experiments [5]. The powder neutron diffraction technique is particularly sensitive to cation distribution in the crystalline lattice and the large contrast between the scattering length of transition metal ions and both lithium and manganese allows accurate location of the doping ions in the lattice despite their low concentration. The diffraction powder patterns were collected at room temperature on the D1A diffractometer and the structural and profile analyses refinements were carried out by the Rietveld method (GSAS), (figure 1).

Doping the $LiMn_2O_4$ spinel with small amounts of trivalent (figure 2) and divalent metal ions (figure 3) has a remarkable effect on the electrochemical characteristics. The Ni- and Ga/Cr doped systems show the best performance and at the same time they possess low fade rates ($4.5 \cdot 10^{-2}$ mAh/g cycle) and higher capacities (111 and 117 mAh/g, respectively). However, whereas the absolute capacity of the *Zn*- and the *Mg*-doped spinel is lower (95 and 103 mAh/g, respectively), the cyclic fading performance is significantly better. This is thought to be associated with the occupancy of the tetrahedral sites by Zn and Mg [6].

Neutron diffraction analysis has confirmed the presence of Zn(II) ion on the tetrahedral sites of the spinel lattice, while all the other doping ions, irrespective of

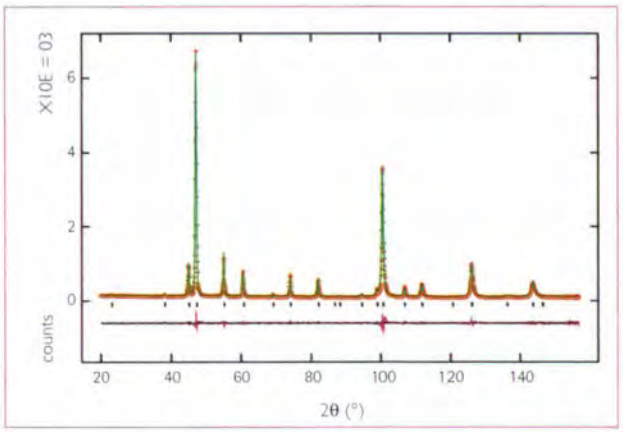

Figure 1: Neutron powder diffraction of $Li_{1.02}Mn_{1.95}Ni_{0.05}O_4$ taken at room temperature, showing the (+) experimental data, calculated (solid line) and the difference.

charge, are located on the octahedral sites (*16d*). Incorporation of all of the doping ions, with the exception of the Ti(IV) ion, reduces the lattice parameter a with respect to the undoped one, while remaining in the *Fd-3m* space group. The A-site of the spinel is fully occupied by Li^+ in all samples, except for those doped with Zn. In the latter, the Zn ions are confirmed to remaining on the A site during electrochemical cycling and therefore acting as pillars supporting the lattice framework during Li removal. The capacity fading is lower for samples with the lower unit-cell parameters *a*. Divalent ions (Zn, Ni) provide the lowest cyclic fading, followed by trivalent ions (Co, Cr), and by Ga-doped material. The underlying reason behind ordering of Zn ions occurs in the empty tetrahedral (*8a*) site, which then hinders full Li re-insertion. The electrochemical behaviour of the Ti(IV)-doped material is similar to that observed in the undoped Mn spinel. This suggests that Ti^{4+} ion substitutes the Mn^{4+} ion in the spinel structure, and this accounts for the larger *a* parameter of Ti-doped spinel over that

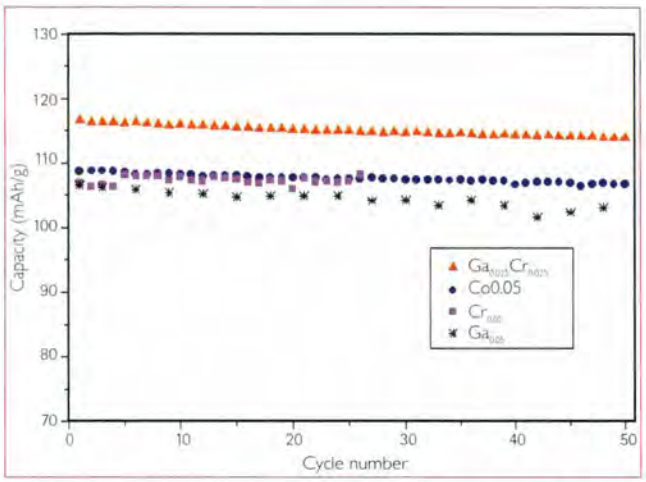

Figure 2: Discharge capacities of M(III) ion doped spinels $Li_{1.02}Mn_{2-x}M_xO_4$ (x<0.05), M(III) = Co, Cr, Ga and Ga/Cr, measured at room temperature and at C/2 discharge-charge rate.

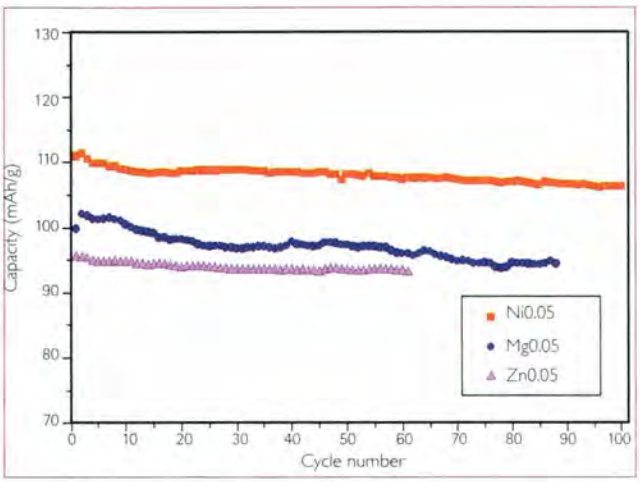

Figure 3: Discharge capacities of M(II)-ion doped spinels $Li_{1.02}Mn_{2-x}M_xO_4$ (x<0.05), M(II) = Zn , Ni, Mg, measured at room temperature and at C/2 discharge-charge rate.

reside also on the (*8a*) sites [6]. For these Zn samples the excess Li is displaced on the octahedral (*16d*) site. The substitution of Li in (*8a*) with such divalent ions as Zn(II) and Mg(II) does bring about significant structural stability during electrochemical cycling. The average charge on the A-sites increases while the charge of the B-site decreases compared with the undoped sample. As each oxygen ion is coordinated with one A cation and three B cations, creating a distorted octahedron, then the increase in charge on the A site can alleviate the distortion. A second factor relates to the doping ions the improved electrochemical properties with reduced lattice parameters may be related to the increased stability in the more compact and undistorted lattice, which is more resilient to the volume changes occurring during Li extraction/insertion. It should also be noted that the samples with the most attractive capacity properties have a 1st-cycle charge/discharge efficiency of 97-99%, indicating an easy reinsertion of extracted Li^+. However, the *Zn* containing samples have an efficiency of only 90%, thereby causing reduced capacity. It is probably that as Li^+ is extracted, some of the undoped one, and the ratio $Mn^{3+}/Mn^{4+} \geq 1$ causes increased prominence of the Jahn-Teller effect and a poorer electrochemical performance.

In conclusion, with a combination of neutron powder diffraction and electrochemical experiments we have shown the relationship between the metal-ion site occupancy of doped $LiMn_2O_4$ spinels and the electrochemical performance of these cathode materials in term of capacity and stability to the charge-discharge cycling.

References: [1] See for example "Lithium Ion Batteries : Fundamentals and Performance" Eds M.Wakikara &O.Yamamoto ,Wiley-VCH (1998)
[2] G. Pistoia, A.Antonini, R. Rosati, C. Bellitto and G.M. Ingo, Chem. Mater. 9 (1997) 1443
[3] A. Antonini, C. Bellitto, M. Pasquali and G. Pistoia, J. Electrochem. Soc. 145 (1998) 2766
[4] C. Bellitto, M.G. DiMarco, W.R. Brandford, M.A. Green and D.A. Neuman, Solid State Ionics 140 (2001) 77
[5] C. Bellitto, E. M. Bauer, G. Righini, M.A. Green, W.R. Brandford, A. Antonini and M. Pasquali, J. Phys. and Chem. of Solids, 65 (2004) 29
[6] T. Ohzuku, S. Takeda and M. Iwanaga, J. Power Sources 81-82 (1999) 90

chemistry and structure

Hydrogen-bond network breakage as a first step to isopropanol crystallisation

M. Jiménez-Ruiz *(ILL)*
A. Sanz, A. Nogales and T.A. Ezquerra *(CSIC, Madrid)*
D. Martín y Marero *(CSIC, Zaragoza)*

Here we present an experimental study of isopropanol crystallisation in real time by means of a novel experimental set-up combining simultaneously structural measurements with dynamical techniques. This set-up, developed at the ILL, consists of a sample cell that allows simultaneous measurements of neutron diffraction (ND) and dielectric spectroscopy (DS) [1]. By performing the simultaneous experiment, information can be obtained from both phases, amorphous and crystalline, and this can provide a complete description of the changes occurring during the crystallisation process. The use of this novel set-up allowed us to demonstrate that breakage of the hydrogen-bond network is a precursor step for the crystallisation of isopropanol [2].

Glass forming liquids are a class of materials that can be maintained out of equilibrium in the amorphous state, without crystallising. Below the equilibrium melting temperature, the supercooled liquid is thermodynamically unstable due to its higher free energy as compared to that of the crystal, and consequently above the glass transition temperature T_g, the supercooled liquid tends to reduce its free energy by undergoing a first order phase transition. By means of this transition, referred to as crystallisation, molecules self-assemble forming crystals. In order to obtain precise information about the changes occurring in a supercooled liquid during crystallisation, a real time experiment may be crucial since it allows us to monitor simultaneously and in real time both the crystal development and the dynamic changes occurring in the amorphous phase. Therefore, an improvement in the understanding of crystallisation in terms of interrelation between crystalline and amorphous development can be obtained when diffraction experiments are simultaneously accompanied by dielectric spectroscopy.

Recently we have developed an experimental set-up which allows us to perform, for the first time, simultaneous measurements of time resolved neutron diffraction (ND) and dielectric spectroscopy (DS) [1]. A picture of the ND-DS sample holder is shown in figure 1. The liquid is placed in a container between two metallic electrodes and is subjected to an alternating electric field of angular frequency ω. Dielectric spectroscopy measures the complex dielectric permittivity $\varepsilon^* = \varepsilon' - i\varepsilon''$ as a function of frequency, where ε' is the dielectric constant and ε'' is the dielectric loss, and is a very suitable method to study molecular dynamics in liquids above T_g. Simultaneous ND and DS experiments

Figure 1: Picture of the neutron diffraction — dielectric spectroscopy cell (ND-DS).

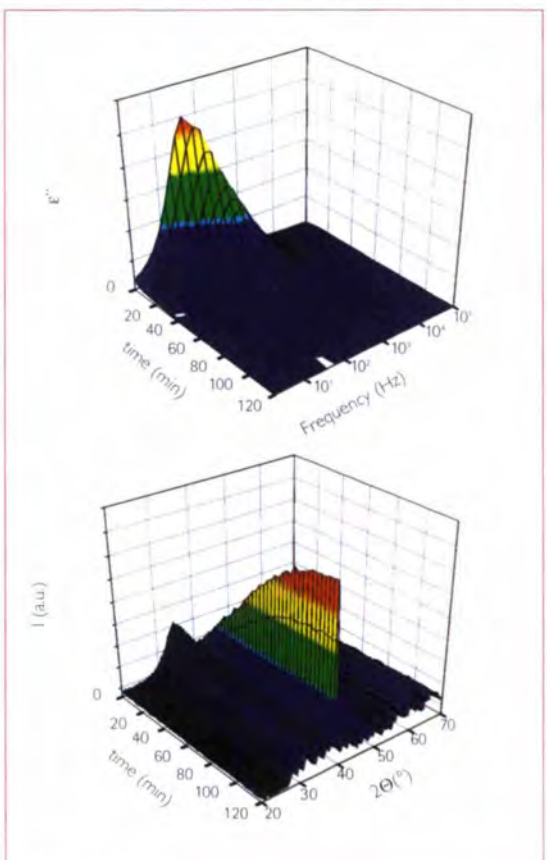

Figure 2: Simultaneous dielectric loss spectroscopy (DS) (top) and neutron diffraction (ND) (bottom) experiments as a function of time during an isothermal experiment (T = 139 K). The ND patterns were recorded with an acquisition time of 3 min.

were performed on the diffractometer D1B at a fixed wavelength of $\lambda = 2.52$ Å. Dehydrated deuterated isopropanol (2-propanol D8) was quenched in the glassy state at 75 K from room temperature. Crystallisation temperatures, T_c, were reached by heating the sample from 75 K up to T_c. Figure 2 presents ND-DS data during a crystallisation experiment at $T_c = 139$ K. The ND intensities are given as a function of the scattering angle 2Θ and the ε'' data from DS are presented as a function of frequency. The initial amorphous state is characterised by an amorphous halo in the ND diagram and by the primary relaxation process of isopropanol in the DS data. As time increases, the onset of crystallisation is denoted by the incipient appearance of Bragg peaks in the ND patterns and a decrease of the dielectric relaxation intensity.

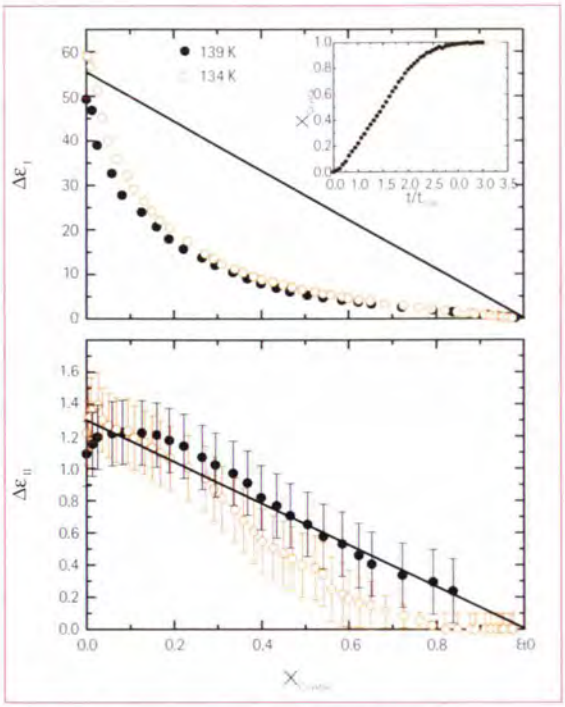

Figure 3: The relaxation strength of each process for the primary $\Delta\varepsilon_I$ (upper plot) and the secondary $\Delta\varepsilon_{II}$ (lower plot) relaxation processes as a function of crystallinity.

The dielectric losses are described considering two relaxations: primary and secondary, being Cole-Davidson processes. The fraction of relaxing species can be estimated from the relaxation strength that corresponds to the area below each relaxation. Figure 3 shows the area ($\Delta\varepsilon$) below the primary and the secondary relaxation as a function of the crystallinity, estimated from the ND data at $T_c = 139$ K. Primary relaxation (figure 3, top) decreases dramatically in the first stages of crystallisation and shows a strong deviation from the two-phase model (phases that correspond to network and crystalline). This can be interpreted as due to the existence of an intermediate step between the situation in which the molecule is in the network and that in which it occupies a position in the crystal. On the other hand the dynamics of the hydrogen-bond network, represented by the mean average frequency of the relaxing species F^I_{max}, shows an increase in the initial crystallisation stages [2]. Both experiments and computer simulations, indicate that in hydrogen-bonded liquids the primary relaxation time is described by the wait-and-switch model [3-5]. First a molecule of the network switches its position to reorient itself, but it must wait until a favourable condition for reorientation exists in the network. The mean relaxation, time $\tau=1/(2\pi F_{max})$ is expected to depend inversely upon the number density of available hydrogen bonding sites [4]. Therefore, in our case, interpreting the decrease of $\Delta\varepsilon_I$ as due to a depletion of the hydrogen-bond network is consistent with a parallel increase of the available hydrogen-bond sites as indicated by the increase of F^I_{max}. Secondary relaxation (figure 3, bottom) follows the two-phase model and the associated process appears as a consequence of the collective motions in the amorphous phase above T_g. Consequently, $\Delta\varepsilon_{II}$ is expected to decrease with increasing crystallinity as shown in figure 3 (bottom). Moreover, in this case the observed decrease is much closer to two-phase behaviour, indicating that the relaxing species, which are lost in the amorphous phase, are almost completely transferred to the crystalline phase.

In conclusion, the first simultaneous experiment allowed us to confirm that a breakage of the hydrogen-bond network occurs as a first step in the formation of crystals during the crystallisation of isopropanol.

References: [1] M. Jiménez-Ruiz, A. Sanz, A. Nogales and T.A. Ezquerra, Rev. Sci. Instr. 76 (2005) 043901
[2] A. Sanz, M. Jiménez-Ruiz, A. Nogales, D. Martín y Marero and T.A. Ezquerra, Phys. Rev. Lett. (2004) 015503 93
[3] P. Petong, R. Pottel, & U Kaatze, J. Phys. Chem. A. (1999) 6114-6121 103
[4] T. Sato and R. Buchner, J. of Chem. Phys. (2003) 4606-4621 118
[5] L. Saiz, E. Guàrdia and J.-A. Padro, J. of Chem. Phys. (2000) 2814-2833 113

chemistry and structure

Combined analysis of textured alumina ceramics by neutron diffraction

E. Guilmeau *(National Institute of Advanced Industrial Science and Technology, Osaka)*

D. Chateigner *(CRISMAT-ENSICAEN Laboratory, Caen)*

T.S. Suzuki and Y. Sakka *(National Institute for Materials Science, Tsukuba)*

C. Henrist *(University of Liège)*

B. Ouladdiaf *(ILL)*

The orientation distributions of α-Al_2O_3 textured ceramics are determined from neutron diffraction spectra. A curved position-sensitive detector coupled to a tilt angle (χ) scan allowed treatment of the whole diffraction pattern in a Rietveld-WIMV-Popa algorithm. Four textured alumina ceramics were prepared by slip-casting under a high magnetic field and sintered at 800°C, 1300°C, 1400°C and 1600°C. With increasing sintering temperature, the texture strength is enhanced and the c-axis distribution is sharper.
The effectiveness of this approach for determining crystallite size is also evident. As a global trend, the calculated crystallite size and observed grain size are similar and increase with increasing sintering temperature. We see here the power of Rietveld texture analysis to provide a basis for the correlation of texture, microstructural parameters and anisotropic properties.

Texture analysis is being increasingly recognised as an important tool in the characterisation of many polycrystalline materials in order to understand their anisotropic properties. The development of texture in α-Al_2O_3 ceramics is required to improve thermal conductivity, optical, and mechanical properties [1, 2]. The particular type of texture often found in α-Al_2O_3 textured materials is an axially symmetric fiber texture (*i.e.*, random in-plane distribution of crystallite a and b axes). This type of texture can be best characterised by the c-axis orientation distribution, but in the case of slightly oriented materials, this is difficult to measure using X-rays because of the low structure factors of all the (00*l*) reflections. To overcome this problem, the solution is to calculate the orientation distribution of the crystallites from several other (*hkl*) distributions, *i.e.*, to acquire as many pole figures as possible for the non-parallel (*hkl*) crystallographic planes. In this paper, we used an approach that combines classical Rietveld, analysis with texture and crystallite size analysis, as implemented in the MAUD software [3]. We illustrate the advantages to analyse jointly structure, texture and microstructure of α-Al_2O_3 ceramics. The mechanism of texture development during the sintering treatment is discussed.

The materials were processed using the slip casting method [4]. A high magnetic field of 10T, parallel to the slip casting direction, was applied to a suspension of fine α-Al_2O_3 spherical particles (∅~150 nm) at room temperature. Due to the anisotropic magnetic susceptibility of the hexagonal structure, a high magnetic field applied during the slip casting is highly effective in rotating the particles and generating a (001) preferred orientation parallel to the magnetic field. After slip casting, four samples were prepared by sintering at 800°C, 1300°C, 1400°C and 1600°C. The specimens were measured using D1B. Diffracted neutrons are collected by a curved position sensitive detector composed of 400 cells spread over 80° (resolution 0.2°) in 2θ. An Eulerian cradle allows χ angle rotation. Scans were performed from $\chi = 0$ to 90° (step 5°) using a fixed incidence angle ω of 35.6° ({006} Bragg position).

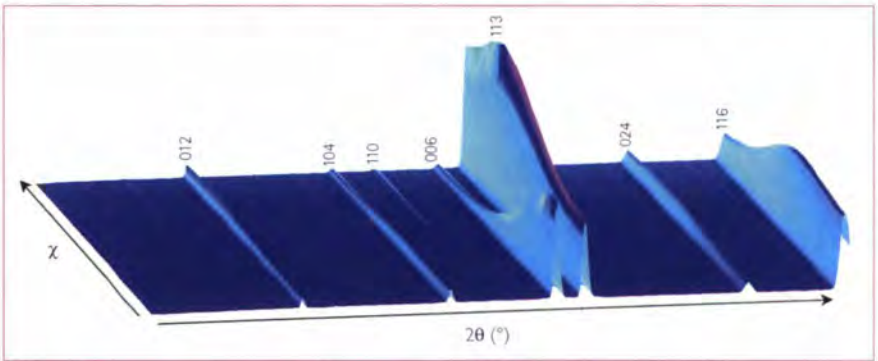

Figure 1: Neutron diffraction patterns for a 0° to 90° χ-scan (sample sintered at 1300°C).

Figure 1 shows a typical neutron diffraction pattern obtained for our samples using a 0 to 90° χ-scan (sample sintered at 1300°C). This graph highlights without ambiguity the (00l) texture of the α-alumina specimen. In particular, we can clearly observe the intensity decrease of the (006)

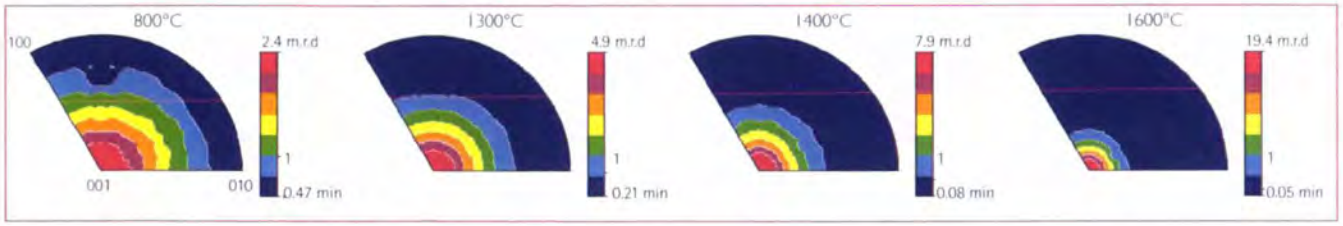

Figure 2: Inverse pole figures calculated for the z fibre direction (parallel to the magnetic field) for samples sintered, respectively, at 800°C, 1300°C, 1400°C and 1600°C. Major (001) component. Linear density scale, equal area projection.

line when χ increases and the appearance of the (110) line when χ tends to 90°. The refinement reliability is established by R_I, R_{PI}, R_{wp} and R_B factors equal to 4.6%, 4.1%, 6.5% and 4.8%, respectively. The corresponding fit/measured visual agreement can be checked elsewhere [5].

The orientation distribution (OD) is represented by inverse pole figures (figure 2) calculated for the z fiber direction (parallel to the magnetic field). This figure illustrates two interesting points. First, it shows that the only component present in the four samples is the (001) crystallographic planes perpendicular to the slip casting direction. Secondly, the degree of orientation is improved for the higher sintering temperatures: the maximum of the distribution density is increased and the c-axis distribution gets sharper. Based on the peak deconvolution (Popa formalism), the calculated crystallite sizes have been found to be equal to 137 nm for the sample sintered at 800°C and larger than 500 nm for samples sintered at 1300°C, 1400°C and 1600°C (crystallite sizes larger than 500 nm are not measurable under our resolution conditions). These sizes are well correlated to the scanning electron microscopy (SEM) analyses where we determined the grain sizes by the linear intercept method on the surface parallel to the magnetic field. The measurement was performed for two scanning directions, i.e. parallel and perpendicular to the magnetic field. The values, reported in Table 1, showed the spherical shape of the grains in a sample sintered at 800°C, where the grain size and the respective aspect ratio increase with increasing sintering time. Table 1 shows a resume of the results. The correlation of the calculated (001) orientation distribution, accessed by the Texture Index values, crystallite sizes, and microstructural observations, clearly proves that the growth of the initial small particles starts at temperatures above 800°C and that enhanced anisotropic grain growth by increasing sintering temperature is an important factor for texture development [5]. This mechanism is consistent with previous conclusions reported in different papers on the texturation of α-Al_2O_3 ceramics [6,7].

In conclusion, the Rietveld texture methodology combined with neutron diffraction is promising for generalising the characterisation of the polycrystalline materials and extending the refinement to the determination of the structure, μstrain [8], and phase proportions.

Specimens (sintering temperature)	ODF (001) inverse pole figure Min	Max	Texture Index (F2)	Refined crystallite size (nm)	SEM Calculated grain size(nm) $d_{//}$	$d_{\perp}$	Aspect Ratio ($d_{\perp}/d_{//}$)
800°C	0.47	2.4	1.24	137 (13)	~150	~150	1
1300°C	0.21	4.9	2.13	> 500 nm	1100	1170	1.063
1400°C	0.08	7.9	3.16	> 500 nm	2610	2970	1.138
1600°C	0.05	19.4	7.78	> 500 nm	7300	8800	1.205

Table 1: Minima and maxima of (001) inverse pole figures and texture index. Refined crystallite size (Popa formalism) and calculated grain size by line intercept method (SEM analysis), parallel ($d_{//}$) and perpendicular ($d_{\perp}$) to the magnetic field direction.

References:
[1] T. Carisey, I. Levin and D. G. Brandon, J. Eur. Ceram. Soc. 15 (1995) 283
[2] E. Suvaci and G. L. Messing, J. Am. Ceram. Soc. 83 (2000) 2041
[3] L. Lutterotti, S. Matthies and H. R. Wenk, Proceedings of the 12th International Conference on Textures of Materials, Vol. 2, 1999, 1599. Montreal: NRC Research Press., Freeware available at: http://www.ing.unitn.it/~luttero/maud/
[4] T. S. Suzuki, Y. Sakka and K. Kitazawa, Adv. Eng. Mat. 7 (2001) 490
[5] E. Guilmeau, D. Chateigner, T. Suzuki, Y. Sakka, C. Henrist, and B. Ouladdiaf, Chem. Mat. 17 (2005) 102-106
[6] A. Böcker, H. J. Bunge and J. Huber, W. Krahn, J. European. Cer. Soc. 14 (1994) 283
[7] M. M. Seabaugh and G. L. Messing, J. Am. Ceram. Soc. 83 (2000) 3109
[8] M. Morales, D. Chateigner, L. Lutterotti and J. Ricote. Mat. Sci. For. 408-412 (2002) 113

No strain, no gain!

Abdel Benmarouane (Univ. Rennes) pointing out the power of texture at ILL to Husin Sitepu (SRC, Canada).

John Bouchard (British Energy), Anne Dale, Darren Hughes (FaME38), Richard Burguete (Airbus UK) taking the strain out of a day of stress at the Engineering workshop.

The SALSA team. From the left: Pierre Thomas, Roland Gandelli, Steven Rowe, Marc Jacques, Loick Pajou, Jean-Marc Delpierre, Amandine Bouvier, Thilo Pirling, Giuliana Manzin and Giovanni Bruno.

materials

Tilo Seydel, College 7 Secretary

Materials science at the ILL makes a particularly broad use of the available neutron scattering techniques and instrumentation. Its methods range from imaging and diffraction to spectroscopy and include highly specialised tools such as surface reflectometry and backscattering. Both structural and dynamic properties on molecular scales are investigated in this vastly interdisciplinary field to elucidate questions related to composition and functioning of modern materials. The unique properties of neutrons to probe the magnetic behaviour of samples are equally exploited.

Providing a link between fundamental research and a potential industrial benefit

Materials science is a field where experiments are frequently motivated by engineering and possible applications, thus providing a link between fundamental research and a potential industrial benefit. It is often this motivation that distinguishes ILL's college 7 from topically neighbouring colleges, such as crystallography and magnetism (college 5). Examples of materials studied using neutrons include, for instance, metals and ceramics, catalysts and magnetic films, as well as biomaterials, clathrates and zeolites. Materials are thereby studied both with view at bulk or at surface or interface properties. Due to restrictions in space in this booklet, the examples selected for this chapter can provide just a glimpse of the magnitude of the subject area.

Clay mineral nanoparticles are a class of materials very much in the focus of current scientific interest in particular with view at their complex interaction with water. Actual and potential applications of clays range from car painting and cosmetics to nuclear waste management. Some clay minerals occur naturally whilst an enormous quantity is nowadays produced artificially. In a study using neutron diffraction amongst other techniques, E. Rinnert and co-workers investigate the structure upon hydration of saponite clays. By combining the experimental results with information from numerical simulations they infer on the status and orientation of water molecules of the swelling clays.

Degradation of ancient books and the resulting loss of cultural heritage is a serious concern to libraries. Giving an example of recent biomaterials research applying neutron small-angle scattering, C. Mondelli and co-workers report on a study aiming at understanding the correlation between the degradation of paper and the degree of crystallinity of the cellulose it consists of. Their ongoing work points towards the fact that the degradation process may induce changes in the microfibrillar arrangement of the cellulose.

The term "agostic" is derived from Greek and roughly translates into "to hold on to oneself". In organometallic chemistry "agostic" commonly refers to a somewhat unusual CH - metal bonding interaction, and there has been recently much interest in further understanding this class of interactions. W. Baretta and co-workers have used neutron diffraction to establish the non-classical nature of the agostic interaction. Their results may contribute to the design of new coordinatively unsaturated metal complexes.

The importance of materials research carried out using both neutron and synchrotron radiation scattering techniques is stressed by the presence of the Facility for Materials Engineering

The importance of materials research carried out using both neutron and synchrotron radiation scattering techniques, on the joint ILL/ESRF campus, is underlined by the presence of the Facility for Materials Engineering (FaME38). This new facility provides all means to support visiting researchers from academia and industry. Some of its infrastructure and services are summarised in the contribution by A. Steuwer et al.

materials

Structural properties of cellulose in ancient paper with different states of degradation

C. Mondelli *(INFM-OGG ILL)*
M. Missori *(Istituto Centrale per la patologia del Libro, Rome)*
C. Castellano and A Congiu *(University of Rome)*
R. Schweins *(ILL)*

Protecting ancient hand-made paper from decay poses a serious problem for numerous libraries, archives and museums all over the world. In order to develop the appropriate conservation methods, an advanced knowledge of the state of conservation of the artwork and of the degradation process that affect them is imperative. The aim of this research is to investigate by neutron techniques cultural heritage of biological origin such as the writing supports and, in particular, paper.
While some aspects of paper degradation such as acid hydrolysis and oxidation are quite clear, few information is available in literature about the correlation between the state of degradation of ancient paper and the structure of the cellulose, in particular its crystallinity. We have recently performed a SANS experiment in order to correlate the state of degradation of our paper samples to the crystallinity of their cellulose.

An important part of the preservation of cultural heritage consists of limiting as much as possible the deterioration of hand-made paper artefacts such as books, documents or artistic drawings present in numerous libraries, archives and museums all over the world. In order to define appropriate conservation methods, a detailed knowledge of the degradation processes that affect ancient paper is necessary.

Paper sheets are quite complex materials consisting in a felt of cellulose fibres, which in ancient times was derived from linen, together with other substances, principally gelatine of animal origin, although the materials used depend strongly on the production technique employed [1,2].

The process of paper degradation may be seen as a combination of acid hydrolysis, which deteriorates the mechanical properties of sheets, shortening the cellulose polymeric chains (from the order of 10^4 Å to 10^2 Å), and the so-called "slow-fire" process, caused by the oxidation of the materials present in the paper, followed by the development of carbonyl and carboxyl ligands. The oxidation process causes the mechanical weakening and the discoloration of the remaining substratum [3-5]. Furthermore these processes may be catalysed by the presence of heavy metals. On the other side occasional events such as high levels of humidity, water, fire, UV radiation and so on, can also deteriorate the paper independently of its age. Moreover, the degree of crystallinity of the cellulose is expected to change with time from its native values of 45-65%. Cellulose is a nano-compound of crystallites linked by disordered regions. The cellulose molecule in the crystals forms sheets via hydrogen bonds. Only the disordered regions are accessible from water in an irreversible way, and this phenomenon may be part of the degradation process. However, while the acid hydrolysis and the oxidation have been widely studied by several experimental techniques, there are little information in the literature about the correlation between the state of degradation of ancient paper and the structure of the cellulose, in particular its degree of crystallinity [6].

Figure 1: An example of the watermark present in a paper produced in 1410 in Perpignan.

In order to look at this question, a small-angle neutron scattering (SANS) experiment was done on D11 at the ILL. We have studied several ancient samples coming from end sheets of ancient books, i.e. the sheets of paper used by the bookbinder at the beginning and the end of a book. This is very helpful in order to determine precisely the age of the paper.

Additionally they often present also a watermark (see figure 1), which allows for a precise identification of the

mill where the paper was produced. The ancient paper used in the experiment was not printed. As it was the habit in ancient times, the paper was sized with gelatine in order to improve the paper writing quality.

Samples showing various levels of degradation and discoloration, have been already used for other kinds of investigation [6] and their degradation state has already been characterised by means of optical reflectance spectroscopy [7]. All samples measured are listed in table 1 and shown in figure 2. As shown in the figure, papers produced in the same period may present an astonishing difference in their state of conservation. The sample produced in Milan in 1430 looks like just recently made while the sample produced in Nuremberg, in the XV century looks totally fired. In order to have a reference, we also investigated a controlled system by measuring a modern handcraft pure cellulose Whatman sheet artificially aged. The aging procedure consisted in keeping the sample 28 days at 80°C at a relative humidity of 65% respectively.

Whatman cellulose, modern	aged artificially
Milan, 1430	very good state
Milan, 1430	relative bad state
Nuremberg, XV century	very bad state

The data were collected at $\lambda = 6$ Å in a Q-range between 0.002 and 0.2 Å^{-1}. Only one sheet of paper was used for each sample in order to prevent surface scattering. In order to compare directly the different samples the curves are scaled by their thickness.

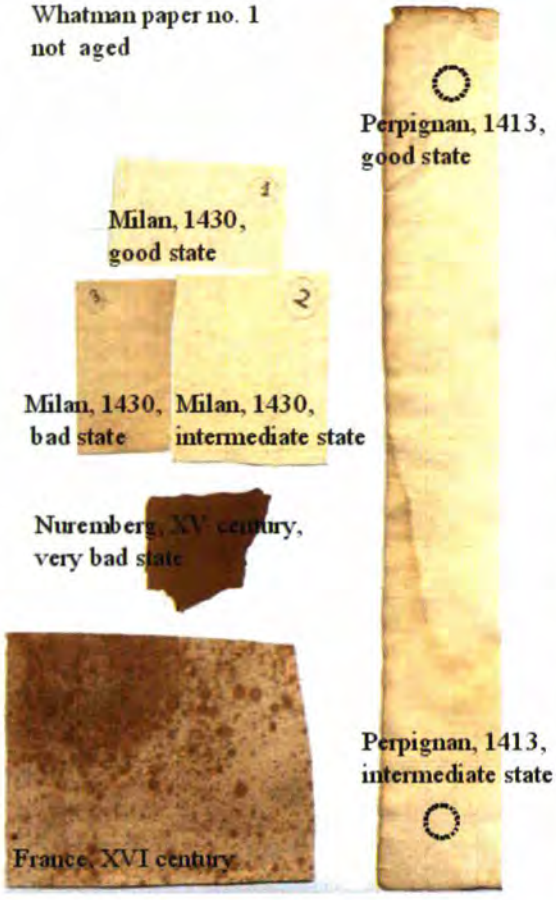

Figure 2: Differences in the visual appearance of various ancient papers produced in the XV century with different degree of degradation.

The preliminary results from SANS are shown in figure 3. The collected data have a high quality, enough to see the differences produced in ancient papers from the deterioration process. A clear trend between the scattered intensity and the state of degradation exists. The main differences appear in the region between 0.02 and 0.1 Å^{-1} corresponding to distances about 100-300 Å, where a small peak whose intensity is larger for the more deteriorated paper is observed. It has been suggested that the origin of the signal in this region is due to a regular arrangement of the cellulose microfibrils [8].

Thus our data indicate that the degradation processes induce non trivial changes in this arrangement. We are currently analysing in detail the data to determine the nature and origin of the changes measured.

With this experiment we also demonstrate that neutrons are a good tool to study rare and precious samples as the specimens of cultural heritage in a non destructive way.

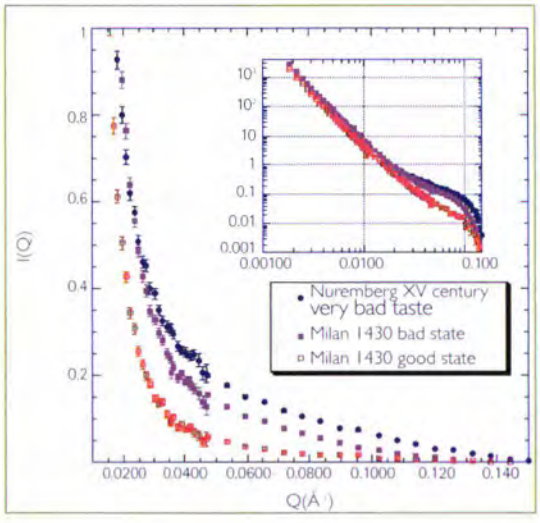

Figure 3: Intensity of integrated SANS signal as a function of Q. We can see that the differences are relevant for different degrees of deterioration even if the sample comes from the same sheet of paper. There is a trend with the degree of deterioration and a weak structuring appears around 0.04 Å^{-1}. In the inset the full measured range is represented in log-log scale, the slope of the linear part is −3.5.

References:
[1] P. Calvini, E. Franceschi and D. Palazzi, Science and Technology for Cultural Heritage 5 (1996) 1-11
[2] A.-L. Dupont, in: D.Vincent, D Alan and P. Smith, Ed., Works of art on paper books, documents and photographs - techniques and conservation, International Institute for Conservation, Baltimore (2002) 59-64
[3] M. Ali, A.M. Emsley, H. Herman and R.J. Heywood, Polymer 42 (2001) 2893-2900
[4] H. Arai, Int. Biodet. & Biodeg. 46 (2000) 181-188
[5] N.L., V. Manturovskaya, Restaurator, Ed. by K.G. Saur Verlag GmbH, Munich, 21 (2000) 85-100
[6] G. Righini, A.L. Segre, G. Mattogno, C. Federici, and P.F. Munafò, Naturwissenschaften 85 (1998) 171-175
[7] M. Missori, M. Righini and S. Selci, Opt. Commun 231 (2004) 99-106
[8] C. Czihak, Thesis of the University of Vienna

materials

Evolution with water content of the structure of water in the interlayer space of synthetic saponite clay minerals

E. Rinnert, C. Carteret and B. Humbert *(UHP-CNRS, Villers-les-Nancy)*
I. Bihannic, M. Pelletier and L.J. Michot *(I.N.P.L.-ENSG-CNRS, Vandœuvre)*
G. Fragneto *(ILL)*
J.D.F. Ramsay *(University of Montpellier)*
A. Delville *(University of Orléans)*
J.-L. Robert *(ISTO, Orléans)*

The interaction of water with synthetic saponite clay samples was investigated by following, along water adsorption and desorption, (i) the adsorbed amount by gravimetric and near-infrared techniques (ii) the molecular structure and interaction of adsorbed water molecules by near infrared (NIR) and Raman spectroscopy under controlled water pressure (iii) the interlayer distance and arrangement of water molecules in the interlayer by X-ray and neutron diffraction under controlled water pressure. The results thus obtained were confronted with Grand Canonical Monte Carlo (GCMC) simulations. Using such an approach, various well distinct hydration steps can be distinguished and the evolution with water content of water structure in the interlayer space can then be studied precisely. In particular, combining neutron diffraction experiments using D_2O and H_2O with GCMC simulations provides detailed information about the status and location of interlayer water molecules.

Swelling clay minerals are formed with two tetrahedral layers (silica) sandwiching an octahedral layer (dioctahedral aluminium hydroxide or trioctahedral magnesium hydroxide) (figure 1). The chemical composition of the sheets includes isomorphic substitutions by less charged cations (e.g. Al^{3+} for Si^{4+} or Mg^{2+} for Al^{3+}). This generates a net negative layer charge compensated by interlayer exchangeable cations whose hydration provokes a swelling of the structure.

Due to their exchange capacity and water retention properties, these minerals are being increasingly used as sealing materials in the design of disposal facilities for hazardous wastes where their main role is to inhibit the migration of contaminants from the waste to the surrounding environment. In that context, understanding the structure and dynamics of water molecules in the interlayer spaces of swelling clay minerals with increasing water chemical potential is of prime importance. Up to now, most experimental work has focused on natural clays with octahedral charge deficit, i.e., montmorillonite and hectorite and has shown that cation hydration is the main parameter controlling water uptake and swelling for water activities ≤ 0.98, in the so-called crystalline swelling regime. This general picture is basically confirmed by numerous simulation studies that can be used to study both the structural and dynamical properties of confined water molecules. In order to overcome the various problems linked with the use of natural heterogeneous samples, we recently carried out a comprehensive study of the status of water in a series of synthetic saponites of general formula $(Si_{8-x}Al_x)\ Mg_6\ O_{20}\ (OH)_4\ Na_x$ with $0.70 \leq x \leq 2$. This was achieved by combining gravimetric water adsorption experiments, Near Infrared and Raman spectroscopic measurements under controlled water relative pressure, Grand Canonical Monte Carlo simulations and X-ray and neutron diffraction experiments under controlled water relative pressure [1]. These latter experiments were carried out at the ILL on the instrument D16 taking advantage of the recently developed controlled humidity chamber. Diffraction patterns were acquired along the water desorption isotherm in reflection on a large q range on oriented clay films using either H_2O or D_2O to vary the contrast between clay layer and interlayer water. Figure 2A presents in the case of the sample with a layer charge of 1.0 the water

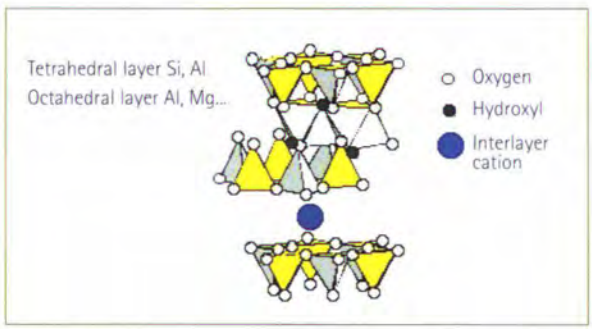

Figure 1: Schematic representation of the structure of a swelling clay mineral.

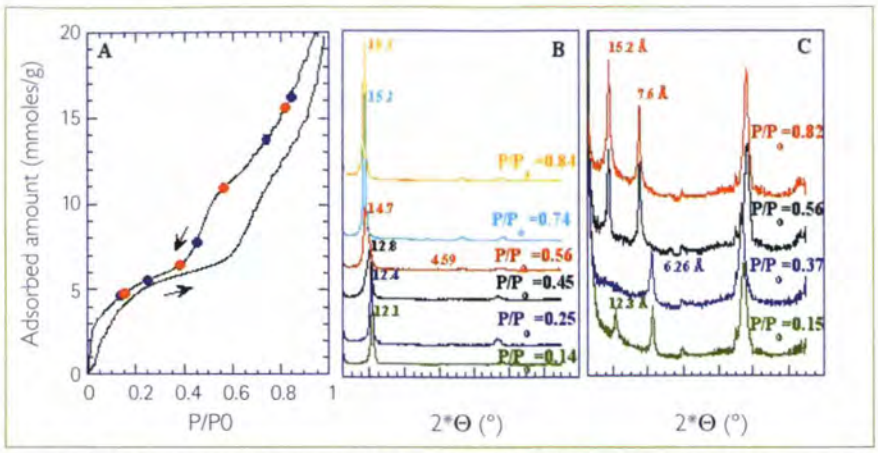

Figure 2: Water adsorption-desorption isotherm (A), H_2O neutron diffraction patterns (B) D_2O neutron diffraction patterns (C) obtained on a synthetic saponite clay (layer charge 1.0).

adsorption-desorption isotherms where blue dots correspond to the neutron diffraction patterns recorded with H_2O (figure 2B) and red dots to those recorded with D_2O (figure 2C).

The use of either isotopes leads to very different diffraction signals. In the case of H_2O (figure 2B), the 001 line is always the highest one and very limited changes in relative intensity are observed with changing relative pressure at constant spacing in agreement with data obtained by X-ray diffraction. In contrast, in the case of D_2O, changes in the amount of adsorbed water provoke strong modifications of the diagrams. The most striking feature is observed for a relative pressure of 0.38 where the (00ℓ) diffraction line is completely extinct. The data obtained by neutron diffraction can be confronted to the amount and positions of water molecules in the interlayer obtained by GCMC simulations. At the extinction point, the interlayer is filled with a well-organised network of water molecules with significant interactions with the clay layer (figure 3, left). The atomic positions derived from GCMC simulations can then be used directly to simulate the neutron diffraction spectra (figure 3, right). It then appears that the extinction of the 001 line is perfectly reproduced. Small differences in the relative intensities of the various peaks can be further exploited to refine the orientation of water molecules.

The same experimental strategy was used all along the water adsorption-desorption isotherm and in combination with results from vibrational spectroscopic studies provides us with a very detailed knowledge of the status and location of water molecules in the interlayer spaces of saponite clays as a function of water content. Modifications in the charge of the samples lead to a shift towards lower relative pressure of all the steps previously defined [2].

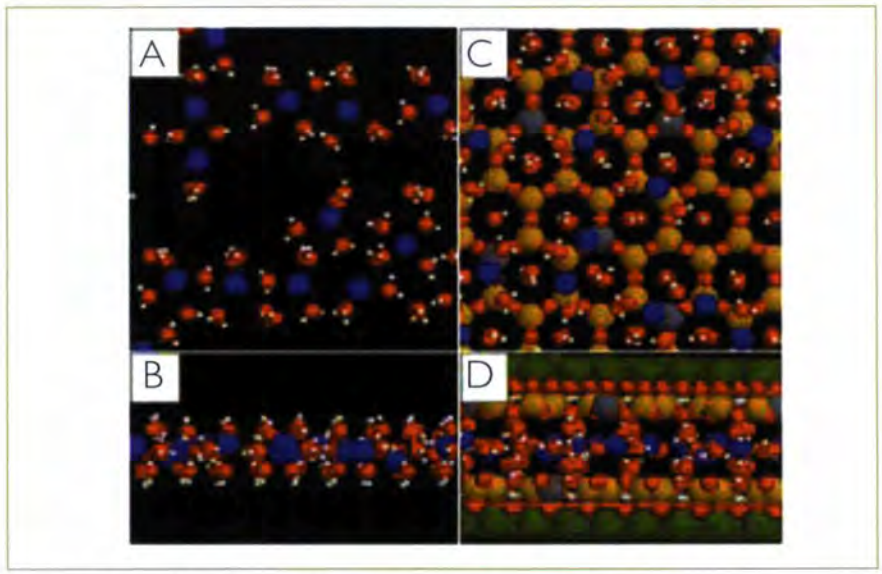

Figure 3: GCMC simulation of the organisation of water in the interlayer of a saponite clay with a layer charge of 1.0 at a relative pressure of 0.40 in desorption. Light grey: Hydrogen, Red: Oxygen, Blue: Sodium, Brown: Silicon, Dark grey: Aluminium, Green: Magnesium. A) view of water in the ab plane ; B) view of water perpendicularly to the c axis; C) and D) with the clay layer.

All these studies can be used as a sound basis to study the dynamical properties of water confined in those materials. Up to now, most dynamical experiments on swelling clay minerals have been carried out considering either the one-layer hydrate or the two layer hydrate whereas our experiments strongly suggest that even at constant spacing very distinct structural arrangements can be obtained. The experimental strategy we would like to apply consists in combining low-frequency Raman experiments, quasi-elastic neutron scattering at beamline IN5, neutron backscattering at beamline IN16 and ^1H NMR relaxometry experiments to probe water dynamics between a few femtoseconds and a microsecond. In parallel, molecular dynamics will be performed to explore time scales between the femtosecond and around 50 ns.

References: [1] E. Rinnert, C. Carteret, B. Humbert, G. Fragneto-Cusani, J.D.F. Ramsay, A. Delville, J.-L. Robert, I. Bihannic, M. Pelletier and L.J. Michot (2004) submitted to J. Phys Chem B
[2] L.J. Michot, I. Bihannic, M. Pelletier, E. Rinnert and J.-L. Robert (2004) in press; American Mineralogist

W. Baratta, P. Rigo *(University of Udine)*
C. Mealli, A. Ienco *(ICCOM-CNR, Florence)*
E. Herdtweck *(TU Munich)*
S.A. Mason *(ILL)*

materials

Non classical metal···H_3C-C agostic interactions in a 14-electron ruthenium(II) system

A neutron diffraction study has established the precise nature of the δ agostic interactions in the complex $RuCl_2[PPh_2(2,6\text{-}Me_2C_6H_3)]_2$ (1). By contrast to classical agostic bonding, it is shown that two ortho-methyl groups of the xylyl substituents interact with the unsaturated metal center through two C-H bonds each. The result is also substantiated by NMR data in solution. Re-examination of all X-ray structures with β, γ, δ and ε M···H_3C-C moieties as well as DFT calculations on models of 1 shows that the agostic interactions span the range between the classical (M···η^2HC) and the non-classical (M···η^2H_2C) types, depending on the number of atoms between the metal and the methyl group.

The coordination of inert C-H bonds to a transition metal is of fundamental interest for stoichiometric and catalytic reactions, with particular regard to the problem of alkane functionalisation via C-H bond activation [1]. Unfortunately, information on the nature of the primary adduct is still very scarce, since saturated hydrocarbons are notoriously unreactive and are very poor ligands [1d]. From DFT calculations a somewhat asymmetric M···η^3-H_2C bonding mode has emerged for adducts between an unsaturated metal center and a methane molecule [2]. This result is in apparent disagreement with the extensive experimental and theoretical information available for agostic complexes that is usually interpreted in terms of dihapto *M···η²-HC* bonding between the unsaturated metal ion and a dangling C-H bond of the same molecular fragment [3].

A neutron diffraction study on the ILL single-crystal diffractometer D19 at 100 K of the 14-electron complex $RuCl_2[PPh_2(2,6\text{-}Me_2C_6H_3)]_2$ (1), precisely defines the geometric features of the δ agostic interaction between the unsaturated metal center and two *ortho*-methyl groups of the xylyl substituents [4] (see different views in figure 1).

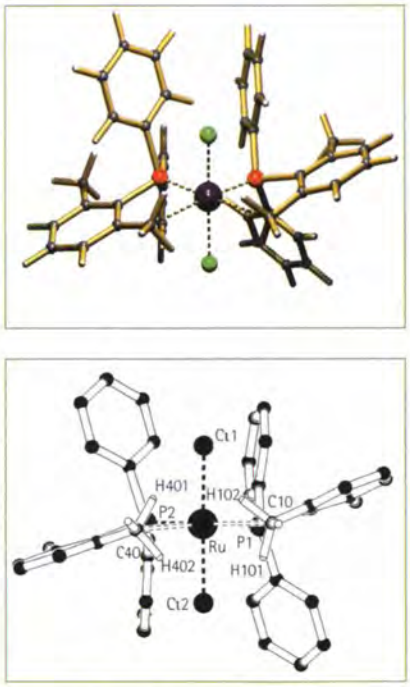

Figure 1: (a) Birds-eye view of the complex 1 in the solid state. Colour code: violet=Ru, red=P, green=Cl, grey=C, white=H (b) View down the pseudo C_2 axis (hydrogen atoms are omitted except those of agostic CH_3 groups).

Two CH_3 carbon atoms lie in the RuP_2 equatorial plane with relatively short non bonding Ru···C distances (2.637(7) and 2.668(6) Å). The correct and accurate location of the *ortho*-methyl hydrogen atoms clearly indicates a double agostic arrangement for each methyl group. In fact, two hydrogen atoms lie closer to the metal and are off the mean plane Ru,P1,P2,C10,C40 (figure 1b), whereas the third hydrogen atom is approximately in the mean plane but away from the metal. For each methyl group the two shorter Ru···H distances are clearly asymmetric (Ru···H101 = 2.507(11), Ru···H102 = 2.113(10) Å and Ru···H401 = 2.137(12), Ru···H402 = 2.399(14) Å). Moreover, ideal M···η^3-H_2C coordination is not achieved because the metal atom does not lie exactly in the CH_2 plane. In spite of the non negligible standard deviations, the geometry of the CH_3 groups is much more reliably determined by neutrons than by X-rays and confirms the perturbing effects of the agostic interaction. The two C-H bonds closest to the metal are slightly longer than the others and particularly significant is the opening of the H-C-H angles subtended by the metal atom. Thus the values of 112.0(8)° and 110.4(10) for H101-C10-H102 and H401-C40-H402 are definitely larger than all the other H-C-H angles at the interacting methyl groups (in

the range 103.8(10) – 104.8(10)°) indicating that the interaction with the metal affects significantly the geometry of the methyl group.

In order to compare the experimental results with those in the literature, we made a survey of all X-ray structures (no neutron data have been previously reported), deposited in the CSD, which feature β, γ, δ and ε M···H_3C-C agostic interactions, as well as a unique case of intermolecular interaction (figure 2).

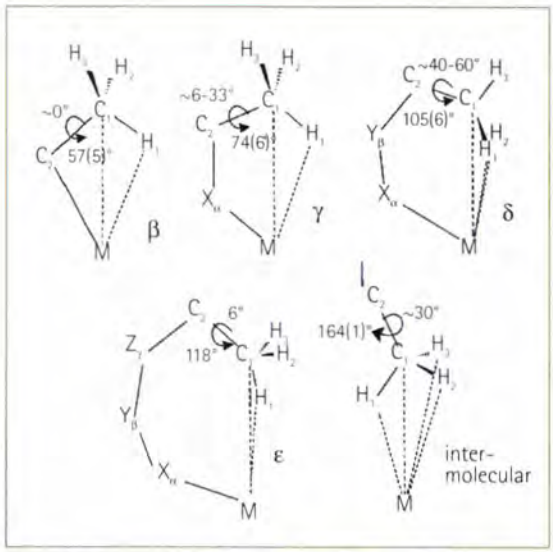

Figure 2: Variation of the methyl torsion about the C1-C2 bond in agostic complexes (β through ε) and in one documented intermolecular case.

In the β agostic complexes, the sp^3 character of the alkylic carbon atom is fully consistent with the metal lying in the C_2,C_1,H_1 plane and this arrangement represents the most classical form of M···η^2-HC interaction. When the angle M···C_1-C_2 is larger than 55° (γ through ε cases), rotation of the methyl group about the C_1-C_2 bond is forced so that the hydrogen atom closest to the metal slips off the $M,C1,C_2$ plane. Such a rotation is progressively larger (< 30° for the γ complexes, > 30° for the δ ones) but, even at the 60° limit, the connectivity between the metal and the agostic methyl group does not allow the metal to attain ideal M···η^3-H_2C coordination.

As shown in figure 3, a linear correlation is found between the angle at the methyl carbon atom and the CH_3 torsion itself related to the different types of metal···methyl connectivity, and the agostic interactions span the range between the classical (M···η^2-HC) and the non-classical (M···η^3-H_2C) types. A solution study of 1 shows intramolecular rearrangement of each xylyl substituent that equilibrates the environments of its two *ortho* CH_3 groups. Activation parameters, evaluated from the analysis of ^1H NMR line shape as a function of temperature, are $\Delta H^{\ddagger} = 9.6 \pm 0.2$ kcal mol^{-1} with $\Delta S^{\ddagger} = -15.4 \pm 0.7$ eu ($CDCl_3$) and are consistent with a relatively strong agostic interaction.

Theoretical calculations reproduce well the non classical Ru···η^3-H_2C agostic mode for the model complex $RuCl_2[PH_3(2,6\text{-}Me_2C_6H_3)]_2$ (1a). and significantly, the classical Ru···η^2-HC agostic geometry features an optimized transition state (for the rotation of the CH_3 group about the external C-C bond) and implies an energy barrier of 3.4 kcal mol^{-1}. Finally, the MO analysis addresses the intrinsic stability of the isolated 14-electron complex $RuCl_2(PH_3)_2$. Calculations of the adduct between the latter and two CH_4 molecules highlight the appreciable involvement of one carbon p orbital in each interaction which is of the ideal non-classical M···η^3-H_2C agostic type.

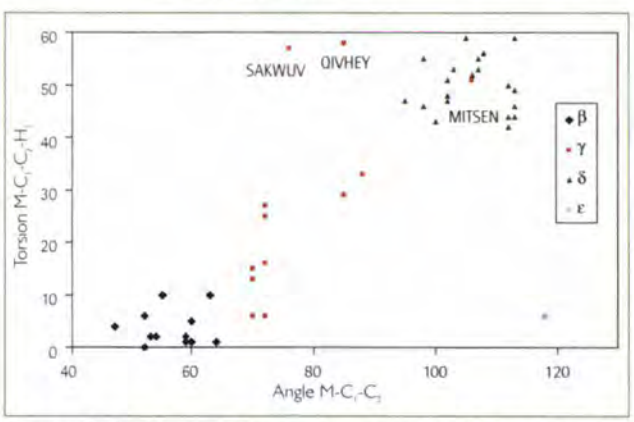

Figure 3: Scatter plot showing the essentially linear relationship between the opening of the M···C_1-C_2 angle and the torsion of the CH_3 group about the C_1-C_2 bond.

In summary, these studies have led to the following important conclusions. A non-classical agostic interaction, where a whole CH_2 group acts as a donor in place of the single C-H bond (M···η^3-H_2C *vs.* M···η^2-HC coordination), has been definitely established, through a neutron diffraction study of 1. For agostic complexes, which have links between the CH_3 group and the metal center, the interaction type depends on the length of the joining chain. For short chains, only the M···η^2-HC coordination mode is allowed but the M···η^3-H_2C type becomes favored for long chains or intermolecular adducts. The present results will be helpful for designing new coordinatively unsaturated complexes as well as for elucidating the key steps in the metal-promoted C-H bond activation of saturated hydrocarbons.

eferences: [1] a) J.A. Labinger and J.E. Bercaw, Nature (2002) 417, 507; b) A.E. Shilov and G. B. Shul'pin, Chem. Rev. (1997), 97, 2879
[2] a) G.S. Hill and R. J. Puddephatt, Organometallics 1998, 17, 1478; b) N. Koga and K. Morokuma, J. Am. Chem. Soc.(1993) 115, 6883
[3] M. Brookhart, M.L.H. Green and L.-L. Wong, Prog. Inorg. Chem. (1988) 36,
[4] W. Baratta, C. Mealli, E. Herdtweck, A. Ienco, S.A. Mason and P. Rigo, J. Am. Chem. Soc.(2004) 126, 5549

materials

FaME38 – A leap into the Void

A. Steuwer, P.J. Webster, Z. Chen, D.J. Hughes, N. Roche, B. Malard, N. Ratel and M. Peel
(FaME38 at the ILL)

FaME38, the Facility for Materials Engineering at the ILL-ESRF, is continuing the development and support of materials engineering research using neutron and synchrotron radiation. Most of this year, 2004, has seen the installation of the Support Laboratory and User Centre, and FaME38 is now in full swing, supporting academic users on- and off-site, providing expertise and experience, and promoting industrial collaboration, with several commercial projects completed. FaME38 opened its doors twice this year, once an open day for staff on-site and once internationally for a successful workshop on Engineering Applications of Neutron and Synchrotron Radiation. FaME38 is well-prepared for the continuation and exploitation stage starting 2005, for which a continuation proposal has been submitted to the EPSRC, UK. Exciting times are ahead: SALSA is going to be commissioned in 2005, (see page x in this report) and the tomography beam line NEUTROGRAPH is showing very promising engineering results. Advanced software tools are being developed for data analysis and visualisation. Some highlights are presented below. For current information consult the website on http://www.ill.fr/fame38 .

FaME38 Laboratory User Support Developments

The full suite of laboratory equipment, including a co-ordinate measuring machine (CMM) to determine the precise shape and position of samples, a high-specification microscope, a metallographic sample preparation system, and an automated hardness tester, are now in place and operating. The Laboratory and User Centre have already supported a number of ILL users most of whom now mount and pre-position their samples using the CMM and a range of newly-designed FaME38 holders on 'VAMAS-standard' base-plates. The suite of instruments will soon be enhanced when three thermo-mechanical testing machines from Instron arrive and are commissioned. These rigs will allow in-situ testing from the micro-scale on an ESRF X-ray tomography beam-line to macro-scale testing of bulk materials on ILL neutron beam-lines. As with the User Centre and the Laboratory, these facilities will be available to ILL and ESRF Users upon request. Additionally, FaME38 has successfully carried out feasibility studies on D20 to establish its suitability for fast and stroboscopic engineering measurements.

SALSA

The staff at FaME38 are looking forward to the commissioning of the new, dedicated, strain scanning instrument SALSA at the ILL in the next year. This instrument, developed jointly by the ILL and the University of Manchester, will, with the ILL reactor's high neutron flux, allow the rapid determination of stresses and strains in bulk engineering components and materials. FaME38 has been working with the SALSA team on developing software tools for the optimization of beam time. This includes the development of a virtual beam-line representation.

that will allow users to prepare, simulate and optimise their experiments via the web prior to arriving at the ILL.

Neutron Tomography

FaME38 is assisting and collaborating with the team of Heidelberg University that is developing the NEUTROGRAPH beam-line facility at ILL to establish novel ways of employing neutron tomography and radiography for materials engineering research. They can now provide, non-destructively, reconstructed images of industrial components for engineers that are the equivalent of those available routinely to medicine from medical X-ray units and body-scanners. Because of the high flux at the ILL, it is possible to investigate dynamic processes with a time resolution of less than one millisecond in bulk samples (see figure 1). New avenues of research include: dynamics of water distributions, two-phase flows, precipitation densities in age-hardening materials, damage and defor-

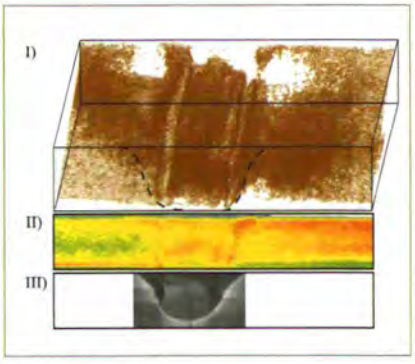

Figure 1: Comparison of the neutron tomography reconstruction of a friction stir weld in an age-hardening aluminium alloy with an optical micrograph in the weld zone. I) Volume rendered tomograph; II) A 2D slice of I); III) An optical micrograph of a similar FSW.

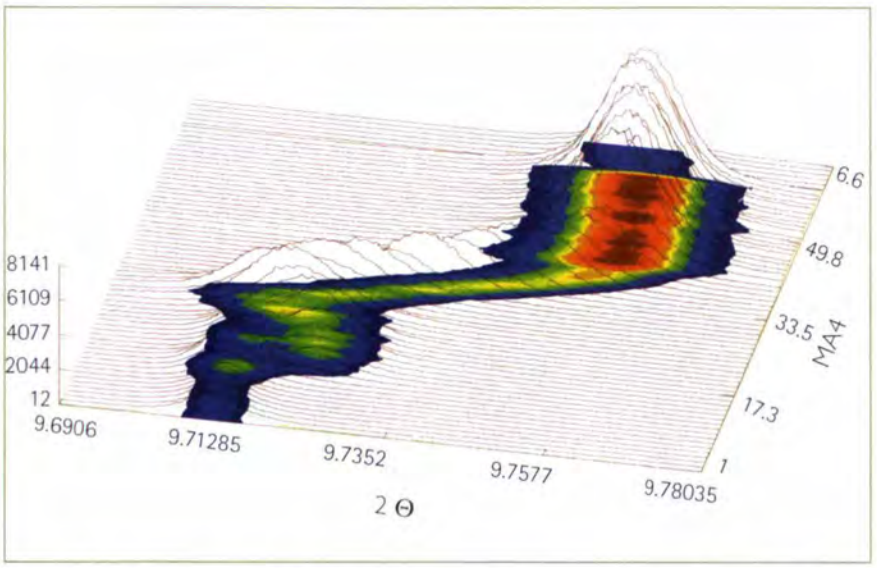

Figure 2: A screen shot of the LAMP environment configured for peak fitting of a series of diffraction peaks.

mations, fuel cells, heat-exchangers, fuel injectors, internal combustion engines, archaeological artifacts, fossils, historical weapons and tools.

Software

An important aspect of FaME38 work is continuously developing a variety of software tools that are user-friendly for materials engineers, with the aim of making strain-scanning experiments simpler, faster, and more efficient. A lightweight, cross-platform, application is being developed which will be able to fit peaks and allow strain analysis, as soon as the data are collected, from all the various instruments on the joint ILL-ESRF site, bridging the gap between control software and real results.

The 40-month EPSRC-funded start-up phase of FaME38 is due to finish at Easter 2005 when it is intended that the facility will be finally commissioned and be fully available to users. The ILL has been involved with engineering studies for many years, for example strain scanning since the early 1980s, and has many unique resources, and expertise, that could be exploited by engineers. Unfortunately conventionally-trained engineers have, until recently, generally been slow to recognize and to use these resources, and those of most other neutron and synchrotron X-ray central facilities. This is largely because the facilities were never originally intended, nor designed, for engineering research. In particular, the equipment has usually had to be substantially adapted; the hardware to scan large components in real space rather than small samples in reciprocal space for example; and the software, though flexible, has not been engineer-user-friendly or capable of on-line data analysis.

FaME38 was set up specifically to address these limitations so that engineers would be able to conduct experiments routinely, accurately and efficiently without having to have an expert knowledge of neutron science. This has largely been achieved with ~100-fold improvements in many critical areas such as positioning accuracy, set-up times, counting efficiency and data visualization, processing and analysis. Facilities and expertise for materials engineering research are now available on-site and we look forward to their rapidly increasing exploitation by both academic and industrial engineers.

Liquids and glasses are thirsty work

Ferdinando Formisano (INFM, Italy) is happy to announce the first acquisition of the monochromatic direct beam on the BRISP detector.

Elisa Fabiani (INFM, Italy), recently qualified PhD in the TOF-HR group.

Miguel Gonzalez, newly appointed as D1B responsible.

Jacquie Cole (St Catherine's College, Cambridge) is a regular user of D4, D10 and VIVALDI.

liquids and glasses

Gabriel Cuello, College 6 Secretary – http://www.ill.fr/Colleges/C6/

Much of the intense research interest in amorphous solids is driven by their technological importance. Examples include the use of ultra transparent optical fibres for telecommunications, amorphous semiconductors in xerography and solar cells, and the ubiquitous everyday uses of organic glasses as structural materials. The molecules in a liquid or amorphous system are arranged tighter and are more orderly than in a gas, but less orderly than in a crystal. In crystalline solids, such as table salt or sugar, the atoms are stacked in a precise three-dimensional order that repeats throughout the crystal, and we say these substances have long-range order. In gases, the atoms or molecules have no order at all but move freely, allowing gases to expand and fill a container. Amorphous solids have no long-range order, but their molecules have some order with respect to the nearest neighbours. Every molecule in an amorphous solid has the same number of nearest neighbours, and each of these neighbouring molecules is roughly the same distance from one other. But the position of molecules that are further away from a particular one becomes more and more random with increasing distance, showing that amorphous solids have just short- or intermediate-range order.

Much of the intense research interest in amorphous solids is driven by their technological importance

The determination of the structural and dynamical properties of a liquid or an amorphous solid is a difficult task because any scientific insight must be achieved without the help of the mathematical amenities useful in the crystalline solid state. Special experimental techniques need to be employed and among them, neutron scattering is one of the most powerful. In the case of local structural studies, only a limited amount of information is generally obtainable, and the construction of structural models is the most useful route to a further understanding. A good example is the article by Cuello et al., where a combination of neutron diffraction experiments and numerical simulations is required in order to search for some kind of clustering in molten metallic alloys which present an anomaly in the sound propagation. More and more experiments in our College have applications in Earth and Environmental Sciences.

The absence of a periodic lattice has several effects; there is no reciprocal lattice and so the wave vector is no longer a good quantum number for the excitations in the system. Thus, the phonon states cannot be described in terms of dispersion curves; instead the only quantity which is a valid description of excitations in a non-crystalline material is the density of states. Neutrons are a direct probe of the density of vibrational states. In many respects the vibrational behaviour of amorphous solids is very similar to that of the corresponding crystalline forms, with the exception that selection rules for transitions are relaxed and sharp features of vibrational modes are smeared out due to the lack of periodicity. Where the amorphous materials do differ markedly from their crystalline counterparts is in the realm of vibrational properties at very low temperatures, the heat capacity, thermal conductivity and other vibrationally dependent properties being singularly anomalous for the amorphous state. This is the case for the solutions of alpha-cyclodextrine, water and 4-methylpiridine that were studied by Plazanet et al. These solutions are homogeneous and transparent at ambient temperature and solidify when heated, i.e., the solutions freeze on heating. The authors postulate a rearrangement of hydrogen bonds as responsible for this striking phenomenon. Another variety of randomness is spin disorder, in which the underlying perfect crystalline lattice is preserved, but each atomic site possesses a spin or magnetic moment, and this is randomly oriented; these materials are termed spin glasses. Pickup et al. have performed a neutron spin-echo experiment on a rather unconventional spin glass, $Co_{50+x}Ga_{50-x}$. They found that a model to explain the universal dielectric response can be used to explain the complex spin relaxation above the glass transition temperature.

The highest number of proposals is still in the field of non-polymeric glasses and amorphous materials. Issues to be addressed here include the effect of confinement, ionicity vs. covalency, and manifestations of intermediate-range order. We also observe a shy return to the issue "excess" of low frequency modes - the so-called "Boson peak". A wide range of interesting proposals appear under the heading of molecular liquids and gases: from the magnetic and structural correlations in liquid oxygen, to biologically relevant solvation in water. In terms of industrial applications, we note significant interest from those involved in nuclear waste containment and separation. Finally, just a mention that the two most highly demanded instruments in our College (D4 and IN1) returned to operation this year for the happiness of our users.

The highest number of proposals is still in the field of non-polymeric glasses and amorphous materials

liquids and glasses

Are there clusters in Fe-Ni-S molten alloys?

G. J. Cuello *(ILL)*
R. Fernández-Perea and C. Cabrillo *(C.S.I.C., Madrid)*
F. J. Bermejo *(University of the Basque Country, Bilbao)*
G. Román-Ross *(UJF-CNRS, Grenoble)*
J. Campo *(C.S.I.C., Zaragoza)*

We have performed a neutron diffraction study on molten alloys of Fe-Ni and Fe-Ni-S systems searching for evidence of clustering in these liquids, which are supposed to be constituents of the Earth's outer core. The presence of clusters could explain the observed anomaly in sound propagation. Although we have found large structural differences on adding sulphur to Fe-Ni alloys, we have not found any evidence of clustering, and the question about the origin of the anomaly in the sound velocity remains open.

The present understanding

of the nature of the inner core of planets identifies light alloying elements as necessary ingredients to explain a wealth of seismic data. The outer liquid core of the Earth is less dense than bulk iron [1]; several light elements (*e.g.*, O, S, Si and C) have been suggested as possible alloying elements, which upon dissolving in liquid Fe in the outer core can account for its lower density. Special attention was paid to the characterisation of thermal and mechanical properties of mixtures such as Fe-Ni sulphide alloys, since their accurate knowledge is required as input for thermo-mechanical models of the planetary cores.

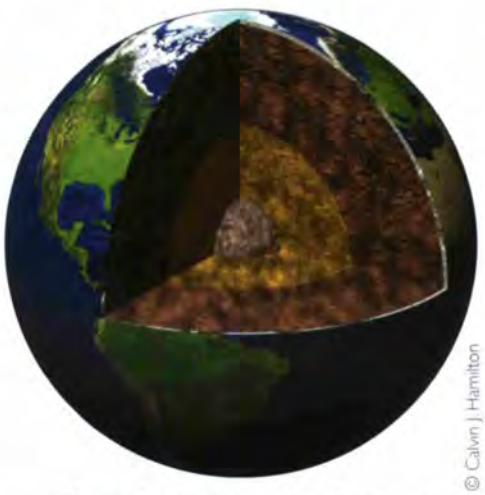

© Calvin J. Hamilton

Figure 1: Artistic view of the Earth's interior.

This kind of result is relevant also to studies of solar system formation and comparative planetology. The Earth, Io, Ganymede and Mars seem to be the only bodies in the solar system for which a metallic core has been directly detected either by means of seismic waves or by measurements of the gravitational field. Given their relative locations in the solar system, this remarkable similarity must be accounted for in theories of the solar system's origin and evolution.

A highly anomalous behaviour has been recently reported [2] on the ultrasonic sound velocity and attenuation in the mixture 85%Fe-5%Ni-10%S for temperatures above the melting point up to 2000 K under its saturated vapour pressure. In fact, and contrary to data for the pure liquid-metal components [3], the acoustic velocity for such a sample increases with temperature, whereas in molten Fe, Ni and S it decreases. The existence of some form of microscopic aggregation is postulated as a plausible explanation for the observed acoustic anomaly [2]. In fact, some electronic properties of the pure liquid components are shown to be deeply affected by the presence of elements such as Si or S [4], something that is expected to lead to substantial changes of structure. If such "molecular" units exist in the liquid as a consequence of some sort of S-induced rearrangements, then the break-up of these units with increasing temperature could explain the increase in sound velocity as well as the anomalous behaviour of its attenuation.

We have performed on D4 (the liquid and amorphous diffractometer at the ILL) a neutron diffraction study of the liquid mixtures referred to above within the temperature range 1700 - 2000 K aiming to

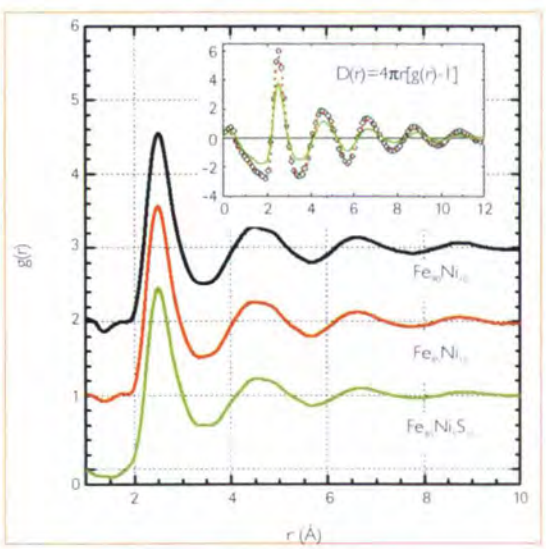

Figure 2: Pair correlation functions and density functions (inset) for the three samples.

detect significant differences of structure at scales of a few tens of Å's. The obtained pair distribution functions show the presence of significant oscillations that reveal rather long-ranged density correlations extending up to distances as long as 15 Å (figure 2). The most remarkable feature here is the closeness of the phases of all three weighted pair distribution functions for distances smaller than 6 Å, as well as the notable differences exhibited by the $Fe_{85}Ni_5S_{10}$ samples with respect to the two binary alloys above such a cut-off value.

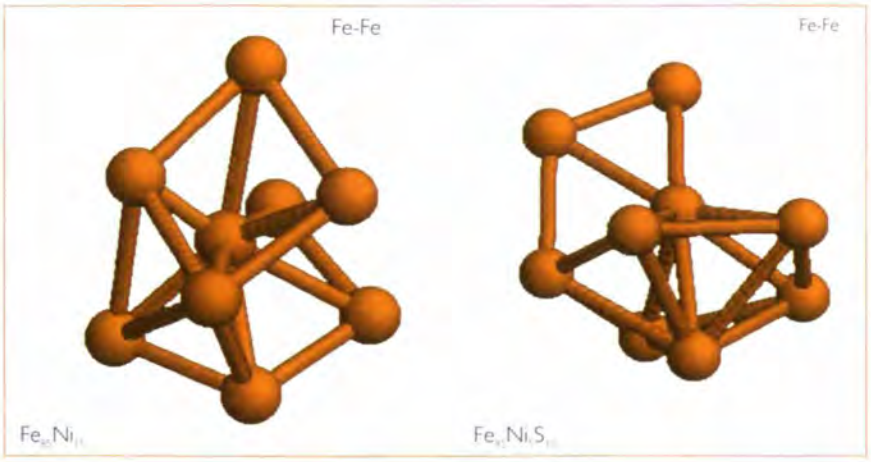

Figure 3: Two snapshots of the Fe environment as obtained from Reverse Monte Carlo simulations.

The radial distribution functions, the integral of which measures the number of particles within a volume element defined by a sphere of a given radius, show significant differences between all three samples. In fact, a rough estimate of the differences in microscopic densities is provided by integrals of such functions using as upper limits their local minima that are located at about 3.3 Å and 5.6 Å. The particle numbers obtained are 13.7, 12.6 and 12.2 corresponding to the first peak of $Fe_{90}Ni_{10}$, $Fe_{85}Ni_{15}$ and $Fe_{85}Ni_5S_{10}$, respectively.

To understand in greater detail the observed trends in terms of particle configurations, we have carried out a set of Reverse Monte Carlo simulations [5]. For such a purpose we have constructed simulation cells containing 20000 atoms with proportions corresponding to the three compositions. Several starting configurations were chosen. First we chose a random configuration of all the atomic species with the only imposed constraint being that the distance between all atoms cannot be less than 1.8 Å. A second set of simulations was carried out for the Fe-Ni-S sample where the initial configuration consisted of all sulphur atoms arranged in S–S pairs and S–S–S triplets. In all cases the initial configurations were later modified following a Monte Carlo strategy [5] so that the calculated structure functions fitted the experimental neutron diffraction patterns. This algorithm adequately reproduces the experimental observations in terms of particle configurations which give plausible atomic structures compatible with the observed structure factors.

No significant S–S correlations were found in $Fe_{85}Ni_5S_{10}$ after extensive searches over many particle configurations and initial conditions. Our present data, and the subsequent analysis on the basis of Reverse Monte Carlo results, are consistent with a fully randomised distribution of S atoms over the whole metallic Fe-Ni matrix. Moreover, no clear signature of a well defined S–S bond is seen, either as a molecular form-factor contributing to $S(Q)$ at large Q values, or as an identifiable peak appearing at about 2 Å in the static correlation function. This finding is in apparent contrast with the conjecture of formation of long aggregates of "molecular" S and their break down with increasing temperature as a main mechanism to explain ultrasound data [2]. On the other hand, our results are in line with first-principles calculations [6], where no tendency to polymerisation of S was found.

Our data show that relevant structural details of alloys suspected to be present within the Earth's outer core can be derived by means of neutron diffraction. This opens the way for future experiments using isotopic substitution in order to derive first hand experimental information on the partial pair correlation functions. The present data suggests rather well defined Fe–S bonds, possibly of a covalent character, although the binding strength does not seem to be high enough to consider such units as "molecules".

eferences:
[1] F. Birch, J. Geophys. Res. 69 (1964) 4377
[2] P. M. Nasch, M. H. Manghnani and R. A. Secco, Science 277 (1997) 219
[3] T. Iida and R. I. L. Guthrie, The Physical Properties of Liquid Metals, Oxford (1993), chapts. 4 and 6. See also R. S. Hixson et al., Phys. Rev. B 42 (1990) 6845
[4] H. Vollstädt et al., Phys. Earth Planet. Inter. 22 (1980) 267; Y. Kita, Trans. ISIJ 22 (1982) 571
[5] R. L. McGreevy and L. Pusztai, Mol. Simulation 1 (1998) 359
[6] D. Alfè and M. J. Gillan, Phys. Rev. B 58 (1998) 8248, and references therein

liquids and glasses

Excitations of metastable superfluid ^{4}He

J.V. Pearce and H. Schober *(ILL)*
H.R. Glyde, D.R. Daughton and N. Mulders *(University of Delaware)*
J. Bossy *(CRTBT, CNRS)*

Liquid ^{4}He confined in porous media is an ideal system in which to reveal the interdependence of superfluidity, well-defined excitations and Bose-Einstein condensation in quantum liquids. In porous media, liquid ^{4}He can be taken to higher pressure, to negative pressures, and can be perturbed in a controlled way by the disordered environment. These changes affect the excitations, Bose-Einstein condensation, and superfluidity differently. Our recent neutron scattering measurements at pressures up to 40 bars show that, for example, superfluidity can exist without well defined phonon excitations, previously thought impossible.

Liquid ^{4}He displays spectacular properties including Bose-Einstein condensation (BEC), superfluidity and characteristic phonon-roton excitations that have remarkably narrow widths (long lifetimes). For example, at a temperature of 1 K, the width of a phonon-roton mode in superfluid ^{4}He is less than one thousandth that of a longitudinal phonon in solid ^{4}He. Superfluidity of liquid ^{4}He confined in porous media such as aerogel and Vycor has been extensively investigated for more than 50 years. Indeed, the demonstration of superflow through capillaries and channels has been an integral part of characterising superfluidity since its initial discovery in 1938 [1]. In sharp contrast, measurements of excitations and BEC in porous media using neutron scattering began only recently [2] and have now revealed the basic nature of the excitations and new layer modes in confinement.

In his pioneering theory of superfluidity, Landau [3] proposed that superflow follows because superfluid ^{4}He supports well defined phonon-roton excitations. Particularly, there could be no low-energy excitations to which a moving superfluid could excite and lose energy, i.e. there must be an energy gap [4]. In an alternate theory, superfluidity follows from phase coherence created by BEC [4,5] even if only a finite fraction of the fluid is condensed. In bulk liquid ^{4}He the onset temperature of BEC, of well defined phonon-roton excitations, and of superfluidity, T_λ, is the same at all pressures. In porous media, the superfluid-normal phase transition temperature T_c is suppressed to temperatures below the bulk value T_λ [6] (e.g. T_λ = 2.17 K and T_c = 1.92 K in 44 Å pore diameter gelsil at SVP). In addition, both T_c in porous media and T_λ in the bulk are further lowered if pressure P is applied (see figure 1). Bulk liquid ^{4}He freezes at P = 25.3 bars. In porous media, however, as a result of confinement, the liquid phase exists up to higher pressures before freezing (up to 35-45 bars depending on the pore diameter and structure of the confinement). Yamamoto et al. have recently reported that T_c goes to zero at P ~ 35 bars in 25 Å gelsil glass [7]. Importantly, this means there is a normal liquid phase between the superfluid and the solid phase at low T in 25 Å gelsil, suggesting that there is a "quantum" superfluid-normal phase transition or quantum phase transition (QPT). It is not clear how Landau's theory applies to a normal phase at T = 0 K. In addition, the condensate fraction, n_0, is predicted to drop from 7.25% at SVP to 2% at 40 bar.

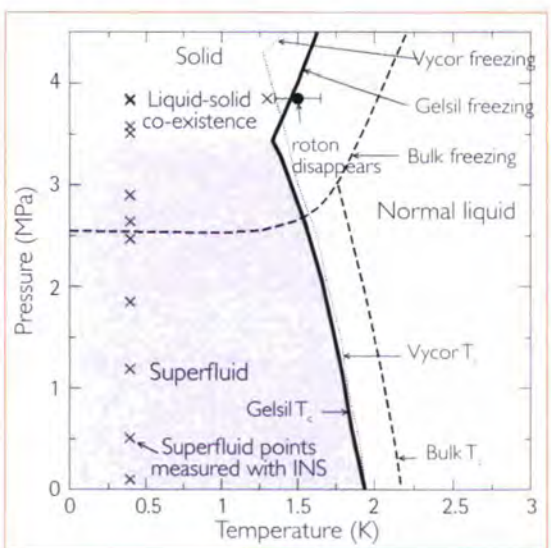

Figure 1: Phase diagram of ^{4}He confined in 44 Å porous gelsil. Dashed line is bulk system, dotted line is ^{4}He in Vycor from ref. [6], and bold solid line is ^{4}He in the current gelsil, measured using ultrasound [8]. Freezing occurs over a P range of ~ 5.5 bars, reflecting the distribution of pore sizes. The filled circle is the temperature at which the roton disappears at 38.5 bars. Crosses show the superfluid points measured with neutrons.

We have investigated phonon-roton excitations in 44 Å gelsil, where T_c lies substantially below T_λ (T_c ~ 1.3 K at 35-

40 bars) [8], using the IN6 time-of-flight spectrometer at ILL. We have measured the dynamic structure factor $S(Q,\omega)$ with IN6 (see figure 2), and the dependence of T_c of this system using ultrasound.

At pressures above P = 24.7 bars, the intensity in the phonon mode disappears. At wave vectors $Q < 1.0$ Å^{-1} there is no well-defined mode. Sharp phonon-roton modes are observed at higher wave vectors only ($Q > 1.6$ Å^{-1} at P = 38.5 bars). Figure 3 shows the dispersion of the observable excitations. Essentially, the phonon and maxon mode energies increase with pressure while the roton energy, Δ, decreases. When the mode energy reaches the two-roton energy 2Δ, the mode can decay to two rotons resulting in substantial broadening and a broad resonance in place of a well defined mode (see figure 4).

In summary, we have made the first neutron scattering measurements of metastable superfluid ^{4}He at pressures above 25.3 bar, and find that the phonon-roton dispersion curve of superfluid ^{4}He in 44 Å gelsil disappears from $S(Q,\omega)$ as a well defined mode in the phonon-maxon region, $0.4 < Q < 1.6$ Å^{-1}, while the roton is observed at all pressures up to solidification. No roton is observed in the solid phase.

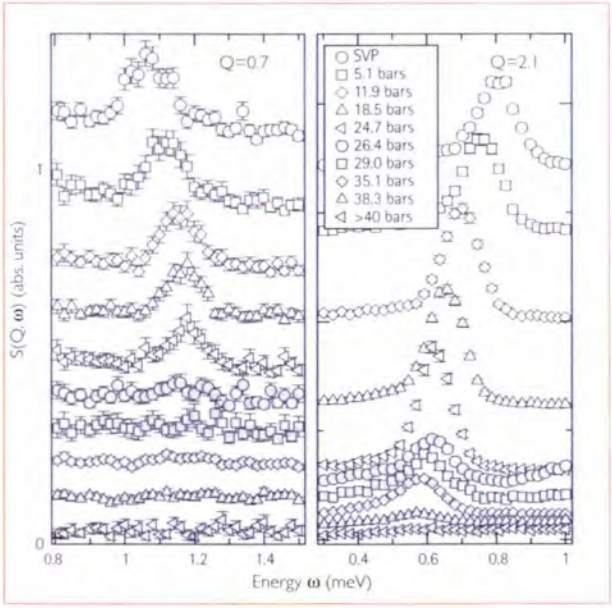

Figure 2: P dependence of $S(Q, \omega)$ of ^{4}He confined in gelsil, at a phonon Q (left) and the roton Q (right). Open symbols: P < 25.3 bars, shaded symbols: P > 25.3 bars.

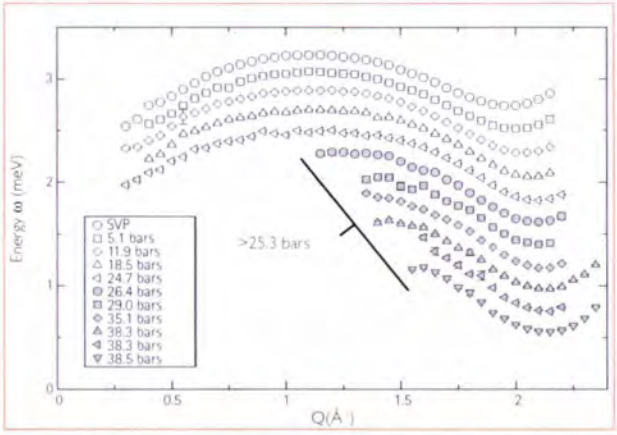

Figure 3: P dependence of the dispersion of the excitations. Open symbols: liquid ^{4}He at P < 25.3 bars, shaded symbols: metastable liquid ^{4}He. Data at each P is offset by 0.2 meV for clarity.

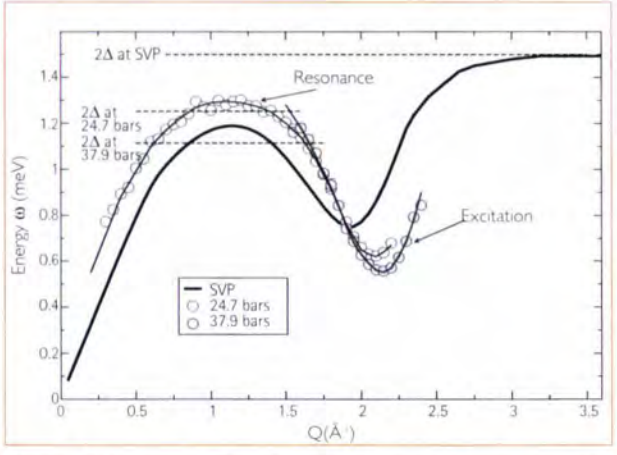

Figure 4: Dispersion of the phonon-roton excitations, showing the change in the dispersion as a function of P. Δ is the roton energy. Solid lines through points at 24.7 and 37.9 bars are guides to the eye.

References:
[1] P. Kapitza, Nature 141 (1938) 74
[2] O. Plantevin, B. Fåk, et al., Phys. Rev. B 57 (1998) 10775
[3] L.D. Landau, J. Phys. USSR 5 (1941) 71; 11 (1947) 91
[4] P. Nozières and D. Pines, "Theory of Quantum Liquids", Vol. II, Addison and Wesley, New York (1990)
[5] F. London, Nature 643 (1938) 141
[6] L. Cao, D.F. Brewer, et al., Phys. Rev. B 33 (1986) 106
[7] H. Yamamoto, H. Nakashima, et al., Phys. Rev. Lett. 93 (2004) 075302
[8] J.V. Pearce, J. Bossy, et al., Phys. Rev. Lett. 93 (2004) 145303

liquids and glasses

Freezing on heating of liquid solutions

M. Plazanet, M.R. Johnson and R. Schweins *(ILL)*
C. Floare *(UJF Grenoble and NIRDIMT, Cluj-Napoca)*
H.P. Trommsdorff *(UJF Grenoble)*

Solutions composed of alpha-cyclodextrine, water, and 4-methylpyridine are homogeneous and transparent at ambient temperature and solidify when heated to temperatures between 45°C and 75°C. Quasi elastic and elastic neutron scattering show that molecular motions are slowed down in the solid and that crystalline order is established. The solution "freezes on heating". This process is fully reversible, on cooling the solid melts. A rearrangement of hydrogen bonds is postulated to be responsible for the observed phenomenon.

α-Cyclodextrine (αCD) is a cyclic, oligosaccharide capable of trapping guest molecules having the size of one benzene ring, to form crystalline inclusion complexes. In preparing the inclusion complex of 4-methylpyridine (4MP) in αCD (figure 1) we have discovered an unusual phase behaviour. At room temperature, solutions containing up to 300 g/l of 4MP in αCD are homogeneous and transparent. When heated to between 50°C and 80°C, these solutions, which also contain the crystallisation water of αCD, solidify. After cooling the solution to room temperature, the solid melts and the original solution is recovered. A first note [1] on this serendipitous discovery has stirred considerable interest under the title "Law-breaking liquid defies the rules" [2].

Figure 1: Inclusion complex of 4MP in αCD.

In order to characterise and to understand changes of structure and molecular dynamics associated with this transition, elastic and quasi elastic neutron scattering experiments and molecular dynamics simulations have been carried out at the ILL. Quasi elastic neutron scattering (QENS) measures the scattered intensity as a function of momentum transfer, $Q = k_i - k_f$, and of energy transfer, $\Delta E = E_i - E_f$. The spectrum of scattered neutrons, $S(Q,\omega = \Delta E/\hbar)$, is the Fourier transform of the intermediate scattering function, $I(Q,t)$:

$$S(Q,\omega) = \frac{1}{2\pi}\int_{-\infty}^{\infty} I(Q,t)\ \exp(i\omega t)dt, \text{ with } I(Q,\tau)=\langle \exp(iQr(t+\tau))\cdot\exp(-iQ\cdot r(t))\rangle$$

$I(Q,t)$ is a correlation function, which involves the particle position, r(t), and characterizes the decay in time of the single particle fluctuations. The broadening of the energy distribution of the scattered neutrons is thus proportional to the decay of the particle-particle correlation function. This way molecular dynamics is monitored. Instruments of different resolution explore different time scales ranging from ps (IN5) to ns (IN10) and longer. The angular distribution of the scattered intensity is determined by the amplitude and geometry of the motion of the particles. Measurements with IN10 and IN16 (energy resolution ~ 1μeV), show that at room temperature, when the sample is liquid, all components diffuse on time scales faster than the upper limit of about 10^{-9} s set by the energy resolution window of these instruments. As the sample is heated, one of the components in the system slows down, making the sample solid. This slowing down upon heating results in a net increase of intensity of scattered neutrons in an energy window of 1μeV around $\Delta E = 0$, as shown in figure 2, which pres-

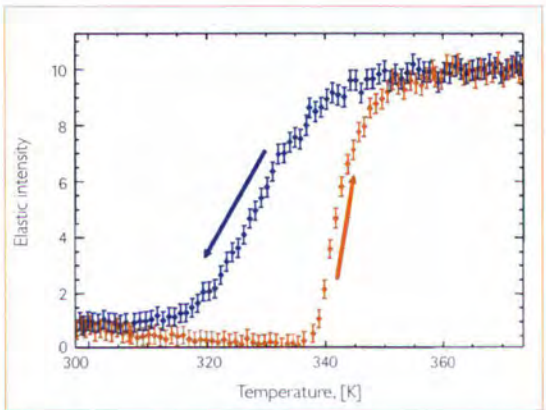

Figure 2: Intensity of scattered neutrons in an energy window of 1 μeV around $\Delta E = 0$, recorded at IN10 as a function of heating and cooling the sample at a rate of 6°/hour.

ents curves recorded when heating and cooling the sample at a rate of 6°/hour. From the intensities, it is however clear that only part of the molecules are immobilised. Even at high temperature, in the solid phase, a mobility is still observed on the time scale of 10^{-11} s set by the resolution window of 100 μeV of IN5. Only αCD is immobilised on these time scales, but the 4MP solvent remains liquid.

These observations raise the question about the structure of the solid phase: Is the solid ordered or disordered? Which length scales are involved? Do sizable clusters of αCD exist already at room temperature? These issues were addressed by neutron diffraction on D11 and D16. At lower temperatures, diffraction typical for a normal liquid is observed, while sharp diffraction rings emerge in the high temperature, solid phase. Figure 3 shows the diffraction pattern observed on D16 for the solid phase. The first 5 prominent diffraction peaks correspond to lattice spacings of 44.8, 22.5, 20.4, 15.0, and 11.9 Å. While the space group could not be assigned unambiguously, based on this data, all possible structures have unit cells of about 15000 Å^3 and correspond to a probable composition: 4×[αCD + 6×H2O + ca. 15×4MP]. At still higher temperatures, above ca. 100°C, the normal melting of the solid phase is observed.

How can these surprising observations be rationalised?

At first sight, it seems difficult to reconcile our observations with the requirement that entropy must increase with

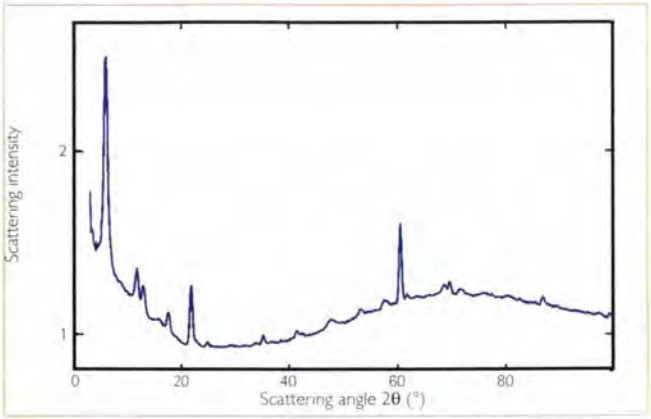

Figure 3: Diffractogram, recorded with D16, of the solid phase at 70°C.

increasing temperature, since crystalline order is established and molecular motions are slowed down. The critical influence of small quantities of water and of H/D replacement suggest a rearrangement of hydrogen bonds as possible mechanism of the solidification. MD calculations indicate indeed that a structure of αCD with all *intra*-molecular hydrogen-bonds established is most stable. The opening of H-bonds with increasing temperature provides the possibility for *inter*-molecular H-bonds via the water molecules and the establishment of long-range order. How the ordering of the αCD molecules affects the entropy of the liquid phase remains a matter of exploration. What our measurements do seem to indicate is that the diffusion of the 4MP solvent is increased in the ordered structure.

The observations reported here open many avenues for future work. An obvious first objective is the determination of the crystal structure of the solid. Based on this structure, accurate MD calculations over long times should be made in order to understand this solidification phenomenon and the critical role of the small amounts of water and the H-bonds that they form with αCD and 4MP. In this way, this relatively simple molecular system will be a very useful benchmark system to test the validity of force fields and of molecular mechanics/dynamics calculations, calculations that can not be tested in such detail for more complex biological systems. Precise calorimetric measurements must also be made to follow enthalpy changes of the phase transition. In view of possible exploitations of this solidification phenomenon in various conceivable applications, other systems should be explored. The observation of this phenomenon in a number of cyclodextrine/pyridine systems suggests that more solutions could be found with analogous behaviour. In a search for such systems, the solubility, the ability to establish intra and intermolecular hydrogen bonds, and the competition between these will be crucial factors.

References: [1] M. Plazanet, C. Floare, M.R. Johnson, R. Schweins and H.P. Trommsdorff, J. Chem. Phys. 121 (2004) 5031
[2] http://physicsweb.org/articles/news/8/9/15/1

liquids and glasses

A universal dynamic relaxation function for glassy systems?

R.M. Pickup and R. Cywinski
(University of Leeds)
C. Pappas *(HMI, Berlin)*
B. Farago *(ILL)*

Neutron spin-echo has been used to follow the evolution of the spin dynamics as the glass temperature of the unusual spin glass system $Co_{50+x}Ga_{50-x}$ is approached from above. Although the observed spin relaxation spectra are not consistent with conventional relaxation functions, a model originally formulated by Weron to explain the universal dielectric response law describes the $Co_{50+x}Ga_{50-x}$ data extremely well. The Weron model is based upon the assumption that individual dipoles and their environments do not remain independent during the relaxation process, and in this respect it may provide a more appropriate, and generally applicable, model for spin glass relaxation.

Spin glass phenomenology is an extremely rich and rewarding field of study. Random or frustrated exchange arising either from a frustrated topology of concentrated magnetic spins or oscillatory exchange mechanisms between dilute spins can result in spin freezing processes that are in many ways analogous to the freezing processes in more conventional structural, molecular and polymer glasses. Indeed spin glasses, despite their own intrinsic complexities, are often used as relatively simple model systems with which to develop our understanding of the generic glassy state.

The best known feature of a spin glass is the sharp cusp-like peak in the low field susceptibility at the glass temperature, T_g. Less well known is the persistence of complex spin relaxation in the paramagnetic state of spin glass systems to temperatures approaching $4T_g$ [1,2]. Despite often quite severe count-rate limitations, neutron spin-echo (NSE) has proved useful in probing such relaxation in a number of spin glass systems. It is generally found that above T_g the relaxation spectra follow similar functional forms to those observed for structural glasses with exponential, stretched exponential (Kohlrausch) and power law relaxation all being reported.

As part of a wider study of spin relaxation phenomena in spin glasses we have recently carried out NSE measurements on the $Co_{50+x}Ga_{50-x}$ system. $Co_{50+x}Ga_{50-x}$ is a rather unconventional spin glass. The compound crystallises with the B2 (CsCl) structure, but even at stoichiometry (x=0) thermal vacancies occur on the Co sublattice, with the associated Co atoms migrating to the Ga sublattice. Excursions to the Co-rich side of stoichiometry further increase the number of such Co "antistructure" atoms. Whilst the $Co_{50}Ga_{50}$ matrix is itself Pauli paramagnetic, clusters of antistructure atoms do appear to possess localised magnetic moments, which in turn polarise the neighbouring structural Co atoms [3]. Progression from Pauli paramagnetism at x=0, spin- then cluster-glass phases through to percolative ferromagnetism beyond x=5 is therefore extremely rapid. The NSE measurements reported here were made on the $Co_{55}Ga_{45}$ compound, for which the glass temperature, T_g, is close to 17K. Both above and below T_g the magnetic response is dominated by long range spin correlations or clusters [3]. At first sight, the relaxation spectra above T_g appear to follow a stretched exponential or perhaps power law time dependence, as might be expected for spin glasses (figure 1). However neither function represents the data well: the temperature dependences of the parameters resulting from a fit of the stretched exponential form to the data are not physically meaningful, whilst a fit of a simple power law to the data provides values for the t=0 correlations well in excess of 1 (figure 2).

This is, perhaps, not too surprising, as most relaxation models are based upon the conventional Debye mechanism with a

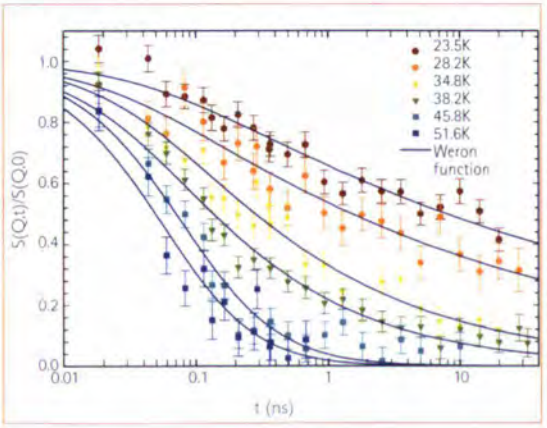

Figure 1: Neutron spin-echo spectra from $Co_{55}Ga_{45}$ over a range of temperatures above T_g = 17K. The solid lines represent a fit of the Weron relaxation model to the data.

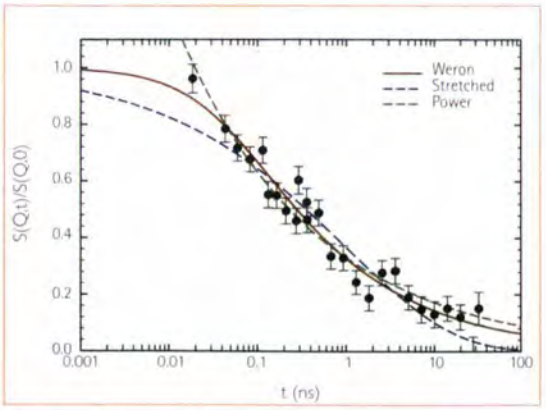

Figure 2: Neutron spin-echo spectra obtained from $Co_{55}Ga_{45}$ at a temperature of T=34.5K. The lines represent fits of the stretched exponential, power law and Weron relaxation functions to the data.

single, local relaxation time, τ, assigned to the relaxing entities, giving $S(t)\sim\exp(-t/\tau)$. The frequently observed Kohlrausch form, $S(t)\sim\exp(-(t/\tau)^{\beta})$, is then considered to be a consequence of a distribution of parallel but independent relaxation processes, each with its own local τ. For pre-percolative $Co_{55}Ga_{45}$, however, it seems likely that the relaxation processes of the concentrated spins are not entirely independent. A hierarchical model of spin relaxation, requiring a serial summation of individual relaxation processes constrained by strong intra-cluster interactions and weak, long range, inter-cluster interactions, might be more appropriate.

Just such a model has been suggested by Weron to explain the universal dielectric response law [4]. Weron introduces the concept of a "waiting time", with the time scale for any individual relaxation to equilibrium being stochastically dependent upon the sum of the waiting time and the relaxation time. The result is a universal, but simple, generalised power law relaxation function $S(t)\propto[1+k(t/\tau)^{\alpha}]^{-1/k}$ which includes the exponential and stretched exponential forms as special cases. In the Weron function k is related to the strength of interaction and tends to zero in the absence of such interactions, and α is associated with the exponent β in the stretched exponential form, taking the value 1 in the Debye limit.

The Weron function fits the $Co_{55}Ga_{45}$ NSE spectra extremely well as can be seen in (figure 1) and (figure 2). We find that α maintains the Debye value of 1 at all temperatures, whilst τ diverges at low temperatures, as expected (figure 3). The dimensionless interaction parameter k increases dramatically as T_g is approached, and is found to scale remarkably well with the ac susceptibility of $Co_{55}Ga_{45}$ (figure 4). Unfortunately, the physical significance and origin of k remains somewhat obscure at this stage, and neither the Weron theory nor our data offer any real clues. Further NSE measurements on a range of spin glasses are clearly needed.

To our knowledge this is the first time that the Weron model has been applied to the phenomenon of complex magnetic spin relaxation processes, although Weron's incorporation of macroscopic interactions appears to be both logical and appropriate for many spin glass and cluster glass systems. Indeed, our preliminary survey of NSE spectra obtained over the last 25 years from spin glasses above T_g suggest that the Weron model may well provide a better description of the existing data than that offered by more conventional relaxation models derived from the perspective of parallel rather than hierarchical relaxation processes. It remains to be seen whether the Weron model is more generally applicable to the relaxation processes in conventional structural glasses above T_g, but early indications suggest that this might also be the case.

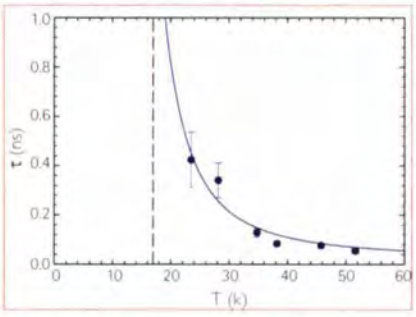

Figure 3: The temperature dependence of the relaxation rate, τ, obtained from the fit of the Weron function to the NSE spectra of $Co_{55}Ga_{45}$. Note that τ diverges at low temperatures following an Arrhenius law (solid line).

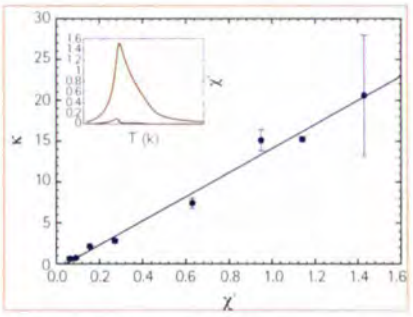

Figure 4: The interaction parameter k scaled with the real component of the ac susceptibility of $Co_{55}Ga_{45}$. The inset shows the real and imaginary components of the ac susceptibility of $Co_{55}Ga_{45}$ as a function of temperature.

References: [1] A.T. Ogielski, Phys. Rev. B 32 (1985) 7384
[2] I.A. Campbell, Phys. Rev. Lett. 72 (1994) 1291
[3] R. Cywinski, J. Phys. F: Metal Phys. 7 (1977) 2567
[4] K. Weron, J. Phys: Condens. Matter 3 (1991) 9151

Life is beautiful

B. Gallet using the protein purification system (FPLC) (Photo : Studio Reviré)

Ingrid Parrot and Valérie Laux-Lesourd working at the molecular biology laboratory (Photo : Studio Reviré)

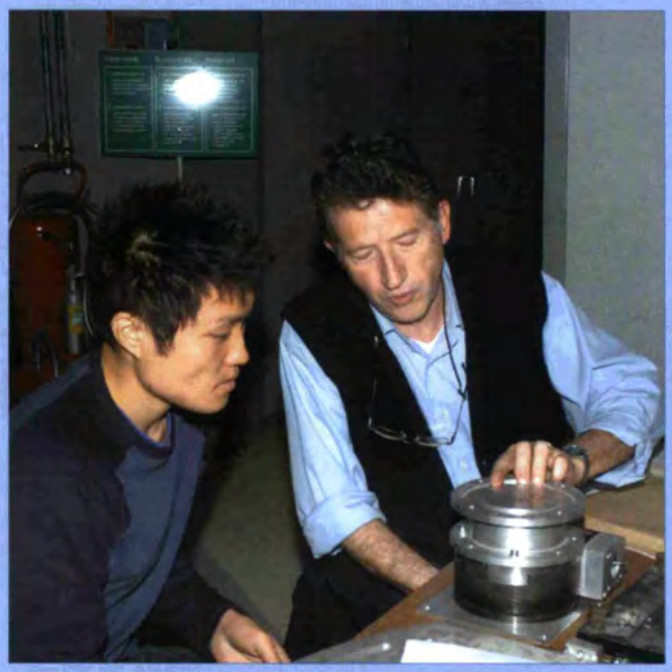

Jean-Claude Marmeggi (right) training Kentoro Horibe.

The PSB (Partnership for Structural Biology) building will host the new European Centre of Excellence which will tackle fundamental research problems related to human health.

biology

Bruno Demé, College 8 secretary – http://www.ill.fr/Colleges/C8/

This year again, scientific highlights in biology illustrate well the growing impact and the diversity of studies dealing with model and biological membranes. Two contributions deal with specular reflectivity studies on solid supported bilayers. One is a study of the neural cell adhesion molecule where neutrons and X-rays were used to determine the physical dimensions of the natural and modified membrane-bound ectodomains of neural cell adhesion molecules. The other reflectivity study is aimed at localising hydrolysis products resulting from the enzymatic activity of phospholipase A_2 from snake venom. It reports how, in a selectively deuterated phospholipid bilayer, the composition of the bilayer evolves while phospholipids are broken down during hydrolysis by phospholipase A_2. A membrane diffraction study on novel synthetic glycolipids shows how the "cylindrical" or "bent" shape of the headgroups affects the swelling properties upon hydration and the stiffness of the bilayers, that is their ability, in a regular stack, to fluctuate around their mean position. The fourth contribution using model membranes gives a first high energy-resolution wave vector-resolved insight into collective lipid membrane dynamics. It is an investigation of molecular motions in model membranes using inelastic scattering on a backscattering spectrometer. Finally, a last contribution reports on a solution structure study of the nucleocapsid-binding domain of the Sendai virus phosphoprotein, a virus from the family that contains important human and animal pathogens like influenza, measles, rabies and Ebola viruses. The study describes structural properties of the phosphoprotein, an extremely flexible and long molecule, using a combination of crystallography, NMR and SANS.

This year again, scientific highlights in biology illustrate well the growing impact and the diversity of studies dealing with model and biological membranes

Talking about SANS, it is worth mentioning the completion of the fast SANS-detector (2MHz) Millennium project on D22. After installation during the 2003-2004 winter shutdown, the instrument has been operating during the 3 reactor cycles in 2004, reaching routinely count rates one order of magnitude higher than before with the previous detector.

2004 has been an important year for the Partnership for Structural Biology (PSB). The PSB is a strong collaboration between EMBL, ESRF, IBS and ILL. It was set up in November 2002, and this year, it entered a very concrete phase with the start of the PSB-IVMS building construction. Together, the PSB and the IVMS (Institut de Virologie Moléculaire et Structurale) will form the Centre for Integrated Structural Biology (CISB). Started in June 2004, completion of the CISB building is expected for September 2005. At that date the deuteration-laboratory will move from its current location in ILL20 to the new building. This laboratory for the deuteration of biological molecules was set up jointly with the EMBL as part of the ILL strategy for the expansion of the life sciences program in neutron scattering. The laboratory provides support to scientists wishing to make their own deuterated materials for neutron scattering experiments. The laboratory has received to date fourteen proposals (among them four for the year 2004) for deuterating proteins and nucleic acids. It will become one of the platforms of the PSB which will push this effort further by creating a unique centre of modern techniques to tackle fundamental problems related to human health. The deuteration facility, as well as the other platforms available through the PSB, will continue helping ILL users to carry out their neutron scattering experiments in structural biology and biophysics using increasingly sophisticated samples.

2004 has been an important year for the Partnership for Structural Biology

The meeting Neutrons in biology, to be held at the ILL (4-7 September 2005) as a satellite meeting of the IUPAB/EBSA Biophysics congress, will be a good opportunity to present recent achievements and to get an overview of the results obtained during the last years.

biology

In-plane and out-of-plane fluctuation of synthetic glycolipid lamellae

M. Tanaka, F. Rehfeldt and E. Schneck *(TU Munich)*
B. Demé *(ILL)*

The in-plane and out of plane cooperativity in artificial models of cell glycocalix under controlled osmotic pressure and temperature was studied using the D16 membrane diffractometer coupled with a humidity chamber [1]. Rocking curves of oriented multilamellar stacks using the 2D detector allow for the analysis of the scattering along different orientations referring to in-plane and out-of-plane contributions independently. In-plane membrane fluctuations produce diffuse scattering along $q_{//}$, while fluctuations of the periodicity affect the sharpness of the Bragg peaks along q_z (specular reflectivity). The analysis of the measured lamellar periodicities yields quantitative force-distance relationships, which clearly reveal the competitive interplay between repulsive hydration forces and attractive "zipper" forces depending on the conformation of carbohydrate head groups.

The surface of plasma membranes is rendered with glycocalix, oligo- and polysaccharide chains adjacent to glycolipids, peptidoglycans, and glycoproteins. They serve as stabilisers to retain plasma membrane structures as well as "repellers" to a certain distance between neighbouring cells via relatively weak (generic) forces, like electrostatic interaction, hydrogen bonding, and long-range van der Waals interaction. As simple and well-defined glycocalix models, we have chosen lamellar stacks of glycolipids (synthesised by R.R. Schmidt, Univ. Konstanz). Planar multilamellae were prepared by casting of glycolipid solutions on a silicon wafer, and were subjected to diffraction measurements in a D_2O atmosphere. Following our previous studies using calorimetry (DSC) and X-ray scattering (SAXS/WAXS) [2], we carried out SANS measurements below and above the chain melting temperature. In figure 1a and b our experimental setup is described and the chemical structures of three glycolipids are presented. In nature gentiobiose is claimed to be responsible for the toxicity of lipoteichoic acid in Gram positive bacteria (similar to the function of lipid A in Gram negative bacteria). Figure 1c presents a typical reciprocal space map of a lamellar stack of a lipid with "*bent*" gentiobiose head groups with deuterated lipid anchors (*Gent-D*) swollen in an H_2O atmosphere (at T = 80 °C and a relative humidity of 99 %.), which exhibits clear Bragg peaks up to the fourth order. Furthermore, we carried out contrast variation experiments with *Gent-H* in a D_2O atmosphere. The reciprocal space maps obtained also exhibit clear peaks up to the fourth order, which are complementary to the results obtained with *Gent-D* in an H_2O atmosphere.

From the reciprocal maps recorded with the 2D detector, the specular reflections from *Gent-D* lamellae in an H_2O atmosphere can be extracted as functions of temperature and osmotic pressure. As can be seen in figure 2a, the increase in relative humidity at 30°C ($T < T_m$) leads to a change in the lamellar periodicity from 64.1 Å to 66.4 Å, accompanied with a

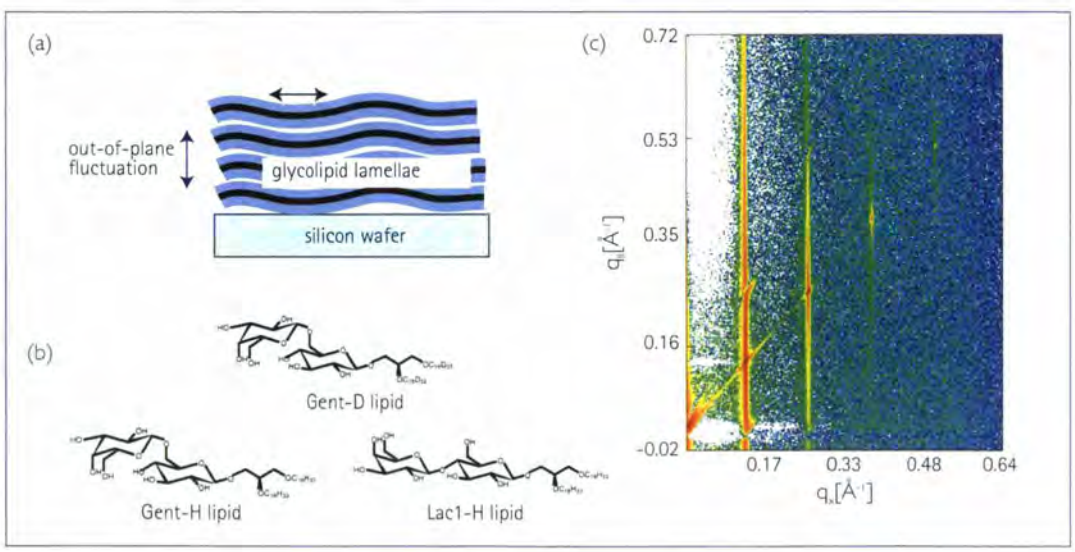

Figure 1: (a) Experimental setup, (b) chemical structure of glycolipids and (c) reciprocal space map ($q_{//}$ vs. q_z) of Gent-D lamellae in H_2O atmosphere. The line going through the Bragg peak maxima corresponds to the specular reflectivity or q_z orientation ($q_{//} = q_z$).

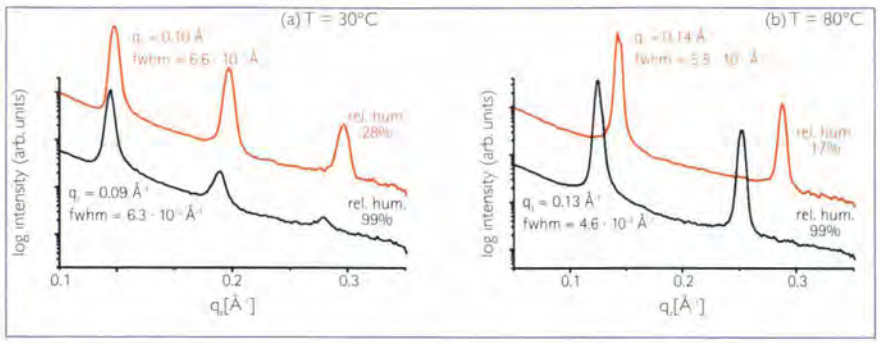

Figure 2: Intensity extracted from reciprocal space maps along the q_z orientation showing specular profiles for Gent-D in H_2O measured at (a) $T<T_m$, and (b) $T>T_m$.

slight decrease in the out-of-plane ordering. On the other hand, at 80°C ($T > T_m$), *Gent-D* lamellae show a significant increase in the lamellar periodicity from 44.0 Å to 50.3 Å according to the increasing relative humidity (figure 2b). Similar tendencies were observed for the other glycolipids with protonated alkyl chains, *Gent-H* and *Lac1-H* lipids, *i.e.* changes in lamellar spacing are more prominent at $T > T_m$ (data not shown). This can be attributed to the larger area per molecule at $T > T_m$[2], which provides larger free voids for hydrating water molecules.

The analysis of the lamellar periodicities obtained from the Bragg peak positions enables us to plot quantitative force-distance (osmotic pressure *P vs.* saccharide layer thickness *d*) relationships at different temperatures. Figure 3 shows the force-distance relations of two fully protonated glycolipids with almost identical monosaccharide components and lipid anchors: (a) *Gent-H* with "*bent*" gentiobiose head (red), and (b) *Lac1-H* with "*cylindrical*" lactose head (blue) swollen in a D_2O atmosphere. The saccharide layer thickness of *Gent-H* is smaller than that of *Lac1-H* at all pressure conditions, which can be attributed to the bending of the saccharide junction to the molecular axis. The force distance curves of both glycolipids follow an exponential decay, $P = P_0 \exp(-D/\lambda)$, where λ is the characteristic decay length and D is the thickness of saccharide layer [3]. The characteristic decay length of $\lambda \sim 5$ Å can be calculated for both lipids. Interestingly, the obtained pressure-distance relationships exhibit a clear deviation from the expected exponential decay in the low pressure regime, $\Pi < 4 \cdot 10^7$ Pa, suggesting the existence of an additional attractive force contribution, such as a "zipper" interaction from the hydrogen bonding between apposing sugar head groups.

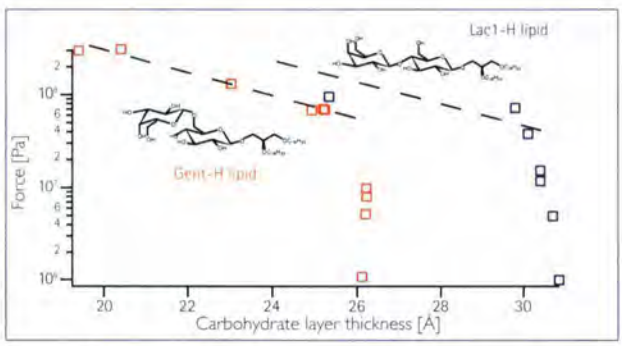

Figure 3: Influence of saccharide conformation on the force-distance relationships.

In contrast to the out-of-plane fluctuation of the periodicity that influences the sharpness of the specular peaks, the in-plane fluctuation of the membrane can be detected from the diffuse scattering signals. As presented in figure 1c, the Bragg peaks observed for highly swollen Gent lipid (both *Gent-D* and *Gent-H*) lamellae are accompanied with strong diffuse scattering at $T > T_m$. On the other hand, the scattering peaks from *Lac1-H* lamellae exhibit very small diffuse scattering (data not shown). A significant difference in in-plane fluctuation strongly suggests that "cylindrical" lactose head groups form tighter lateral hydrogen bonding networks than those formed between "bent" gentiobiose head groups. Such steric (entropic) effects of saccharide head group conformation on the lateral hydrogen bonding show very good agreement with our previous interface rheology experiments that demonstrate a strong influence of the length and conformation of saccharide head groups on the viscous and elastic modulus of glycolipid monolayers at the air/water interface [4].

Our experimental strategy is thus promising to study the in-plane hydrogen bonding network and out-of-plane hydration forces in synthetic and natural glycolipids and lipopolysaccharides under well-defined temperature and pressure conditions.

eferences: [1] F. Rehfeldt, E. Schneck, B. Demé and M. Tanaka, in preparation
[2] M. Schneider, R. Zantl, C. Gege, M. Rappolt, R.R. Schmidt and M. Tanaka, Biophys. J. 84 (2003) 306
M. Tanaka, M. Schneider and G. Brezesinski, Chem. Phys. Chem. 4 (2003) 1316
[3] V.A. Parsegian, N. Fuller and P. Rand, Proc. Natl. Acad. Sci. USA 76 (1979) 2750
[4] M. Schneider, K. Lim, G. Fuller and M. Tanaka, PCCP 4 (2002) 1949
M. Tanaka, S. Schiefer, C. Gege, R. Schmidt and G. Fuller, J. Phys. Chem. B 108 (2004) 3211

biology

Structural studies of the neural cell adhesion molecule

C.P. Johnson and E. Leckband *(University of Illinois)*
G. Fragneto *(ILL)*
F. Legrand and V. Dubosclard *(UJF Grenoble)*
O. Konovalov *(ESRF)*

The structures of adhesion proteins play an important role in the formation of intercellular complexes and the control of intermembrane spacing. We investigated with neutron and X-ray specular reflectivity the structure of the ectodomain of the neutral cell adhesion molecules (NCAM). The measurements with unmodified NCAM indicate the presence of a bend in the extracelullar region C-terminal to the fifth immunoglobulin domain. Measurements with the polysialic acid-modified form of NCAM reveal that, at physiological ionic strength, the carbohydrate chains extend beyond the range of the unmodified protein. The excluded volume of the polymer is also ionic strength-dependent, as expected for a polyelectrolyte. These results provide structural insights into the configuration of the NCAM ectodomain and the regulation of NCAM function by post-translational modification [1].

Expressed in both developing and adult vertebrate organisms, the neural cell adhesion molecule (NCAM) is a cell surface glycoprotein, which mediates cell adhesion, signaling, migration, and plasticity in the central nervous system. NCAM binds homophilically to other NCAM molecules on opposing cell surfaces. All expressed isoforms possess an extracellular region composed of five tandem immunoglobulin (Ig) domains followed by two, membrane-proximal fibronectin (FNIII) domains.

In the early stages of development, NCAM is post-translationally modified with up-to-two linear α, 2,8-polysialic acid chains N-linked at distinct sites on the fifth Ig domain. This polysialic acid (PSA) modification alters the function of NCAM. In contrast to the unmodified protein, the PSA-NCAM exhibits anti-adhesive properties. The post-translational modification of NCAM enhances cell motility, increases intercellular space, and increases neural plasticity. The lengths of the carbohydrate chains vary widely, ranging from 25-100 monomers, and they are polydisperse. The sialic acid monomers are negatively charged, and inter-segment repulsion increases the excluded volume of the chains. Adhesion between PSA-NCAM expressing cells also depends on the ionic strength. At physiological ionic strength, the cells do not adhere, but cell adhesion is recovered at high (3M) salt concentrations.

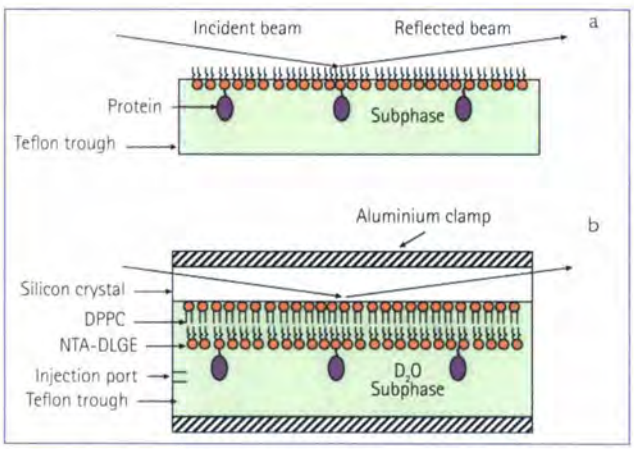

Figure 1: (a) Schematic of the lipid monolayer and trough used in X-ray reflectivity measurements. (b) Schematic of the supported lipid bilayer and sample holder for neutron reflectivity studies. The protein is immobilized to the lipid bilayer, which is supported on an oxidised silicon block. The silicon proximal lipid layer is gel phase DPPC, and the distal lipid film is fluid NTA-TRIG-DLGE.

X-ray and neutron reflectivity complement each other to determine the physical dimensions of the membrane-bound NCAM ectodomain and of PSA-NCAM monolayers supported on lipid membranes. A better contrast between the different layers is obtained with the neutrons while a higher spatial resolution is reached with the X-rays. Here, NCAM and PSA-NCAM were engineered with C-terminal polyhistidine tails. These were in turn immobilized and oriented on Ni-NTA-lipid monolayers.

Figure 1 shows the different sample systems for X-ray (ID10B, ESRF) and neutron studies (D17, ILL).

The neutron measurements were performed in time-of-flight mode with a spread of wavelength from 0.2 to 2 nm and with 2 buffer solutions of different scattering length density (SLD): D_2O solutions with a SLD of 6.4×10^{-6} Å^{-2} and "Silicon matched water" (SMW), a blend of H_2O/D_2O with a SLD of 2.1×10^{-6} Å^{-2}. The constraints imposed by the simultaneous (global) fitting of both solvent contrasts yielded a unique model that agrees closely with that obtained from the X-ray reflectivity data.

To determine the thickness of the NCAM-His_{10} bound to the lipid bilayer, we carried out reflectivity measurements of the protein monolayer. PSA-NCAM-His_{10} was also investigated, in order to determine the steric dimensions of the carbohydrate at low

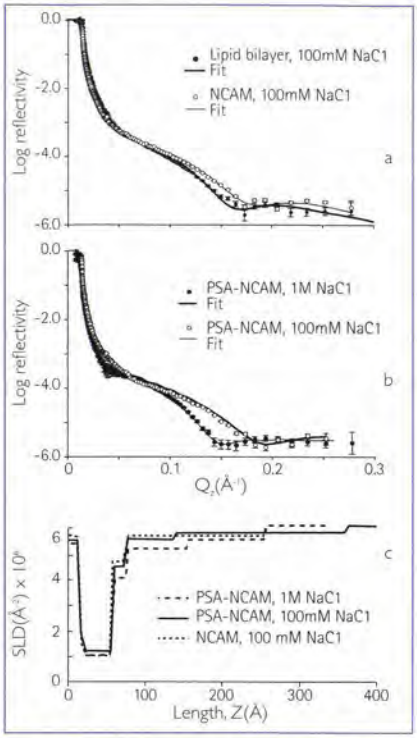

Figure 2: Specular Neutron Reflectivity Profiles of NCAM and Lipid Monolayers. The solid lines are the best model fits to the data. (a) Lipid bilayer (black circles) and immobilized NCAM-His_{10} (open circles) monolayers on the lipid bilayer. (b) PSA-NCAM-His_{10} immobilized on a supported lipid bilayer in 1M NaCl (black circles) and 100mM NaCl (open circles). (c) scattering length density profiles of NCAM and PSA-NCAM on the lipid bilayer: NCAM in 100mM NaCl (dotted line), PSA-NCAM in 100mM NaCl (solid line), and PSA-NCAM in 1M NaCl (dashed line).

(100mM) and high (1M) NaCl concentrations. The X-ray and neutron reflectivity analyses of the unmodified NCAM ectodomain indicate that the protein adopts a bent configuration. In both analyses, the single box describing the full NCAM ectodomain was much smaller than the 280 Å end-to-end length that would be expected for the fully extended, i.e. straight protein. This indicates that the seven domains do not adopt a rigid, linear structure oriented perpendicular to the membrane. However, since electron microscopy (EM) images and previous force measurements indicate that the Ig1-5 segment is relatively rigid, the bend in the ectodomains seen in the EM images can account for the fitted thickness of the NCAM-His_{10} layer. The location of the bend or hinge was postulated to lie between the fifth Ig domains and first FNIII domain. These reflectivity results, together with previous force measurements support this model for the bent ectodomain configuration.

The large increase in the thickness of the PSA-NCAM-His_{10} relative to that of the NCAM-His_{10} suggests the mechanism by which PSA inhibits cell adhesion. The structural interpretations of the X-ray and neutron reflectivity spectra of NCAM-His_{10} monolayers in 100mM and 1 M NaCl solutions are shown in figure 2. In both the X-ray and neutron reflectivity data, the best-fit models of the overall thickness of the PSA-NCAM layer in 100 mM NaCl agree within 5 Å, and both models exhibit high roughness values for the glycoprotein layers. The glycoprotein thickness from both models further shows a large increase in the overall thickness relative to that of the unmodified NCAM. These data therefore quantitatively show that the PSA chains extend beyond the unmodified protein at near-physiological NaCl, and would thereby generate an electrosteric repulsive barrier that prevents the close approach of opposed cells.

These measurements provide a structural interpretation of the ionic strength dependence of adhesion between cells expressing PSA-NCAM. The fitted model for PSA-NCAM-His_{10} in 1 M NaCl shows a significant shift in both the electron density and the SLD. With both X-ray and neutron reflectivity models, the overall thickness descreases, and the segment density near the base of the protein increases. The interpretation of these model results is shown in figure 3. These results support previous evidence for the reduction in the excluded volume of PSA at high ionic strength. They show further that, in 1M NaCl, the PSA does not extend the entire length of the glycoprotein, since the density of the outer layer matches that of the unmodified NCAM. The polymer segment density clearly shifts at high ionic strength, such that the N-terminal Ig domains could lie outside the excluded volume occupied by the carbohydrate. These results explain the onset of adhesion between PSA-NCAM expressing cells in 3M NaCl. The chain collapse reported in this study would reduce the osmotic repulsion between cells, and expose the adhesive Ig domains. Both effects would enable NCAM from adjacent cells to adhere.

These structural analyses support the hypothesis that PSA regulates NCAM function, and cell adhesion in general, by increasing the excluded volume of NCAM, and hence the range and magnitude of the repulsive pressure between adjacent cells. Despite the independent fitting of both the neutron and X-ray reflectivity data, the resultant models agree qualitatively for every sample in which a comparison can be made. The added constraints placed on the global neutron reflectivity fits and the use of multiple contrasts eliminated many models that would be considered degenerate with only one solvent contrast.

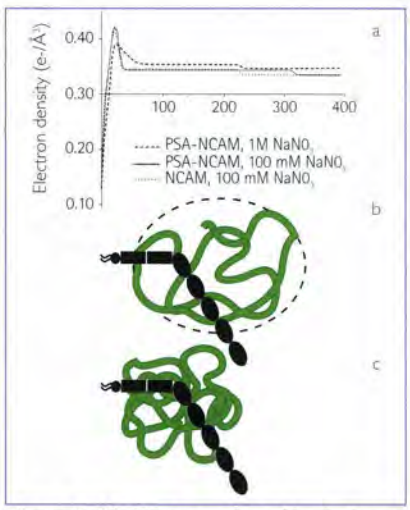

Figure 3: Model interpretations of the density profiles from X-ray and neutron data. The box models describing the X-ray reflectivity profiles are shown in (a). The black figure in (b) and (c) indicates the NCAM ectodomain configuration compatible with the measured thickness and proposed bend in the structure. The structure in (b) shows the proposed excluded volume of the PSA in 100m M NaCl, and (c) indicates the excluded volume of PSA in 1M NaCl.

eferences: [1] C. Johnson, G. Fragneto, O. Konovalov, V. Dubosclard, J.-F. Legrand and D. Leckband, Biochemistry 44(2) (2005) 546

biology

Distribution of reaction products in phospholipase A_2 hydrolysis

H.P. Vacklin and R.K. Thomas
(University of Oxford)
F. Tiberg *(Camurus, Lund)*
G. Fragneto *(ILL)*

We have used specular neutron reflection, measured on D17, to determine the structure of a selectively deuterium labelled phospholipid bilayer, and report how its composition evolves while the phospholipids are broken down during hydrolysis by phospholipase A_2 (PLA_2) from the venom of the snake Naja mossambica mossambica. There is a significant asymmetry in the distribution of the reaction products between the membrane and the aqueous environment which suggests that the lipid substrate undergoes dramatic physical changes during the hydrolytic reaction. The concomitant increase in PLA_2 affinity for the bilayer also suggests a membrane-composition-related regulation process of the activity of this class of enzymes.

Phospholipase A_2 (PLA_2) selectively cleaves the sn-2 ester bonds in 3-sn-phosphoglyceride lipids, the main lipid component of mammalian cell membranes. PLA_2 is present in a wide range of biological environments from invertebrate and insect venoms to the mammalian immune system [1], and performs a large number of different physiological functions although the chemistry at its catalytic site is preserved across species and class. The atomic resolution structures of many PLA_2s have led to an established understanding of the catalytic mechanism, but it only catalyses hydrolysis in the presence of an aggregated lipid interface, and is therefore an interfacially activated enzyme. The complex reaction kinetics of PLA_2 have been previously analysed assuming that the lipid membrane retains its structure during hydrolysis [2], and so called "interface quality" effects, such as membrane curvature or microheterogeneity, have been invoked to account for the diverse behaviour of PLA_2 in phospholipid membranes.

The vast majority of PLA_2s do not act in response to a specific activating receptor, and readily hydrolyse simple phospholipid model membranes. In the hydrolysis of long-chain membrane phospholipids, the reaction progress is found to be dependent on the type of phospholipid, with some enzymes exhibiting a long dormant phase before the onset of rapid hydrolysis. The extent of reaction also varies, although the enzyme itself is still found to be catalytically active if fresh phospholipid material is presented. *In vivo*, the activation and regulation of this group of enzymes is still poorly understood, although there are some indications of a link between molecular specificity and biological function. Although the reaction kinetics have been investigated for decades, the experimental techniques used have not allowed the determination of the amount or the location of the enzyme at a lipid interface, or the composition of the membranes during hydrolysis. Neutron reflectivity of supported phosphocholine bilayers recorded during *Naja mossambica mossambica* PLA_2 hydrolysis has shown that the enzymatic breakdown of the lipids leads to the destruction of the supported bilayer by solubilisation of up to 90% of the lipid material [3]. The enzyme was found to reside in a 21±1Å thick layer at the lipid-water interface with partial penetration into the outer membrane leaflet increasing with lipid chain saturation. The extent of the reaction decreased with chain saturation, indicating that the hydrophobic region exerts a regulating force on the enzyme, which is also supported by the strong and irreversible binding of PLA_2 to a hydrophobic self-assembled monolayer.

We have now monitored the surface composition of a bilayer of d_{31}-POPC, which has a perdeuterated sn-1 palmitoyl (C16:0) chain and an unmodified sn-2 oleyl (C18:1) chain. A reaction scheme with the scattering length densities that formed the basis of our data analysis of the phosphocholine components can be found in [3].

The reflectivity profiles, collected on D17 at the ILL in the time-of-flight mode, of d_{31}-POPC before, after 70 minutes and after 10 hours of PLA_2 hydrolysis are shown in figure 2. The bilayer initially has a lipid volume fraction of 0.82±0.05 in the hydrocarbon core region, and a thickness of 44±2Å, with the scattering length density of the chain region found to be $3.17\pm0.15 \times 10^{-6}$ Å^{-2}. During the first 70 minutes of the reaction the membrane thickness decreases to 31±2Å, but most remarkably, the scattering length density of the lipid chain region decreases to $1.4\pm0.15 \times 10^{-6}$ Å^{-2}, which corresponds to 1:3 ratio of deuterated palmitoyl chains and oleyl chains. This indicated that 50% of the lipid molecules have been hydrolysed and that all the released d31-lyso-palmitoylphosphocholine has left the interface. At this stage of the reaction, a 22±1 Å thick layer of the enzyme was found at the membrane-water interface,

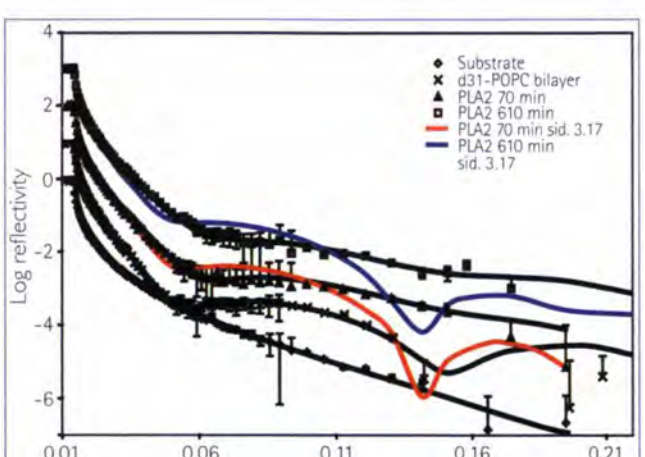

Figure 2: Neutron reflectivity profiles of d_{31}-POPC before and during PLA_2 hydrolysis. The black lines indicate data fits from optical matrix simulations of reflectivity and statistical error bars are given for each data point. The red and blue lines are the calculated reflectivities at 70 min. and 610 min. assuming that the scattering length density of the hydrocarbon chains remains 3.17×10^{-6} Å^{-2} and both reaction products leave the interface at the same rate.

occupying 40±5vol% of the outer lipid headgroup region. After 10 hours the reaction had gone to near completion, with a 23±1 Å layer of oleic acid (ρ = -0.2±0.15 x 10^{-6} Å^{-2}) remaining on the surface at a volume fraction of 0.55±0.05 and a 21±1Å thick layer of PLA_2 with an increased volume fraction of 0.5±0.05. The errors in bilayer structural parameters were derived from the maximum acceptable variation in the fitted parameters, in other words the thickness, volume fraction and scattering length density of each part of the lipid layer.

The reflectivity profiles were also calculated for the situation where both reaction products leave the interface at equal rates and the chain region scattering length density remains at 3.17±0.15 x 10^{-6} Å^{-2}. The solid red and blue lines in figure 2. represent these reflectivities at the same areas per molecule as the black lines for 70 and 610 minutes after the start of the reaction and demonstrate the sensitivity of neutron reflection to the layer composition. Figure 3 shows a schematic model of PLA_2 interaction with the phospholipid bilayer. This is the first direct measurement of the distribution of the reaction products in PLA_2 hydrolysis and it confirms that the interaction of the enzyme increases with increasing fatty acid content of the layer. The solution partitioning of lyso-lipid and the accumulation of fatty acid in the membrane are consistent with their solubilities, with the lyso-lipid having a large zwitterionic headgroup and the fatty acid a long saturated hydrocarbon chain. The increasing membrane association of the enzyme with increasing fatty acid content can be understood as an increased electrostatic interaction arising from the presence of negatively charged fatty acid, but our earlier results on DOPC, POPC and DPPC [3] showed that enzyme penetration into the bilayer increases with lipid chain saturation, which suggest that the interaction is also favoured by hydrophobicity. The increased binding of PLA2 to the d31-POPC bilayer with accumulating palmitic acid now confirms that even a long chain lyso-lipid can be lost from the membrane as a result of hydrolysis.

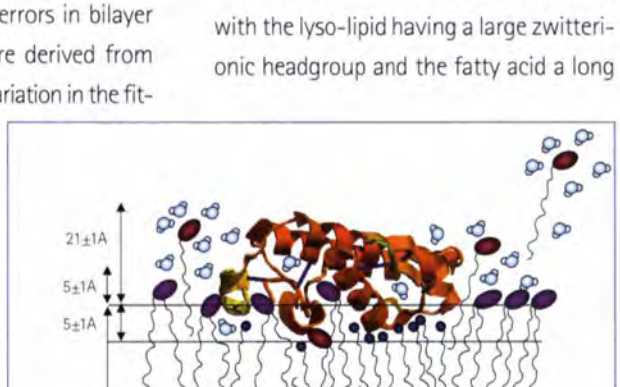

Figure 3: Model of PLA_2 interaction with a phospholipid bilayer. The enzyme resides at the lipid-water interface and penetrates 5Å into the hydrocarbon chain region. Fatty acid accumulates in the bilayer as the lyso-phospholipid partitions into the solution.

Our results challenge the view that the enzyme operates independently of the membrane lipid composition, and call for the development of kinetic analyses to describe the effects of changing composition. The biological functions of PLA_2 are diverse, and it is likely that its regulation is related to the lipid composition in each environment. Since PLA_2 plays a major role in inflammatory response, it is a good candidate for drug development aimed at its selective inhibition, but advance is hampered by a lack of understanding about the subtleties of PLA_2 regulation. We have shown that neutron reflection gives unique information about the composition of phospholipid membranes, and offers itself as a valuable tool to study the regulation of PLA_2 and indeed any membrane binding protein.

References: [1] D.A. Six and E.A. Dennis, Biochimica Et Biophysica Acta-Molecular and Cell Biology of Lipids 1488 (2000) 1
[2] M.K. Jain, J. Rogers, D.V. Jahagirdar, J.F. Marecek and F. Ramirez, Biochimica et Biophysica Acta 860 (1986) 435
[3] H. Vacklin, F. Tiberg, G. Fragneto and R.K. Thomas, Biochemistry 44 (2005) 2811

L. Blanchard, M. Blackledge and D. Marion *(IBS, Grenoble)*
N. Tarbouriech *(EMBL, Grenoble)*
W. Burmeister and R. Ruigrok *(EMBL and UJF, Grenoble)*
P. Timmins *(ILL)*

biology

Structure and dynamics of the nucleocapsid-binding domain of the Sendai virus phosphoprotein in solution

Negative strand RNA viruses contain RNA that is not in the sense of that of mRNA (+ sense), which can be directly translated into viral proteins, but in the opposite sense. This implies that, upon entry of the infected cell, the viral RNA has to be transcribed into mRNA before proteins can be produced. This group of viruses contains important human and animal pathogens like influenza, measles, rabies and Ebola viruses. The viral RNA is never naked when replicated or transcribed but always covered by a nucleoprotein, forming the nucleocapsid (NC). The viral RNA-dependent RNA polymerase is bound to this matrix through another viral protein, the phosphoprotein (P). Here we describe structural studies on P using a combination of crystallography, Nuclear Magnetic Resonance (NMR) and Small-Angle Neutron Scattering (SANS). P is an extremely flexible and long molecule. The combination of techniques that we used gives a view on the structure and function of the protein that any of the techniques alone cannot give.

We study the replication mechanism of this group of viruses because this mechanism needs specific interactions between many viral proteins (unique to these viruses and not found in humans) that may form targets for antiviral treatment. Much of our recent work was done on proteins and complexes from two viruses in this group, measles virus and Sendai virus, a parainfluenza-like virus (parainfluenza viruses cause serious respiratory disease in human children and adults).

For traditional structural biology, the phosphoprotein of Sendai virus is a very difficult protein. Intact P has a tendency to aggregate. Therefore, our studies have concentrated on the C-terminal region of the protein that, by itself, can support transcription by the viral polymerase. The N-terminal half of P, amino acids (aa.) 1-344, is only very poorly conserved between different viruses in this group and is not predicted to have regular secondary structure (no presence of α-helices or β-sheets) but to be natively disordered [1]. By limited protease digestion and various expression techniques, we were able to define at least two ordered domains in the C-terminal half of P, the oligomerisation domain (aa. 344-455) and the NC-binding domain (aa. 479-568) [2].

The new Carl-Ivar Brändén building that will house the PSB Laboratory (Partnership of Structural Biology) and the IVMS (Laboratory for Molecular and Structural Virology) on the ILL-ESRF site.

The oligomerisation domain could be crystallised and its structure was solved by scientists at the ESRF in Grenoble [3]. This domain consists of a tetrameric coiled coil of α-helices. The polymerase binds to aa. 411-455 in this domain, which is at the same time its most flexible part, indicated by high temperature factors. The NC-binding domain was too flexible to crystallise and its structure was solved by NMR by scientists at the IBS in Grenoble. It appeared that the N-terminal part of this domain (aa. 479-516) was also not regularly structured but that aa. 517-568 formed a three-helix bundle. The dynamical properties of aa. 479-516 were neither those of an ordered nor of a non-structured domain, but somehow in between, as if the structure consists of rapidly exchanging structural intermediates.

In order to have an estimate of the dimensions of the C-terminal half of P, we performed SANS on D22 on the entire domain and on the domain formed by aa. 479-568. Combining all the data from X-ray crystallography, NMR and SANS we were able to derive the model shown in figure 1. The C-terminal part of P is a tetrameric molecule with a length of 16.0 nm and a width of 4.1 nm. The two ordered helical domains are connected by sequences that seem to allow for flexibility but that are not disordered, otherwise the width of the domain would have been larger. Even the coiled coil structure

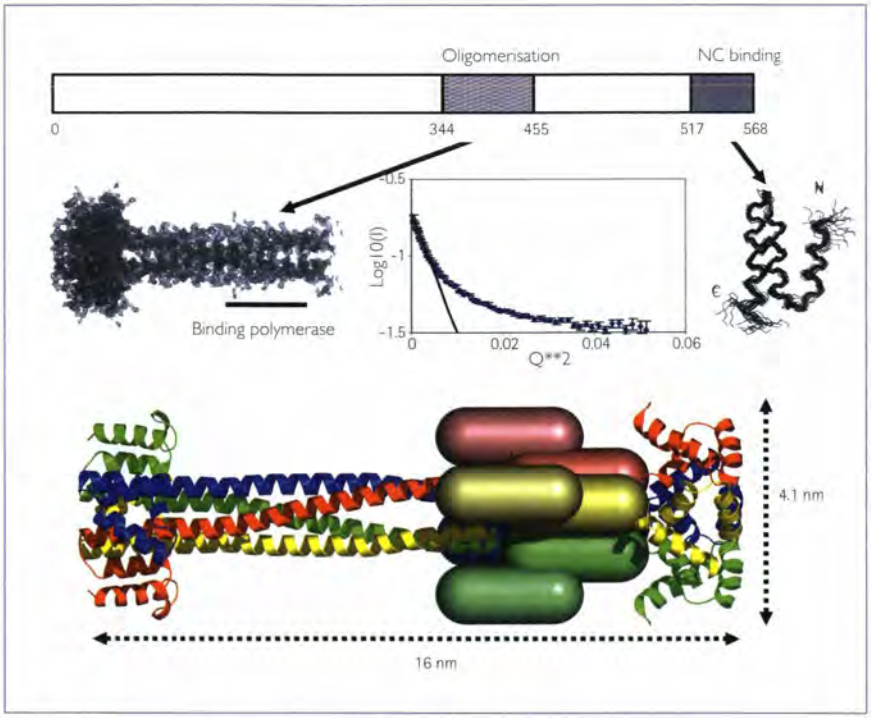

Figure 1: Structure of the phosphoprotein of Sendai virus.
Top: Linear representation of P with indication of the oligomerisation and the NC binding domain.
Middle: Experimental data on the structure of P; electron density map of the oligomerisation domain (left), Guinier plot of SANS data for the NC-binding domain (479-568) (centre) and superposed backbones of the 20 NMR structures with the lowest overall energy of the NC binding domain (right).
Bottom: Model of the entire C-terminal domain based on the data from crystallography, NMR and SANS.

is relatively flexible in the area where the polymerase binds. The triple helical bundles at the C-terminal end are only small and have exposed hydrophobic amino acid side-chains. Stabilisation of this domain may come from its interaction with the nucleocapsid. This molecule is made to be flexible in order to continuously make and break contacts with its partners; the polymerase and the nucleocapsid. The combination of techniques as used here was necessary to start to elucidate its structure and function.

This work is described in reference 4 and is a long-standing collaboration between the EMBL, ESRF, IBS and the ILL (the "PSB partners"), the Laboratory for Molecular and Structural Virology, FRE2854 CNRS-Université Joseph Fourier, Grenoble, together with Dan Kolakofsky, Department of Microbiology, Geneva University Medical School and Fabian Wild, INSERM Unité 404, CERVI, IFR 128, Lyon.

References: [1] Karlin et al., J. Gen. Virol. 84 (2003) 3239-52
[2] Tarbouriech et al., Virology 266 (2000) 99-109
[3] Tarbouriech et al., Nature Struct. Biol. 7 (2000) 777-781
[4] Blanchard et al., Virology 319 (2004) 201-211

M.C. Rheinstädter and T. Seydel *(ILL)*
T. Salditt *(University of Göttingen)*

biology

Probing dynamics at interfaces: molecular motions in lipid bilayers studied by neutron backscattering

Lipid membranes in a physiological context cannot be understood without taking into account their mobile environment. Here, we report on a high energy-resolution neutron backscattering study to investigate slow motions on nanosecond time scales in highly oriented solid supported phospholipid bilayers of the model system DMPC -d54 (deuterated 1,2-dimyristoyl-sn-glycero-3-phoshatidylcholine). This technique allows discriminating the Q-dependent onset of mobility and provides a benchmark test regarding the feasibility of dynamical neutron scattering investigations on these sample systems. Apart from freezing of the lipid acyl-chains, we could observe a second freezing temperature that we attribute to the hydration water in between the membrane stacks. The freezing is lowered several degrees as compared to (heavy) bulk water.

Lipid membranes as model systems for more complex biological membranes [1] cannot be understood without taking into account the structure and dynamics of their aqueous environment. The structure and dynamical properties of the bound water layers next to the bilayer as well as the 'free' (bulk) water further away from the water/lipid interface are of great importance in understanding the thermal, elastic and transport properties of the membrane. While most spectroscopic techniques such as nuclear magnetic resonance or dielectric spectroscopy, are limited to the centre of the Brillouin zone at Q=0 and probe the macroscopic response, neutrons and within some restrictions also X-rays give unique access to microscopic dynamics at length scales of e.g. intermolecular distances. Here, we report on a high energy-resolution (μeV) neutron backscattering study to investigate slow molecular motions on nanosecond time scales in highly oriented solid supported phospholipid bilayers of the model system DMPC -d54 (deuterated 1,2-dimyristoyl-sn-glycero-3-phoshatidylcholine), hydrated with heavy water [2]. The scattering volume restriction resulting from the low scattering volume of quasi-two dimensional planar membranes and the small inelastic signal was overcome by stacking several thousand highly aligned membrane bilayers [3].

The experiment was carried out at the cold neutron backscattering spectrometer IN10 in its standard setup with Si(111) monochromator and analyser crystals corresponding to an incident and analysed neutron energy of 2.08 meV (λ=6.27 Å). Two types of measurements have been performed. With fixed energy-window scans centred at zero energy transfer (FEW-scans), the scattered intensity arising from the sample, which is elastic within the instrumental resolution, was recorded as a function of the sample temperature. From FEW-scans, information on the onset and type of molecular mobility in the sample can be inferred. Thus, glass or melting transitions can be clearly identified and assigned to corresponding length scales by analysing the corresponding Q-dependence. The second type of measurement was performed by Doppler-shifting the incident neutron energy through an adequate movement of the monochromator crystal.

The IN10 analysers cover an angular range of approximately 20° each, resulting in a rather poor Q-resolution, but enhanced sensitivity for even very small inelastic signals. We used six discrete detector tubes of IN10. The broad lipid acyl-chain correlation peak that occurs at $Q \cong 1.4$ Å^{-1} was (mainly) detected in one detector tube ('lipid detector'), as depicted in figure 1. A Q-range of

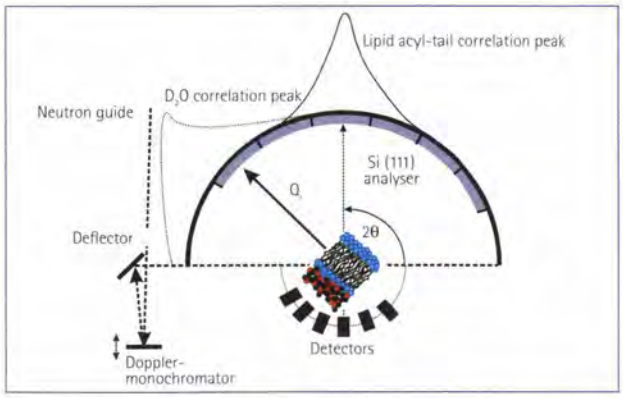

Figure 1: Schematic of the scattering geometry. The inter-acyl-chain correlation peak in the plane of the membranes is located at 1.4 Å^{-1} (the heavy water correlation peak occurs at 2 Å^{-1}). Spatially arranged analysers allow to separately but simultaneously probe the molecular dynamics at different length scales.

0.3 Å^{-1}<Q<1.9 Å^{-1} was simultaneously measured in this set-up to investigate and discriminate molecular dynamics on the different length scales of about 3 to 20 Å.

We performed FEW scans in a temperature range of 100-315 K to map out the transition of the lipids from immobile to mobile as a function of temperature for (a) the scattering vector Q placed in the plane of the membranes and (b) perpendicular to the bilayers. While the in-plane component (Q_y) in the 'lipid-detector' shows a pronounced freezing transition, there is no distinct T-dependence in the perpendicular direction (Q_z). We interpret this in terms of correlated motions, which take place mainly in the plane of the lipid bilayers (in the time and length scales observed). Figure 2 shows the in-plane component of the elastic scattering with the measurement in Q_z subtracted as background. In excellent accordance with other experiments, we attribute the pronounced freezing step ('immobile' within the resolution window) at 294 K (Q centred at 1.42 Å^{-1}) to the main transition of the (deuterated) lipid acyl-chains from the rigid gel phase at low-T into the fluid phase at higher temperatures. When analysing all detectors we find a second transition at about 271 K, mainly in the detector centred at Q=1.85 Å^{-1}, which can be attributed to the hydration water of the membrane stacks, i.e. water molecules in between the stacked bilayers. Even though the detector is not perfectly centred to the maximum of the static structure factor of water at Q=2 Å^{-1} (which is not accessible on IN10), it is positioned to detect a reasonable part of the broad heavy water correlation peak. Within this interpretation, freezing of the hydration water is lowered by about six degrees as compared to (heavy) bulk water at 277 K.

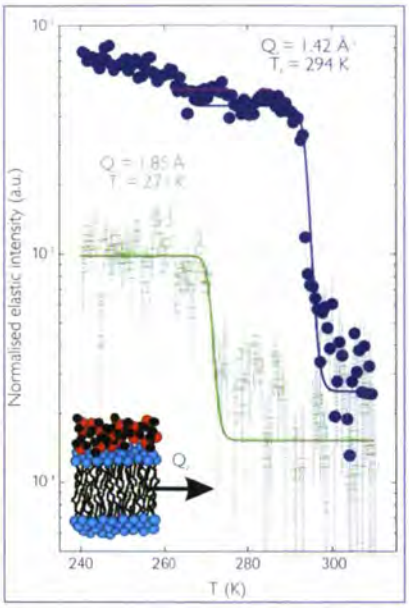

Figure 2: In-plane component of the elastic scattering signal. The mobile-immobile transition (within the resolution window) is clearly different for the lipid acyl-chains (T=294 K) and the position of the water correlation peak (T=271 K). Solid lines are guides to the eye (counting is normalised to monitor).

Figure 3 displays corresponding energy transfer scans. The data have been taken at three different temperatures, for T=250, 290 and 300 K with a typical counting time of about 9 hours per temperature. An elastic peak in the inelastic spectra points to static order at the corresponding length scales, where a fluid system has no order at infinitely long time scales. Even within the very limited statistics, the different dynamics is clearly visible: While the lipid acyl-chains melt between 290 and 300 K, melting at the water position already occurs between 250 and 290 K.

Our experiment gives a first high energy-resolution wave vector-resolved insight into collective lipid membrane dynamics. The dynamical properties of hydration water may be different from those of bulk water because hydrogen bonding to the lipid head groups at the lipid-water interface of the membrane might slow down water rotation and translation [4]. A scenario with gradual freezing of the water molecules, depending on the distance to the water-lipid interface, is under discussion. Only recently, Tarek and Tobias got access to the single-particle and collective dynamics of hydration water of a protein [5] by Molecular Dynamics (MD) simulations and pointed out the importance of water dynamics for the understanding of the dynamical transition of the protein. The membrane-water dynamics must play a crucial role for the understanding of fluctuations in stacked membrane systems as the hydration water e.g. mediates the interactions between two bilayers [6].

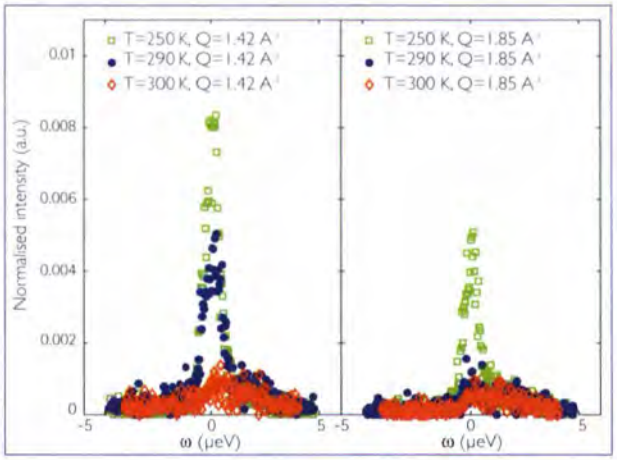

Figure 3: Energy scans at temperatures T=250 K, 290 K and 300 K for the Q-values 1.42 Å^{-1} (lipid acyl-chain correlation peak) and Q=1.85 Å^{-1}. At 290 K, the water signal is already "mobile" within the experimental energy resolution whereas the lipid acyl-chain are still frozen (counting is normalised to monitor).

References: [1] R. Lipowsky, R. and E. Sackmann, Structure and Dynamics of Membranes, Handbook of Biological Physics 1 (1995) Elsevier, North-Holland, Amsterdam
[2] M.C. Rheinstädter, T. Seydel, F. Demmel and T. Salditt, submitted, cond-mat/0501752
[3] M.C. Rheinstädter, C. Ollinger, G. Fragneto, F Demmel and T. Salditt, Phys. Rev. Lett. 93, 108107 (2004)
[4] M. Settles and W. Doster, Faraday Discuss. 103 (1996) 269
[5] M. Tarek and D. Tobias, Phys. Rev. Lett. 88, 138101 (2002); M. Tarek and D. Tobias, Phys. Rev. Lett. 89, 275501 (2002)
[6] J.N. Israelachvili and H. Wennerstroem, Langmuir 6, 873 (1990); L. Perera, U. Essmann and M. Berkowitz, Langmuir 12, 2625 (1996); J. Katsaras and K. R. Jeffrey, Europhys. Lett. 38 (1997) 43

Exploring soft matter

Michael Koza (centre) with Hercules students Jean-Christophe Perrin, Viviane Cristiglio, Pedro Teles and Isabelle Maurin (from the left).

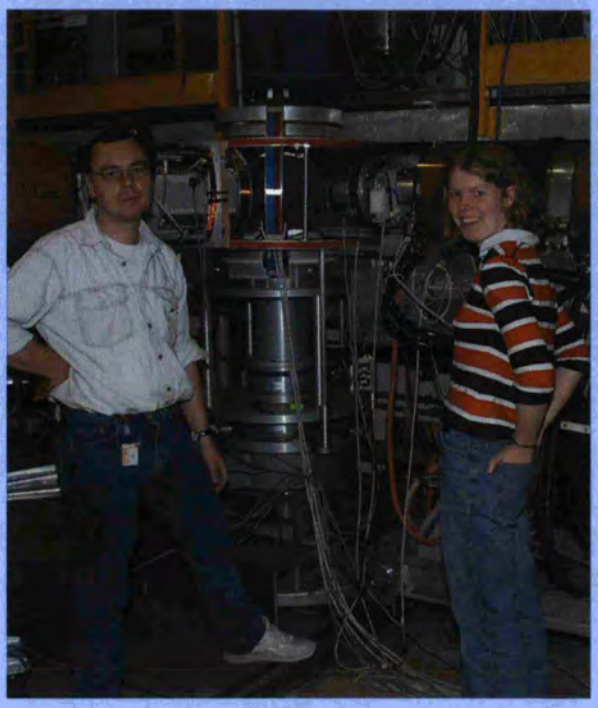

Georg Ehlers (SNS) and Fiona Coomer (Univ. of Edinburgh).

Juan Colmenero (Univ. of Pais Vasco, San Sebastian) is a member of the ILL Scientific Council.

Stuart Hicks (Univ. of Bristol), a young user of D11.

soft matter

Giovanna Fragneto, College 9 Secretary — http://www.ill.fr/Colleges/C9/

The year 2004 has been a particularly beneficial year for soft matter at the ILL. Among the events to cite is the inclusion in the Millennium Programme of the project for the construction of a new instrument dedicated to soft matter and biology, a reflectometer for the study of free liquid surfaces, and the upgrades of the D11 detector and tank. The new reflectometer will be optimised for the study of air/liquid and liquid/liquid interfaces, important areas of study will be adsorption of surfactants and polymers as well as lipid/protein interactions. The high flux will allow the study of kinetics of processes at those interfaces and performances will be competitive with both existing instruments and those to be built at new sources. It will become available to users in 2007. The upgrade of D11 will allow the measurement, on this highly used instrument in soft matter areas, of a wider dynamic range and performances will become closer to those of D22.

During the year talks have started between the ILL and ESRF for the creation of a Partnership for Soft Condensed Matter. A meeting with external experts has taken place in December and a report on the outcome will soon be available with indications for the next steps to be undertaken for a successful start of the project.

The year 2004 has been a particularly beneficial year for soft matter at the ILL

An internal meeting took place also in December where ILL scientists involved in soft matter research could express their views. Although opinions were different, most ILL scientists welcomed the idea as a possibility for enhancing the development of soft matter science on site. Finally, the new ILL topical brochure is being edited and is fully dedicated to soft matter.

This year has also witnessed a noticeable increase in the number of proposal submitted to College 9, particularly for SANS and reflectometry. The highlights in the following pages are a few examples of the activity in the field.

The two contributions from reflectometry represent examples of how fundamental studies on polymer films can lead to important technological applications. The contribution by Cooper et al. is on electro-polymerised films of conducting polymers bearing activated ester groups. Neutron reflectometry and infra-red measurements where performed simultaneously to identify changes in bonding occurring during the nucleophilic substitution reaction. For the first time fast time-resolved reflectivity profiles (2^{10} s) were collected on D17. The contribution by Mitchell et al. is on organic light emitting diodes (LED) used in flat panel displays. Simultaneous reflectivity and photoluminescence measurements were performed on the polymers deposited on an ITO (indium tin oxide) layer and the relationship between the film structure perpendicular to the interface and light emission was investigated. A small (1.5 nm) thermally stable layer of negligible scattering length density was found between the ITO and the polymer layers. It could contain air and therefore influence the performances of the light emitting devices.

The report by J. Eastoe et al. includes SANS results collected on D22 from photo-sensitive surfactants mixed in water-in-oil droplet dispersion with an inert surfactant. The irradiation with UV light selectively destroys the photo-surfactant inducing the shrinkage of the water nanodroplets. The photo-surfactants studied here represent a new generation of surfactants offering new possibilities for controlling surface tensions, molecular aggregation and bulk fluid properties.

This year has also witnessed a noticeable increase in the number of proposal submitted to College 9, particularly for SANS and reflectometry

J.-F. Berret et al. report on the formation of colloidal complexes resulting from the electrostatic self-assembly of polyelectrolite-neutral block copolymers and oppositely charged surfactants. A core-shell microstructure is revealed by a plethora of techniques including SANS. This is a new self-assembly mechanism interesting as it allows for the association of components of different nature such as organic and inorganic or synthetic and biological.

soft matter

Seeing dynamic changes in electroactive polymer films with neutron reflectivity

J.M. Cooper, N. Gadegaard and A. Glidle *(University of Glasgow)*
A.R. Hillman and K.S. Ryder *(University of Leicester)*
E.L. Smith *(University of Loughborough)*

Studies of thin electroactive polymer films deposited on surfaces are integral to many applications drawn from diverse fields in analytical and materials science and technology. In this report we describe two methods we have developed so that Neutron Reflectivity (NR) measurements can be used to probe, in real-time, the structural changes that occur when polymer films interact with external chemical species or electrochemical driving forces.

Thin electropolymerised films of conducting polymers bearing activated ester groups, such as the pentafluorophenyl activated ester of pyrrole-N-propionic acid (poly(PFP)), are particularly versatile in fabricating interfaces tailored to perform specific functions. After deposition, reaction with solution based molecules containing suitable nucleophilic groups (amines, for example) can generate specifically functionalised thin films and interfaces.

In many applications it is desirable to know the distribution of the functional species within the polymer film. Different scenarios can be envisaged for the progression of a reaction 'front' *inside* a thin film. These vary from gradual spatial progression in a direction perpendicular to the film/solution interface (z-direction), to homogeneous modification that occurs at a similar rate at all 'z' distances within the film i.e. the reaction proceeds via percolation of reactant species from fissures or channels within the polymer matrix. Which scenario, or variant, best approximates the actual situation depends on factors that can be externally controlled. For example, the reaction time, the internal polymer microstructure and the size-dependent diffusion of solution-based nucleophiles within the film, can all influence the reaction profile.

NR is one of the few techniques that can 'see inside' polymers with a spatial resolution on the nanometer scale. This makes it highly suitable to study the spatial progression of these polymer modification reactions. However, the NR profile gives information about the atomic composition and solvation of thin polymer films, but not about the *chemical* structure or nature of the *molecular* species present. This makes interpreting measurements of multicomponent films difficult.

We have developed a methodology combining NR measurements with a chemical species assay from infra-red (IR) measurements to identify changes in bonding that occur during nucleophilic substitution [1]. This global assay can then be used to constrain model profiles and interpret them in the context of different chemical species. To illustrate this technique we have probed the reaction profile of amine terminated poly(propylene glycol)s (PPGs) with poly(PFP). This particular surface modification has applications as both an anti-biofouling coating [2] and a model for the immobilisation of macromolecular biological species such as oligonucleotides and microenzymes.

In early experiments [1] to monitor the progress of polymer modification reactions, we made a series of discrete NR and FTIR measurements after halting the reaction at specific periods of time. Thus we could only determine the spatial reaction profile at a few time points. Recently, however, as a consequence of the high flux available on D17, we have made *in situ* kinetic NR measurements whilst concurrently collecting reflectance IR data. Our combined NR/IR reflectance cell (see figure 1) was mounted on the D17 reflectometer.

Using the combined NR/IR reflectance cell, we have collected NR profiles and IR spectra every 15 minutes during the course of the reaction between poly(PFP) and amine terminated PPGs of different molecular weights. The upper panel of figure 2 shows selected NR profiles collected during the course of the reaction between PPG800 and a poly(PFP) film. Readily discernable changes in the fringe pattern can be seen as the reaction proceeds and are associated with changes in the IR spectrum (loss of

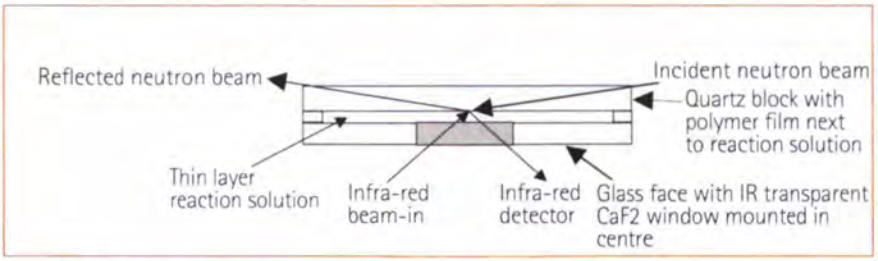

Figure 1: Schematic of combined cell showing neutron and IR optical paths.

pentafluorophenyl ring and ester group vibrations and gain in amide group signals). Quantification of the IR spectra constrains the model fits to the NR data by ensuring that spatial integration of the polymer scattering length density (Nb) is consistent with the IR determined composition. The lower panel of figure 2 shows a set of constrained scattering length density (Nb) profiles corresponding to different extents of reaction. The evolving shape of these profiles, most obviously of the film in d6DMSO, indicates both that the region of the film closest to the solution interface is the first to react with solution based PPG800 molecules and that the reaction front gradually proceeds in the z-direction. This contrasts with the NR/IR results we have obtained when following the reaction of the shorter chain PPG130 with poly(PFP). In that case, the reaction proceeds almost homogeneously throughout the thickness of the film. This difference accords with a size dependence of PPG chain diffusion within the polymer. Whilst this result is as expected, the NR/IR technique has provided an experimental tool with which to measure this phenomenon.

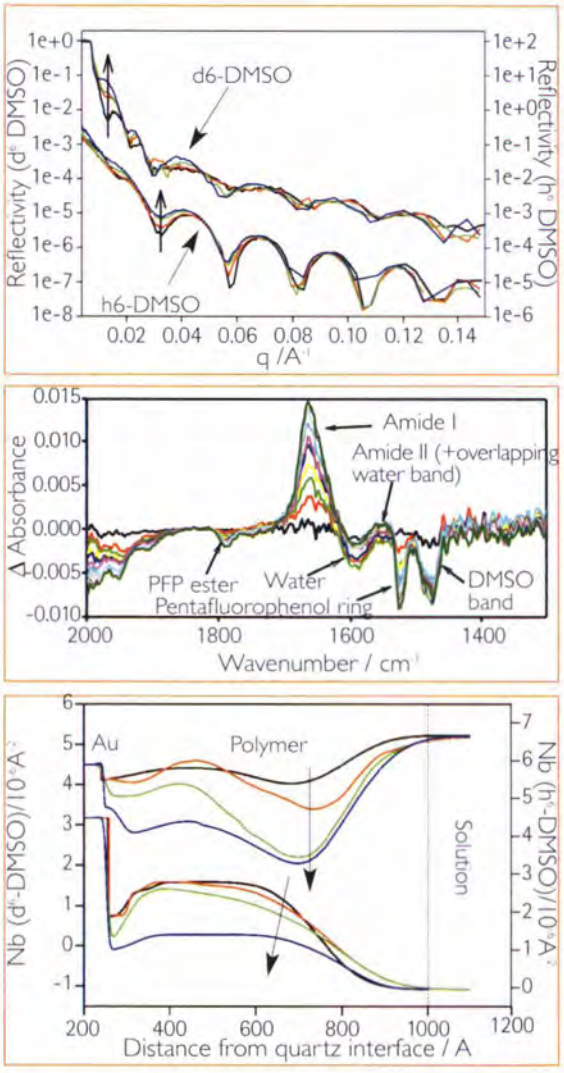

Figure 2: Top: NR profiles for unreacted polymer (black) and after reaction with increasing amounts of PPG-800 (red through yellow) in h^6- and d^6-DMSO.
Middle: Reflectance FTIR profiles collected simultaneously with NR profiles, every 15 min during reaction. Positive changes in absorbance corresponds to formation of bonds, negative changes to bond breaking.
Bottom: Fitted Nb profiles for unreacted polymer (black) and after reaction with increasing amounts of PPG-800 (red through yellow). Electrode interface is at 250 A.

In a second instrumental development, to follow the solvation changes and film swelling during redox cycling of a polymer film, we have written IDL routines to link the collection of data on D17 with the control of our external instrumentation (a potentionstat). This allows us to collect a series of short time (ca. 2-10 s) NR profiles corresponding to sequential potential windows during the electrochemical oxidation-reduction cycling of poly(vinylferrocene) (PVF), a redox polymer used in sensor applications (figure 3). To obtain NR profiles with sufficiently good statistics, we repetitively cycled the film for ca. 8 h and used the box-car averaging method to store reflectivity data corresponding to specific potential windows in appropriate memory 'bins'. An example of NR data accumulated in this fashion during the oxidation-reduction cycling of PVF is shown in figure 3 [3]. Subsequent analysis revealed that not only is there substantial swelling as the film is oxidised (see fringe pattern changes in figure 3), but also that the film solvation changes from being almost dry in the neutral, undoped state to ca. 25% solvated when fully doped [4]. Significantly, by collecting the time resolved data of figure 3, we discovered that the majority of this increase in solvation occurs during the first 5% of film oxidation. Currently, we are extending these temporal studies to see if we can use NR to observe whether, or not, neutral analyte molecules (e.g. glucose) are transported into the bulk of the film with the solvent, during the dramatic oxidation induced increase in solvation.

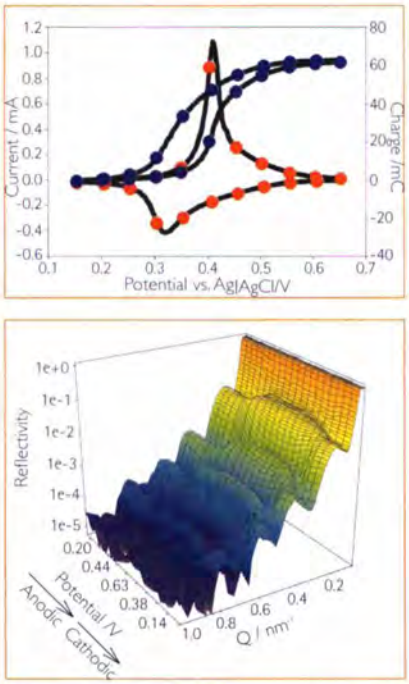

Figure 3: Upper: Voltammogram and integrated current for PVF redox cycle in 0.1 M $NaClO_4$. Markers shows limits of potential windows between which 'binned' NR profiles are collected. Lower: Binned NR profiles for PVF cycled in 0.1 M $NaClO_4/D_2O$.

References: [1] A. Glidle, L. Bailey, C.S. Hadyoon, A.R. Hillman, A. Jackson, K.S. Ryder, P.M. Saville, M.J. Swann, J.R.P. Webster, R.W. Wilson and J.M. Cooper, Anal. Chem. 73 (2001) 5596
[2] A. Glidle, T. Yasukawa, C.S. Hadyoon, N. Anicet, T. Matsue, M. Nomura and J.M. Cooper J. M. Anal. Chem. 75 (2003) 2559
[3] J.M. Cooper, R. Cubitt, R.M. Dalgleish, N. Gadegaard, A. Glidle, A.R. Hillman, R.J. Mortimer, K.S. Ryder and E.L. Smith, J. Am. Chem. Soc. 126 (2004), 15362
[4] A. Glidle, J.M. Cooper, A.R. Hillman, L. Bailey, A. Jackson, and J.R.P. Webster, Langmuir, 19 (2003) 7746

soft matter

Physical structure and optical properties of conjugated polymers

W.J. Mitchell, P.L. Burn and R.K. Thomas *(University of Oxford)*
G. Fragneto *(ILL)*
J.P.J. Markham and I.D.W. Samuel *(University of St. Andrews)*

Organic light-emitting diodes (LEDs) based on conjugated polymers are set to play an important role in the flat panel displays market. The morphology and interfacial interactions of the polymer films control key device properties including charge injection and mobility, and luminescence efficiency. Neutron reflection (NR) in combination with photoluminescence (PL) measurements on partially deuterated light-emitting conjugated polymers allows the direct relationship between film structure and light emission and the interface with an indium tin oxide anode to be probed.

Conjugated polymers are an important class of organic semi-conductors, which are being intensively investigated as the light-emitting layer in organic light-emitting diodes (LEDs). Cambridge Display Technology Ltd, Philips, Dupont, Covion Organic Semiconductors GmbH, and Dow Corp all have conjugated polymer programmes. LEDs based on conjugated polymers have improved dramatically since their initial discovery in 1989 and Philips has now brought polymer based LEDs to a commercial reality with a LED based battery indicator in a razor. The morphology of the materials plays a critical role in controlling the properties of the polymers and the performance of the devices [1,2]. In the context of LEDs intermolecular interactions between polymer chains are critical. Strong inter-chain interactions are needed for good charge mobility but such interactions can be bad for light-emission due to excited dimer formation, which changes the colour and reduces the efficiency of emission. The interfaces between each of the layers in the device and in particular the conjugated polymer/electrode interface critically affect the device performance [3]. Photoluminescence is a very useful technique as it probes the light-emitting properties of the material. By combining NR and PL measurements on indium tin oxide (ITO) using partially deuterated polymers the relationship between film structure and light emission and the polymer-electrode interface can be probed simultaneously. We illustrate the technique with poly[2-(2'-d_{17}-ethylhexyloxy)-5-methoxy-1,4-phenylenevinylene) (MEH-PPV) (figure 1) which has a similar scattering length density (SLD) to the ITO substrate [4,5].

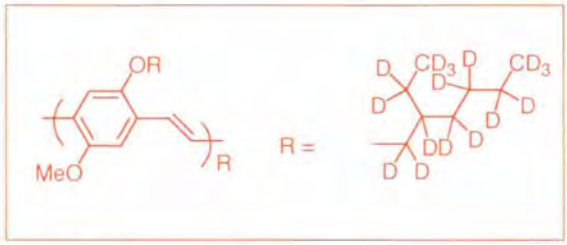

Figure 1: Structure of MEHPPV.

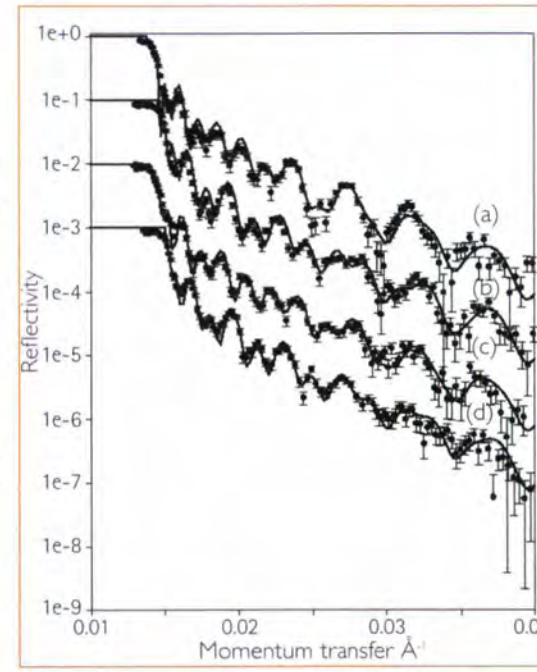

Figure 2: Measured NR profiles and fits (solid lines) of MEHPPV at: a) r.t.; b) 70 °C; c) 220 °C; d) r.t. after 220 °C anneal. The reflectivity scale corresponds to the profile for a). The other plots are offset successively.

The NR profiles of the polymer/ITO layers (figure 2) at different temperatures were collected on D17 with the *in situ* PL measurements carried out simultaneously using a 408 nm nitride laser for excitation and a fibre coupled Ocean Optics CCD spectrograph for detection. Whilst the properties of the ITO stayed constant the polymer film

thickness and SLD was strongly dependent on the thermal history of the film and the values are summarised in figure 3 with the PL spectra at each temperature shown in figure 4. A key observation was that the NR profiles at each stage of the thermal history of the film were more complicated than expected for a composite film comprising individual layers with the same scattering length density. The complexity in the profiles arises from the presence of a small (1.5 nm) thermally stable layer with negligible SLD between the bulk polymer and ITO layers. This low contact layer could be due to a number of reasons including the failure of the polymer to wet the ITO surface, the non-uniformities of the ITO supporting the fairly rigid thick layer of polymer, or the loss of an intervening layer of spreading solvent on evaporation under vacuum. The discovery that a low contact layer can be present, has important implications for LEDs prepared by depositing the polymer directly onto the electrode surface. Such a layer will be detrimental to charge injection from the electrode to the bulk polymer layer leading to poor device performance and the presence of air in the low-contact region could also lead to accelerated device degradation.

Thermal annealing of the polymer layer can occur during device production or operation and hence it important to understand the affect of temperature on the properties of the polymer film. Surprisingly for MEHPPV it was found that even modest heating (70 °C) caused the film to become thinner with a concomitant increase in

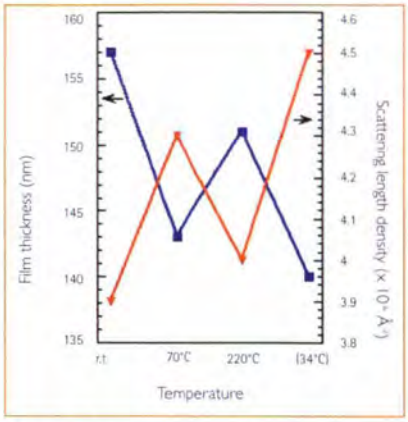

Figure 3: Summaries of the scattering length density (triangles) and film thickness (squares) determined from the NR profiles versus temperature.

SLD (figure 3). This change occurs well below the glass transition temperature (196 °C) of the polymer and is thought to arise from the rearrangement of the polymer chains enabled by the bulky flexible 2-ethylhexyloxy side groups. Importantly, the densification and thinning of the film does not cause the PL emission of the films to change appreciably (figure 4) although the more efficient packing of

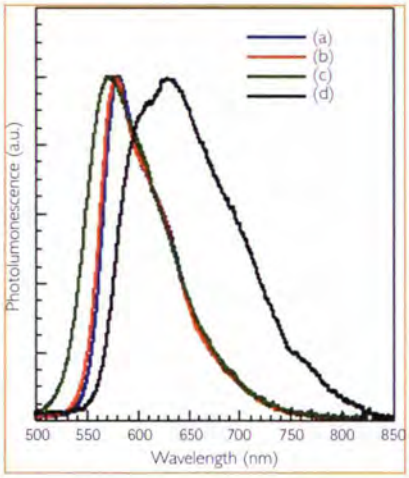

Figure 4: PL spectra of MEHPPV at: a) R.T.; b) 70 °C; c) 220 °C; d) R.T. after 220 °C anneal.

the polymer chains should lead to improved charge mobility. The fact that MEHPPV anneals significantly at 70 °C is important for device manufacturing and testing, as it is well within the temperature range at which devices might be prepared and used. Heating the film above the Tg simply causes the film to expand and the SLD to decrease by the commensurate amount (figure 3). At the elevated temperature the long wavelength side of the PL emission is the same as at lower temperatures but the peak and blue edge of the spectrum has moved to shorter wavelengths, which is consistent with more disorder in the conjugated backbone associated with the expanded film. Finally, after cooling the MEHPPV film was significantly thinner, denser and better ordered when compared with the pre-annealed film. The large red-shift of the peak and red tail in the PL spectrum (figure 4) of the film after the high temperature anneal are due to better intramolecular order and increased π-π interactions. In the device context although charge mobility might be improved the high temperature anneal is detrimental to the films emissive properties.

In conclusion, these studies show that NR in combination with PL measurements is a powerful technique for relating physical structure to the optical properties of conjugated polymer films.

eferences: [1] T-Q. Nguyen, I.B. Martini, J. Liu and B.J. Schwartz, J. Phys. Chem. B. 104 (2000) 237
[2] J. Liu, Y. Shi, L. Ma and Y. Yang, J. Appl. Phys. 88 (2000) 605
[3] P.K.H. Ho, J-S. Kim, J. H. Burroughes, H. Becker, S.F.Y. Li, T.M. Brown, F. Cacialli and R. H. Friend, Nature 404 (2000) 481
[4] G.R. Webster, W.J. Mitchell, P.L. Burn, R.K. Thomas, G. Fragneto, J.P.J. Markham and I.D.W. Samuel, J. Appl. Phys. 91 (2002) 9066
[5] W.J. Mitchell, P.L. Burn, R.K. Thomas and G. Fragneto, Appl. Phys. Lett. 82 (2003) 2724

soft matter

Novel core-shell structures for colloids made from surfactants and polymers

J.-F. Berret and P. Hervé *(CNRS - Cranbury Research Center Rhodia Inc., Cranbury, USA)*

I. Grillo *(ILL)*

We report on the formation of colloidal complexes resulting from the electrostatic self-assembly of polyelectrolyte-neutral block copolymers and oppositely charged surfactants. The copolymers investigated are asymmetric and characterised by a large neutral block. Using light, neutron and X-ray scattering experiments, we have shown that the colloidal complexes exhibit a core-shell microstructure. The core is described as a dense and disordered micro-phase of micelles connected by the polyelectrolyte blocks, whereas the shell is a diffuse brush made from the neutral chains. Colloidal complexes with core-shell structures resemble the well-known amphiphilic block copolymer micelles. The self-assembly mechanism is however different here. It is based on the complexation between opposite charges. This mechanism has recently attracted much interest because it allows the association of components of different nature, such as organic and inorganic or synthetic and biological.

During the last decade, there has been a widespread interest for the design and synthesis of new polymer-based colloidal particles. Among these particles, colloidal complexes have emerged as a new type of microstructure, with potential applications in home and personal care, catalysis and drug delivery. Colloidal complexes result from a self-assembly mechanism between polyelectrolyte-neutral co-polymers and oppositely charged species. The first macromolecules or macro-ions having been complexed with these polymers were synthetic and biological macromolecules [1,2], proteins [3] and surfactant micelles [4]. In this report, we re-examine the case of surfactant micelles using small-angle neutron scattering (SANS) on D22. Two systems are compared. The first (1) is a dilute aqueous solution containing a polyelectrolyte (poly(sodiumacrylate) and a surfactant (dodecyl trimethyl/ammonium bromide (DTAB)) of opposite charge. The total concentration of active matter is a few percent (by weight) and the charge ratio, Z is 1. Z is the ratio between the numbers of surfactant molecules and charged monomers. The second system (2) is an aqueous solution at the same concentration and same charge ratio, where the polyelectrolyte is replaced by a diblock co-polymer. The first block of the co-polymer is the same charged chain as in system (1) and the second block is neutral and water-soluble [5]. Details of the structure and molecular weights are given in the captions.

In system (1), the polymer-surfactant solution undergoes a phase separation resulting in two well separated and stable thermodynamic phases. The lower phase is a white precipitate, whereas the upper phase is fluid and transparent. Figure 1 shows the X-ray scattering intensity of the precipitate. The 10 Bragg reflections observed

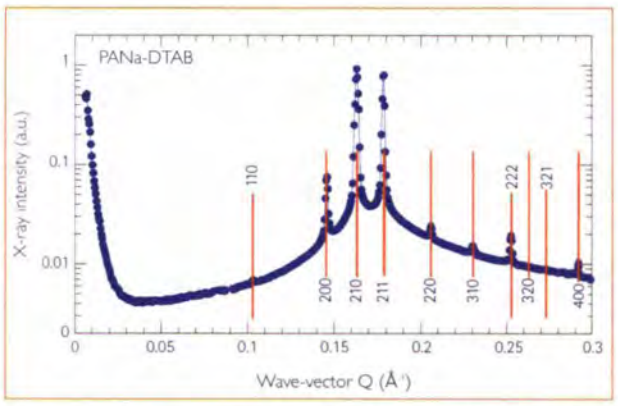

Figure 1: X-ray scattering intensity of the precipitate obtained by mixing poly(sodium acrylate) and dodecyltrimethylammonium bromide solutions at total concentration c = 2 wt. % and charge ratio Z = 1. The molecular weight of the polyelectrolyte is 30 000 g/mol, corresponding to 420 monomers. The succession of Bragg peaks is consistent with a cubic structure of symmetry Pm3n. The lattice parameter of the elementary cell is 8.61 nm [6].

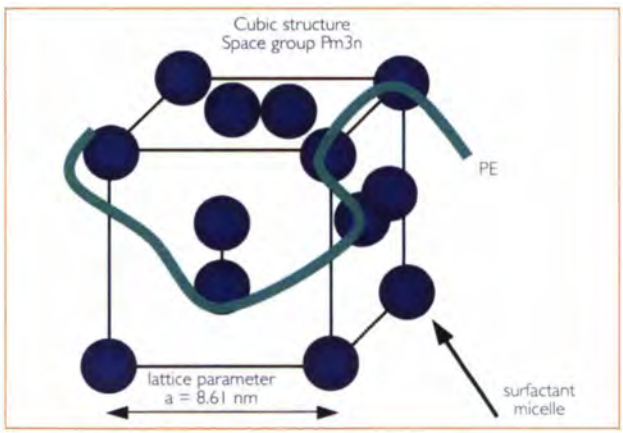

Figure 2: Schematic representation of the cubic structure associated with the space group of symmetry Pm3n. The spheres are the surfactant micelles (radius 2 nm) and the polyelectrolytes are assumed to wrap around them. For Pm3n cubic structure, each face of the lattice cell has two surfactant micelles and the micellar volume fraction is 0.524.

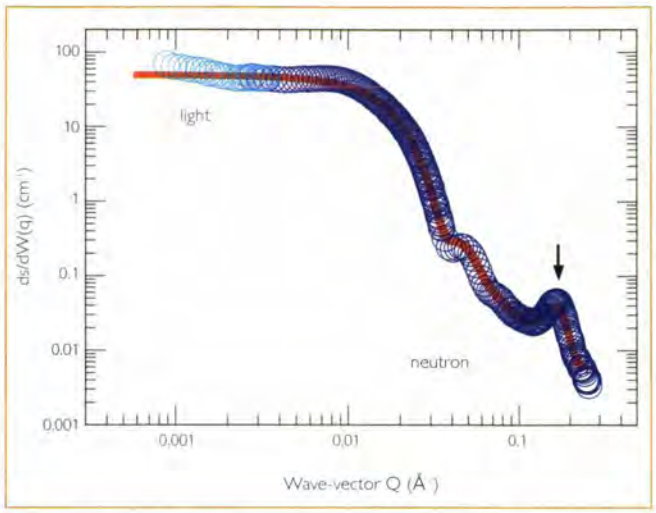

Figure 3: Light and neutron scattering intensities of solutions obtained by mixing poly(sodium acrylate)-b-poly(acrylamide) and dodecyltrimethylammonium bromide solutions at total concentration c = 1 wt.% and at charge ratio Z = 1 [7]. The neutron scattering data were collected on the D22 spectrometer at the ILL. The molecular weights for both blocks are 5 000 g·mol^{-1} for the charged segment and 30 000 g·mol^{-1} for the neutral one. For this solution, the solvent is D_2O. An arrow indicates the position of a structure peak at 0.16 Å^{-1}. The peak corresponds to an interaction distance of ~ 4 nm, i.e. twice the radius of a micelle. Continuous line : calculation of the form factor of the mixed aggregate represented in figure 4 [9]. Here, we assume a distribution in aggregation numbers, around an average value of 105 and with a standard deviation of 52.

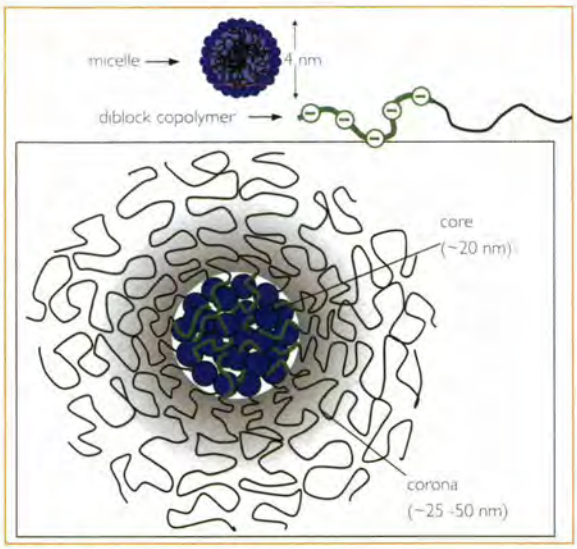

Figure 4: Representation of a colloidal complex formed through the association of oppositely charged block copolymers and surfactant micelles. Depending on the molecular weights of the copolymers, the radius of the core ranges from 10 to 20 nm and the corona thickness between 25 and 50 nm [6].

between 0.1 Å^{-1} and 0.3 Å^{-1} attest to the existence of a long-range cubic order, associated with the space group *Pm3n* [6]. The cubic symmetry suggests that the surfactants are organised in spherical micelles, these micelles being at the nodes of the cubic lattice (figure 2). In this arrangement, the polyelectrolytes are wrapped around the micelles and can connect several of them. When the former homopolyelectrolyte chain is now part of a diblock co-polymer, the phase separation described previously ceases to occur [6,7]. For system (2), the mixed solutions appear homogeneous and transparent. Figure 3 shows the scattering cross-section measured by light and small-angle neutron scattering on such solutions. $d\sigma/d\Omega(q)$ is dominated by the two features : a strong forward scattering (at low wave-vectors) and a structure peak at high wave-vectors. In order to interpret the spectra of figure 3 quantitatively, we have assumed for the surfactant-polymer complexes a core-shell structure similar to that shown in figure 4 [6-9]. In this model, the core is a dense and disordered assembly of surfactant micelles connected by the polyelectrolyte blocks. The corona is a diffuse shell of the neutral chains which is detected at much lower wave-vectors. Dynamic light scattering experiments actually show rather monodisperse hydrodynamic sizes around 50 nm (radius), which we attribute to the overall dimension of the colloids. The continuous line in figure 3 has been calculated by Monte Carlo simulations using a hard sphere interaction potential between micelles [9], and an average aggregation number of 105 micelles. The agreement between experimental data and the model is excellent, especially at high q where the structure factor is correctly reproduced.

Co-polymers of different molecular weights and of different nature have been studied in order to demonstrate the universality of the electrostatic self-assembly process using surfactants. Eight different polymers have been investigated and hierarchical structures similar to that of figure 4 were observed [6]. We have found that the size of the colloids depends predominantly on the degree of polymerisation of the charged block. We suggest that the mechanism of formation of the colloidal complexes is identical to that of the phase transition encountered in the polyelectrolyte-surfactant mixtures. With the co-polymers, the growth processes are arrested at a stage that is controlled by the neutral blocks. The polymer brush surrounding the core not only prevents the macroscopic phase separation. It also stabilises the aggregate.

ferences: [1] K. Kataoka, H. Togawa, A. Harada, K. Yasugi, T. Matsumoto and S. Katayose, Macromolecules 29 (1996) 8556
[2] M.A. Cohen-Stuart, N.A.M. Besseling and R.G. Fokkink, Langmuir 14 (1998) 6846
[3] A. Harada and K. Kataoka, Macromolecules 31 (1998) 288
[4] T.K. Bronich, A.V. Kabanov, V.A. Kabanov, K. Yui and A. Eisenberg, Macromolecules 30 (1997) 3519
[5] M. Destarac, W. Bzducha, D. Taton, I. Gauthier-Gillaizeau and S.Z. Zard, Macromol. Rapid Commun. 23 (2002) 1049
[6] J.-F. Berret, B. Vigolo, R. Eng, P. Hervé, I. Grillo and L. Yang, Macromolecules 37 (2004) 4922
[7] J.-F. Berret, G. Cristobal, P. Hervé, J. Oberdisse and I. Grillo, Eur. J. Phys. E 9 (2002) 301
[8] P. Hervé, M. Destarac, J.-F. Berret, J. Lal, J. Oberdisse and I. Grillo, Europhys. Lett. 58 (2002) 912
[9] J.-F. Berret, P. Hervé, O. Aguerre-Chariol and J. Oberdisse, J. Phys. Chem. B 107 (2003) 8111

soft matter

Photo-tuneable films

J. Eastoe, M. Sanchez-Dominguez and P. Wyatt *(University of Bristol)*
R.K. Heenan *(ISIS, CCLRC, Chilton)*
I. Grillo *(ILL)*

Surfactants are molecules that adsorb at interfaces, thereby modifying surface properties: this is the physical chemistry underlying biological cell membranes, lung action, emulsion and foam formation and detergents. For chemically inert surfactants used in common commercial products, control over molecular aggregation and adsorption states is normally only achieved after significant changes in salt concentration, level of acidity or temperature. Deliberate destabilisation or resolution of microemulsions and emulsions can be important in areas such as pharmaceuticals, organic synthesis, oil recovery, drug delivery, cosmetics and nanotechnology. The resulting separation of oil and water components gives a route to product recovery or release. Small-angle neutron scattering (SANS), coupled with sample contrast variation via selective deuteration, is an especially powerful technique for studying surfactant-containing systems.

A new approach is to use photo-sensitive surfactants, such as compound 1 (figure 1), and now UV light can be used as an external stimulus. In the case of photoscission (photolysis) reactions, oil-loving organic chains can be split away from the water soluble portion (figure 1). Hence with photo-degradable surfactants like 1 it is possible to controllably "switch off" the surface activity, by light-driven generation of inactive compounds like 2 and 3. In fact 3 is actually an oily substance with no interfacial activity whatsoever. The photochemical reactions can be followed, and characterised by Nuclear Magnetic Resonance (NMR) spectroscopy, prior to neutron scattering experiments. Analyses of these NMR spectra suggest that the reaction is essentially complete, and a photostationary state is reached after typically 2 hours of irradiation, corresponding to a composition of 37% of 2, 53% of the non-surface active 3 and 10% residual photo-surfactant 1.

As a good example, consider a water-in-oil nanodroplet dispersion (microemulsion), stabilised by a mixture of 1 and an inert surfactant, which in this case is common Aerosol-OT (figure 2 left). Nanometer-sized spherical water droplets are encapsulated by the interfacial surfactant film, and dispersed in an oily organic solvent (heptane). Application of UV light (hv) is expected to selectively destroy the photo-surfactant 1, leaving the inert co-surfactant Aerosol-OT intact. As a result of the photo-chemical breakdown of 1 the composition of the stabilizing layer will change in favour of the inert surfactant. This should then feed through to changes in the stability of the microemulsion, and also the preferred size of the nanodroplets (figure 2 right).

Figure 3 shows the effect of irradiation with UV light: initially the stable microemulsion sample is transparent (a) since dilute nanometer-sized aqueous droplets are present. After a burst of UV light larger micron sized drops form (b), from which the majority of the water phase then separates (c) leaving residual water as smaller microemulsion droplets. Hence UV light has caused a partial destabilisation of the dispersion, through loss of encapsulated water from the oily medium.

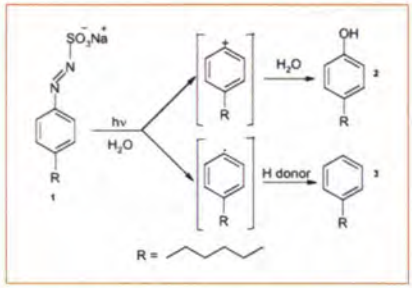

Figure 1: The chemistry behind photodegradable surfactants.

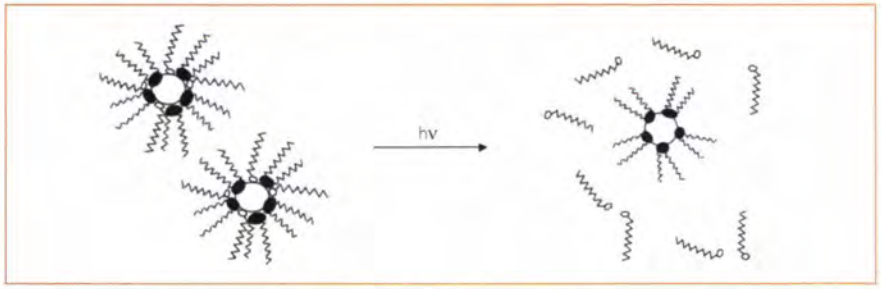

Figure 2: Concept behind photo-tuneable surfaces comprising a photo-destructible surfactant

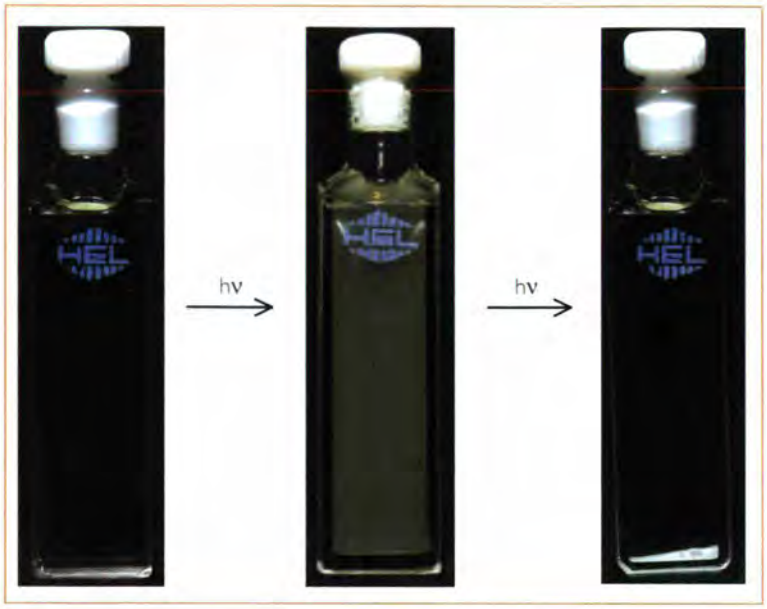

Figure 3: Shows the effect of irradiation with UV light: initially the stable microemulsion sample is transparent (a) since dilute nanometer-sized aqueous droplets are present. After a burst of UV light (b), a milky emulsion containiing micron-sized droplets begins to form, which eventually resolves into a clear upper microemulsion phase and a denser, opaque water-surfactant mixture seen at the bottom of the sample (c). Hence UV light has caused a partial destabilisation of the dispersion, through loss of encapsulated water from the organic medium.

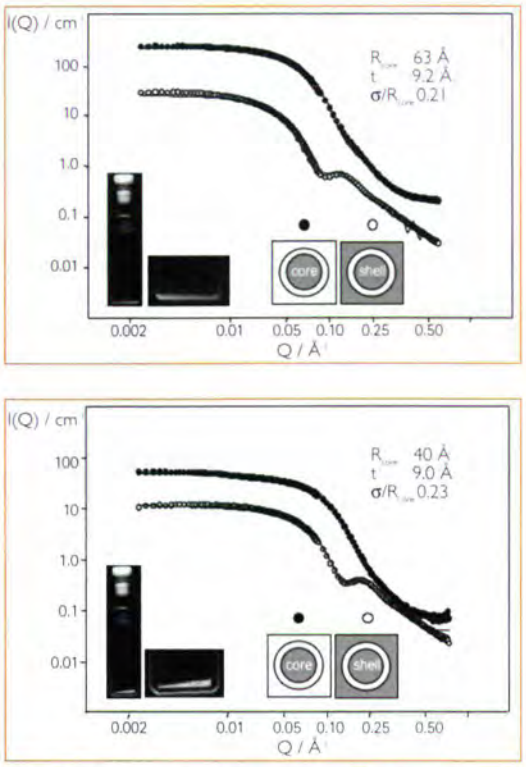

Figure 4: SANS data from water core (●) and surfactant shell (○)contrasts before (a) and after (b) irradiation. Lines are simultaneous fits to both data sets, to find the water droplet radius Rcore, the surface layer thickness t and the polydispersity σ/Rcore.

Small-angle neutron scattering (SANS), coupled with sample contrast variation via selective deuteration, is the only viable way to study changes of the nanodroplet structure. This is especially powerful since the water droplet cores and interfacial film can be studied separately in complementary experiments.

The SANS instrument D22 was used to follow this UV-induced shrinkage of the water nanodroplets. In order to obtain detailed information on the effects of irradiation on interfacial and nanodroplet structure, SANS experiments with water core (D_2O + *h*-surfactants + *h*-oil) and surfactant shell contrast (D_2O + *h*-surfactants + *d*-oil) were performed. This latter arrangement highlights a "hollowshell" of surfactant, with a characteristic interference pattern (figure 4). These contrast-variation SANS data were fitted simultaneously. After extensive trials, and based on previous literature, the most appropriate model was found to be for polydisperse spheres of water with an outer surfactant shell. These detailed analyses reveal a shrinkage of the water cores from a mean radius of 63 Å before to 40 Å after UV irradiation, corresponding to a decrease in nanodroplet volume of about 75%. Therefore UV-driven destruction of photosurfactant 1 is equivalent to reducing the effective surfactant concentration, thereby controlling the stability and size of the dispersed water droplets.

Chemicals like 1 represent a new generation of surfactants with added functionality and tuneability, and they offer exciting new possibilities for controlling, surface tensions, molecular aggregation and bulk fluid properties such as visco-elasticity (rheology). Recent research shows this to be a general concept, and photo-surfactants can be employed to control many different properties such as adsorption, micellisation and formation of vesicles, emulsion stability and gelation of both aqueous and organic phases.

eferences: [1] J.Eastoe, M.Sanchez-Dominguez, P.Wyatt, H.Cumber, G.Burnett and R.K.Heenan, Photoresponsive microemulsions, Langmuir 19 (2003) 6579
[2] J.Eastoe, M.Sanchez-Dominguez, P.Wyatt, H.Cumber and R.K.Heenan, Light-sensitive microemulsions, Langmuir 20 (2004) 1120

Back to fundamental

Paolo Mutti (PN3 responsible) being interviewed by Paola Catapano (on behalf of Italian television – RAI 3).

Werner Heil (Univ. of Mainz) discussing with Hans Börner (Nuclear and Particle Physics group leader).

The Perkeo team on their spectrometer at PF1. First row: Anthony Hillairet, Marc Deissenroth, Marc Schuman, Michael Kreuz. Second row: Thomas Moschoutis, Daniela Mund, Hartmut Abele, Jochen Krempel, Torsten Soldner.

nuclear & particle physics

Paolo Mutti, College 3 Secretary — http://www.ill.fr/nfp/npp/Home.htm

Four instruments devoted to a variety of topics operate in this College. Two instruments, the high resolution gamma-ray spectrometers PN3 (GAMS) and PN1 (Lohengrin) the fission product mass spectrometer, cover the field of nuclear physics. PF1 and PF2 are used mainly in the field of particle physics.

College 3 for nuclear and particle physics is running four instruments devoted to a variety of topics in the physical research

The year 2004 has been very successful for Lohengrin thanks to the new set of very efficient germanium detectors, which have increased the detection efficiency for doubly coincident gamma rays by about an order of magnitude. New microsecond isomeric states were measured in ^{123,126,127,128,130}In and ^{125}Cd. These data on the Indium isotopes give valuable information on systematic trends close to the doubly magic ^{132}Sn nucleus and allow shell model predictions to be tested. Theoretical interpretations of the structure of these very exotic nuclei were made by Covello's group (Napoli). While the energy levels of ^{129,130}In isotopes were reproduced quite well by realistic shell model calculations, the lighter In isotopes were not so well reproduced, probably due to changes in theproton-neutron interaction. A new isomeric state was found in ^{95}Kr. For the first time gamma-ray spectra of this nucleus, which is nine neutrons away from stability were observed. This isomer allows systematic trends in neutron-rich nuclei with 59 neutrons to be studied, since other isomeric states in this mass region had previously been measured at Lohengrin.

The GAMS spectrometers came back in operation after the forced stand-by during 2003 due to exchange of the H6/H7 beam tube. After teething problems were solved both instruments performed well, and the background has been significantly reduced. Tests indicated the viability of Positron Anihilation Spectroscopy on GAMS. An adequate count rate with 10 times better resolution than classical PAS was obtained. Running the two instruments on opposite sides of H6/H7 in coincidence mode promises further improvements including a remarkable 7 orders of magnitude gain in background at constant signal. Additionally, a more complete determination of the X and Y components of the electron momentum vector might become possible.

The PF1 cold-neutron facility was dedicated to further precision measurements of the A- and B- asymmetry coefficients in the beta-decay of free neutrons (respectively the correlation between the neutron spin and the electron momentum; and the correlation between the neutron spin and the neutrino momentum). These measurements were strongly motivated by the current discussion of possible non-unitarity of the Cabibo-Kabayashi-Maskawa matrix. This problem arises due to last most precise neutron asymmetry measurements. The realisation of these experiments was made possible thanks to recent improvements in the setup of the PF1 facility. Particularly important was the increase in neutron flux due to the new H113 neutron guide as well as the almost complete (99.7%) neutron polarisation achieved with the newly developed geometry of crossed supermirror polarisers. The treatment of the experimental data is still in progress.

At PF2 the EDM measurement has now nearly been terminated. Detailed studies of systematic effects mainly due to the magnetic field were carried out. The experiment will give an accuracy on the EDM of the order of 10^{-26} ecm. A new experiment to observe the neutron quantum states in the gravitational field was performed at the PF2 ultra-cold neutron beam. For this measurement a neutron detector with very high spatial resolution was developed with the aim of detecting directly the neutron density distribution. This method has the advantage of a better statistical sensitivity and a smaller systematic error since the effect of the scatterer/absorber does not influence the neutron wave-function. At the PF2/MAM neutron beam a new measurement of the neutron life-time was carried out during 2004. The experimental setup consisted of a gravitational trap for UCN which allows the measurement of the UCN energy spectrum after the neutrons are stored in the trap. The new value obtained for the neutron life-time is in good agreement with the prediction of the Standard Model.

A new experiment to observe the neutron quantum states in the gravitational field was performed at the PF2 ultra-cold neutron beam

nuclear & particle physics

Quantum falling in the gravitational field

V.V. Nesvizhevsky, H.G. Börner and A.K. Petoukhov *(ILL)*
A.M. Gagarski and G.A. Petrov *(PNPI, Gatchina)*
L. Lukovac *(UJF, Grenoble)*
H. Abele and S. Nahrwold *(University of Heidelberg,)*
S. Baeßler and S. Raeder *(University of Mainz)*
T.M. Kuzmina *(KRI, St. Petersburg)*
J. Schrauwen *(FUNDP LISE, Namur)*
V.G. Tishchenko *(JINR, Dubna)*
K.V. Protasov *(LPSC, Grenoble)*
A.Yu. Voronin *(Lebedev Institute, Moscow)*

If the energy of a massive object is well defined and the domain of its motion is restricted by a confining potential, then it should be held in bound quantum states – with well pronounced variation of the probability density to observe this object in different spatial points. Some time ago we showed for the first time that neutron quantum states in the gravitational potential can be observed. Now we were able for the first time to directly measure the standing wave of the neutron density in the gravitational field above a horizontal mirror. This was done by developing a position-sensitive neutron detector of extra-high spatial resolution.

Quantum states of neutrons in the gravitational field [1] were recently observed in the neutron transmission measurement through a horizontal slit between a mirror and an absorber/scatterer [2]. The most convincing "signature" for this observation consisted in an abrupt change in the neutron transmission at a slit size approximately equal to the "height" of the lowest quantum state of ~15 μm. We call this approach the "integral" method for measuring the neutron density distribution in quantum states above a mirror. A position-sensitive detector with a spatial resolution of ~1 μm could allow us to measure such a density distribution, directly using the so-called "differential" method. This one has the advantage of much better statistical sensitivity. Additionally, it introduces smaller systematic errors because the influence of the absorber/scatterer to the neutron wavefunctions does not need to be taken into account any longer. In our first experiment, a neutron detector with such an extra-high spatial resolution was not available and therefore we had to develop it [3]. We report here the first measurement of the spatial variation of the neutron density in the Earth's gravitational field using such a detector. Figure 1 illustrates the corresponding experiment with neutrons. Neutrons move classically along the horizontal direction and quantum-mechanically along the vertical direction. The first slit between the mirror 1 and the scatterer is wide enough to transmit the lowest quantum state with small losses while it is narrow enough to suppress considerably the higher quantum states. A measurement of the spatial density variation at the first slit exit would not be very spectacular as the lowest quantum state wavefunction is too smooth and broad (see figure 2). This is why we use the mirror 2 at a height of 21 μm lower than that of the mirror 1 [3]. In such a configuration there are no neutrons populating the lowest quantum state above the mirror 2. The population of the lowest quantum state above the mirror 1 is transmitted preferably to the 3rd quantum state above the mirror 2. Admixtures of other states can be calculated precisely in a model-independent way giving the blue curve in figure 3 [4]. Figure 4 shows the result in an artist's view. It shows an apple moving in the gravitational field. Its energy is well defined at its height before starting to fall down. Its domain of motion is restricted from above by the gravitational field. In principle, one could therefore expect to observe a manifestation of its quantum motion. If one would be able to introduce at the bottom a kind of mirror for such an apple, then it would be settled in bound quantum states because the mirror together with the gravitational field provides a potential well. One can notice in

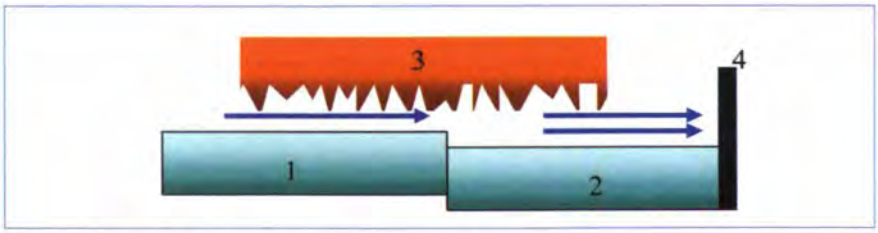

Figure 1: General scheme of the experiment: 1,2 – mirrors, 3 – scatterer, 4 – position-sensitive neutron detector. Arrows indicate the neutron beam.

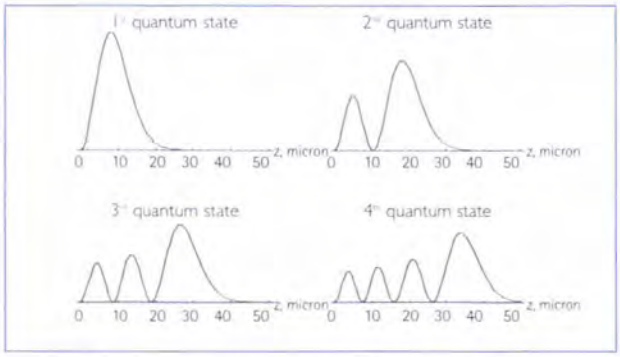

Figure 2: Probability density distribution for 4 lowest quantum states.

figure 2 that all quantum states, except the first one, show similar behaviour at small height and therefore contribute "coherently" to the variations of the neutron density. The green curve in figure 3 corresponds to the best fit of the experimental results using a set of precise wave-functions with free values for the quantum states populations; the interference between the quantum states is neglected. The difference between the blue curve and the experimental data is probably due to the finite (but nevertheless extremely high!) efficiency of the scatterer and the finite precision in the adjustment of the optical elements of the installation. However, evidently, the theoretical curves reproduce well the essential features of the measured experimental results. In particular, one should note a pronounced narrow lowest peak, an indication to the second peak and well pronounced third broad peak. The decrease of the neutron intensity at large heights corresponds well to the known asymptotical shape of the Airy-function responsible for the neutron wave function. Distances between the peaks correspond to the expected values. The background level is negligible. One should note that an experiment of such a type is statistically limited, thus the presented picture corresponds to 3 days of measurement. However, the considerable variation of the neutron density and very high spatial resolution of the neutron detector allow us to clearly identify the phenomenon and to estimate relatively well the parameters of the quantum states. Treatment of more experimental data is in progress. More experiments are planned in the near future.

The observation of neutron states, besides the fundamental importance of as the first experimental manifestation of quantum states of matter in a gravitational field, provides also a valuable tool for many other studies. For example, it can be used to search for additional fundamental short-range forces [5], to study the quantum-

Figure 4: "Quantum apple": an illustration for the quantum motion of an object in the gravitational field.

mechanical localisation [6] or surface potentials. It also could serve as a unique method to measure long-term interaction of a wave with rough and mirror surfaces.

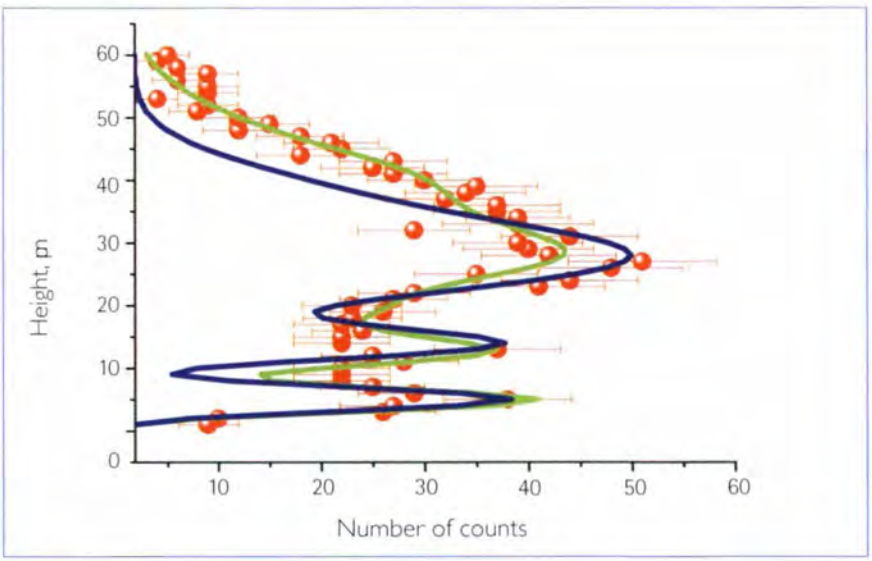

Figure 3: The neutron density distribution in the gravitational field is measured using a position-sensitive neutron detector of extra-high spatial resolution. The red circles indicate the experimental results. The blue solid curve corresponds to the theoretical expectation under the assumption that all distances are installed precisely, the scatterer is ideally efficient and there are no transitions between the quantum states; the interference between the quantum states is neglected. The green curve corresponds to the best fit using precise wave-functions and free values for the quantum states populations.

eferences: [1] V.I. Luschikov and A.I. Frank, JETP Letters 28(9) (1978) 559-561
[2] V.V. Nesvizhevsky, H.G. Börner, A.M. Gagarski et al, Physical Review D 67 (2003) 102002; Nature 415 (2002) 297-299
[3] V.V. Nesvizhevsky, H.G. Börner and A.M. Gagarski et al, NIM 440A(3) (2000) 754-759
[4] V.V. Nesvizhevsky, Uspekhi Fizicheskikh Nowk 47 (5) (2004) 515-522
[5] H. Abele, S. Baessler and A. Westphal, Lect. Notes Phys. 631 (2003) 355; V.V. Nesvizhevsky and K.V. Protasov, Classical and Quantum Gravity 21 (2004) 4557-4566
[6] R.W. Robinet, Phys. Reports 392(1-2) (2004) 1-119

nuclear & particle physics

Measurement of the neutron lifetime using a gravitational trap and a low-temperature Fomblin coating

A. Serebrov, V. Varlamov, A. Kharitonov and A. Fomin *(PNPI, Gatchina)*
Yu. Pokotilovski *(JINR, Dubna)*
P. Geltenbort *(ILL)*

We present a new value for the neutron lifetime of 878.5 ± $0.7_{stat.}$ ± $0.3_{syst.}$. This result differs from the world average value (885.7 ± 0.8 s) by 6.5 standard deviations and by 5.6 standard deviations from the previous most precise result [1]. However, this new value for the neutron lifetime together with a β-asymmetry in neutron decay, A_0, of -0.11189(7) [2] is in a good agreement with the Standard Model.

The present measurements were carried out at the high flux reactor at the ILL using the PF2/MAM instrument. The experimental set-up is sketched in figure 1. It is a gravitational trap for UCN and at the same time it can be used as a differential gravitational spectrometer. Therefore, the distinguishing feature of this experiment is the ability to measure the UCN energy spectrum after its storage in the trap.

The UCN storage trap *1* is mounted inside a cryostat vacuum vessel *2*. The trap *1* has a window that can be rotated about a horizontal axis so that UCN are held in the trap by gravity when the trap window is in its upper position.

The neutron lifetime is measured with the size extrapolation method using two sizes of UCN trap. The total probability of UCN losses τ_{st}^{-1} is broken up into two parts: the first part is the probability of neutron beta-decay τ_n^{-1} and the second one is the probability of UCN losses τ_{loss}^{-1} : $\tau_{st}^{-1} = \tau_n^{-1} + \tau_{loss}^{-1}$.

The UCN storage time τ_{st} is calculated from the measurements of the number of neutrons remaining in the trap after different holding times: $\tau_{st} = (t_2 - t_1)/Ln(N_1/N_2)$, where N_1 and N_2 are the numbers of neutrons remaining in the trap after holding times t_1 and t_2 respectively.

As the UCN are held by the trap material then τ_{loss}^{-1} contains the probability of losses at the trap walls: $\tau_{loss}^{-1} = \eta \cdot \gamma(E)$, where $\gamma(E)$ is the effective frequency of collisions, which depends on the UCN energy and the trap size. The neutron lifetime value can be obtained by a linear extrapolation of τ_{st}^{-1} to zero value of γ.

In the experiment, we have used a new type of wall coating, a low-temperature Fomblin (LTF) that can be evaporated onto the surface in vacuum. This perfluorinated oil has a composition containing only *C*, *O* and *F* and thus a low neutron capture cross section.

The results of measurements of the UCN storage time for different energy intervals and for different traps (wide and narrow) are presented in figure 2 as a function of effective frequency of collisions γ. The extrapolation of all data to the neutron lifetime gives a value of 877.60 ± 0.65 s with a χ^2 of 0.95.

For the size extrapolation method we have to connect the values for the different traps for the same UCN energy interval, and then to calculate the average value of all determinations of the neutron lifetime.

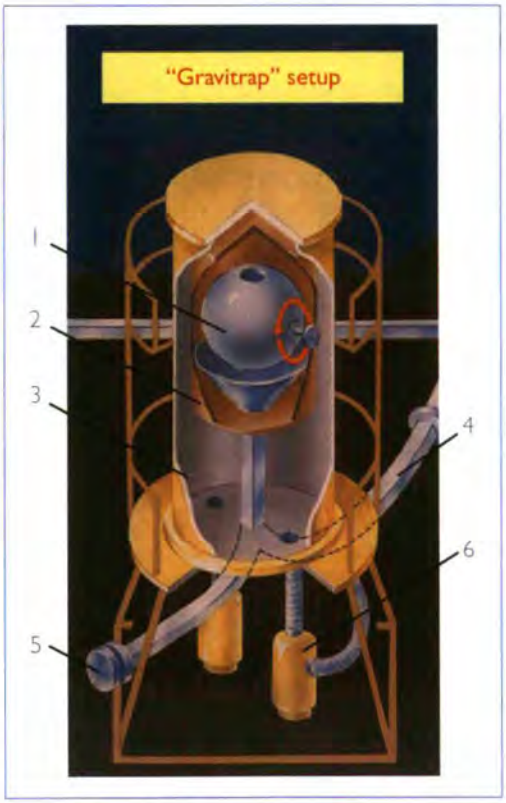

Figure 1: The Scheme of "Gravitrap", the gravitational UCN storage system. 1: UCN storage trap; 2: "high" vacuum volume; 3: "rough" vacuum volume; 4: neutron guide from UCN Turbine; 5: UCN detector; 6: vacuum pumps.

The average value of the neutron lifetime from the size extrapolation method is 878.07 ± 0.73 s. To both estimate the accuracy of and to check the reliability of the size extrapolation method using the calculated γ-function, we have used a Monte Carlo (MC) simulation of the experiment.

In the present experiment the storage time is very close to the neutron lifetime. The difference between the best-measured storage time and the neutron lifetime is about 5 s only. This gives confidence in the reliability of the result obtained. The new result for the neutron lifetime (878.5 ± 0.8 s) can be used for the unitarity test of Cabibbo-Kobayashi-Maskawa (CKM) matrix. Figure 3 shows a plot of V_{ud} versus $-G_A/G_V$ from [3] with the new result for the neutron lifetime. The authors of work [3] favour result $A_0 = -0.1189(7)$ [2] for β-asymmetry in comparison with the world average value $A_0 = -0.1173(13)$. (In earlier experiments the large corrections had to be made for neutron polarisation, electron magnetic mirror effects and background, which were all in the 15% to 30% range). We follow recommendations of work [3] but the G_A/G_V-value from the world average value A_0 is shown in figure 3 also.

The new lifetime result is different from the world average value (885.7 ± 0.8 s) by 6.5 standard deviations, and by 5.6 standard deviations from the previous most precise result [1]. However, the new result for the neutron lifetime together with the current value for the β-asymmetry in neutron decay ($A_0 = -0.1189(7)$ [2]) is in a good agreement with the Standard Model.

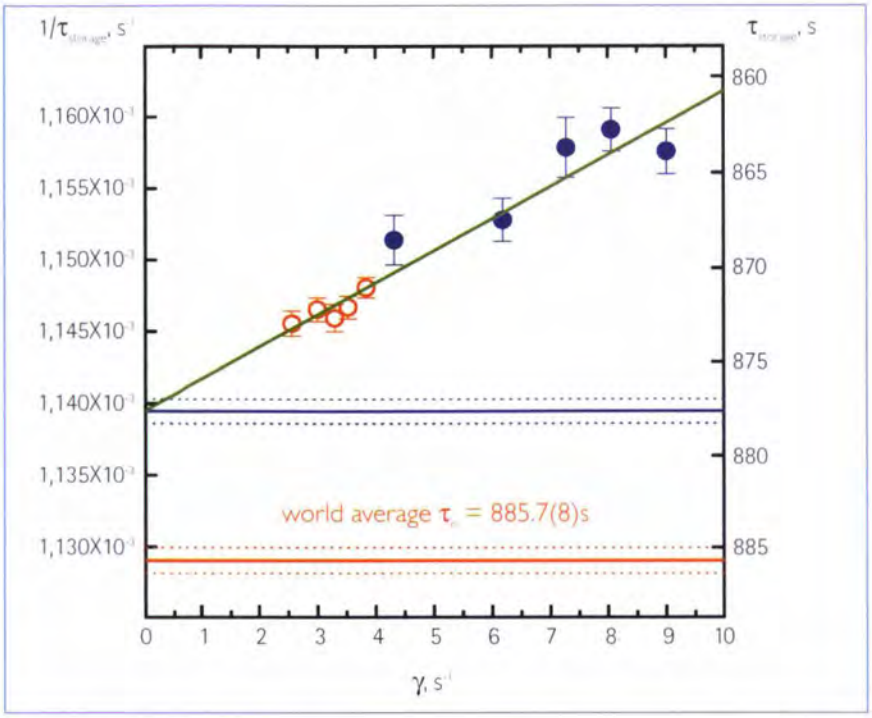

Figure 2: Result of extrapolation to the neutron lifetime using joint energy and the size extrapolation method. Measurements made with a spherical (open circles) and cylindrical (filled circles) traps.

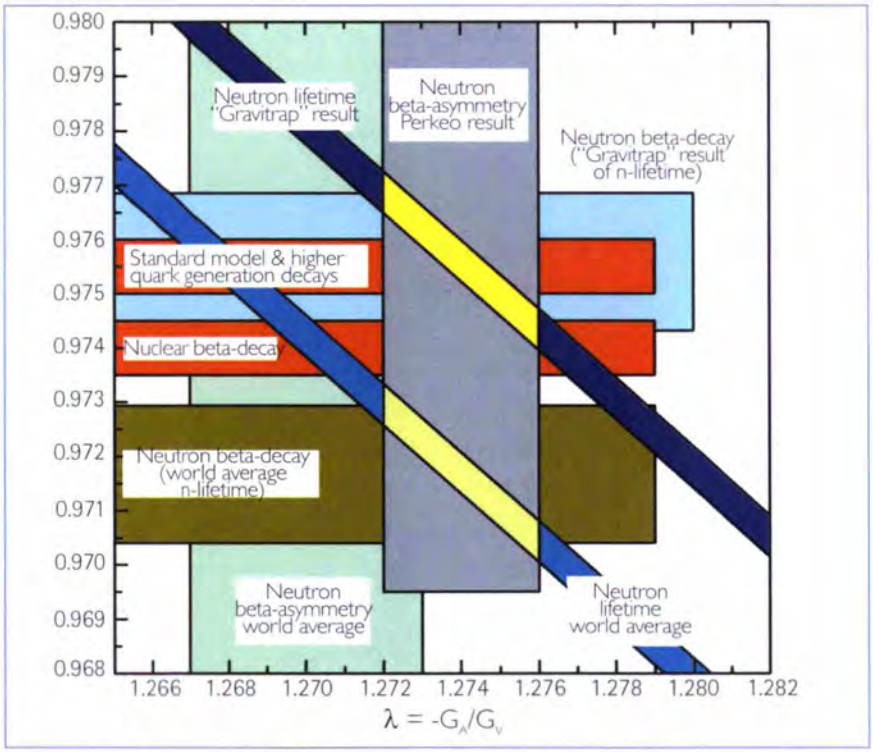

Figure 3: $|V_{ud}|$ versus $-G_A/G_V$. $|V_{us}|$ was derived from higher quark generation decays via $|V_{ud}| = \sqrt{1 - |V_{us}|^2 - |V_{ub}|^2}$ predicted from unitarity, from Ft values of nuclear-decays, and neutron β-decay.

References: [1] S. Arzumanov, L. Bondarenko and S. Chernyavsky et al., Phys.Lett.B 483 (2000) 15-22
[2] H. Abele, M. Astruc, S. Baessler et al., Phys.Rev.Lett. 88 (2002) 211801
[3] H. Abele, E. Barberio, D. Dubbers et al., Eur.Phys.J. C 33 (2004) 1-8

nuclear & particle physics

Temperature dependence of ultracold neutrons loss rate

E. Korobkina and R. Golub
(HMI Berlin)
J. Butterworth and P. Geltenbort
(ILL)
S. Arzumanov
(Kurchatov Institute, Moscow)

Ultracold neutrons (UCN) are playing an increasingly important role in experiments studying the fundamental properties of the neutron as they can be stored and hence observed for long times (several hundreds of seconds). This can lead to a significant increase in accuracy compared to experiments where cold or thermal neutrons are used. However, in storage type experiments, the UCN upscattering to the meV range due to wall interaction, which is the main cause of UCN losses over a wide temperature range, has to be well understood. To study the low-temperature dependence of UCN losses and to find a quantitative model based on available data in surface and solid state physics, a dedicated ultra-high vacuum cryostat has been developed. UCN loss rates can be studied in a well controlled environment over a wide temperature range. In this report the results of our first experiment are summarised.

The so-called "UCN anomaly", i.e. the discrepancy between measured ultracold neutron loss rates and those theoretically predicted for pure materials has been the subject of study for over 30 years. Such investigations are of great interest and necessary for fundamental particle physics experiments with UCN, where their trapping due to the nuclear Fermi-potential and production at low temperatures is involved (e.g. the life time of the free neutron, its electric dipole moment) as well as for certain solid state physics experiments. Nevertheless the available data about the upscattering of UCN to the meV range, which is the main cause of UCN losses in storage experiments, are contradictory and rather poor especially at low temperatures. UCN losses were intensively studied experimentally at room temperature in the 1970's-80's but no theoretical model explaining the available UCN upscattering data could be established as yet. The only well-established fact is that UCN losses are caused by hydrogen contamination in the surface layer. Regrettably, there has not been a rigorous theoretical study of UCN upscattering in the past. The earlier theoretical works were trying to describe experiments at the level of loss probabilities of 10^{-3} - 10^{-4} per collision, while in modern experiments loss probabilities down to 10^{-5}-10^{-6} per UCN bounce on the surface are achieved.

The low-temperature behaviour of the upscattering loss rate is crucial for distinguishing between different models. However, it is rather difficult to study experimentally because stable and well controlled surface conditions have to be provided over a wide temperature range. In 2001 a dedicated ultra high vacuum cryostat has been commissioned at one of the beam positions of the ultracold neutron facility PF2.

Copper was chosen as a first sample for surface investigations because this material is well studied not only in UCN storage at room temperature but also in surface physics and in neutron scattering. In our specially designed set-up in addition to a high efficiency oil-free pumping system large area cryopumping surfaces at both 77K and 4K were used to avoid the cryo-adsorption on the surface of the sample. Under those experimental conditions no temperature hysteresis in the UCN loss rate was measured. Comparison of the data at 300K before and after heating to 450K showed that cleaning and oxidation treatment made the surface of the sample hydrophobic. Therefore, the measured data can be explained by inelastic scattering of UCN by Hydrogen atoms which are chemically bound to atoms of the Copper surface but not to any physisorbed contaminations. Next, questions such as which atoms were responsible for the observed upscattering and why this upscattering becomes "frozen" only well below 77K were addressed. For this reason the chemical content and the profile of the surfaces of the Copper samples were studied using elastic recoil detection analysis at the Ion Beam Laboratory [4] of the Hahn-Meitner-Institute, Berlin, after the UCN measurements done at the ILL. It turned out that the Hydrogen content in the bulk of Copper (deeper than 2 µm from surface) was 0.1% compared to 8% in

Peter Geltenbort and Thomas Brenner on PF2.

the surface layer (7.2 10^{17} at/cm^2, 100Å) ; the rest was Cu (55%), C(10%), and O(25%). For such a quantity of Hydrogen two different models of the Hydrogen distribution in the surface layer can be considered. One is a homogeneous dilute solution, while the second is a hydrogenated film or clusters. In both cases the shape of the temperature dependence arises from the temperature behaviour of the inelastic upscattering cross section, while the actual loss rate depends also on the ratio between the Fermi potential of the layer, V_f and the neutron energy, E_{UCN}. For the homogeneous dilute solution $V_f > E_{UCN}$ holds. The neutrons

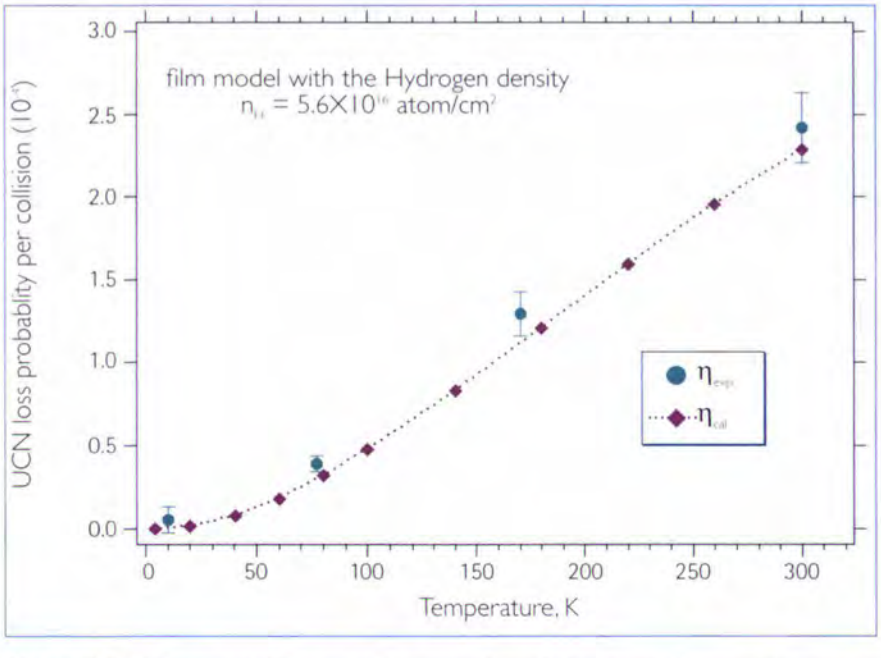

Figure 1: UCN loss probability per collision: purple - calculated with the upscattering cross section of ice; green - derived from experiment using the film model.

are then totally reflected and their losses are due to the quantum effect of subbarrier (neutron energy is below the potential barrier produced by the bulk material) penetration. For the hydrogenated film or clusters one has $V_f < E_{UCN}$, because of the negative neutron scattering length of Hydrogen atoms which are more localised in this model. The losses can then be calculated using the upscattering cross section which follows the 1/v law. For the same Hydrogen concentration the two models differ significantly in the predicted loss rate and its dependence on the neutron energy. These calculations are in good agreement with prompt (n,γ) studies of UCN [2]. This experiment yielded an estimate for the inelastic upscattering cross section at room temperature of $\sigma_s(300K) \approx 5b$ (for 25 meV neutrons).

The information about the atomic surface density allowed to rule out reliably the model of subbarrier interaction where the loss rate is negligible. In turn, the analysis of the low temperature shape of the temperature dependence of the loss rate and its comparison with (n,γ) data at 300 K have led to the conclusion that the UCN are not being scattered by a H-Cu compound. The only way to explain the experimental data is to assume that Hydrogen is bound to a light mass in a molecule with a strong low energy vibration peak with $E \leq 8$ meV. Oscillation frequencies below 10 meV are rather unusual for metal hydrides but typical for intermolecular vibrations of molecules weakly bound to a crystal. A literature search of phonon spectra for different Hydrogen compounds revealed that ordinary ice has a remarkably strong translational branch with a low energy peak at 7 meV. Such a molecule is light, has a negative Fermi potential, is commonly present on surfaces and tends to adsorb preferably in the form of clusters. Calculations of the UCN upscattering cross section using the phonon spectrum of ordinary ice and the loss probability in the film model, are in very good agreement with the experimental data as shown in figure 1 [1].

Thus, the presence of ice clusters embedded into the surface oxide layer could explain reasonably well both the shape of the temperature dependence and the absolute value of the loss rate. A similar behaviour was observed for UCN absorption in stainless steel samples where about 1% of Titanium gave rise to the same loss rate as 50% of Iron due to the presence of Ti-C clusters on the surface with $V_f < E_{UCN}$ [2]. At present, the subbarrier model of UCN upscattering is only consistent with the experimentally determined loss rate for vapour deposited heavy water ice [3]. For metals, however, the film or cluster model describes much better the experimental results. Finally, at low temperatures the loss rate is also extremely sensitive to the lowest frequencies of Hydrogen oscillations, which are common, for instance, in ice and glassy states of amorphous materials. Therefore, the upscattering of neutrons will dominate the losses even below liquid nitrogen temperatures (77K). While being so troublesome for UCN storage for so many years, these losses open a challenging opportunity to use UCN to study ultra-low energy excitations in surface nanolayers.

References:
[1] E. Korobkina, R. Golub, J. Butterworth, P. Geltenbort and S. Arzumanov, Phys. Rev. B 70 (2004) 035409
[2] S. Arzumanov, L. Bondarenko, P. Geltenbort, E. Korobkina, V. Morozov, Yu. Panin, A. Fomin and S. Chernjavsky, NIM A 440 (2000) 690
[3] S. Arzumanov, L.N. Bondarenko, V.I. Morozov, Yu. Panin, P. Geltenbort, Phys. of Atomic Nuclei 66 (2003) 1820
[4] W. Bohne, J. Röhrich, G. Röschert, The Berlin time-of-flight ERDA set-up, NIM B 136-138 (1998) 633-637; http://www.de/isl/ana/ana-1.html

Simulating is stimulating

Eva Scholtzova, Slovak Academy of Science, Bratislava.

Anders Mellergard, Studsvik, Sweden.

Chuhong Zhang and Jeerachada Tanchawanich, Heriot-Watt University, Edinburgh.

Doug Tobias, University of California, Irvine, and Mark Johnson.

Lina Henao, Cermav, UJF Grenoble.

modelling & theory

Mark Johnson, Leader of Computing for Science — http:/www.ill.fr/computing/club.html
Efim Kats, Head of Theory Group — http:/www.ill.fr/Colleges/C2/TheoryCollegeHome.html

In parallel with instrument developments at the ILL, modelling and theory continue to progress, helping to analyse and understand in more detail the ever more precise data obtained on our instruments. The scope of modelling activities depends significantly on the performance of computational codes and the hardware on which they run. ILL currently has two 16-processor clusters and with the many Linux machines on instruments and elsewhere in the Institut, considerable computational power is available to our scientists and visitors. On the theory side, significant advances based, for example, on advances in statistical mechanics, are leading to more reliable models.

Modelling and theory continue to progress, helping to analyse and understand in more detail the ever more precise data obtained on our instruments

The three papers in this section illustrate the progress being made in modelling and theory and also the benefit of combining these research methods with experiment. In particular, the articles of Poehlmann and Bichara describe work based on ab initio molecular dynamics simulations on model amorphous and liquid systems of hundreds of atoms running up to nearly 50 ps. In this work, neutron diffraction measurements of the static structure factor serve to validate the simulations which are then investigated in atomistic detail in order to extract structural details. The scale of such ab initio calculations is increasing to the point that the investigation of base-pair opening in DNA, treated theoretically here, will soon be tackled by these computational methods, constituting a topical example of a combined approach to research by experiment, modelling and theory.

The work presented by M.Poehlmann et al., concerns the role of water in silicates. Such is the ubiquitous nature of silicates that the states of dissolved water revealed by simulations and experiment are relevant to fields as diverse as semiconductors and volcanism. The presence of water gives rise to electronic states in the band gap, enhancing electronic conductivity, and possible mechanisms for proton conduction, which will be the subject of future experiments when appropriate conditions of high temperature and pressure can be achieved on our instruments. A similar computational approach is employed by Bichara and Johnson to study liquid germanium telluride over the temperature range in which volume contraction on heating gives rise to a maximum density. Technological applications of these materials, for example in phase change recording devices, require the interplay between electronic and atomic structure and the resulting density anomalies to be understood.

The three papers in this section illustrate the progress being made in modelling and theory and also the benefit of combining these research methods with experiment

Bicout and Kats from the ILL theory group have looked at the dynamics of base pair opening in double stranded DNA. The fundamental biological processes, such as replication and transcription, require that the highly stable double helical structure of DNA must locally open to expose the bases. Recent experimental studies conducted by the group of A. Libchaber have attempted to interrogate the significance and properties of such bubble states with a special fluorescence correlation spectroscopy technique. The authors propose and investigate a model which characterises some physical features of base pair opening. When properly interpreted and treated the model yields quite reasonable values for a variety of measured quantities such as bubble survival probability, life time and characteristic size distribution.

modelling & theory

From explosive volcanism to semiconductors: structural and dynamical properties of hydrous silica(tes)

M. Pöhlmann *(ILL, TU Munich and University of Montpellier II)*
H. Schober, G. Cuello, T. Hansen and M. Johnson *(ILL)*
A. Meyer and A. Müller *(TU Munich)*
M. Benoit and W. Kob *(University of Montpellier II)*

The presence of water drastically alters the physical properties of silica and silicates. For example, the decrease in viscosity plays a decisive role in explosive volcanic eruptions [1]. Water is also used to passivate defects in SiO_2 in semiconductor devices [2]. In silicates, water can dissolve to form SiOH groups but molecular water may also be present. To date the water-induced microscopic mechanisms leading to the modification of the macroscopic properties of silicates, like viscosity and electric conductivity, are not well understood.
We have combined first-principles molecular dynamics computer simulations with neutron scattering techniques in order to understand the influence of water on mass transport in silica(tes) as well as their electronic properties.

It is well known that, due to the different scattering lengths of hydrogen and its isotope deuterium, neutron scattering is one of the most suitable experimental techniques for investigating water containing systems. Structural and dynamical properties like the static structure factor S(q) and the vibrational density of states are accessible with this experimental probe. On the other hand, exactly these quantities can be extracted from molecular dynamics computer simulations. Classical molecular dynamics are not able to give a realistic description of hydrous silicate systems since reliable potentials for water and the dissolution products OH^- and H_3O^+ do not exist. Therefore, a quantum-mechanical treatment of the electrons, as in the Car-Parrinello method, must be used. Since this type of *ab initio* calculation is computationally demanding (CPU time as well as memory), we have used parallel supercomputers extensively. Our calculations were performed using the "CPMD" code, developed by Prof. Parrinello's group [3].

Exploring mechanisms associated with explosive volcanism requires a clear understanding of the liquid state. Considerable progress was made recently for sodium silicate systems [4], also by combining molecular dynamics computer simulations and neutron scattering. Due to the chemical similarity of the systems $(1-x)SiO_2+xH_2O$ and $(1-x)SiO_2+xNa_2O$ $(0 \le x \le 1)$, it can be assumed that both systems have similar mechanisms for mass transport. However, hydrous silicates are much more challenging to investigate:

Experiments are currently limited to the glassy state. Pressures of several kbar and temperatures in excess of 1000 K are required to bring water-silicate mixtures into equilibrium. Since such pressure equipment is not currently available on neutron scattering instruments, experimental data can only be obtained below temperatures where water is released from the silicate.

Simulations are in principle limited to the liquid state. Today's computer power puts clear limits on the *ab initio* equilibration of viscous liquids. For a system size of about one hundred atoms, the time limit is some tens of pico-seconds (these are six orders of magnitude less than in the classical approach used for sodium silicates). The lowest temperature at which equilibration can be achieved is 3000 K. Information on the glass can only be obtained from samples based on ultra-rapid quenches.

The set-up and the main results of the CPMD simulation for the liquid state of a system with the composition $SiO_2+11.8mol\%H_2O$ were recently described in references [5,6]. Also structural information on quenched samples has been obtained from experiments [7]. Figure 1 shows a snapshot of the computer simulation of hydrous silica at a temperature of 3500 K.

Apparently all hydrogen atoms are attached to the silica matrix in the form of SiOH groups. It can be seen that the structure of the hydrous liquid exhibits other states whose appearance is not *a priori* evident. In particular SiO dangling bonds highlighted in yellow and oxygen tri-clusters (highlighted in blue) are present. The contribution of these defects to the diffusion process of hydrogen was also revealed in reference [6].

It is remarkable that even at temperatures of 3500 K and 3000 K the silica tetrahedral

network is preserved. Also during an ultrafast quench, with a quench rate of the order of 10^{14} K/s, the tetrahedral network is not destroyed (in agreement with other studies [8]) and hence the structure at ambient temperature obtained from the computer simulation should be realistic. Indeed this can be demonstrated for the neutron scattering structure factor. Figure 2 shows the simulated neutron scattering structure factor for dry and hydrous silica at ambient temperature, compared with the same quantity recorded on D20.
Generally the experimental and simulated curves are in rather good agreement. Deviations occur only for very low q and between 9 $Å^{-1}$ and 12 $Å^{-1}$. At low q the deviations from the simulation to the experiment can be ascribed to the rapid cooling rate in the simulation. The deviations between 9 $Å^{-1}$ and 12 $Å^{-1}$ most probably arise from the corrections made to the experimental data. Experiment and simulation therefore clearly demonstrate that water does not significantly affect the silica tetrahedral network. Comparison with studies of sodium silicates, shows that the influence of sodium oxide on the structure of silica is much greater than the influence of water. This effect is predominantly related to the different sizes of the hydrogen and the sodium atom [6].

The neutron scattering structure factor S(q) is one of the few ways to calibrate simulation with experiments and thereafter microscopic information can be extracted with greater confidence from the simulation. Due to the *ab initio* character of the simulations, they are able to reveal electronic features of the system [9]. In particular our simulations were able to confirm predictions made many years ago on states in the electronic band gap that lead to electronic conductivity [10] and may be responsible for the breakdown of semiconductor devices. Proton conductivity, associated with the different states of hydrogen in the silicate network, remains to be investigated by quasi-elastic neutron scattering. Finally this work demonstrates that the combination of neutron scattering and *ab initio* molecular dynamics simulations allow problems to be investigated in detail, which are relevant to the semiconductor industry and other fields where silica and silicates are important.

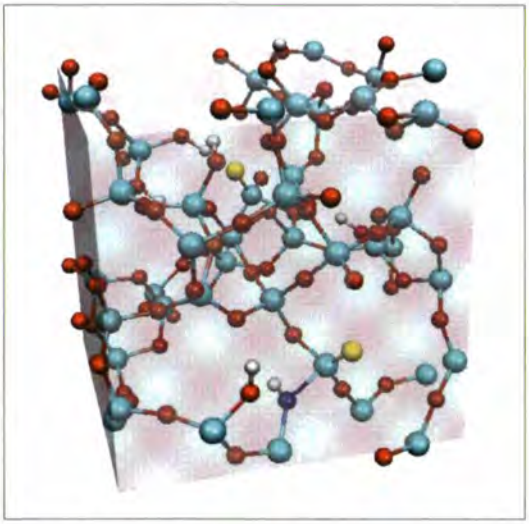

Figure 1: Snapshot of SiO_2 + 11.8mol%H_2O at 3500 K. Silicon (green spheres), oxygen (red spheres), and hydrogen (white spheres) and the defect states, SiO dangling bonds (yellow spheres) and O bridging hydroxyl groups (blue spheres).

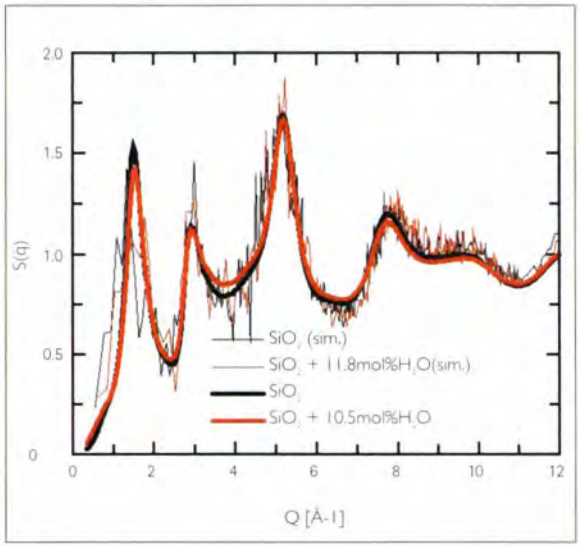

Figure 2: Neutron scattering structure factor of pure and hydrous silica at 300 K as obtained from the experiment (bold lines) and the simulation (thin lines).

References:
[1] D. B. Dingwell. Science, 1054 (1996) 273
[2] C. R. Helms and E. H. Poindexter. Rep. Prog. Phys., 791 (1994) 57
[3] CPMD Version 3.3. J. Hutter, A. Alavi, T. Deutsch, M. Bernasconi, S. Goedecker, D. Marx, M. Tuckerman and M. Parrinello, MPI für Festkörperforschung and IBM Zurich Research Laboratory (1995-99)
[4] A. Meyer, J. Horbach, W. Kob, F. Kargl, and H. Schober. Phys. Rev. Lett., 027801 (2004) 93
[5] M. Pöhlmann, A. Meyer, M. Benoit and W. Kob in High Performance Computing in Science and Engineering, Munich 2004. Transactions of the Second Joint HLRB and KONWIHR Result and Reviewing Workshop, 2-3 March 2004, Technical University of Munich. Springer-Verlag, Berlin, Heidelberg, New York (2004) 199
[6] M. Pöhlmann, M. Benoit and W. Kob. Phys. Rev. B, 184209 (2004) 70
[7] M. Pöhlmann, A. Meyer, A. Müller, H. Schober, T. Hansen, and G. Cuello. Submitted to Phys. Rev. B
[8] K. Vollmayr, W. Kob and K. Binder. Phys. Rev. B, 15808 (1996) 54
[9] M. Pöhlmann, H. Schober, M. Benoit and W. Kob in Proceedings of the 2004 Nanotechnology Conference and Trade Show, Boston (Ma), USA, Vol. III, p. 73. The Nano Science and Technology Institute, Cambridge 73 (2004)
[10] J. Robertson in The physics and technology of amorphous SiO_2. R. Devine (Ed.). Plenum Press, New York, 1988

modelling & theory

Why some liquids contract on heating – an *ab initio* molecular dynamics study of Germanium Tellurides

C. Bichara *(CNRS, Marseille)*
M. Johnson *(ILL)*

Between 600 and 750 K and in a 20% composition range ($0.0<x<0.20$) $Ge_xTe_{(1-x)}$ alloys undergo a strong but continuous and reversible structural change. As in the case of water, the liquid contracts upon heating. This volume contraction is maximal (about 8%) at the eutectic ($x = 0.15$) composition, the maximum density reaching 0.0289 atoms/Å^3. Other thermodynamic properties such as the specific heat and the compressibility display sharp but finite maxima [1] and the electrical conductivity of the liquid gains one order of magnitude in less than 100K [2]. Structural changes were probed in X-Ray and neutron scattering measurements [3,4], showing a decrease of the second peak of the measured total structure factor upon heating. The real space analysis shows a gradual increase of the number of first neighbours, but, since partial structure factors were not measured, an atomistic picture of the structural changes was not obtained. In this context, *ab initio* molecular dynamics simulations have been performed.

Concerning the structural changes in $Ge_xTe_{(1-x)}$ alloys, a number of issues are still unresolved. The contributions of Ge and Te atoms to the structural change have to be separated and the nature and driving force for the structural change have to be elucidated. At least two mechanisms should be considered. Although no sp^3-bonded stable $GeTe_2$ compound exists in the phase diagram, a metastable state could exist, analogous to the $GeSe_2$ compound in the parent GeSe system. In the low temperature liquid, Ge would be sp^3 bonded and the observed structural change would then correspond to a change of the coordination state of Ge from sp^3 to p, with an increase of its coordination number from 4 to 6. Such a mechanism has recently been suggested to explain the structural differences between amorphous and crystalline $Ge_2Sb_2Te_5$ films that are used for optical reversible data storage [5]. Another possibility would be to relate the structural change to the $\alpha \Leftrightarrow \beta$ second order transition that takes place in the solid compound at about 700 K. A similar behaviour is observed in pure undercooled liquid Tellurium. Both have been interpreted in terms of a Peierls distortion mechanism that stabilises a distorted phase of alternating short and long bonds at low temperature. In this second case, the role of Ge atoms, that seem to maximise the effect at the eutectic composition, must be understood.

In order to shed light on these issues we have performed first principles Molecular Dynamics simulations of the time evolution of a small model system with a minimal number of assumptions. The temperature and density of the system of 56 or 112 atoms with a atomic composition corresponding to $GeTe_6$ are fixed following the experimental values (633 K – 0.0277 Å^{-3}; 673 K – 0.0282 Å^{-3}; 733 K – 0.0288 Å^{-3}; 943 K – 0.0285 Å^{-3}). Earlier simulations [6] were not conclusive because poor statistics did not allow a clear cut distinction to be made between sp3 or p bonding for Ge. Using the VASP code [7] we were able to improve the quality of the results by performing longer runs (up to 36 picoseconds) and using a more accurate description of the electronic structure.

Comparing the calculated total structure factors with the experimental ones given in [4] shows that the general trends are correct (figure 2). In particular the intensity of the second peak decreases when the temperature is raised. The analysis of the partial contributions reveals that this change is essentially due to the GeTe partial structure factor. Because of the low Ge content the GeGe contribution to the total structure factor is less than 4% and can be neglected. The question is therefore to understand in which way the local environment of Ge is modified. The bond angle distribution of the six first neighbours of

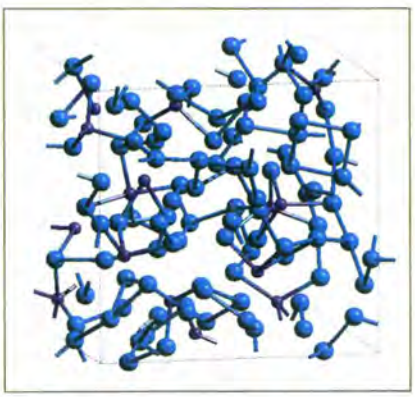

Figure 1: An instantaneous configuration of 112 atoms at 633 K and a density of 0.0277 atoms/Å^{-3} (Ge = dark blue, Te = turquoise).

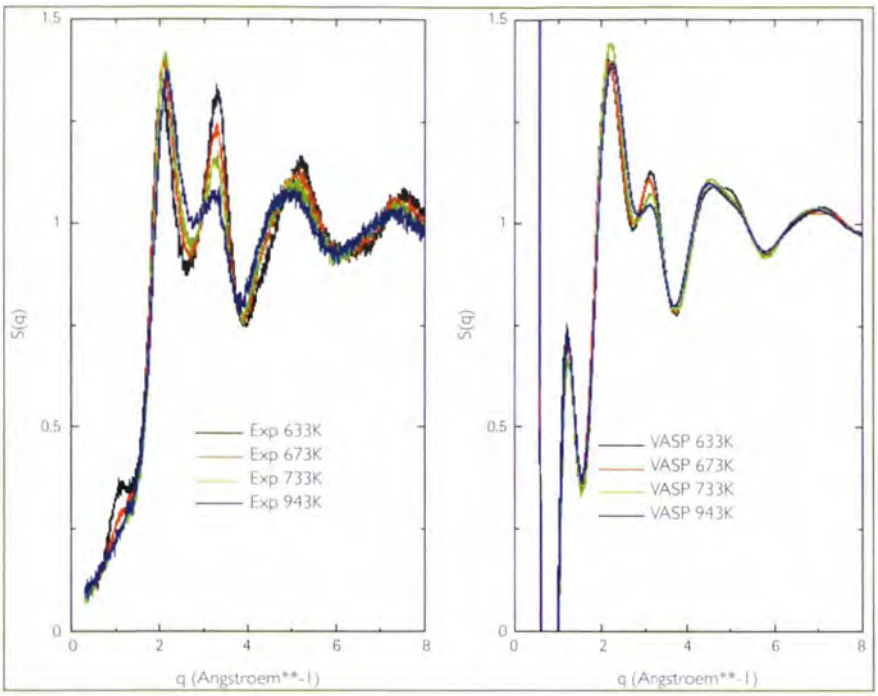

Figure 2: Experimental (left panel) and calculated (right) total structure factors.

each atom are well defined and peaked below 100 degrees and, more importantly, there is no change with temperature, apart from the usual thermal damping (see figure 3, left). Ge and Te clearly remain p-bonded so the first mechanism, involving a sp^3-bonded, metastable state, can be ruled out.

Further information is obtained from the temperature dependence of the characteristic distances of atomic shells. Histograms of first, second etc. neighbour distances are calculated and the average (first moments) of these histograms are plotted as a function of the temperature. Figure 3 (right) shows that between 633 K and 733 K, in the temperature range in which the average atomic volume contracts, the 3 (or 4) shorter bonds around Ge slightly increase or remain constant. The volume contraction affects mainly the longer distances. Such a behaviour is commonly observed in the high pressure phases of crystalline p-bonded materials such as pure Se and Te, the structure of which results from a Peierls distortion of a simple cubic structure [8]. At low temperature, because of the symmetry breaking mechanism analogous to the Peierls distortion in a solid that stabilises the energy, Ge atoms occupy an off-centre position inside the octahedral cage formed by its six Te neighbours (no short GeGe bonds were observed). At higher temperature, entropy favors a centred, average position for Ge atoms and this more symmetric situation leads to an overall reduction of the atomic volume, before thermal expansion and chemical disordering wash out these correlations at even higher temperatures.

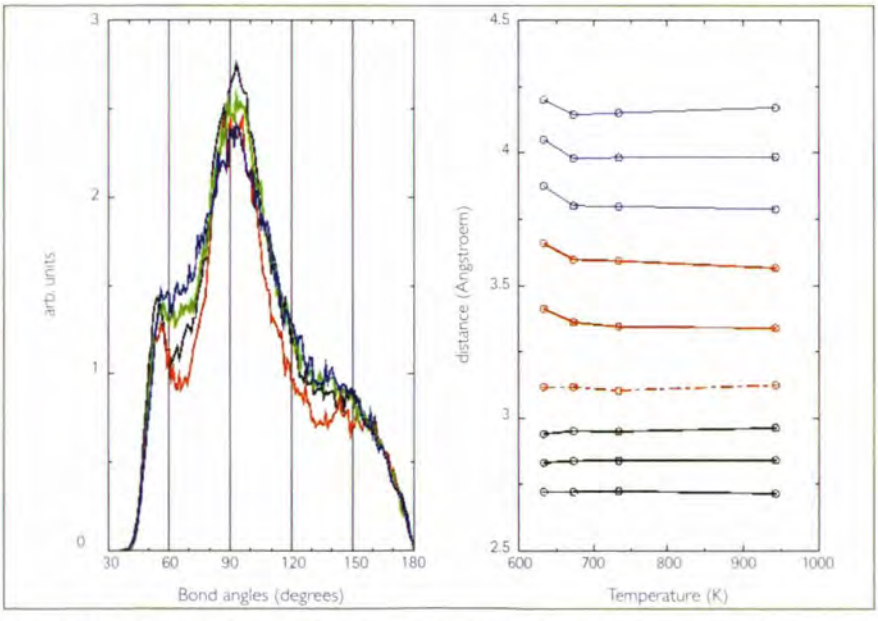

Figure 3: Left panel : Bond angle distribution around Ge atoms. Right panel : Black curves show the nearest neighbour distances around Ge atoms which increase or remain constant with increasing temperature. At bigger inter-atomic separation, these distances decrease (red curves). The blue curves show distances to atoms beyond the first neighbour shell.

At the present stage of our investigations we can conclude that the driving force for the structural changes in $GeTe_6$ lies in this Peierls-like mechanism acting in the low temperature liquid but not at higher temperature due to the entropy gain in a more symmetric local environment. Further work will be devoted to the analysis of the electronic structure and to try and understand why the structural change is most pronounced at the eutectic composition.

eferences: [1] Y. Tsuchiya, J. Phys. Soc. Jap., 60, (1), 227-34, 1991; Y. Tsuchiya, J. Non-Cryst. Solids 156-158 (1993) 704-707
[2] Y. Tsuchiya and H. Saitoh, J. Phys. Soc. Jap., 62, -4- (1993) 1272-8
[3] H. Neumann, W. Hoyer, W. Matz and M. Wobst, J. Non-Cryst. Solids, 97-98 (1987) 1251
[4] C. Bergman, C. Bichara, J.-P. Gaspard and Y. Tsuchiya, Phys. Rev. B67 (2003) 104202
[5] A.V. Kolobov, P. Fons, A. I. Frenkel, A. I. Ankudinov, J. Tominaga and T. Uruga, Nature Materials, 3, -10- (2004) 703-8
[6] J.-Y. Raty, J.-P. Gaspard and C. Bichara, J. Phys. : Condens. Matter, 15 (2003) S167-73
[7] see http://cms.mpi.univie.ac.at/vasp/
[8] J.-P. Gaspard, A. Pellegatti, F. Marinelli and C. Bichara, Philos. Mag. B., 77, 3 (1998) 727-44

D. J. Bicout and E. Kats (ILL)

modelling & theory

Bubble relaxation dynamics in double-stranded DNA

The paper deals with the two-state (opening-closing of base pairs) model used to describe the fluctuation dynamics of a single bubble formation. We present an exact solution for the discrete and finite size version of the model that includes end effects and derive analytic expressions of the correlation function, survival probability and lifetimes for the bubble relaxation dynamics.

Upon heating, a double stranded DNA (ds DNA) undergoes a denaturation process with the formation of bubbles of increasing size and number and, eventually, leading to the separation of the two strands [1]. On the other hand, many of DNA biological activities require the unzipping of the two strands by breaking hydrogen bonds between base pairs. Such open regions of complex DNA, enclosing up to 10-30 broken base pairs, represent a first step of the transcription processes and are called the transcription bubbles. Several theoretical models have been proposed to describe the phenomenon of bubble formation (for a review see e.g., [2]). However, the issue remains unsettled with various, and even contradictory, results reported in the literature. This is indicative of the complexity of the problem which involves number of factors (e.g., base pair sequences, molecular environment, counterions, and so on) that can influence the denaturation process in various ways (see e.g., [3-5]). In addition, as an one or quasi-one dimensional system, the ds DNA is expected to be very sensitive to thermal fluctuations. Therefore, it seems appropriate in a first step to study the fluctuations of local breathing or unzipping of a ds DNA that opens up bubbles of a few tens of base pairs.

The characteristic dynamics of these local denaturation zones (bubbles) in the structure of a ds DNA have been recently probed through fluorescence correlation spectroscopy [6, 7]. This is an essential issue not only for physiological processes involving ds DNA but also for providing insights on the general nature of fluctuations in such systems. From a theoretical modelling perspective, however, we have just begun to understand these experimental results. We denote by $b_n(t)$ the probability density of bubbles of size n ($0 \le n \le N+1$) of open pairs at time t in the system. Assuming that all conformations of the ds DNA can be described as two states (closed or open), the fluctuations dynamics in the number n of open base-pairs in the bubble is described by the master equation,

$$\begin{cases} \frac{db_0}{dt} = k_- b_1 - k_1 b_0 \\ \frac{db_1}{dt} = k_1 b_0 + k_- b_2 - (k_+ + k_-) b_1 \\ \cdots \quad \cdots \\ \frac{db_n}{dt} = k_+ b_{n-1} + k_- b_{n+1} - (k_+ + k_-) b_n \\ \cdots \quad \cdots \\ \frac{db_N}{dt} = k_+ b_{N-1} + k_2 b_{N+1} - (k_+ + k_-) b_N \\ \frac{db_{N+1}}{dt} = k_+ b_N - k_2 b_{N+1} \end{cases}$$

where, in addition to the rates $k_\pm$ in [7], we have explicitly introduced the opening and the closing rates k_1 and k_2, respectively, for opening the first (n=0) and closing the last ($n=N+1$) pairs since two ends of the DNA helix are sealed (see figure 1).

The quantity of interest is the correlation function $C_N(t)$ which describes fluctuations in the bubble population at equilibrium. $C_N(t)$ is measured by fluorescence correlation spectroscopy method [7] and can be related easily to the bubble survival probability $B_N(t)$. Depending on the bubble size N and the parameter $\sigma \equiv (k_+/k_-) = \exp(-\epsilon/k_BT)$, ($\epsilon$ is the bubble extension energy, and k_BT is the thermal energy) the discreteness of the system is an ingredient which might be taken into account to

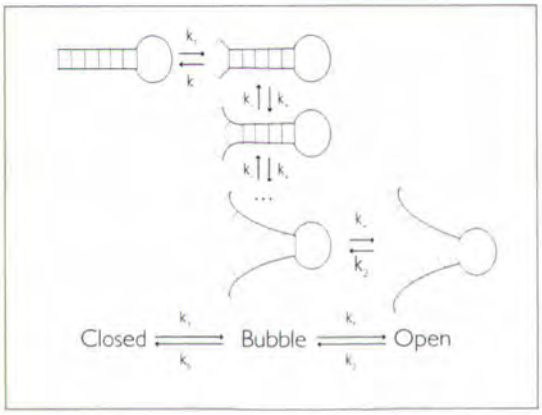

Figure 1: Sketch illustrating the opening-closing bubble reaction kinetics.

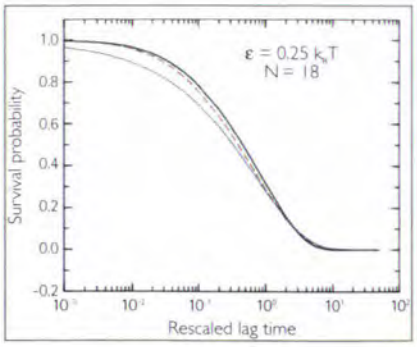

Figure 2: Bubble survival probabilities, from top to bottom, $B_N(t)$ (solid line), $B_\infty(t)$ (long-dashed line) and $B_{\infty,c}(t)$, i.e. continuous limit (dotted line) versus the rescaled lag times t/τ_N, t/τ_∞ and $t/\tau_{\infty,c}$, respectively.

capture the correct bubble dynamics. This is illustrated in figure 2 where exact survival probability is compared with its $N \to \infty$ limit and the continuous model. Figure 3 shows the departure in the bubble lifetime to the continuous limit as a function of bubble size. It clearly appears from figures 2 and 3 that the continuous limit [7] becomes a fairly good approximation to exact result for $\sigma^N << 1$ (where $\sigma \leq 1$ is the control parameter for the ds DNA melting). As $\sigma \leq 1$ according to the experimental situation in [7], the closing of bubbles is the fastest process in the bubbles kinetics.

The parameter σ also controls the denaturation transition. As $\sigma \to 1$, there is a kind of "critical slowing down" where the fluctuations of bubbles are described by an unbiased diffusion process. For instance, the bubble lifetime reduces to

$$\tau_N = \frac{(N+1)(N+2)}{12k_-}$$

in the $\sigma \to 1$ limit, and τ_N diverges with the bubble size.

It may be useful for practical purposes to have an idea of numerical values of physical parameters entering in the problem. In the absence of direct measurement of k_-, for instance, one can use the experimental data in [7] in conjunction with theoretical results to estimate the closing rate k_-. The results of such an estimation are presented in table I.

ϵ/k_BT		0.1	0.5	1
Lifetime (μs)		k_- ($\times 10^6$ s^{-1})		
τ_N	95	0.300	0.0675	0.0263
τ_∞	95	1.162	0.0680	0.0263
$\tau_{\infty,c}$	95	1.110	0.0550	0.0180

Table I: Estimate of k_- using the expressions of the bubble lifetime in the case of $k_+ = k_2 = 0$. In ref. [7] the experimental bubble lifetime is equal to 95 μs at T = 303K for N = 18.

All our results are consistent with available data and amenable for further experimental tests.

Given the closing and opening rates of base pair, the model presented above allows to study a number of phenomena related to the denaturation mechanisms of DNA such as heating, changing buffer surrounding, or applying external torques of forces.

Likewise, the model can easily be modified to include the intermediate states between bond and broken states (see details in our paper [8]).

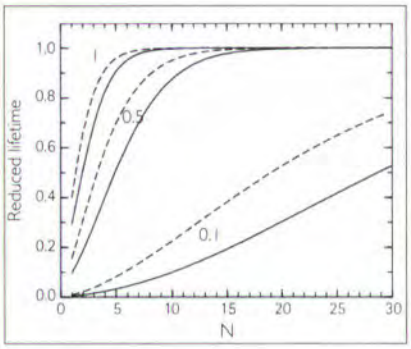

Figure 3: Reduced lifetime, as a function of bubble size, N (i.e., the number of open pairs). Quoted numbers represent the bubble extension energy ϵ/k_BT.

References: [1] D. Poland and H.A. Sheraga, theory of Helix - Coil Transitions in Biopolymers, Academic Press, New York (1970)
[2] R.M. Wartell and A.S. Benight, Phys. Rep., 126 (1985) 67
[3] M. Peyrard and A.R. Bishop, Phys. Rev. Lett., 62 (1989) 2755
[4] Y. Kafri, D. Mukamel and L. Peliti, Phys. Rev. Lett., 85 (2000) 4988
[5] N. Singh and Y. Singh, Phys. Rev. E, 64 (2001) 042901
[6] G. Bonnet, O. Krichevskii and A. Libchaber, proc. Natl. Acad. Sci. USA, 95 (1998) 8602
[7] G. Altan-Bonnet, A. Libchaber and O. Krichevskii, Phys. Rev. Lett., 90 (2003) 138101-1
[8] Phys. Rev. E 70 (2004) 010902 (R)

Leading techniques

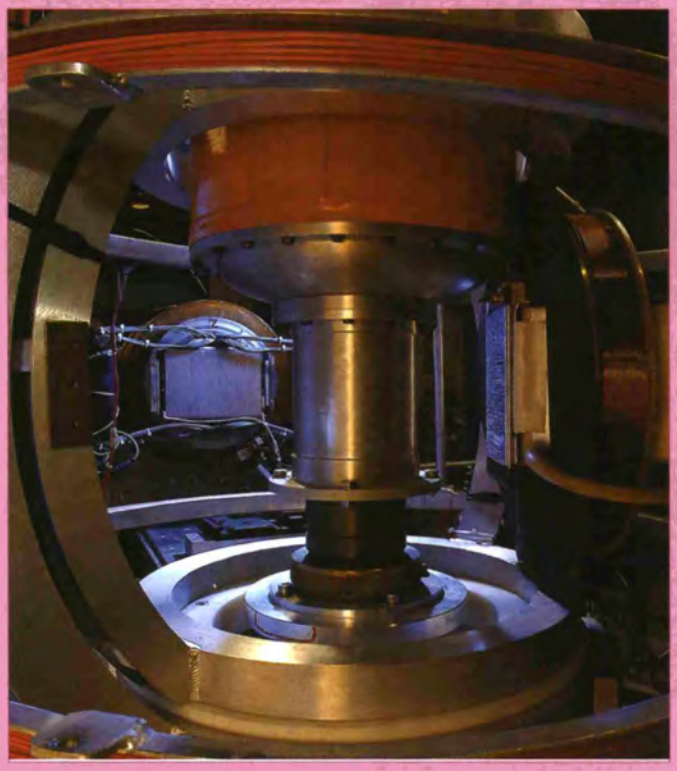

The IN11 sample area, with the cryostat, the sample field coils and the π- flipper.

Michael Koza, checking the IN6 detector bank.

The D11 team (from the left: Ralf Schweins, Peter Lindner and David Bowyer) testing the new prototype sample changer.

millennium programme & technical developments

2004 was quite a special year for the Millennium Programme with three very compact reactor cycles, a 5th anniversary at the end of the year, the start of new projects and changes in project management methods.

In this 5th year of the Millennium Programme another sizable part of the original set of projects was completed. Particularly important for the users was the completion of the new fast small-angle detector for D22 and the first bank of polarising analysers for the diffuse scattering instrument D7. In addition, however, the world of exotic neutron-rich nuclei can now be explored much better thanks to the new detectors purchased in the framework of the microball project.

There was also major progress in the area of neutron delivery: two zircaloy beam tubes were manufactured, one of which has already been installed at H9. And there was much activity around the neutron guides, particularly H1/H2, with a steadily growing team involved in the work.

In this 5th year of the Millennium Programme another sizable part of the original set of projects was completed

With the first series of projects completed or close to completion, it was very important that we were able to start 2 of the 8 new instrument projects decided by our committees in autumn 2003: the rebuild of (1) the secondary spectrometer of the time-of-flight instrument IN5, which will have a vacuum flight chamber and a much larger solid-angle detector bank, and (2) the backscattering instrument IN16B, which is set to incorporate many technologically challenging solutions.

We were also delighted to learn towards the end of the year that we have been given the go-ahead to pursue the Millennium Programme even more intensely in 2005 and beyond. This will include the reinforcement of staff working on Millennium projects.

Werner Press

W. Press *(ILL)*

millennium programme

The 5th anniversary of the ILL Millennium Programme

You only need to look around the DPT design office to realise just how many draftsmen are working on all kinds of projects. Despite a slight increase in staff numbers, there were a number of bottlenecks in 2004 and the three very compact and demanding reactor cycles did not help the situation. Once again, in 2004 we can report on both the completion of some projects and the start of other new projects. There was greater involvement than in the past from the Instrument Subcommittee (with Dieter Richter as new chairman) in the preparation of new projects. And as usual there were intensive discussions within the Scientific Council. ILL-specific management training was also initiated, with risk analysis playing a more important role in the new project plans. The users from the diffraction community continued to benefit considerably from the Millennium Programme. Following **VIVALDI** and the complete renewal of the **secondary diffractometer of D2B**, further options are now or will very soon be available: **D19** was equipped with three new 'bidim26' two-dimensional detectors and the strain imager **SALSA** had its very first test with neutrons. Intense work continued on the big **banana detector for D19** (with the Univ. of Durham) and considerable efforts were made to complete the basic version of SALSA (with the Univ. of Manchester), the aim being to start commissioning SALSA at the restart of the reactor, followed shortly after by the D19 banana detector. Discussions and planning of a next-generation powder diffractometer were also started and **DRACULA**, as its name suggests, should prove to be a very ambitious project.

The D19 banana detector.

A Fan-blade of an aero-engine (about 1m high) mounted on the hexapod sample stage of SALSA. On the left: the automated variable slit system for beam definition.

Major progress was also made in small-angle scattering. The **fast small-angle detector** was installed on **D22** and now performs to our full satisfaction. Some additional tuning in the 1st cycle of 2005 should secure operation at a data rate of up to 2 MHz, with plans for a further increase to 10 MHz. We were less successful with the **D11 collimation**, where the new guides were delivered but proved to be unsatisfactory. This causes considerable delays! On the other hand, the idea of allowing D11 to benefit from the fast D22 detector led to a positive decision. Intense discussions are also under way about a 3rd small-angle scattering instrument. ILL obviously wishes to enhance its performance in fields where it already excels. Here we must mention the remarkable progress and results produced by the **tomography station**, whether in the area of kinetic processes, Antarctic fossil rock or material for the aircraft industry.

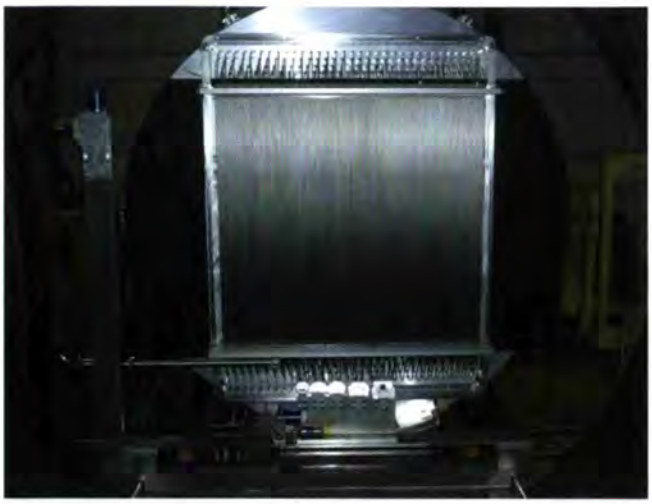

The fast small-angle detector on D22.

Some new instrumentation was also delivered in the field of three-axis spectroscopy: **IN20**, one of the instruments where polarised neutrons have their home, was completed in early 2004 and the **flat-cone (multi-analyser)** option for three-axis instruments is progressing in leaps and bounds. Surely, the upgrade of the cold neutron instrument IN14 will soon be on the agenda as well.

The **diffuse scattering instrument D7** is now equipped with the first complete bank of polarising analysers. There has been a tremendous leap forward both in terms of intensity, with an increase of more than one order of magnitude, and understanding. The users are extremely pleased. When the second bank will be ready, the performance will again be doubled. In parallel, the **flight chamber of IN5** is being rebuilt and there will be a new detector bank covering a much larger solid angle. The **backscattering instrument IN16** is also being rebuilt. The latter project involves considerable technological challenges, e.g. the material stability of the rotating disk of the phase space transformer. On this behalf we are in constant dialogue with our colleagues at NIST and Jülich.

On the nuclear physics side, the **microball option of Lohengrin,** now equipped with 2 "Clover" detectors, is much more sensitive when listening to γ-transitions of exotic neutron-rich nuclei. The Ultra-cold neutron (UCN) delivery seems to be preparing the way for the next nuclear physics Millennium Project.

"More than simply neutrons" is the motto of both the **deuteration facility**, which is working very well, and the facility for mechanical engineering. The initial investment in **FaME38**, which is an interface between engineers and scattering techniques, on site as a joint ESRF/ILL initiative, is more or less completed. A new application to EPSRC was submitted in 2004 and we sincerely hope that it will lead to further support for the facility (the partnership would then be transferred from the Univ. of Salford to the Univ. of Bristol).

The **modernisation of our infrastructure** covers a vast area, ranging from sample environment, where efforts in 2004 concentrated on the work on a Paris-Edinburgh pressure cell which can be operated at low temperatures, to instrument control software (CASE). This latter topic, on which a great deal of work has been carried out over the last two years, has now acquired the status of a Millennium project, thus securing its financial basis and further development. Its aim is to move from MAD to more modular, object-oriented control within the next 2-3 years.

Much is to be gained from improving our neutron guides, which represent the most important projects in infrastructure. Here a vast programme centred around the neutron delivery system for the guide hall ILL7 is ongoing and has a particularly high priority. All the guides close to the reactor will be renewed, including their mechanics. A major step is a transition from Ni to multilayer coatings (m=2) as well as an optimisation of cross sections. The **H1/H2 guide renewal**, including safety aspects and additional shielding, is expected to cost around 2.5 M€ and will require considerable manpower and effort. Its installation must be correlated with the replacement of the H1/H2 beam tubes during the long shutdown in 2005/06. Furthermore, we are continuing to plan, build and install new guides, optimised for the needs of new instruments, such as the quasi-Laue instrument LADI-3 for biology and the horizontal reflectometer. Once the replacement of H1/H2 has been completed, we aim to speed up this renewal process. Much thought is necessary to minimize the "down-times" needed for the installation of such new guides (and instruments) after the return to full reactor operation in the summer of 2006. Both zircaloy beam tubes have been delivered - H9 is installed and H11 will follow during the next long shutdown.

The Refit programme, reactor operation and modernisation are all carried out in parallel; this can also cause certain problems. Compact reactor cycles early in the year tie up a considerable amount of manpower, but are also the only time when tests with neutrons can be performed. While we are gradually getting more used to dealing with this, we were very pleased to learn of the Associates' decision to provide the Millennium Programme with a more dynamic budget starting in 2005. In the future this will allow us both to complete projects faster and start new projects at an increase rate.

millennium programme

First neutrons on SALSA

T. Pirling and S. Rowe *(ILL)*
G. Bruno *(University of Manchester)*

At the beginning of August 2004 SALSA, the Strain Analyser for Large and Small scale engineering Applications, saw its first neutrons. Although provisional, the configuration used allowed testing the instrument under real conditions.
This initial operation of the instrument was the result of more than three years of dedicated design, development, manufacture and assembly by many groups, both within and outside the ILL. The project is one of the first five of the ILL's Millennium Programme, which started in the year 2000 [1]. SALSA enjoyed the joint financial and manpower contribution from both, the Manchester Materials Science Centre (Prof. P.J. Withers), funded by the EPSRC, and the ILL.

The idea of the instrument was introduced in 2000, and optimisation studies were performed in collaboration with Jan Šaroun from the Nuclear Physics Institute, Řež near Prague [2,3] for the neutron guide and the monochromator, and with J.P.Merlet, INRIA Sophia-Antipolis for the hexapod sample stage. The main output was i) a monochromator, using bent perfect crystals, in combination with a super mirror guide of m=2 would give optimum performance, ii) a parallel kinematic hydraulic robot would meet all the specifications for sample manipulation. The output excavation of the site started in 2001 and provided the necessary floor to beam axis distance to achieve the specified z-movement range. In 2002, the new 9 m long and 30 x 200 mm² section super mirror guide between D1A/D1B and SALSA was installed. During 2003, a newly conceived exit assembly was delivered and positioned. Finally, in 2004, the last instrument parts were delivered, tested and installed: they included the monochromator from Missouri University Research Reactor (USA), the hexapod sample stage from Ölhydraulik Elemente Hagenbuch, Ebikon, Switzerland, the motorised slit system from Swiss Neutronics and the base Δtable.

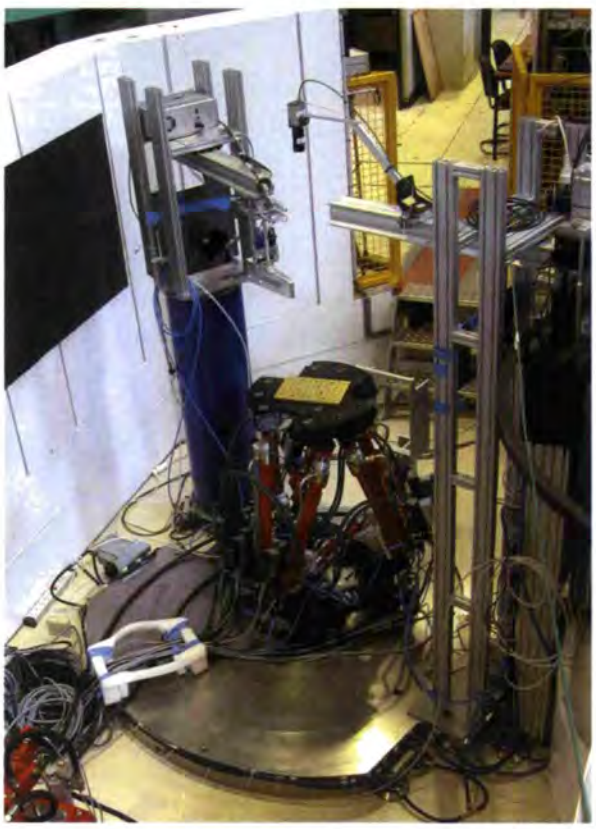

Figure 1: SALSA as set-up for the first tests. The optics, detector and hexapod are linked by the delta-table. An omega rotation and a translation of the hexapod increase the work space for large samples. The connections and the optics support are still provisional.

The list of specifications, assembled with international experts, included sample weights over 250 kg, sample dimensions up to more than 1 meter and positioning precision of 50 µm. A further demand was the ability to measure big samples of any shape, i.e. wing sections from airplanes, without the need of special sample preparation (in particular cutting), to pursue the use of a non-destructive technique. Variable wavelength was demanded to enable measurements in different materials, such as metals, alloys and composites. Finally, quick, reproducible and automated sample alignment and user-friendly operation as well as reliable data analysis completed the specifications.

A lot of effort was put into the development of the sample stage. This was important because a strain imager has to deal with a big variety of sample shapes and weights. At the same time the orientation of the sample in the beam is crucial. The scattering vector defines the direction in which the strain is being measured. Therefore tilt *and* position of the specimen have to be adjusted at the same time. A sample stage that allows such flexibility is a hexapod or Stewart-Platform (see figure 1). This is a robot with parallel kinematics and six degrees of freedom. The advantage of the hexapod conception for SALSA's sample stage is the flexibility of movements, the high precision and its high stiffness. The final design allows a tilt range of ± 30° and a translation range of ± 300 mm. The nominal payload is 500 kg and the upper limit lies at 1000 kg.
Translations, tilts or even oscillations of the specimen around the gauge volume are possible.

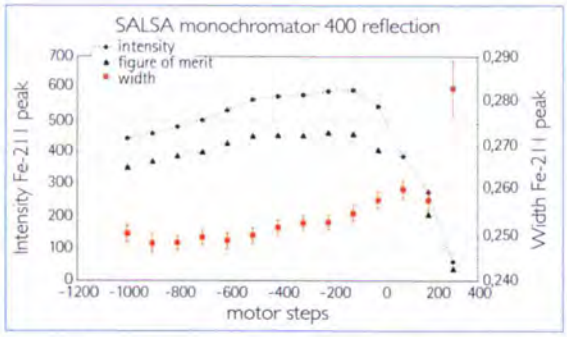

Figure 2: Optimisation of the curvature of the monochromator crystals. The radius of curvature is decreasing towards positive motor sreps (=more bending). The figure of merit shows a flat maximum between -500 and -100 motor steps. A curvature of 5.4 m is achieved at -350 motor turns. This is the optimum for $2\theta = 840$.

Preliminary tests allowed determining the repeatability of positioning to 3 µm with the smallest displacement width at 5 µm under the conditions of zero load as well as 940 kg. Further tests for the determination of the absolute positioning accuracy will follow. The mathematical model gives a maximum positioning error of 50 µm.

The hexapod is moving freely on a platform, the Δtable. This is a thick steel plate, which links the variable take-off, the hexapod and the detector. It is large enough to allow a full 360° rotation around the diffractometer omega axis and an additional translation of up to 700 mm. This option increases the workspace and allows measurements on the extremities, even of samples up to 1.4 m in length.

The rotation around the omega-axis of the diffractometer enables the typical 90° turns for the measurement of two perpendicular strain components with only one set-up.

Moreover, the Δtable provides the ability to vary the take-off angle between 55° and 125°. It also supports the beam optics. This is a key issue, because the same alignment is kept while changing the take-off angle and no re-calibration is needed. Figure 1 shows all these components in an instrument overview [4].

Similarly, the casemate exit assembly is a novel design. Control is greatly simplified and safety increased.

The double bent, variable horizontal focusing monochromator takes advantage of the divergence of the neutron beam providing high intensity, without loss in resolution. Unlike common flat perfect crystal or mosaic monochromators, it allows finding an optimum resolution at each 2θ angle.

The MURR monochromatorw - designed and built by Mihai Popovici - contains 36 stacks of 5 mm high slices of Silicon crystals, cut in the (400) plane and arranged to have a fixed vertical curvature. The horizontal curvature is variable in order to optimise intensity and resolution. Figure 2 shows the optimisation curve of the monochromator during the tests in August. The horizontal curvature of the crystals was changed while recording intensity and peak width of the Fe(211)-reflection from a powder. The wavelength was 0.16 nm and the scattering angle 84°. Figure 2 shows that the flatter the crystals, the higher the resolution, but the lower the intensity. With greater curvature the diffracted intensity I_d increases until it reaches a maximum. One way to find the optimum settings for an experiment is to use a figure of merit f, putting weight on resolution σ, defined as the peak width (Gaussian standard deviation): $f = \frac{I_d}{\sigma^2}$

In fact, figure 2 shows a flat maximum of the figure of merit between -500 and -100 motor steps.

A nose-shaped slit system allows automated selection of the horizontal and manual choice of the vertical size of the gauge volume. It also allows remote control of the sample-slit distance and the reproducible mount of oscillating collimators or even mixed collimator-slit configurations.

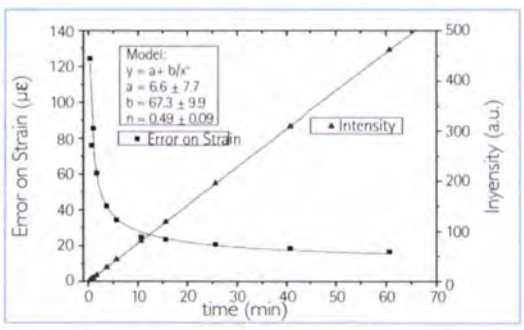

Figure 3: The time evolution of the error on the strain follows the inverse square root law foreseen by both Webster [5] and Withers [6]. The stabilisation occurs after 10-15 min counting time.

First test with neutrons

The same Fe powder peak was measured for different counting times. The results shown in figure 3 imply that: a) the error in strain is about 25 µε and b) the convergence of both the lattice parameter value and the measurement error occurs after 10-15 min.

The final assembly of the instrument was completed in 2004. Alignment, optimisation of hard- and software parameters, and testing of all components will take place during the first reactor cycle in 2005. The second cycle will be used for commissioning experiments, and for the third cycle SALSA will finally become a scheduled public ILL instrument.

The SALSA team is confident that the new instrument will go beyond the original specifications and become a world-class instrument.

eferences:
[1] T. Pirling and S. Rowe, A Strain-imager at the ILL, ILL Annual report 2000, 84-85
[2] J. Šaroun and T. Pirling, Optimisation of focusing monochromator for the neutron strain-scanner at a supermirror guide, internal report 2000
[3] J. Šaroun, T. Pirling and R.B. Rogge, Optimisation of a focusing monochromator for neutron strain-scanning diffractometer, Appl. Phys. A 74 [suppl] (2002) 1489-1491
[4] G. Bruno, T. Pirling, P. Withers, W. Hutt and S. Rowe, SALSA: Strain Analyser for large and Small Scale engineering Applications, J. Neutr. Res. 11 (2003) 235-239
[5] P.J. Webster and W. Kang, J. Neutr. Res. 10 (2002) 93-110
[6] P.J. Withers, M.R. Daymond and M.W. Johnson, J. Appl. Cryst. 34 (2001) 737-743

millennium programme

Small-angle spectroscopy at thermal energies: the BRISP project

D. Aisa, E. Babucci, F. Barocchi, A. Cunsolo, F. D'Anca, F. Formisano, E. Guarini, A. Laloni, A. Orecchini, C. Petrillo, F. Sacchetti and G. Venturi *(INFM, Italy)*

T. Gahl, S. Jahn, W.C. Pilgrim and J.-B. Suck *(TU Chemnitz and University of Marburg)*

H. Mutka *(ILL)*

Since the first agreement between Italian and German research teams in 2000, the development of BRISP, a time-of-flight spectrometer optimised for small-angle inelastic experiments with thermal neutrons, has overcome all the addressed technical challenges and is becoming a well-established part of CRG activities at the ILL. The spectrometer will soon become operational and is entering its final assembling/commissioning phase. During 2004 remarkable steps forward have been made, as important as the first extraction of the monochromatic beam and its first imaging on the detector.

The Time-of-Flight (ToF) Brillouin Spectrometer BRISP is designed for neutron inelastic scattering experiments where wide (thermal) energy ranges at small momentum transfer are desired. The original features of BRISP are the use of monochromators delivering thermal energy neutrons in combination with a thorough collimation in both the horizontal and vertical directions and with a very large (2 m^2) two-dimensional small-angle position-sensitive detector (PSD). Depending on the incident wavelength, at momentum transfers ranging from 0.5 to 0.05 $Å^{-1}$, exchanged energies up to 10-15 meV will become accessible with resolutions between 2.5 and 5% [1,2], and for the first time with the great advantage of the efficient ToF data acquisition. The new perspectives opened by this innovatory spectrometer span from the study of collective excitations with velocities up to 3500 m/s in liquids and glasses, to the investigation of spin dynamics in magnetic systems, and to biophysics or materials science applications.

So far, the construction of BRISP has offered major technical challenges, starting from the early stages of the project when the building of a 4 m-high seism-proof steel platform holding the heavy instrumental assembly was required. The design and development of the main shielding and the spectrometer components have also proved to be quite demanding technical tasks. During 2003 the shielding was refined, the choppers' rotation and control were duly tested, the long honeycomb collimators, specifically conceived for BRISP [3], were constructed (figure 1). The sample chamber with a sample environment equipment composed of a Maxi Orange cryostat and a furnace were acquired and tested, for experiments in the temperature range 1.5 to 2000 K. After the final approval of the shielding through radiological measurements in Spring 2004, the first graphite monochromator – selecting neutrons of 20 and 80 meV ([002] and [004] reflections) and fully developed and aligned by INFM – was installed inside the main shielding.

In July 2004 the first monochromatic

Figure 1: BRISP layout.

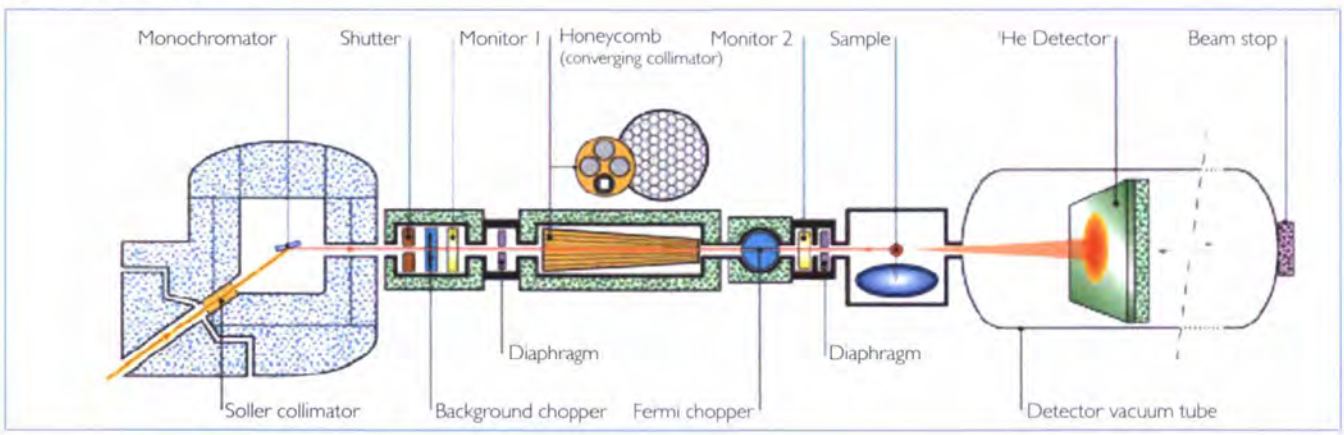

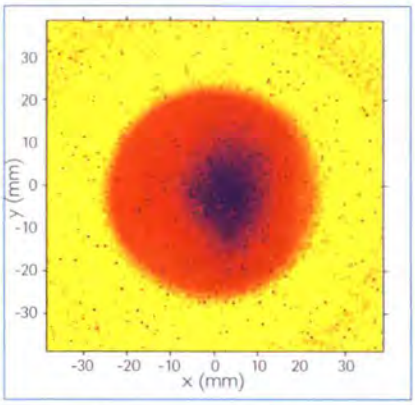

Figure 2: First extraction of the BRISP monochromatic beam. On 26 July 2004 an optimised monochromatic beam was extracted and the total flux was measured using a calibrated ^{3}He monitor. A flux of about 2 x 10^8 n/s was obtained over a surface of 13 cm^2, after a fine tuning of both Soller collimator and monochromator. The measured peak flux density was 1.5 x 10^7 n/cm^2/s, a value quite close to the expectation. Subsequently, a CCD camera was used to take a 2D-picture of the beam, and the resulting image is reported in this figure.

beam extraction was achieved. Thanks to a fine tuning of both Soller collimator and monochromator orientations, the flux was optimised up to the measured value of 2 x 10^8 n/s from the whole monochromator surface. The peak flux density was measured to amount to 1.5 x 10^7 n/s/cm^2, in good agreement with previous simulations [1,2]. The results are shown in figure 2 where a sketch of the transverse section of the beam is reported, as detected by a CCD camera. The extraction of the monochromatic beam is by itself quite an encouraging result and opened the opportunity for a subsequent check of the BRISP detector bank and its acquisition electronics [4]. To this purpose the BRISP detector was equipped with one bank composed of 32 individual vertical Reuter Stokes PSD tubes. This configuration is intended only as preliminary, since an array of 96 tubes grouped in 3 banks is foreseen for the commissioning phase, while 160 tubes arranged in 5 banks will be used in the final upgrade. In August 2004, the detector was placed in front of the incident beam, attenuated by a 5-mm sheet of absorber (elastobore) to roughly 10^3 n/s/cm^2, and the first images of the spectrometer monochromatic neutrons were successfully acquired. A three-dimensional plot of the intensity profile, corresponding to a 10 s acquisition time, is reported in figure 3.

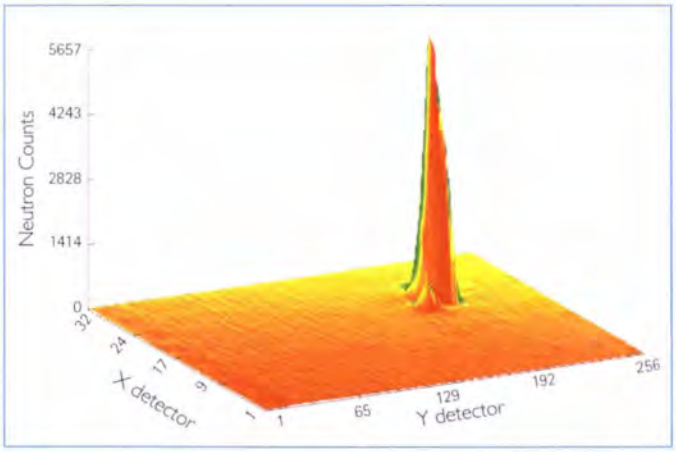

Figure 3: First image of the monochromatic beam on the BRISP detector. On 4 August 2004, the detector was set under high voltage for the first time. First neutron pulses, due to background neutrons on the BRISP site, could be recorded on the analogue outputs of the detector bank. After connecting the detector to the data acquisition electronics, a first picture could be obtained, thus proving the correct functioning of all the acquisition channels. On 6 August, after radiological tests of the setup, the shutters were opened and the BRISP detector took its first images of the BRISP monochromatic beam with a 10s acquisition time.

The two trial tests described above represent the best achievements of the first era of the BRISP construction and allow the present and future efforts of the BRISP team to be directed towards other challenging tasks, such as the mechanical and optical alignment of the whole spectrometer components and the setup of the data acquisition electronics and software, to be accomplished by the beginning of the first cycle in 2005. The other two cycles in 2005 will then be devoted to the commissioning of the instrument. This will allow testing of all the components and a fine-tuning of the performance of the whole instrument in the present basic configuration. The next stage will witness further developments and upgrades in the near future. Among these, the installation of copper monochromators for higher flexibility in the choice of incident energies (namely 52 and 138 meV), of a new Fermi chopper rotor for higher flux on the sample, and of a high-angle detector bank are already envisaged for the project development.

Acknowledgements

The precious help and support of the ILL technical staff played a fundamental role in the achievement of the recent results. The financing of the detector tubes and the relevant electronics by three grants from the BMBF (German Federal Ministry for Education and Research) is gratefully acknowledged.

eferences: [1] S. Jahn and J.-B. Suck, Appl. Phys. A 74 (2002) S1465
[2] G. Venturi, E. Guarini, F. Formisano, A. Orecchini, A. Cunsolo, C. Petrillo, F. Sacchetti and F. Barocchi, J. Neutron Research 11 (2003) 165
[3] C. Petrillo, E. Guarini, F. Formisano, F. Sacchetti, E. Babucci and C. Campeggi, Nucl. Instr. Meth. A 489 (2002) 304
[4] P. van Esch, T. Gahl and B. Guerard, Nucl. Instr. Meth. A 526/3 (2004) 493

G. Manzin *(ILL)*

technical & computing developments

A gas proportional scintillator counter for thermal neutron instrumentation

It has been demonstrated [1] that a micropattern structure, installed in a gas volume suitable for neutron detection, can generate a number of photons during the avalanche process sufficient for detection via optic readout. A gaseous scintillation detector consisting of an $^3He+CF_4$ filled micropattern detector coupled with an optical readout was then investigated for an application for high resolution and high counting rate position sensitive neutron detectors. The performances of this detector are comparable to the ones of a neutron scintillator with in addition a very good gamma separation. The gas mixture was carefully studied and several systematic measurements were carried out in order to optimise it for light emission and position resolution. The possibility of detecting the primary light (prior to electron avalanche multiplication) makes this device very interesting and promising for application to neutron scattering instruments.

Every avalanche multiplication process or charge migration in a gas volume is accompanied by photon emission resulting from the inelastic collisions between electrons and gas molecules, when the electron's energy is higher than the radiative excitation threshold. The use of this light producing phenomenon, particularly abundant in pure noble gases, has given birth to an entire family of detectors called Gas Proportional Scintillation Counters (GPSC). In general, gas scintillation counters are very similar to charge readout gaseous detectors, but the electronics used for the charge readout is replaced by an optical readout chain. The gas mixture can be different from the ones typically used in gas counters. It is chosen in order to maximise the emitted light and in such a way that the latter is compatible with the spectral sensitivity of the optical system used, in general in the visible or near UV region. The detectors used for ionising particles based on photon emission by gases rely on the radiative output of the medium corresponding either simply to an energy input, that is the energy lost by the detected particle, or to further energy supplied to the medium by an external electric field in such a way that the output photon flux is increased by several orders of magnitude. The incoming particle dissipates energy through ionisation and excitation processes. The radiative de-excitation of the medium gives rise to the primary scintillation; gas scintillation counters are based on information from this light pulse. If an electric field is applied to a gas scintillation counter the drift of primary electrons, and eventually also secondary electrons near the electrodes (if the field is strong enough for avalanches to build up), further excites the medium which de-excites by emission of the secondary scintillation. The gas scintillation proportional counter is based on the secondary scintillation, which can be controlled by appropriate shaping of the electric field configuration, and uses also the primary ionisation. Although the photon flux carries an important fraction of the energy deposited by the particle or supplied by an external field, gaseous detectors until now have been mainly used as charge collecting devices. The development of light gaseous detectors has been slow and some potentialities have not been yet fully exploited or even considered. The detector used for this study was made of an MSGC plate assembled in a gas tight stainless steel box. This gas vessel has a diameter of 20 cm and two opposite windows: an Aluminium one, 5 mm thick, in order to allow the neutrons to enter the gas volume, and a Quartz (Suprasil) one again 5 mm thick, to allow photon readout. A special light- tight flange is used to position a 1-inch photomultiplier in front of the Quartz window. Similarly, it is possible to position a CCD camera for imaging purposes. The bidimensional MSGC used for the tests is of the Bidim-bis type developed at the ILL and described in [2]. For this application the MSGC plate needs to be assembled in the gas vessel in a reverse way compared to a normal neutron detector (i.e. with the cathodes facing the Aluminium entrance window) because we need the anodes, where the light is produced, to be facing the Quartz window. In order to understand the light emission process, several measurements with an ^3He-CF_4 gas mixture were performed, varying the amount of CF_4 in the mixture or the concentration of the ^3He. We can observe that the number of emitted photons reaches a plateau for a CF_4 pressure higher than 2,5 bar, independent of the ^3He concentration. The

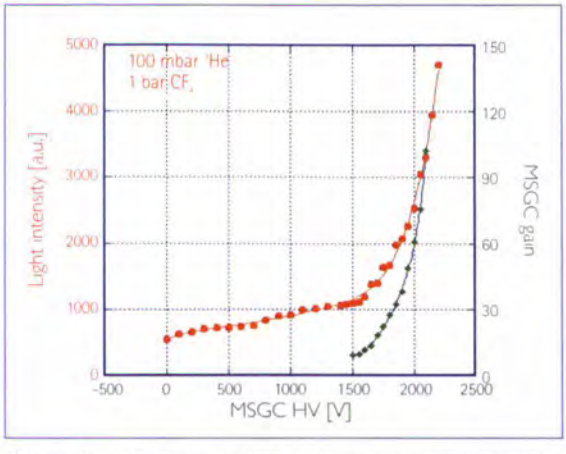

Figure 1: Light intensity and LSGC charge gain as a function of the MSGC high voltage.

fact that the light emission is independent of the ^{3}He concentration tells us that only CF_4 molecules contribute to the process.

Coupling the detector with a CCD camera it is possible to visualise or record some images irradiating the detector with a neutron beam through a mask. From figure 1 we can see that it is possible to observe photons emitted in the gas volume well before the avalanche multiplication takes place in the detector, even when no high voltage is applied to the MSGC. This means that the interaction of the charged particles generated by the neutron absorption in the gas volume is sufficient to produce photons in a number high enough to be detected by the CCD camera. When applying a high voltage to the MSGC, the anode structure becomes visible in the image, due to the fact that the avalanche electron multiplication takes place in the immediate vicinity of the anode strips and this is also the location of the maximum light emission (figure 2).

The system is clearly able to resolve light sources as close as 1 mm apart; this suggests that by using a structure with a finer pitch it would be possible to obtain a very good position resolution.

The possibility of observing the primary light emitted in the gas, with no amplification on the MSGC plate, is an indication of the good scintillation properties of the chosen gas mixture. Seen as an alternative to charge readout, optical readout of the scintillating avalanches simplifies the readout system, limiting the connection problems, and also allows a deep study of the detector performances.

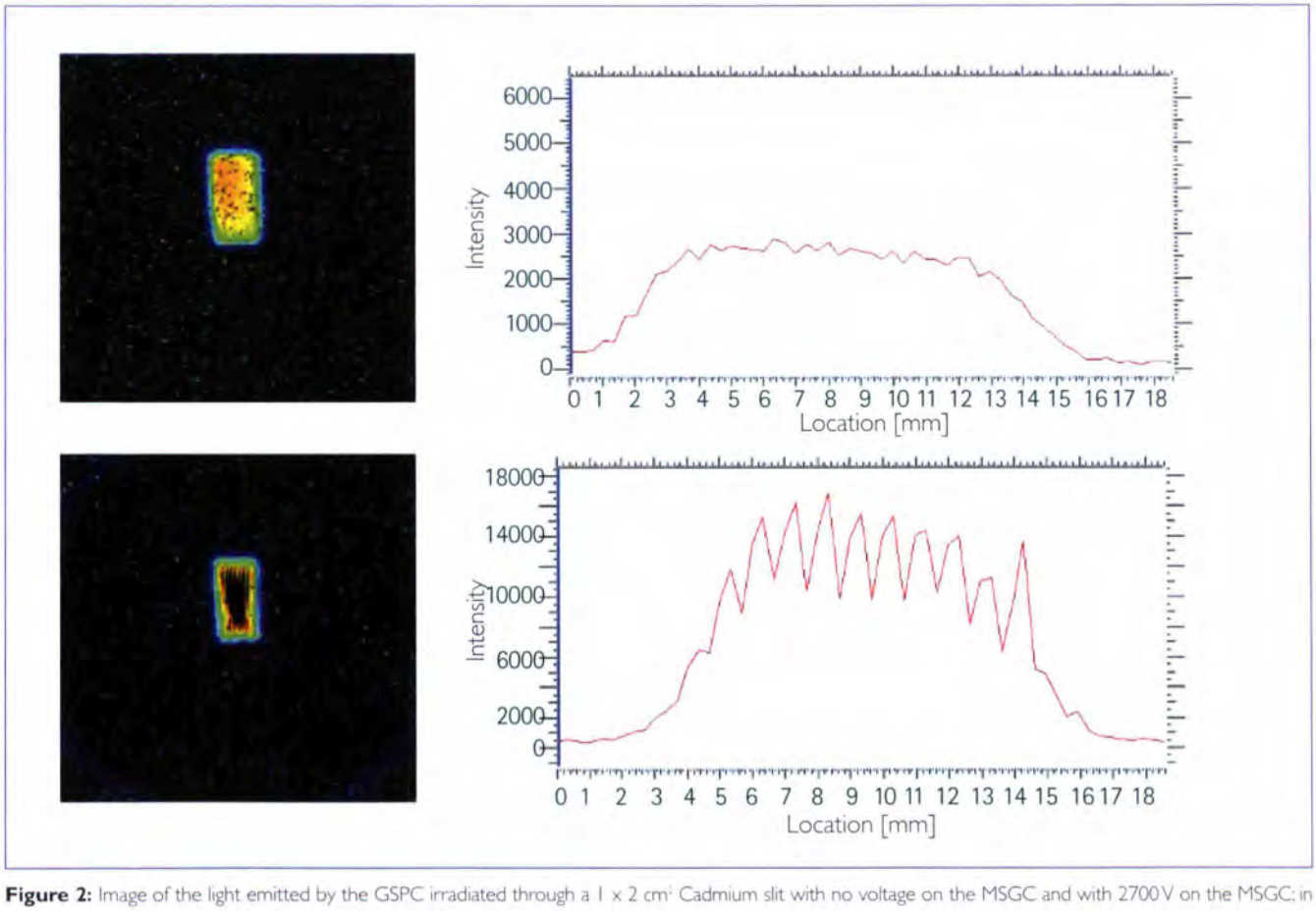

Figure 2: Image of the light emitted by the GSPC irradiated through a 1 x 2 cm² Cadmium slit with no voltage on the MSGC and with 2700 V on the MSGC; in both cases the horizontal projection of the image is also shown.

References: **[1]** F.A.F. Fraga, L.M.S. Margato, S.T.G.G. Fetal, M.M.F.R. Fraga, R. Ferreira Marques, A.J.P.L. Policarpo, B. Guerard, A. Oed, G. Manzin and T. van Vuure, CCD readout of GEM based neutron detectors, Nucl. Instr. and Meth., A475 (2002) 357-361

[2] N. Velletaz, J.E. Assaf and A. Oed, Two-dimensional gaseous microstrip detector for thermal neutrons, Nucl. Instr. and Meth., A392 (1997) 73-79

technical & computing developments

LAMP – 10 years on...

D. Richard, B. Ouladdiaf and M. Johnson *(ILL)*
S. Rols *(University of Montpellier)*

In 2004 LAMP celebrated its 10th birthday. This program, written in IDL, was originally developed to inspect ILL data, following the migration from VMS to Unix operating systems. Today the program aims to give users a common, scriptable and programmable environment in which data can be visualised and manipulated for the widest possible range of instruments. LAMP runs on Unix/Linux, Windows and Mac operating systems and is freely available as a run-time executable (see ftp://ftp.ill.fr/pub/cs/). This article describes recent developments in LAMP.

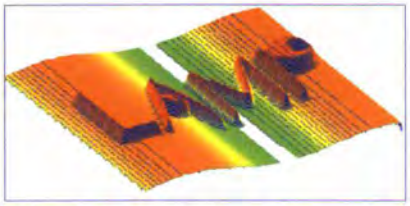

From interactive use to electronic notebooks and scripts in LAMP

The functionality of LAMP in terms of data treatment depends on the macros that have been written by scientists and the Computing for Science Group. Many macros exist, for example, for treating powder diffraction, reflectivity and time-of-flight data. The result of reading raw data is a workspace containing a multi-dimensional array and an associated set of attributes (e.g. axes) and parameters (e.g. sample temperature - see info/data parameters menu). Macros therefore need only contain the code to manipulate the data and its attributes. All commands executed in an interactive LAMP session are recorded in the journal (see info/journal menu). They can be cut and pasted into a text file to make a script of commands which can be executed in a DO box. Scripts are generally limited to sequential execution of commands. Where a large number of repititions in the data manipulation is required, a script file containing FOR or WHILE loops can be executed using the XBU interpreter (see Lamp/Layout menu). Script files amount to a record of a particular experiment. A complementary tool in this respect is the electronic log book which has recently been added to LAMP. By right-clicking in the principle graphics windows, images, text files and comments can be added to the electronic logbook.

New fitting routines in LAMP

In terms of increased functionality, two new fitting routines are now available in LAMP (see tools menu). "str_fit" has been developed for analysing strain scanning measurements in which a Bragg peak is measured as a function of the position in the sample. The diffraction peak in each pattern is fitted with a given theoretical lineshape (e.g. pseudo-voigt), including convolution with a resolution function, and assuming one, two or an unspecified number of peaks in each diffraction profile. The fitted data and residuals can be viewed in different ways. Fit parameters can be plotted and written to file or another workspace. Clearly, "str_fit" is not restricted to strain scanning data. The evolution of any spectral or diffraction profile can be represented in a LAMP workspace and analysed in this way.

The second fitting routine is "Qens_fit", developed to analyse quasi-elastic spectra. Inelastic excitations can also be treated, as in the case of the well-known Fortran program, Profit. The input for "Qens_fit" consists of two workspaces, one containing the data as a function of Q (or temperature, pressure etc), the other contain-

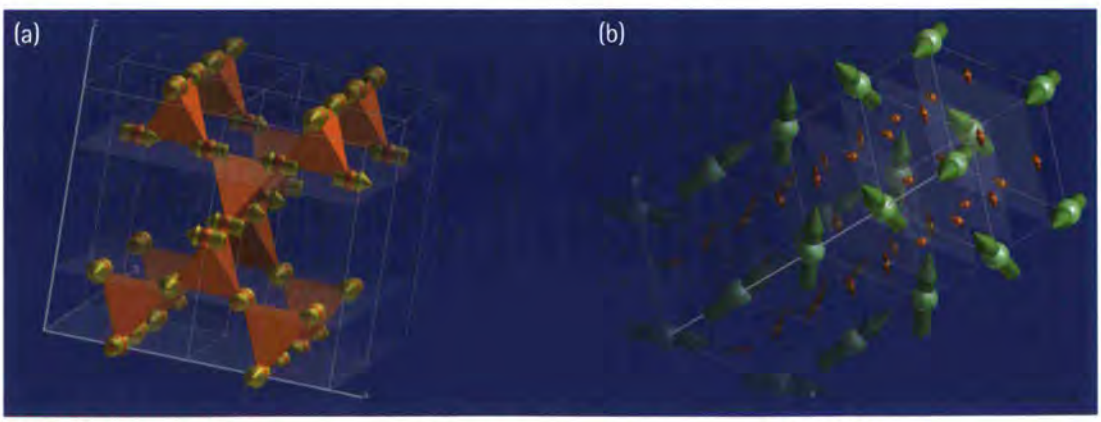

Figure 1: Examples of (a) commensurate and (b) incommensurate magnetic structures in MAGDRAW.

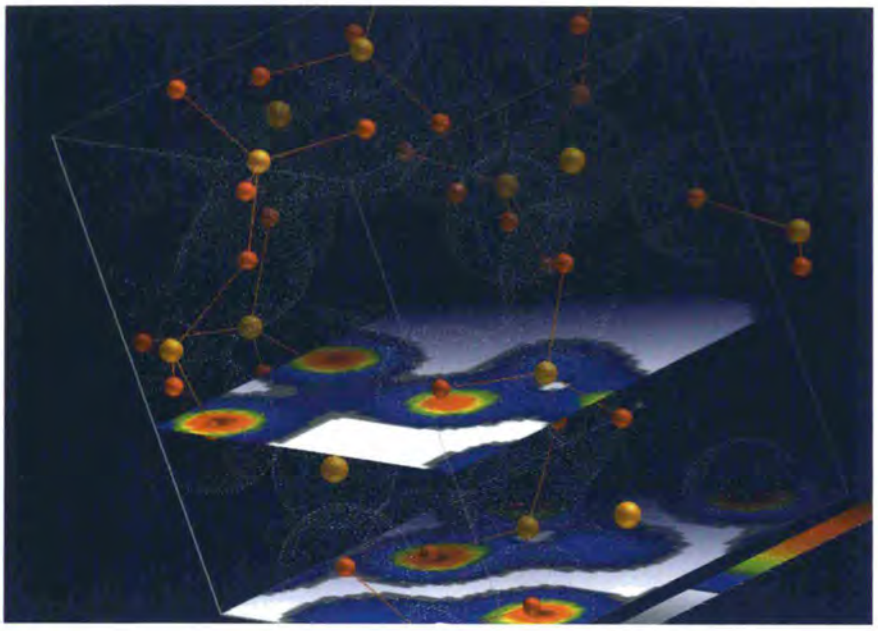

Figure 2: 3D isosurface and 2D contour plot representations of electron density, calculated by VASP, for $LiFePO_4$.

ing the corresponding set of resolution functions, and a fitting model (typically a delta function for the elastic peak and Lorentzians and Gaussians for the quasi/inelastic features). Once one of the spectra has been fitted (e.g. for the highest Q), the remaining spectra can be fitted in one go and parameters can be fixed for all spectra. Instead of fitting independently each spectrum, a physical model can be imposed, for example for diffusion on a sphere. Only simple models are currently available and more will be added.

Atomistic representation in LAMP

A completely new development in IDL is the representation of crystal and magnetic structures (see figure 1a & b). The module MAGDRAW is included in LAMP, allowing it to be distributed freely. MAGDRAW reads the nuclear and magnetic structures following Rietveld refinement in standard programs like FULLPROF. The structure is displayed as a 3D object that can be easily rotated. Miller planes can be shown in the crystallographic cell to help visualise local structure. Standard representations of atoms and structural units (balls, sticks, polyhedra etc) are available. High quality images and animations of, for example, helical spin structures can be saved for publications or presentations. Atomisitic representations in LAMP are also being explored for visualising the results of solid state, first principles calculations on materials. Computational codes like VASP (see http://cms.mpi.univie.ac.at/vasp/), based on density functional theory (DFT), allow electron and spin density to be calculated and these can be displayed with the crystal structure in LAMP (figure 2). The animation capabilities can be used to visualise molecular dynamics simulations and calculated phonons and molecular vibrations.

Running Unix data treatment programs on laptops

The evolution from the unix operating system to Windows and Macintosh is often synonymous with laptop computers being used for data treatment. The technical task of adapting existing unix programs is straightforward, but users find difficulties with three aspects; the command line mode, graphics windows and printing graphics and other output. During the past two years the Open Source GNU programming suite has evolved to offer the same tools for PC-Windows and Macintosh OS-X systems. The unix-like origins of OS-X allows easy porting of SGI data treatment programs, though the majority retain their X-window characteristics. A native Aqua driver has been added to the ILL-PGPLOT library for Macintosh. For PC-Windows a tool "Prop" written in Tcl/Tk provides easy management to launch programs with environment variables correctly set, and to use standard Windows printers for output. Integration of a new windows graphics server allows the plotting window to be resized easily, and a copy sent to a Windows printer. GUI versions of common programs can also be used after minor alterations to the unix originals. A complete package of the SANS programs has been updated with these features. The distribution includes the new libraries and tools as an encouragement for users to adopt the MinGW set of GNU compilers for Windows and join in future developments.

Ron Ghosh

new experimental techniques

With GISANS towards complete reflectometry

V. Lauter-Pasyuk *(TU Munich)*
B. Toperverg *(PNPI St. Petersburg and ILL)*
M. Jernenkov and H. Lauter *(ILL)*

The most exhaustive and detailed information on the 3-dimensional structure of layered samples (i.e. lateral and in-depth arrangement) can be gained from a complete reflectometry study. This consists of both off-specular and Grazing Incidence Small-Angle Scattering (GISANS) and the two together carry the depth-information of the sample. A variation of the grazing incident angle provides focusing of the neutron wave field onto different structural elements across a multilayer stack, and the extracting SANS signal carries a signature of the lateral fluctuations of the scattering length density of these highlighted elements. Due to specifics of off-specular and GISANS kinematics it accesses lateral scales over an enormous range from nano- up to sub-millimetres. This allows not only to probe, for example, the distribution of nano-particles imbedded into matrix-layers, but also to follow their influence on the correlation function and conformity of interfacial roughness.

Specular reflection from multilayered systems probes the depth profile of the mean scattering length density (SLD) averaged over the lateral projection of the coherence length. Lateral fluctuations of the SLD around its mean value give rise to off-specular scattering. At shallow incidence off-specular scattering, measured in slit-like collimation, probes very large lateral scales. The use of point-like kinematics in GISANS permits to greatly extend the capability of reflectometry. At the same time GISANS is introduced in the much wider frame of complete reflectometry. 2D maps of the scattered intensity distribution now provide complete information about the lateral fluctuations:

- the off-specular scattering probes the lateral fluctuations within the reflection plane in the micro- to sub-millimeter range;
- GISANS probes the lateral fluctuations perpendicular to the reflection plane in the nano- to micro-millimeter range;
- a depth profile of the fluctuation's distribution is deduced, recording the off-specular scattering containing GISANS at various angles of incidence α_i, *i.e.* focusing the neutron wave field at particular structure elements of the multilayer.

The combination of different lateral scales with the optical effects provides very detailed SANS patterns strongly varying with α_i. They can readily be understood and quantitatively described in terms of the Distorted Wave Born Approximation (DWBA).

The simple scattering process of SANS inside a multilayer is explained in figure 1a which shows the sketched experimental set-up and the GISANS intensity maps at three values of α_i. The specular reflections are the red spots in the intensity maps. Map A in figure 1a corresponds to the incidence at $\alpha_i = \alpha_c$, the critical angle. Then the wave fields of both, incoming and outgoing waves are enhanced due to the Yoneda effect and the GISANS signal is mostly concentrated around the specular reflection spot $\alpha_f = \alpha_i = \alpha_c$. Turning the sample away from the critical incident angle results in intensity maps B and C in which the Yoneda scattering appears

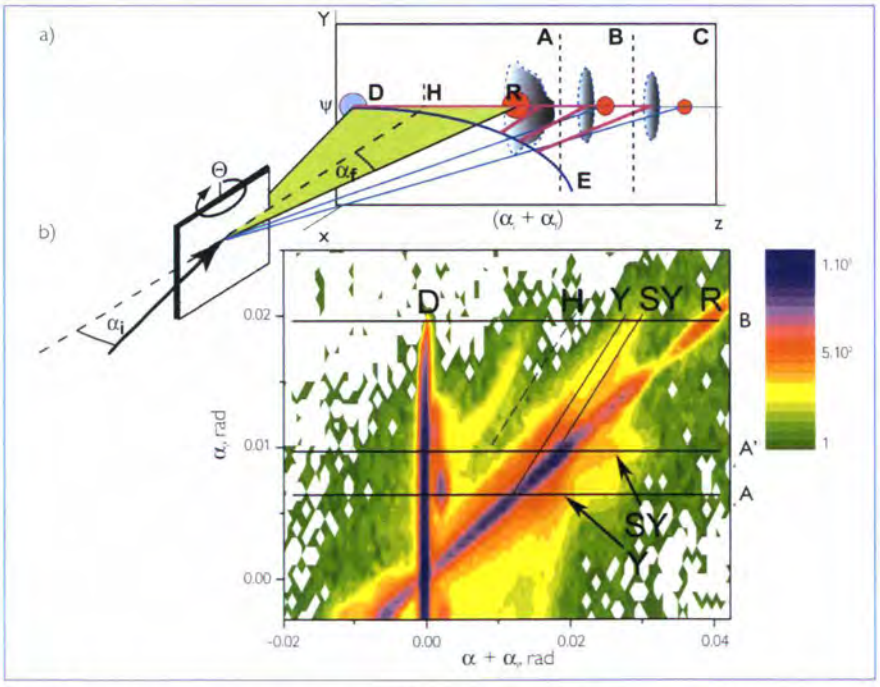

Figure 1: a) schematic presentation of the GISANS set-up on D22. A scheme of GISANS with $\alpha_i = \alpha_c$, the critical angle; B and C $\alpha_i > \alpha_c$; E is the trace of the Ewald sphere in the scattering plane;
b) reflectometry intensity map as a function of α_f and $(\alpha_i + \alpha_f)$ the co-ordinate system on D22. The black lines A' and B mark the position of the detector for which the GISANS spectrum is shown in figures 2a and 2b. D-direct beam, H-horizon, R reflected beam, Y-Yoneda scattering, SY-super-Yoneda scattering. The sample is a copolymer-multilayer [1].

as a spot concentrated at the critical outgoing angle $\alpha_f = \alpha_c$ and extended in y-direction. It is now well separated from the reflected beam. The obtained intensity distributions as a function of Q_x (see rose lines in figure 1a) and Q_y describe the lateral sizes of the SLD-fluctuations, responsible for off-specular scattering and GISANS. Q_y is directly proportional to the scattering angle ψ, while the scattering angle α_f in z-direction depends on both, Q_x and Q_z. They can only be separated with a measurement as a function of α_i. The SANS intensity varies along z-direction due to various factors. The principal one is the variation of wave field amplitudes, which can be found through the fit of the averaged potentials for the specular reflectivity. Then the lateral and transverse structure of the fluctuations is deduced via DWBA, taking into account both the size of the SLD-fluctuations in the direction normal, as well as parallel to the interfacial planes. (The latter is usually probed in conventional off-specular scattering, e.g. GISANS integrated over y-direction.)

As a practical example of the above explanations, we can analyse the experimental intensity maps taken with a copolymer multilayer [1]. In figure 1b the various features of the reflectivity and off-specular scattering are displayed. In order to obtain this map all the GISANS maps are assembled by integrating each of them over the y-direction (thus over the angle ψ). The presentation is unusual, but it has been chosen because it reflects the experimental set-up so that the detector positions for the GISANS maps are easily presentable. Black lines in figure 1b mark the detector positions at which GISANS pictures were taken. The first configuration of interest sketches the features at the edge of the total reflection (A in figures 1a and 1b). But in figure 2a the GISANS map has been chosen marked A' in figure 1b, which is the situation of super-Yoneda scattering at the first Bragg-peak (due to the periodicity in the layer's arrangement). We can clearly see the scattering events below the horizon, which are important for the complete description of the fluctuations creating GISANS and off-specular scattering. Above the horizon the GISANS intensity and the off-specular scattering along $\psi = 0$ are attributed to belong to Yoneda scattering, the super-Yoneda scattering around the reflected beam and the super-Yoneda scattering above the specular scattering with its dependence on Q_z. It is evident that the Q_z dependence will give information about the depth distribution of the fluctuations inside the multilayer. This scattering appears so pronounced because the wave field is enhanced by Bragg condition. This effect is called super Yoneda scattering.

In figure 2b the GISANS scattering from the detector position marked B in figures 1a and 1b has been chosen. Here, again above the horizon, the crossing of the Yoneda and super-Yoneda scattering is highlighted by increased GISANS scattering. At higher angles α_i the reflected beam is met, around which the Bragg-sheet scattering gives rise to enhanced GISANS intensity. New information is obtained here since the Bragg sheet scattering is depth selective. The fit of the GISANS pattern above the horizon in figure 2c shows that already within this limited range important information about the fluctuations giving rise to GISANS, was obtained.

Finally, in figure 2d a GISANS intensity map was chosen to highlight an effect encountered in thick samples in which the reflectivity conditions are running out of the correlation length. Thus here "normal" SANS seems to appear in transmission but also above the horizon being modified by the boundary condition of the multilayer film.

This example illustrates how GISANS coupled to off-specular scattering can give 3D complete and detailed information on layered structures.

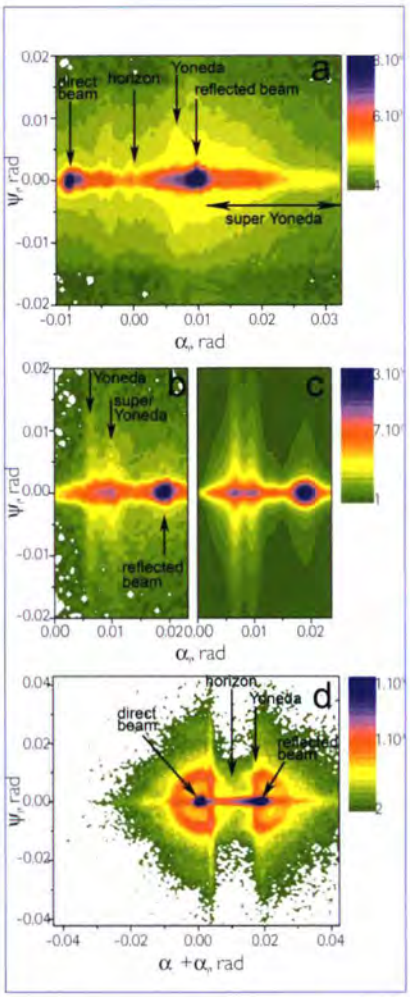

Figure 2: a) GISANS intensity map as a function of ψ (y-direction) and $(\alpha_f + \alpha_i) - \alpha_i$ (z-direction) for the position A' in figure 1b; $\alpha_i = 0$ is the horizon;
b) GISANS intensity map for the position B in figure 1b with scattering above the horizon;
c) calculeted GISANS intensity map for the data in figure 2b, the position B in figure 1b;
d) GISANS intensity map for a 400nm thick copolymer multilayer [1]. $(\alpha_f + \alpha_i) = 0$ is the direct beam position.

References: [1] V. Lauter-Pasyuk, H.J. Lauter, B.P. Toperverg, A. Petrenko, D. Schubert, J. Schreiber, M. Burcin and A. Aksenov, Appl Phys A74(2002) S528; V. Lauter-Pasyuk, H.J. Lauter, G.P. Gordeev, P. Muller-Buschbaum, B.P. Toperverg, M. Jernenkov and W. Petry, Langmuir 189 (2003) 7783

new experimental techniques

The new D23 diffractometer: working at high fields

P. Fouilloux, B. Grenier, L.P. Regnault and E. Ressouche
(CEA, Grenoble)

D23 is a double-monochromator two-axis single-crystal diffractometer with a lifting detector installed on the thermal neutron guide H25. Its efficiency was increased in 2004 by the installation of a completely new non-magnetic, compact and versatile secondary spectrometer. Following this improvement, D23 is now ideal for all kinds of diffraction measurements that require high magnetic fields.

The CRG diffractometer D23

is, with IN22, one of the two machines transferred from the SILOE reactor (CEA-Grenoble) to the ILL (in 1995-96). It has been available to the neutron community since August 1999. It has two different configurations: unpolarised and polarised neutron modes. D23 is devoted to the determination of magnetic structures, magnetisation distribution maps and magnetic phase diagrams at low temperature, high magnetic field and/or under an applied pressure. The wavelength can be changed in the range 0.9-3 Å (unpolarised neutrons) and 1.2-2.4 Å (polarised neutrons). D23, as originally built, was suffering from its old mechanics mainly because it was highly magnetic, and therefore it was impossible to reach very high fields. For this reason, it was decided to replace the secondary spectrometer by a modern one more compact, rapid, non-magnetic and versatile.

All the studies and drawings were made in March 2003 by the company AZ-Systèmes and the mechanics were built at the end of 2003. The new machine (figure 1) was installed and successfully tested at the beginning of 2004, and was available to the community for 2.5 cycles (out of 3) during 2004. Several experiments at high fields were scheduled with both the CEA-12 T and the ILL-15 T cryomagnets, as illustrated in the next section. With this latter device, forces as low as 35 kg (horizontal) and 40 kg (vertical) were measured at 13 Tesla in the worst position [1], demonstrating that D23 is now one of the very few instruments at the ILL, safely supporting all the cryomagnets available. In addition, particular attention was paid to the positioning speed of the different movements. Typically, speeds as high as 6° per second can be reached, making D23 a particularly efficient machine, with an optimised ratio time actually spent counting over the total time of an acquisition (this is of particular importance on a diffractometer, when counting times are of the order of the second). Lastly, the machine is more compact and allows access to a wider angular range: roughly 125° on both sides in $2\Theta_B$, and ± 30° in ν (out of plane angle of the detector). The fact that the arc is symmetric permits working with all types of asymmetric magnets available at the ILL.

Figure 1: The new D23 secondary spectrometer with the 15 T ILL cryomagnet mounted.

What's next?

The new machine has been drawn to be evolutionary: polarised ^{3}He cells are thought of as an alternative to the existing Heusler alloy monochromator, to increase the flux in the polarised neutron mode. The detector can also be replaced for a polarisation analysis option (with an ^{3}He cell as a spin analyser "DECPOL"). All these options are of prime interest to provide the users with a three-dimensional polarisation analysis option as implemented in the new CRYOPAD device.

High Field study of URhGe

One of the first experiments performed at high fields on the new D23 diffractometer was devoted to the intermetallic compound URhGe. This compound is ferro-

magnetic below 9.5 K, and both ferromagnetic and superconducting below $T_s \sim 0.3$ K [2]. A similar behaviour is also found in the related ferromagnetic material UGe_2 between 11 and 16 kbar [3]. Here, the appearance of superconductivity occurs together with a first order reduction in the value of the ordered moment at 0 K [4,5]. A first order transition back to the larger moment phase can be induced by applying a magnetic field along the easy axis.

In URhGe there is also a field induced transition at $H_c \sim 11$ T visible in the high field magnetisation. However it differs from the metamagnetic transition seen in UGe_2, since the change now occurs for a field applied perpendicular to the ordered moment rather than parallel to it. At first sight, this transition could simply be a banal rotation of the moment towards the applied field direction: for d-metal ferromagnets such as iron, the magnetic moment prefers to lie along certain crystal directions in low fields and an applied field of sufficient magnitude can then rotate the moment towards the applied field direction. This physics is well understood when the anisotropy energy is much smaller than the exchange energy, and the magnitude of the ordered moment is conserved. However other measurements reveal that the transition in URhGe is in fact much more complicated, enhancing the importance of characterising the magnetic behaviour carefully. Neutron diffraction offers a big advantage for this, since it allows all the components of the magnetisation to be measured simultaneously, and can also test for the appearance of other orders, such as antiferromagnetism. The newly available field of 15 T has allowed us to investigate this interesting physics on the D23 diffractometer (figure 2).

In this experiment, the field was applied along the *b*-axis, whereas the zero field easy axis is the *c*-axis. Collecting a large series of peaks at $H = 0$ and above the critical field $H_c \sim 11$ T evidenced that the effect of the applied field H is to suppress the ferromagnetic moment along the *c*-axis, m_c, and to induce a moment parallel to H, m_b. A field dependence of 2 Bragg peaks was performed at $T = 2$ K up to 15 T: (i) the (002) peak, not sensitive to m_c, which therefore measures the induced moment parallel to the applied field, its field dependent part being proportional to m_b^2 ($m_b = 0$ at $H = 0$); (ii) the (200) peak, whose intensity, after subtraction of the nuclear part (measured at $H = 0$, $T = 15$ K), is proportional to the square of the total moment, $m_b^2 + m_c^2$. Assuming an isotropic form factor, the moment parallel to the easy axis can be deduced from the difference between the normalised intensities of these two peaks (corresponding to m_c^2). As seen in figure 2, m_c collapses at a metamagnetic field of about 11 T, with a corresponding increase in the induced moment parallel to the applied field, m_b. However, the measurements also show that the total moment does not increase monotonically, but has a dip at the 'metamagnetic' field. Either the form factors for the two moment directions are substantially different, or the total moment is reduced in the vicinity of the transition field, a reduction which remains to be explained.

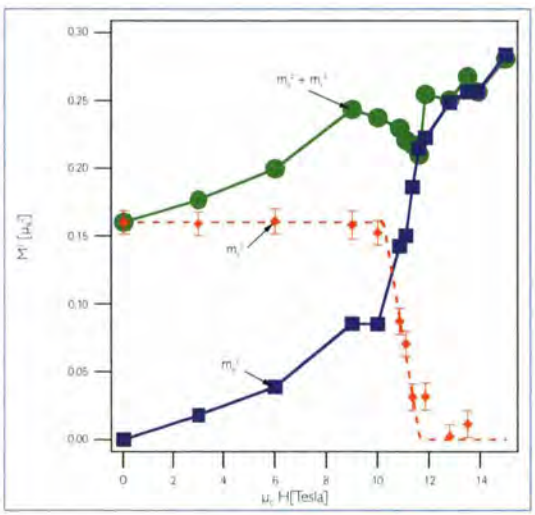

Figure 2: Field dependence of m_b^2, m_c^2 and of the square of the total moment $m_b^2 + m_c^2$ measured on D23 in URhGe at 2 K, in an applied field along the b-axis.

References: [1] M. Enderle, ILL technical report "14.9 T force tests and risk considerations"
[2] A.D. Huxley et al., to be published
[1] D. Aoki et al., Nature 413 (2001) 613
[2] S. Saxena, Nature 406 (2000) 587
[3] A.D. Huxley et al., Phys. Rev. B 63 (2001) 144519
[4] C. Pfleiderer and A.D. Huxley, Phys. Rev. lett. 89 (2002) 147005

Teams teaming up

The « Intercultural Day » organisation team. From the left: Colin Carlile, Massimo Rocchi, Philippe Wittwer, Lætitia Rosselet, Fabian Leistikow, Samuel van den Bergh, Ariane Baran, Kann Hildebrandt and Silke Bachmann.

Ladies for Science: from the left, Brigitte Aubert, Laurence Tellier and Alison Mader.

Alan Hewat liaising with the UK user community.

The ILL PhD students on their clip session day.

workshops in 2004

Workshops in which ILL was a major player in 2004

Position Measurements with slow neutrons @ NIST
5-7 April • P. Geltenbort (ILL), J. Nico (NIST)

Joint IN2P3 and ILL workshop on nuclear and particle physics
6-7 May • N. Alamanos (CEA Saclay), H. Börner & T. Soldner (ILL), J. Collot & J.A. Pinston (LPSC Grenoble), D. Guerreau & M. Spiro (IN2P3 Paris)

MILAND workshop
17-18 June • B. Guerard (ILL)

French Japanese colloquium on quantum complex systems
21-24 July • J. Flouquet (CEA-Grenoble), K. Miyake (Osaka University), C. Lacroix (CNRS-Grenoble) & H. Mutka (ILL)

Engineering Applications Workshop at ILL-ESRF
13-14 September • FaME38, ILL & ESRF

Neutrons and Numerical Methods II
14-18 September • M. Johnson & M. Gonzalez (ILL), Tarek Mounir (Uni. H. Poincaré, Nancy), G. J. Kearley (IRI, Delft)

Colloquium in honour of Roland Currat
15 October • ILL management

Medium Pressure advances for Neutron Scattering
20-23 October • M.H. Lemée-Cailleau (Uni. Rennes & ILL) & N. Kernavanois (ILL)

workshops in 2004

Position measurements with slow neutrons at NIST

On 5-7 April, the International Conference on Precision Measurements with Slow Neutrons was held on the campus of the National Institute of Standards and Technology in Gaithersburg, MD, USA. The conference was the latest in a series that began in 1977 in Grenoble. It highlights new results and developments in the field of fundamental neutron physics utilising cold and ultra cold neutrons. Approximately 125 people from 10 countries participated in the meeting that solicited over 120 abstracts. The conference was sponsored and supported by seven institutions, including the ILL.

The meeting comprised three full days of oral sessions including poster presentations. The proceedings of the conference will be published in a special edition of the NIST Journal of Research, which is available online to the public. The participants enjoyed a banquet at a restaurant on the banks of the Potomac River. After dinner, Prof. Norman Ramsey of Harvard University enchanted the audience with notable stories of his interactions with great physicists throughout his long and illustrious career.

The conference opened Monday morning with discussions on the current state of the neutron electric dipole moment searches and emphasized several ambitious efforts to improve the limit by one to two orders of magnitude within the next few years. Over the next two days, the topics covered a variety of concentrations within the field, including tests of electroweak theory and the Standard Model, production and storage of ultra cold neutrons, neutron interferometry, and new developments in polarisation and polarimetry.

There was a full session on neutron facilities around the world with an emphasis on the increasing number of new sources that are under construction. These facilities demonstrate the growth in field of fundamental neutron physics and present additional opportunities for experiments requiring large densities of ultra cold neutrons, exploiting higher fluences of pulsed cold neutrons, or training future generations of neutron scientists. The conference concluded with a summary by Prof. Dirk Dubbers of the University of Heidelberg. The general consensus among the participants was that, in spite of the progress and many achievements that were presented, new challenges and opportunities in fundamental neutron physics continue to present themselves.

Peter Geltenbort and Torsten Soldner, coordinating the workhops contributions.

Joint IN2P3 and ILL workshop on nuclear and particle physics

The mutual collaboration between the ILL, the IN2P3 (Institut National de Physique Nucléaire et de Physique des Particules) and DAPNIA (Département d'Astrophysique, de Physique des Particules, de Physique Nucléaire et d'Instrumentation Associée, CEA) in the use of neutrons as both a tool and an object for subatomic physics investigation, is a long tradition which has produced many scientific results over the last 30 years. In order to strengthen their partnership and to establish new collaboration grounds, the three institutions have jointly organised a prospective workshop. This workshop took place on 6 and 7 May at our neighbour institute LPSC (Laboratoire de Physique Subatomique et de Cosmologie).

The workshop was attended by 55 scientists, half of them from French laboratories. Most of the talks were given by ILL sci-

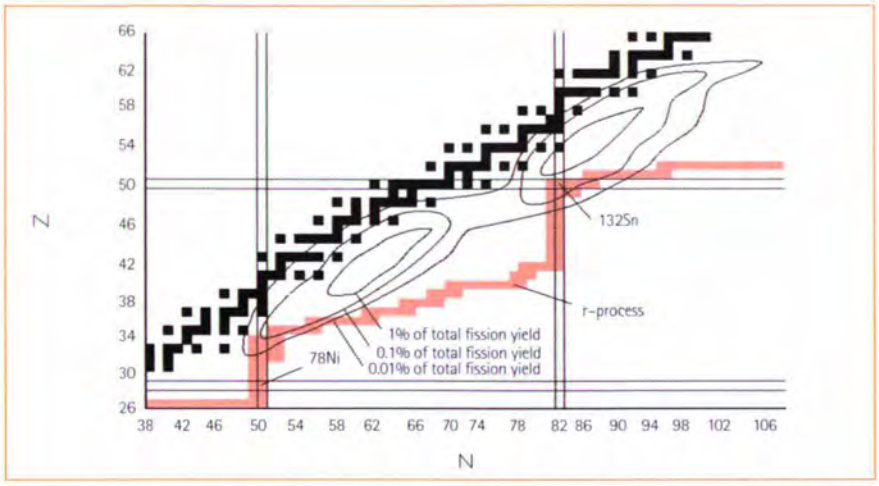

Gary Simpson convinced the participants that Lohengrin is the best facility to investigate neutron-rich nuclei.

entists and prominent users, to present the manifold activities in nuclear and particle physics at the ILL to the French community. The other talks presented activities of French laboratories at other facilities. The first day was devoted to particle physics with cold and ultra-cold neutrons and covered such hot topics as the search for time reversal invariance beyond the Standard Model, the test of the unitarity of the CKM matrix, and the search for non-Newtonian interactions. The second day was dedicated to nuclear physics, in particular to nuclear structure and shapes, experiments with nuclei far from stability, and fission. The workshop concluded with an interesting session on applications: nuclear waste transmutation, new reactor concepts, and neutron tomography.

The comprehensive overview the workshop gave on the science done at the NPP instruments is an excellent basis for closer future collaboration between the three organising institutions.

MILAND workshop at the ILL

Instruments of high-intensity neutron sources, dedicated to single crystal diffractometry (SXD), reflectometry, and small-angle neutron scattering (SANS), are limited nowadays by the position resolution of their detector and/or its maximum sustained counting rate. This situation results from continuous progress made in neutron optics, allowing increased neutron flux on samples, and from an increasing demand to use samples of less than 1mm^3 volume.

This situation has triggered the SANS-2MHz project, with the goal to improve the counting rate of the D22 instrument by a factor of 20. As a result, a new detector has been studied in the framework of the Millennium Programme and TECHNI-FP5 network, and it is now in operation on D22. It is based on position sensitive proportional counters, a technology well suited for very high counting applications, but limited in position resolution to about 5 mm.

In order to provide both a high count rate and a high position resolution for SXD and reflectometry instruments, intense development has been engaged in several institutes, which has gained a strong interest among the future users of the two spallation sources under construction (SNS in the US, JSNS in Japan); actually, the peak count rate of these sources will be more than one order of magnitude higher than ISIS, the actual most intense pulsed source, and progress made in the field of neutron detectors during the last years do not allow to predict an optimum use of SNS and JSNS at the beginning of their operation.

The MILAND 4-year project, coordinated by the ILL, has been launched at the beginning of 2004. It is devoted to the development of a new ^{3}He detector for reflectometry neutron instruments, in terms of sensitive area, counting rate, and position resolution. In order to broadly benefit to the neutron user community, techniques that can be transferred to the industry will be given priority.

The specifications of the MILAND detector were defined according to previous international detector meetings. Compared to the best-performing 2D neutron gas detectors available today, it will improve the spatial resolution by a factor of 2 (for detectors of equivalent size);

global as well as local counting rate capability will be increased by a factor of 5; and all the other parameters (gamma discrimination, counting stability and uniformity, efficiency) will be maintained at the same performance level. 10 physics institutes, which are strongly involved in detector and electronics development, are partners of this project: BNC, BNL, ISIS, ILL, GKSS, LIPP, LLB, SNS, TUM, and Tokyo University. More than 35 people participated in the second MILAND meeting, held in Grenoble on 17 and 18 June. 22 presentations were given, followed by discussions on several topics like "transfer to industry" and "possible applications". These presentations are available on the MILAND web page:
http://www.neutron-eu.net/jra2/index.php

H. Takahashi, from Tokyo University, presenting the latest development of Japanese Electronics for Neutron Detectors.

French Japanese colloquium on quantum complex systems

A joint meeting between the CNRS and the Japanese Society for the Promotion of Science (JSPS) was organised at the ILL in July. Additional support was given by the CEA/DSM and the ILL. The Japanese delegation (40 members) included eminent scientists (J. Akimitsu, H. Fukuyama, K. Miyake, Y. Kuramoto, K. Ueda) and many young researchers (20 PhD students and postdoctorants).
Altogether about 100 contributions were presented and discussed, half of them as oral presentations and half as posters or clips. The meeting contributed very much to reinforce the mutual collaboration between France and Japan, with a good balance between discoveries of new materials, insights given by the combination of microscopic and macroscopic experiments and strong feedback with the theory. The workshop greatly benefited to both the Japanese and European communities. On one hand, the choice of the ILL was very attractive for our Japanese colleagues, eager to collaborate in neutron scattering experiments or to use the experimental results for the simplification of the theoretical models in the complex matter built from strongly correlated electronic systems. The recent progress in inelastic neutron experiments as well as in small-angle scattering, were among the highlights. On the other hand, for the European participants the quality of the work made in Japan represented an excellent and stimulating challenge.

Engineering Applications Workshop at ILL-ESRF

A workshop on Engineering Applications of Neutrons and Synchrotron Radiation took place from 13-14 September at ILL-ESRF. The workshop brought together about 100 leading scientists and engineers who discussed the application of neutron and synchrotron X-ray central facilities for materials science problems. The event was organised by the FaME38 materials engineering facility in collaboration with ILL-ESRF.
The programme included formal presentations, informal workgroup sessions and an opportunity to meet staff at the ILL-ESRF materials science beamlines. The formal presentations were structured into three sessions entitled Progress, Complementarity and Applications chaired by Giovanni Bruno (ILL), Thomas Buslaps (ESRF) and Darren Hughes (FaME38). The presentations showcased the state-of-the-art neutron and synchrotron X-ray facilities now available for engineering analysis and highlighted the materials science challenges

Group photo at the ESRF.

facing industry today.

The keynote presentation in the Progress session was given by Peter Webster of FaME38. He highlighted the enormous potential of synchrotron X-rays and neutrons for the investigation of stresses in engineering components and showed how the recent creation of the FaME38 laboratory helps to optimise experimental efficiency. Mike Prime (LANL, USA) presented a technique that he has developed for measuring residual stress in the keynote talk for the Complementarity session. The 'Contour Method' measures deformation in an electro-machined surface and uses FE analysis to calculate the original residual stress field. It is particularly useful when used in association with neutron or synchrotron X-ray measurements to reveal the full stress field in components. In the session on Applications, Richard Burguete (Airbus, UK) gave an entertaining keynote presentation highlighting the materials science issues currently facing the European aerospace industry. He showed that failure analysis may be achieved using rigorous mechanical testing and non-destructive methods such as neutrons and synchrotron X-rays.

The range of topics of the full programme was diverse, reflecting current 'hot' research topics; residual stress analysis in aircraft wings; near-surface stresses arising from machining; imaging of bonded joints in car components; biomedical applications. A number of new collaborations between on-site researchers and academic/industrial engineering groups were established during the workshop and many more are expected to develop after the event.

The workshop committee would like to thank everyone who helped with the event and making it an exciting forum. The Workshop Proceedings, which include abstracts of the oral presentations and posters, the programme and a list of participants, are available on the FaME38 website (www.ill.fr/fame38).

Neutrons and Numerical Methods II (N2M2)

Almost six years on since the first Neutrons and Numerical Methods workshop (December 1998), N2M2 was held at ILL from 14 to 18 September. The aim of both workshops was to explore the use of total energy calculations to describe the evolution of physical systems, predicted structures and dynamics being compared with neutron scattering data. The meeting was funded by the ILL, NMI3, ISIS and TU-Delft.

The first day took the form of a one-day school, with four introductory talks covering the main types of total energy calculations, based on empirical force fields for large (e.g. macro-molecular) systems and on density functional theory for materials that can be described by a smaller number of atoms (< 1000). About 60 people attended this series of talks. In principle the following morning was free, but about 15 people chose to do tutorials on molecular dynamics simulations or phonon calculations.

The workshop itself started on the Wednesday afternoon (September 15) and lasted for 3 days, finishing on the Saturday morn-

ing (September 18). About 100 people attended the workshop, about one-third wanting to give talks, one-third presenting posters and the rest just came to learn. Finally 24 talks, of which 11 were invited, were retained. Since the workshop was method-based, a wide range of subjects was covered including materials, guest-host systems, liquids and glasses, phonons and vibrations, magnetism, polymers, biological systems and mesoscale systems. Whereas in 1998 the density of numerical results was relatively low due to the computational power available at the time, extremely thorough numerical studies were presented at N2M2. In particular, the ability to perform a large number of first principles calculations using DFT was noticeable. These calculations not only allow geometries and forces to be calculated accurately, but also electronic properties such as densities of states, electron-phonon coupling, spin densities and exchange interactions. In most cases, freely-available computational codes were being used for both force field and DFT-based simulations. In all talks the complementarity of simulations and experiment, and the need for both, was stressed. A high level of agreement between simulation and data gave clear insight into the behaviour of physical systems, but in one notable case, a lack of agreement was used to highlight problems with the samples used in the experiments. Experiments involve many effects, not all of which are known. Simulations involve a known set of physical phenomena, but which may not be complete.

The talks from the school were printed and bound and constitute a useful reference for newcomers to numerical simulations. An abstract booklet was produced for the workshop but there were no proceedings. Instead we plan to collect together full research articles in a special issue of the journal "Chemical Physics" to be published in early 2005.

The N2M2 event took place almost a year after the closely-related Computation Lab (C-lab) project was initiated. This project aims to improve access to numerical modelling software and know-how for neutron users by centralising hardware, software and manpower close to the experiments. Training and transfer of competence to home labs are key goals of the project. The manpower will be provided mainly by the C-lab partners in the form of thesis students and post-docs, the infra-structure will be provided by ILL. The success of the N2M2 workshop is a strong indication that people want to embrace new computational methods to get greater insight into physical systems. The C-lab is the mechanism being put in place by ILL that will help and encourage neutron users to make their first steps into the modern world of research based on experiments, theory and simulations.

Symposium in honour of Roland Currat

Impassible as ever, he's taking off, having provided a good fraction of a century of loyal good service. He has got us all used to his dependable presence, his meticulous reading and re-reading of texts, his smiling humour and suddenly he's up and away. Why now? Well, because it's time.

Time to move on, to leave behind those incommensurate little objects, fascinating phase transitions, magical three-axis devices, time to take stock, and to devote time perhaps to the more advanced aspects of relaxation, eyes fixed on higher peaks.

A good fraction of a century at ILL? Well, yes – Roland joined the ILL over a third of a century ago!

He was amongst those who established ILL's instrumentation, and he has made a clear contribution to the Institut's scientific reputation. Roland was awarded the Prix Ancel by the French Physical Society in 1989 for his work on the dynamics of

Roland Currat, one of the ILL Mousquetaires and leader of the Three Axis Group, retired in March.

incommensurate phases, and he became an acknowledged expert in the dynamics of phase transitions. He was able to attract a whole community of users to the ILL, introducing them to the beauty of resolution functions and the deeper mysteries of crystal symmetry – not to speak of the finer subtleties of coinche!

To thank Roland for his many contributions to the ILL, a **symposium in his honour** was organised on 15 October. The meeting included invited presentations and it was closed by a dinner at the "Clos du Château", in Goncelin.

Roland's path crossed that of many an ILL character (too many to mention in this brief tribute!) and throughout his time at the ILL he has never lost his genial bonhomie, nor his calm and even temper.

Many thanks, Roland, for your talents, your good humour, and your constant attention. Fortunately for us all you will still be around to share in other (scientific) adventures.

Medium Pressure advances for Neutron Scattering (MPa4)

The international workshop on Medium Pressure advances for Neutron Scattering (MPa4NeutronS) was held at the ILL from 20 to 23 October 2004. It was attended by about 90 scientists from Europe, the USA, Australia and Japan, working in scientific and technical fields related to neutron scattering in the medium pressure range (0-35 kbar). The objective of the workshop was to emphasize the uniqueness of the information provided by neutron scattering in a pressure range known to be technically difficult to explore. During the different sessions, oral or poster presentations allowed to identify the scientific cases related to Physics, Materials Science, Geophysics and Bioscience under pressure. Technical aspects, particular to medium pressure, were also thoroughly discussed. As an immediate consequence, new collaborations emerged, related either to the existing high pressure expertise available in neutron centres or to the development of techniques like the new "large volume" cells. This event was directly and jointly organised by the Université de Rennes 1, the Institut Laue Langevin and its Collaborating Research Groups of the CEA/Grenoble, the Laboratoire Léon Brillouin, and the Centre National de la Recherche Scientifique. It has also received the support of NMI3 -the integrated Infrastructure Initiative for Neutron Scattering and Muon Spectroscopy-, of ISIS - the UK pulsed neutron & muon source-, as well as of the Région Rhône-Alpes and the city of Grenoble.

The detailed programme is available on http://www.ill.fr/Events/MPN/.

Grégory Chaboussant (LLB, Saclay France) debating the pressure effects on magnetism with Louis-Pierre Regnault (CRG CEA/Grenoble) and Hannu Mutka (ILL).

Users and science

Katja Jenkins and Giovanna Cicognani (User Office) during the ILL Users Coffee Break.

Nolwenn Kernavanois, busy with College 5B proposals.

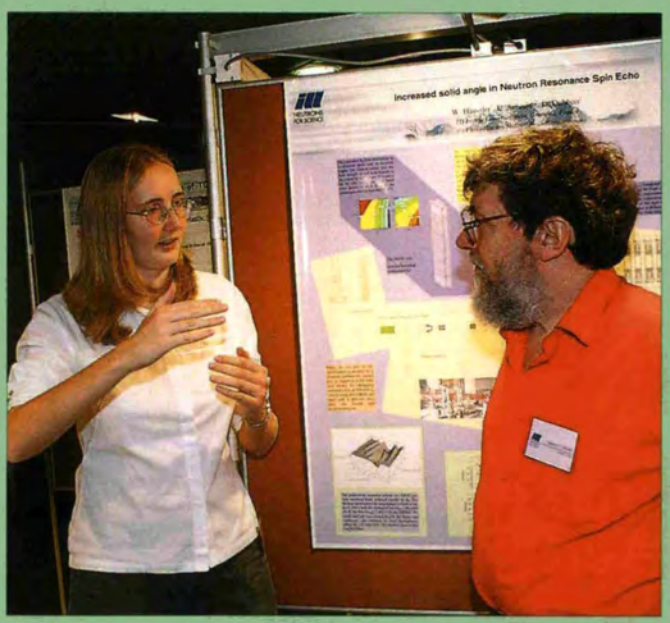

Elisabeth Blackburn discussing her PhD thesis with Ted Forgan.

Valery Nesvizhevsky and Isolde Harbich, sharing a well deserved cup of coffee.

experimental & user programme

- User programme
- Instrument list
- Beam-time allocation
- Instrument performance
- Industrial use of neutrons
- Reactor operation

experimental & user programme

List of instruments - January 2005

ILL's instruments		
D1A (50%)	powder diffractometer	operational
D2B	powder diffractometer	operational
D3*	single-crystal diffractometer	operational
D4 (50% with IN1)*	liquids diffractometer	operational
D7	diffuse-scattering spectrometer	operational
D9*	single-crystal diffractometer	operational
D10	single-crystal diffractometer	operational
D11	small-angle scattering diffractometer	operational
D16	small momentum-transfer diffractometer	operational
D17	reflectometer	operational
D19	single-crystal diffractometer	operational
D20	powder diffractometer	operational
D22	small-angle scattering diffractometer	operational
IN1(50% with D4)*	three-axis spectrometer	operational
IN3	three-axis spectrometer	operational
IN4	time-of-flight spectrometer	operational
IN5	time-of-flight spectrometer	operational
IN6	time-of-flight spectrometer	operational
IN8	three-axis spectrometer	operational
IN10	backscattering spectrometer	operational
IN11	spin-echo spectrometer	operational
IN14	three-axis spectrometer	operational
IN16	backscattering spectrometer	operational
IN20	three-axis spectrometer	operational
PF1	neutron beam for fundamental physics	operational
PF2	ultracold neutron source for fundamental physics	operational
PN1	fission product mass-spectrometer	operational
PN3	gamma-ray spectrometer	operational
SALSA	*strain analyser for engineering application*	*under construction*
VIVALDI	thermal neutron Laue diffractometer	operational

* hot neutron instruments

CRG instruments		
ADAM	reflectometer	CRG-B operational
BRISP	Brillouin spectrometer	CRG-B under development
D1A	powder diffractometer	potential CRG
D1B	powder diffractometer	CRG-A operational
D15	single-crystal diffractometer	CRG-B operational
D23	single-crystal diffractometer	CRG-B commissioning
EVA	reflectometer	CRG-C operational
IN12	three-axis spectrometer	CRG-B operational
IN13	backscattering spectrometer	CRG-A operational
IN22	three-axis spectrometer	CRG-B commissioning
S18	interferometer	CRG-C operational

Jointly funded instruments		
DB21 (50%)	single-crystal diffractometer	operational with EMBL
LADI (50%)	Laue diffractometer	operational with EMBL
IN15	spin-echo spectrometer	operational with FZ Jülich and HMI Berlin

Test beams	
CT1, CT2	detector test facilities
S42	Laue-crystal alignment facility
T3	neutron optics test facility
T13A, C	monochromator test facility
T17	cold neutron test facility

Instrument layout - January 2005

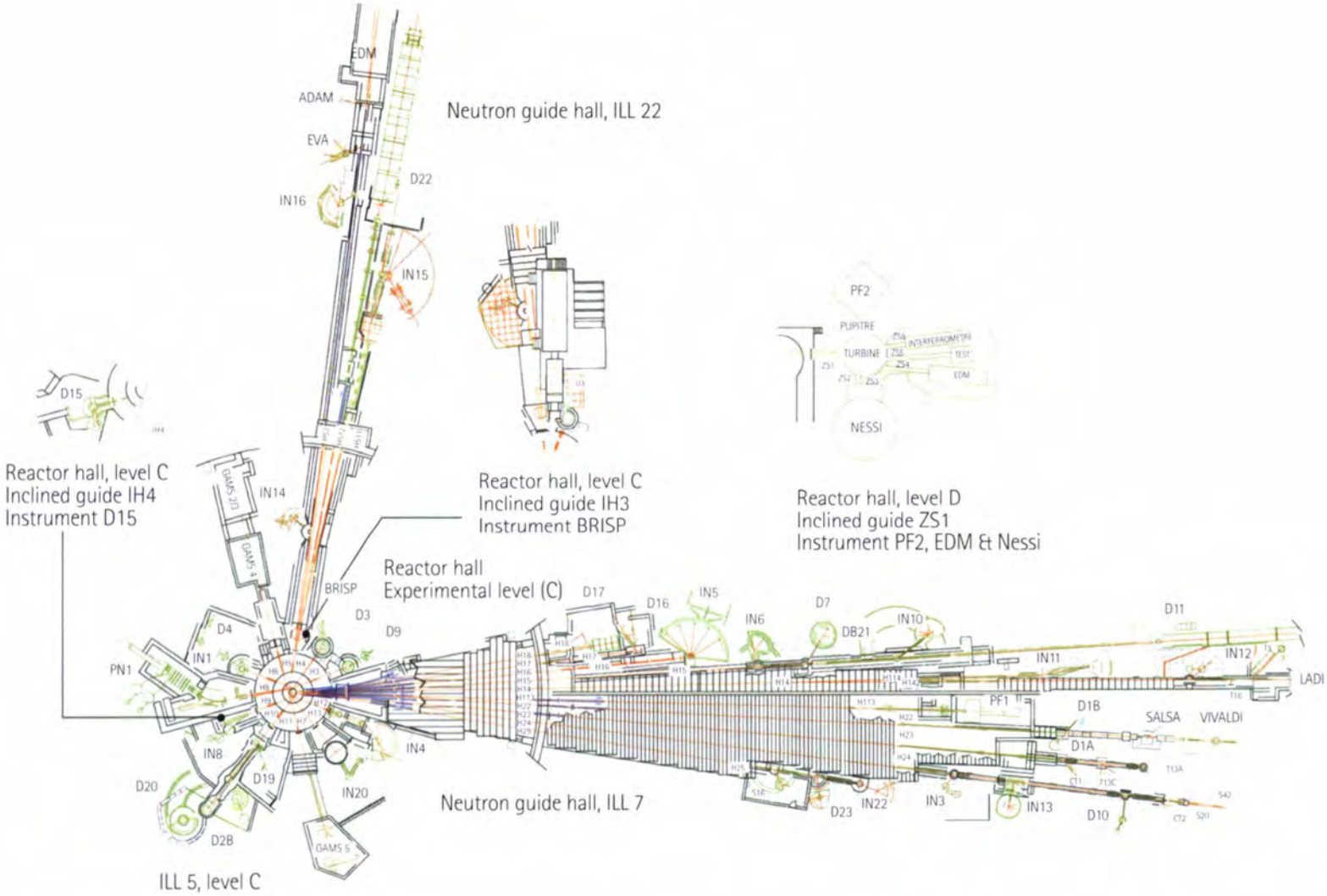

G. Cicognani *(ILL)*

experimental & user programme

User operation

The ILL User Support is there to assist all our users. If you are coming to the ILL to carry out experiments, the User Office is here to give you the organisational and administrative support you need for the successful operation of your experiments. Neutron beams and instrument facilities are free of charge for proposers of accepted experiments. Scientists affiliated to ILL member countries will also, in general, be assisted with necessary travel and daily subsistence for a limited period. The User Support Team makes all arrangements for accommodation and will process claims for expenses after you have completed your experiment.

The ILL Visitors Club

All administrative tools for our scientific visitors are now grouped together and directly accessible on the web, thanks to the Visitors Club. All information is presented in a user friendly environment. After having logged in with your own personal identification[1], you will access directly all the available information which concerns you. Users with particular responsibilities have privileged access to other tools, according to their role. The ILL Visitors Club includes the electronic proposal and experimental report submission procedures and makes available additional services on the web, such as acknowledgement of receipt of proposals, subcommittee results, user satisfaction forms and so on. Moreover, we have introduced an Electronic Peer Review of the proposals submitted, with an application within the Visitors Club, which uses a web-based interface to the SCO Oracle database.

Extensive information about the ILL, its facilities and application for beam-time is available on our web-site (at http://www.ill.fr/).

Christian Vettier – Head of the Science Division – discussing with Jean-Pierre Samama (Chairman of Subcommittee 8, Biology).

Proposal submission

There are three different ways to submit a proposal to the ILL:

- standard submission of a research proposal - twice a year (in the first and third quarters).
- Director's Discretion Time (DDT) – no time restriction.
- Special access for proprietary research and industrial users.

Submission of a standard research proposal

Applications for beam time should be submitted electronically, via our Electronic Proposal Submission system (EPS), available on the Visitors Club web-site. Proposals can be submitted to the ILL twice a year, usually in February and September. The web system is activated two months before each deadline.

Submitted proposals are divided amongst the different colleges, (see indent) according to their main subject area.

Proposals are judged by a Peer Review Committee of the Subcommittees of the ILL Scientific Council. Subcommittee members are specialists in relevant areas of each College and they evaluate the proposals for scientific merit, assigning priorities and beam time to accepted proposals.

Before the meeting, the subcommittee receives a Report on the technical feasibility and safety of a proposed experiment from the appropriate College at the ILL. Two proposal review rounds are held each year, approximately six weeks after the deadline for submission of applications.

There are normally 4.5 reactor cycles a year, each of which lasts 50 days.

The ILL scientific life is organised into 10 colleges

- *College 1 - Instrumentation*
- *College 2 - Theory*
- *College 3 - Nuclear and Particle Physics*
- *College 4 - Structural and Magnetic Excitations*
- *College 5A - Crystallography*
- *College 5B - Magnetism*
- *College 6 - Structure and Dynamics of Liquids and Glasses*
- *College 7 - Materials Science, Surfaces and Spectroscopy*
- *College 8 – Structure and Dynamics of Biological Systems*
- *College 9 - Structure and Dynamics of Soft-condensed Matter*

1 - If you are not yet registered in the Visitors Club and you wish to join it, you can register on the ILL web site (www.ill.fr) or directly at http://vitraill.ill.fr/cv/.

One of the Subcommittees of the ILL Scientific Council (College 5B) evaluating the submitted proposals.

Proposals submitted for the February deadline and accepted will be attributed beam-time for the second half of the year; those submitted for September and accepted, for the first half of the following year.
More detailed information on application for beam-time and dead-lines are given on our web-site at
http://www.ill.fr/pages/science/User/UProposals.htm.

Submission of a proposal to the Director's Discretion Time (DDT)

This option allows a researcher to obtain beam time quickly, without going through the peer-review procedure. DDT is normally used for hot topics, new ideas, feasibility tests and to encourage new users. Applications for Director's Discretion Time can be submitted to the Head of the Science Division, Dr. Christian Vettier, at any time.
During the major refit programme of the ILL's reactor spanning the 2003-2005 period (see p. 130) - DTT has been suppressed to enable us to offer a larger fraction of the available beam time to users, compared to what was achieved before.

Access for proprietary research and industrial users

The ILL's mission is to provide neutrons for both public and industrial research. Our Industrial Liaison and Consultancy Group (ILC) ensures rapid access and total confidentiality to industrial companies, and provides a specialised staff. The ILC Group is in fact composed of scientists with considerable experience and expertise in neutron techniques applied to industrial R&D, and it facilitates and co-ordinates all aspects of industrial R&D at the ILL: initial enquiries, contractual questions, planning, experimental operations. All industrial research programmes are confidential and can be organised at short notice. To apply for proprietary beam time, please contact the ILC at industry@ill.fr or consult the web site under http://www.ill.fr, Industrial Use. Further information on industrial use of neutrons is given on p. 130.

Experimental reports

Users are asked to complete an experimental report on the outcome of their experiments. Following a recommendation of the ILL Scientific Council, the submission of an experimental report is now compulsory for every user who obtained access to ILL beam time. Failure in doing so will lead to rejection in case of application for beam time for a continuation proposal.
All ILL Experimental Reports are now software-archived and accessible via the web server as PDF files (under http://www.ill.fr, Publications). You can search a report by experimental number, instrument, college, date of experiment, title, experimental team or local contact, institute.
Experimental reports of experiments performed in 2004 are included in the attached CD-ROM.

Out of Hours Support

We have actively strengthened the level of technical support outside of working hours. To date Out of Hours Support (OHS) has been implemented within the Instrument Control Service, the Detector Service and the Sample Environment Service.

Deuteration Laboratory

In 2002, a common ILL/EMBL deuteration laboratory has been made available to external users. The aim of the laboratory is to provide a focus for European scientists wishing to make their own deuterated materials for neutron scattering or NMR experiments. Information about the availability of this facility to external users is given on the ILL web-site (http://www.ill.fr, Users & Science, user Information, Proposal Submission). Please contact the Head of the Deuteration Facility, Dr Michael Härtlein (haertlein@ill.fr) for further details.

Facility for Materials Engineering

The joint ILL-ESRF Facility for Materials Engineering (FaME38) is now available to users (see also this Annual Report, p.46). A range of support is provided by the FaME38 team, from advice with experiment proposals to advanced sample metrology. In particular, FaME38 works with users to optimise the experimental methodology before the start of an experiment. This takes the form of standardised specimen mounting, digitisation of samples, definition of measurement macros and liaising with the instrument responsible. It is recommended that users arrive at the ILL a day or two prior to the start of an experiment to enable these off-line preparations to be performed. The extra subsistence costs may be available from SCO if requested beforehand. More information about this support may be found on the FaME38 website (www.ill.fr/FaME38).

Feedback from our Users

The ILL welcomed 1104 users in 2004. Approximately 88% came from the member countries including 281 from France, 198 from Germany and 239 from the UK (figure 1). Many of our visitors were received more than once.

We value feedback from our users as an indicator of how well our facility is fulfilling their needs and to initiate actions when this is not the case. Therefore, we regularly organise User Forums. Users who are on-site that day are invited to an informal meeting with the ILL Directors, the User Support Office and Group Leaders of both the Science and the Project and Technique Divisions. The objective is to obtain important feedback on the quality of the instruments and services at the ILL.

We very much appreciate the enthusiasm and cooperation of our users in giving their views, on such topics as instrument upgrading and implementation, new sample environment and instrumentation, quality of the Restaurant and the Guest House, and so on. Every effort will be made to implement suggestions.

Alejandro Sanz (University A. De Henares), a happy user at the ILL.

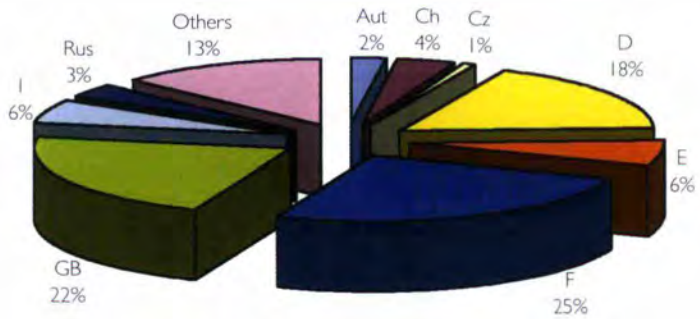

Figure 1: National affiliation of ILL users during 2004.

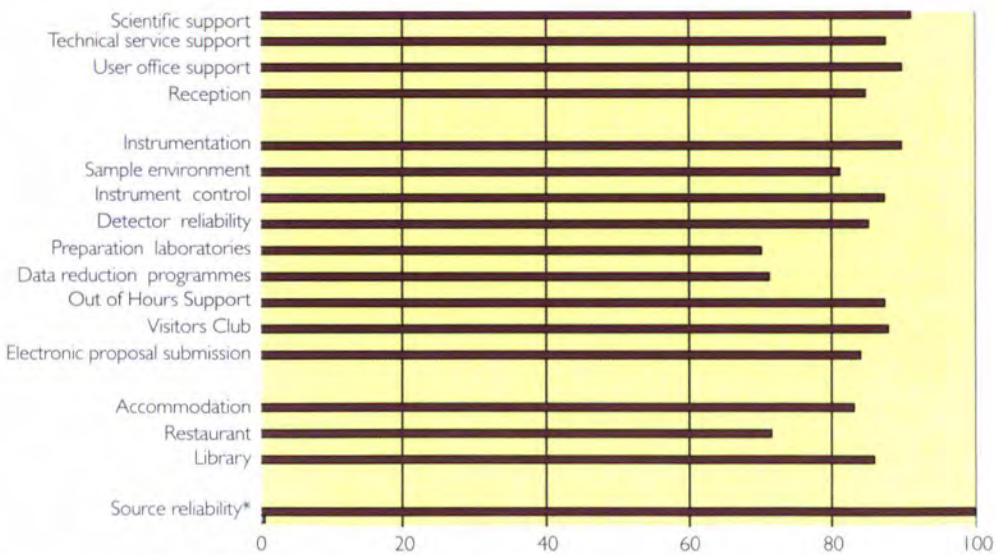

Figure 2: User satisfaction survey results (year 2004), in %.
* The source reliability has been calculated from table 3 (p. 130).

The present system of User Feedback Forms, the User Satisfaction Form, now dealt with electronically, is another measure of gathering the opinion of our users in order to raise a mirror up to ourselves. Users who have just finished an experiment at the ILL are asked to complete the questionnaire and to give us their views on different topics. User comments and solutions are entered into a database and summarised for the ILL Directors, the User Support Office, Group Leaders and Instrument Responsibles.

Levels of satisfaction are in general high. Figure 2 reports the results of the survey during 2004 and shows in most cases very high satisfaction (between 80 and 90%).

Instruments

The instrumental facilities at the ILL are shown in the schematic diagram on p. 123.

Besides the 25 ILL instruments, there are 9 CRG-instruments, which are operated by external Collaborating Research Groups. There are currently three different categories of CRG instruments.

CRG-A in which the external group leases an instrument owned by ILL. They have 50% of the beam time at their disposal and for the remaining 50% they support ILL's scientific user programme.

The CRG-B category owns their instrument and retains 70% of the available beam time, supporting the ILL programme for the other 30%.

Finally, CRG-C instruments are used full time for specific research programmes by the external group, which has exclusive use of the beam.

DB21, LADI and IN15 have a special status, since they are joint ventures of the ILL with other laboratories: in the case of DB21 and LADI with EMBL and for IN15 with FZ Jülich and HMI Berlin.

The list of instruments as of December 2004 is summarised below (CRG instruments are marked with an asterisk *):

- powder diffractometers: D1A, D1B*, D2B, D20, SALSA
- liquids diffractometer: D4
- polarised neutron diffractometers: D3, D23*
- single-crystal diffractometers: D9, D10, D15*
- large-scale structures diffractometers: D19, DB21, LADI, VIVALDI
- small-angle scattering: D11, D22
- low momentum-transfer diffractometer: D16
- reflectometers: ADAM*, D17
- diffuse scattering and polarisation analysis spectrometer: D7
- three-axis spectrometers: IN1, IN3, IN8, IN12*, IN14, IN20, IN22*
- time-of-flight spectrometers: IN4, IN5, IN6
- backscattering and spin-echo spectrometers: IN10, IN11, IN13*, IN15, IN16
- nuclear physics instruments: PN1, PN3
- fundamental physics instruments: PF1, PF2

The reflectometer EVA and the interferometer S18 are CRG-C instruments and they are normally not available as a 'user' instrument, although some beam time is made available for prototype tests of USANS on S18.

Details of the instruments can be found on the web under http://www.ill.fr (Users & Science / Instrument groups & Theory).

Beam-time allocation & utilisation for 2004

Overall, the Subcommittees of the Scientific Council scrutinised 963 proposals requesting 7085 days for 2004, out of which 650 proposals received beam time, allocating 3707 days of beam time on the different instruments. In 2004, the member countries of the ILL were: France, Germany, UK, Spain, Switzerland, Austria, Italy, the Czech Republic and Russia. The distribution of beam-time requested and allocated amongst them is shown in table 1.

In calculating the statistics of beam-time per country, shown in table 1, the attribution is based on the location of the laboratory of the proposers, not their individual nationality. For a proposal involving laboratories from more than one member country, the total number of days is divided amongst the collaborating countries, and weighted by the number of people for each country. When a proposal involves collaboration with a non-member country, the allocated time is attributed entirely to the collaborating member country (or countries), and weighted by the number of people for each member country. When ILL scientists are proposers or co-proposers, the allocated ILL time is attributed to the member countries according to their financial contributions to ILL. Local contacts are not counted as proposers except when they are members of the research team.

The distribution of beam time for these

Table 1: Distribution amongst the Associate and scientific-member countries of beam-time requested and allocated in 2004 during the Subcommittees of the Scientific Council.

			Before national balance		After national balance	
Country	requested days	requested %	allocated days	allocated %	allocated days	allocated %
AUT	133.68	1.89	42.24	1.13	41.53	1.12
CH	240.27	3.39	151.34	4.04	150.01	4.05
CZ	67.64	0.95	43.38	1.16	45.08	1.22
D	1712.07	24.17	997.53	26.65	996.77	26.89
E	379.70	5.36	203.05	5.42	200.94	5.42
F	1974.42	27.87	981.17	26.21	972.89	26.24
GB	1704.69	24.06	987.66	26.39	984.90	26.57
I	304.49	4.30	158.34	4.23	153.92	4.15
RUS	567.77	8.01	178.54	4.77	160.97	4.34
Total	7084.75	100.0	3743.25	100.0	3707.00	100.0

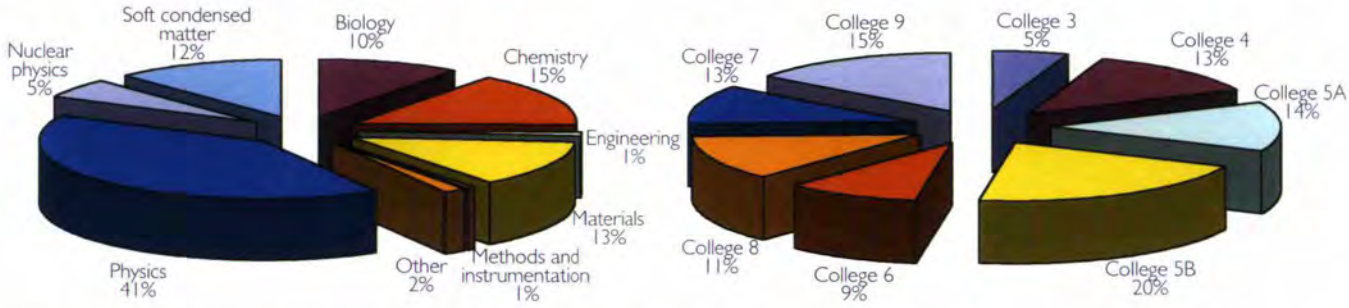

Figure 3: Beam-time allocation in 2004: distribution amongst the different research areas and colleges (see p.124).

experiments amongst the different research areas and colleges is shown in figure 3.
A more complete view is given in table 2. Request and allocation of beam time – as well as the number of scheduled experiments – refer to standard submissions to the subcommittee meetings. The effective number of days given to our users takes into account also Director's Discretion Time (DDT) and CRG's time for CRG instruments.
The instruments D4 and IN1 share a beam. Note that PF2 consists of 5 different set-ups allowing several experiments to run simultaneously. Normally, for official statistics (as for table 1) the total number of days requested and allocated is averaged by a factor 5. However, in table 2 we report the total number of days delivered to users (column 5) on all the 5 instruments (EDM, MAM, TES, UCN, VCN), i.e. 740 in total.

Instrument performance

Table 2 also gives a summary of instrument performance for 2004. For each cycle, a record is kept of any time lost from the total available beam-time and the reasons for the lost time are analysed for all the instruments. The table gives a global summary for the year.
Overall 4977 days were made available to our users in 2004 on ILL and CRG instruments, which represents about 80% of the total days of operation. 126 days were used by ILL scientists to carry out their own scientific research. About 14% of the total beam time available on the ILL instruments is allowed for tests, calibrations, scheduling flexibility, minor breakdowns recuperation.
Totally, 687 experiments were scheduled. During 2004 the reactor operated for 3.0 cycles, representing 150 days of neutrons, instead of the 4.5 cycles normally foreseen (see § Reactor Operation, p. 130).
In 2004, about 284 days were lost due to various malfunctions, which represents less than 5% of the total available beam-time.

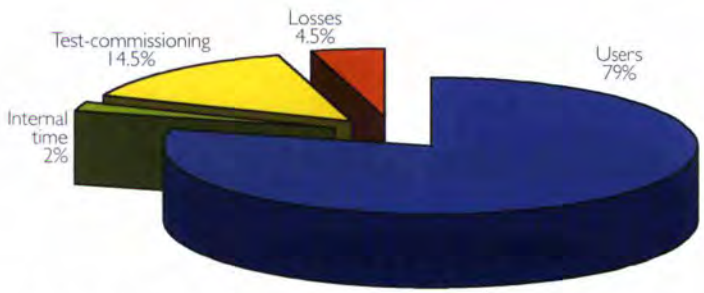

Figure 4: Use of ILL beam time.

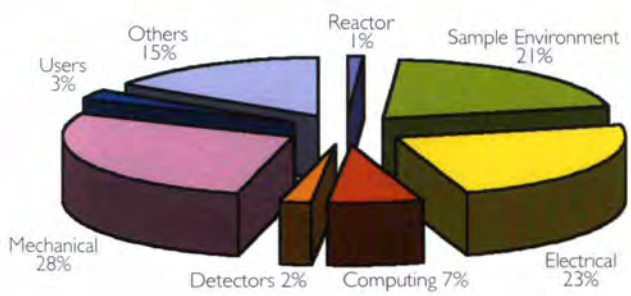

Figure 5: Origin of beam time losses

The breakdown by reasons for beam time losses is shown in the figure 5.

Detailed comments on the larger beam-time losses (20 days or more) are as follows:

- IN15 lost one week because of a big power supply breakdown and 2 weeks because of a selector failure;
- PN3 lost 12 days for the replacement of the broken target changer and 10 days because of electronics failure;
- VIVALDI had various minor problems and then it lost 11 days for a read-head motor failure and 5 days for an intermittent fault in motor drive.

Instrument	Days requested	Days allocated[1]	Number of scheduled experiments	Days used for users[2]	Days lost	Days for commissioning/ test/training	Days for internal research
ADAM	71	47	9	112	0	19	-
D10	178	120	16	136	9	4	-
D11	200	107	55	119	4	27	-
D15	33	39	6	135	8	9	-
D16	140	106	20	103	4	33	10
D17	222	110	32	125	5	18	3
D19	98	88	9	98	4	48	-
D1A	121	99	26	110	6	16	18
D1B	124	69	24	140	4	6	-
D20	248	120	56	118	8	14	10
D22	281	96	45	98	5	47	-
D23	75	50	6	120	4	26	-
D2B	204	109	47	125	2	14	9
D3	177	108	11	102	11	32	5
D4	142	49	10	48	4	14	5
D7	161	70	8	50	2	88	-
D9	126	95	11	97	14	34	-
DB21	77	77	3	50	6	6	-
EVA	34	8	1	32	0	117	-
IN1	176	62	11	66	2	8	2
IN10	39	90	12	101	6	34	9
IN11	243	103	15	121	10	15	5
IN12	60	38	4	139	3	8	-
IN13	151	51	9	138	4	7	-
IN14	262	119	16	117	10	11	12
IN15	220	68	8	98	27	26	-
IN16	320	115	24	135	8	7	-
IN20	271	101	16	115	7	14	13
IN22	139	40	5	138	2	10	-
IN3	27	51	6	55	4	88	-
IN4	177	122	27	117	9	18	6
IN5	255	115	28	127	6	16	1
IN6	223	110	26	137	3	8	2
IN8	318	122	20	116	19	10	4
LADI	141	102	7	70	1	5	12
PF1	209	50	2	48	2	0	-
PF1B	397	150	2	148	2	0	-
PF2*	189	150	12	740	3	0	-
PN1	187	120	9	120	7	22	-
PN3	250	145	8	111	23	17	-
VIVALDI	135	116	25	104	29	17	-
Total	**7 101**	**3 707**	**687**	**4 977**	**284**	**913**	**126**
Percentage of the total available beam time				***79%***	***4.5%***	***14.5%***	***2%***

Table 2: Beam-time request/allocation (via standard subcommittees and DDT altogether) by instrument and instrument performance. CRG instruments are in italic and green.

1- days allocated' refers to only those days reviewed by the subcommittees (i.e., excluding CRG days and DDT).

2- days used' refers to the total number of days delivered to users (i.e., including CRG days for CRGs and DDT).

* PF2 consists of 5 different set-ups where several experiments are running simultaneously.

P. Lindner, T. Pirling
and T. Hansen *(ILL)*

Industrial use of neutrons

Industrial beam time sales have remained stable in 2004: a total of 8 days (2003: 7.5 days) were contracted for proprietary research in 5 different experiments (2003: 3 experiments). This year again, small-angle neutron scattering has been used exclusively, with 7 days at D11 and 1 day at D22.

The main activity in commercial research remains the investigation of irradiated reactor steel samples, a field where UK and French companies have actively been using ILL's unique SANS facilities for many years. Chemical and cosmetics industries are further sectors where our customers find valuable results and where the usefulness of neutron techniques for applied and industrial research is established.

From June 2005 on, stress measurements will be performed on the new instrument SALSA (Stress Analyser for Large and Small scale engineering Applications). It replaces the stress option on the high-resolution powder diffractometer D1A. SALSA provides much higher flexibility for sample manipulation thanks to the hexapod sample stage, a robotic system with 6 degrees of freedom. It now allows sample positioning in translation and tilt with 1/100mm precision for samples of up to 500kg weight and dimensions up to 1.5m. (More details on p.100).

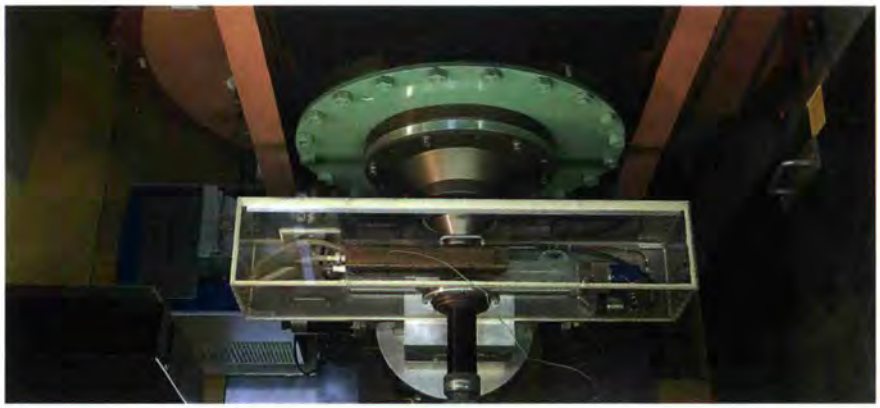

The small-angle instrument D11, which provided 7 days beamtime for industrial research in 2004.

A latest industrial experiment on D1A-(stress option) was the determination of stress variations in fuel providing tubes for the ARIANE rocket. Thanks to the high instrumental resolution it was possible to perform measurements in the only 0.6mm thick Ni-alloyed walls.

Further information is available on our web page www.ill.fr/industry.

Reactor operation

H. Guyon *(ILL)*

Following the ten-year safety review of the ILL's High Flux Reactor carried out at the meeting of the Groupe Permanent in May 2002, the Institute decided to launch a major refit programme in order to ensure compliance, among other things, with changes in seismic regulations. The bulk of the work involved in the programme is scheduled to be carried out between 2003 and 2005, during which time reactor operation is to be based on three reactor cycles per year.

Cycle n°	Start of cycle	End of cycle	Number of days of operation	Number of days scheduled	Number of EFPDS[1] operation	Number of EFPDS[1] scheduled	Number of unscheduled shutdowns
137	25 February 04	13 April 04	48	50	45.6	45.2	0
138	22 April 04	11 June 04	50	50	45.2	45.2	one 12 hour stoppage due to loss of offsite power
139	22 June 04	11 August 04	50	50	45.2	45.2	0
		Total	**148**	**150**	**136**	**135.6**	**1**

Table 3: Three reactor cycles (corresponding to 150 days of operation) were scheduled for scientific work in 2004. These cycles ran according to schedule.

1 -EFPDS : Equivalent Full Power days.

In addition to preliminary reinforcement work, this three-cycle schedule made it possible to complete a number of important operations:

- Three new beam tubes (H8, H3 and H4) were fitted in place of the three beam tubes removed in 2002, making it possible to reinstall the instruments IN1, D4, D3 and D9. The neutron flux performance of the hot source and beam tubes is now even higher than before.
- Two safety rods were replaced in accordance with the maintenance programme.
- Three further beam tubes were replaced at the end of the year: IH1, IH4 and H9. The H9 beam tube is now made of zircaloy, a material which behaves in such a way under neutron irradiation that the beam tube will never have to be replaced again, thereby reducing dose rates due to maintenance work.

A detritiation campaign was conducted in 2004 with the aim of achieving a major reduction in the level of tritium contamination in the primary heavy water circuit. This will facilitate maintenance operations on this circuit and means that another detritiation campaign will not be necessary until 2008. At the end of the 2004 campaign, around 20 g of tritium were transferred to the CEA.

In compliance with the legislation applicable to our installation, reactor operations and maintenance work in 2004 generated the levels of waste and effluents reported in table 4.

Radioactive waste removed from the site in 2004	Quantity
Decay containers (60 l)*	1
5 m³ containers (low-level waste)	4
10 m³ containers (low-level waste)	2
200 l drums of compactable (low-level) waste	27
118 l drums of incinerable (low-level) waste, e.g. gloves, overboots, etc.	4
200 l drums of "incinerable" (low level) waste	44
200 l oil drums (low level waste)	5

*The waste placed in decay containers is still too active and must be held in interim storage for a number of years before it meets the specifications for being accepted by ANDRA (National Agency for the Management of Radioactive Waste) as intermediate-level waste.

Gaseous effluents	Quantity released in 2004
Rare gas (TBq)	8.3 E -01
Tritium (TBq)	1.9 E +01
Gaseous halogen and aerosols (GBq)	2.7 E -02

Liquid effluents	Quantity released in 2004
Activation products, except tritium (GBq)	1.2 E -01
Tritium (TBq)	1.1 E -01

Table 4: Level of waste and effluents generated in 2004.

In order to satisfy as effectively as possible the commitments and recommendations made following the meeting of the Groupe Permanent, the ILL set up a new structure in 2002 known as the "Refit Management Committee". Made up of engineers and technicians both from within the ILL as well as from outside companies, this group completed a large number of studies and related tasks in 2003.

Following a major study phase, the structure of the group is now evolving to allow it to prepare for the necessary work, in close collaboration with the operational groups of the Reactor Division. In 2004, for example, the following work was completed:

Deconstruction of half the buildings located on the upper level (level D) of the reactor building, representing a mass of almost 500 tonnes. This has given access to the reinforced concrete containment of the reactor, thus making it possible to begin work on connecting the floor on level D to the containment. Once this work is completed, the floor will be adequately supported by the containment and all the components of the reactor building will be capable of resisting a safe shutdown earthquake, as defined in the most recent safety regulations.

A number of safety drills were organised during the course of the year, in particular in cooperation with the public authorities. The ILL also took part in a series of public meetings at which the public information document on major risks, known as the DICRIM (Dossier d'Information Communal sur les Risques Majeurs), for each of the towns of Fontaine, Grenoble and Saint-Egrève was presented. At these meetings, the ILL gave a brief presentation of its activities and invited participants to come and visit the site.

Comings and goings

Anne Dale joined the User Office Team in September.

Roland Currat – Three-axis group leader – retired after over a third of a century at the ILL.

Marc Locatelli left the ILL after more than 30 years of loyal and valuable service.

Silke Bachmann – with her beautiful smile – is the new hostess at the ILL.

facts&figures

Name Institut Max von Laue - Paul Langevin (ILL)

Founded 1967

Associates

France
Commissariat à l'Energie Atomique (CEA)
Centre National de la Recherche Scientifique (CNRS)
Germany
Forschungszentrum Jülich (FZJ)
United Kingdom
Council for the Central Laboratory of the Research Councils (CCLRC)

Countries with Scientific membership

Spain
Ministerio de Educación y Ciencia (MEC)
Switzerland
Bundesamt für Bildung und Wissenschaft
Italy
Istituto Nazionale per la Fisica della Materia (INFM)
Consiglio Nazionale delle Ricerche (CNR)
Russia
Federal Agency for Atomic Energy (FAAE)
MENI (Middle European Neutron Initiative) Consortium, composed of
Austria: Österreichische Akademie der Wissenschaften
Czech Republic: Charles University of Prague
Sweden (as from 1 January 2005)
Swedish Research Council

Staff

427 people including 58 experimentalists in the scientific sector.
283 French, 50 German, 49 British, 24 Scientific members, 21 others.

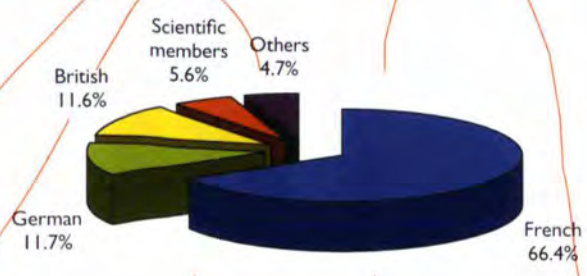

facts & figures

Organisation chart - December 2004

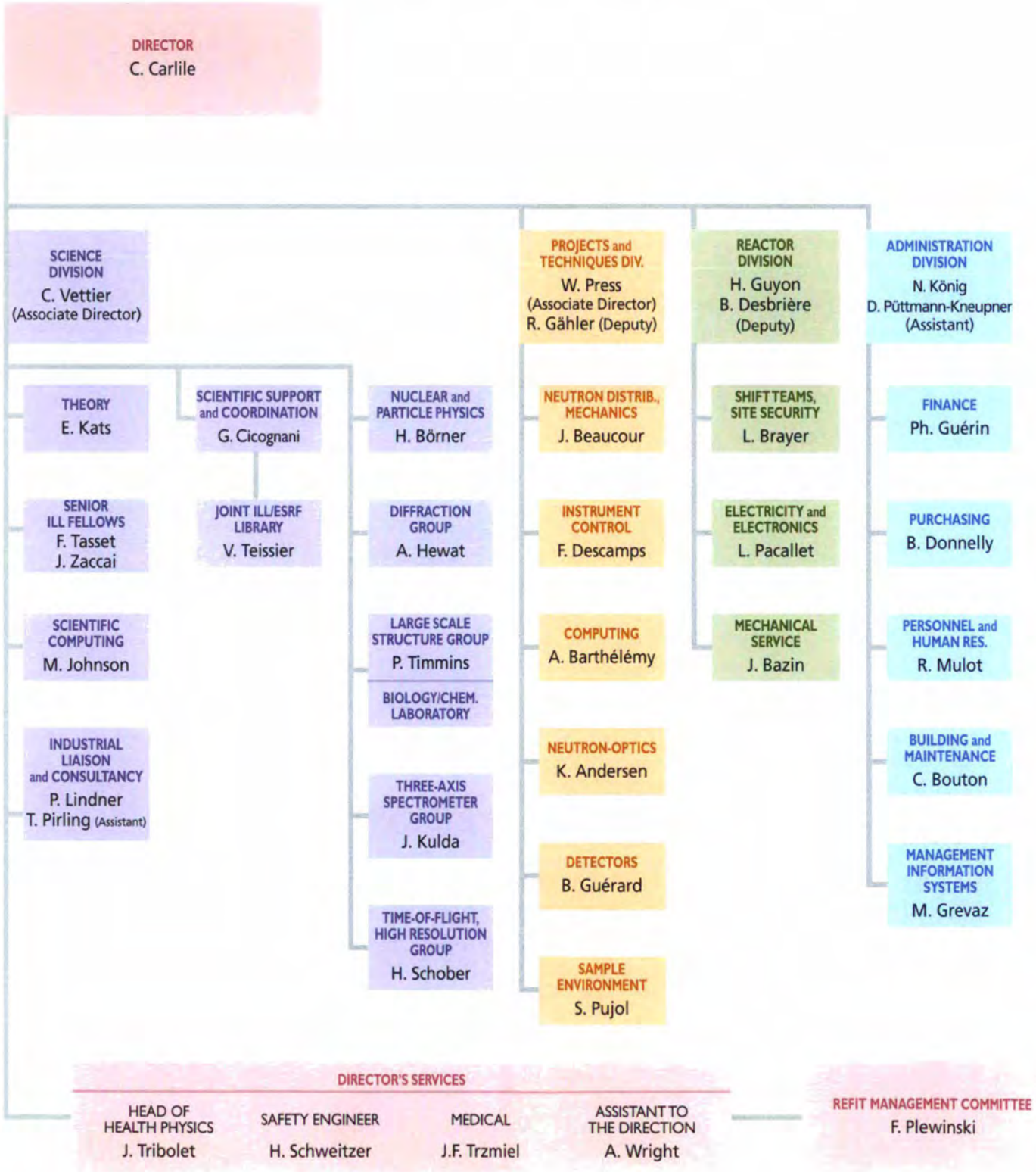

Budget 69.7 M€ (excluding taxes)

Income (M€)

from Associates	57.7	82.78%
from Scientific members	10.6	15.21%
own income	1.4	2.01%
	69.7	100%

Expenditure (M€)

staff costs	34.9	50.1%
operating costs	11.2	16.1%
investment costs	7.3	10.5%
fuel cycle	9.1	13%
Refit Programme	7.2	10.3%
	69.7	100%

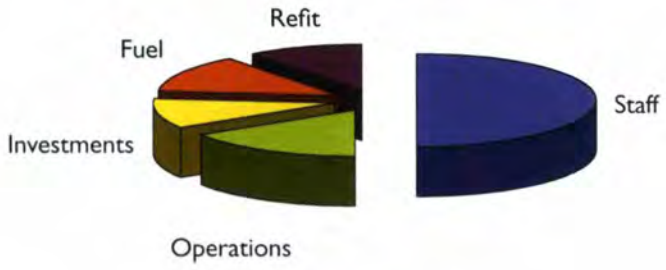

Distribution of ILL purchases
(M€, excluding taxes)

France	16.51	77.4%
Germany	1.80	8.5%
United Kingdom	0.60	2.8%
Scientific members	1.03	4.8%
Others	1.39	6.5%
	21.33	100%

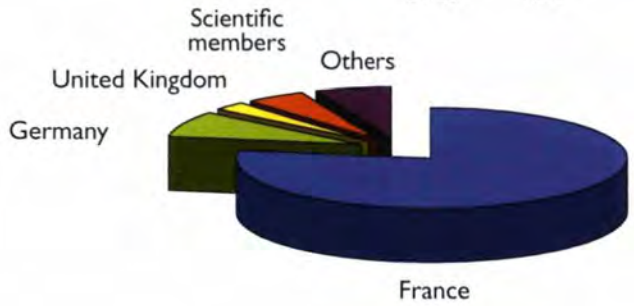

Bodies

Steering Committee, meeting twice a year

Scientific Council with 8 subcommittees, meeting twice a year

Reactor 58 MW, running 3 cycles in 2004 (with cycles of 50 days)

Experimental Programme

687 experiments (allocated by subcommittees) on 25 ILL-funded and 9 CRG instruments

1104 visitors coming from 32 countries

963 proposals submitted and 650 accepted

Life on site

Lætitia Rosselet, our smiling welcome to all ILL visitors.

Christian De Reggi and Nicolas Gauthier sending out the Annual Report.

The ILL hosts the sculpture by Ipoustéguy « Man accomplishing Unity ». Gingko Production (Metz) realised a 26 minute film for France 3-Lorraine and came to the ILL to film the statue, wich is the first monumental composition of the artist.

publications

In 2004, the ILL received notice of 614 publications by ILL staff and users.

The distribution by subject is as follows:

- 32 in Biology
- 53 in Chemistry
- 17 in Engineering
- 44 in Liquids and Glasses
- 176 in Magnetism
- 107 in Materials
- 60 in Methods and Instrumentation
- 26 in Nuclear Physics
- 21 in Physics
- 78 in Soft Condensed Matter

CD-rom (Mac/PC)
"Exploring matter with neutrons"

The CD-ROM "Exploring matter with neutrons" presents the many aspects of neutron science and techniques through about 1700 screens, several thousand pictures, animations and videos. It is part of the NANOPOLIS™ encyclopedia series covering: synchrotron light (tome 1), neutrons (tome 2) and nanotechnologies (tome 3).

The CD-ROM "Exploring matter with neutrons" is divided into five chapters:

Science	the neutron and its properties, magnetism, fundamental physics, etc.
Sources	a description of the main neutron sources,
Tools	experimental methods for studying matter down to the atomic scale,
Applications	scientific and technological applications,
Facilities	pages provided by the main neutron facilities for their own advertising.

This CD-ROM is mainly for teachers, students and scientists and even for the general public interested in science. It can be used either as a teaching tool or to discover the main aspects and the power of neutrons in research and the industry.

Version 1 of the CD was released in autumn 2004 and version 2 is due for summer 2005. The CD is commercially available from <http://www.nanopolis.net> with a special discount for partners.

"Exploring matter with neutrons" is the result of a partnership between iMediasoft® <www.imediasoft.net> and several major neutrons facilities. The project was launched in 1998 following an initiative by the SFN <http://www.sfn.asso.fr>. The ILL is the main author and contributor but many other neutron facilities, universities, laboratories and industries collaborated or provided material.

IMediasoft expects to release a new version each year and thus the contents of the CD will be regularly improved, augmented, modernized. New labs and facilities are welcome to join the team.

Alain Filhol

ILL 2004 CD-rom (Mac/PC)

The enclosed CD-ROM contains both the ILL 2004 Annual Report and the ILL Experimental reports as Portable Document Format (PDF) files. You will need a PDF file reader (Adobe® Acrobat® Reader®) to view it.

The CD-ROM also includes an interactive virtual visit of the ILL instrument hall and of the two guide halls(1). You can also enjoy a panoramic view of the beautiful landscape surrounding the ILL. Once the visit is launched you can click in the map to select a starting point. Then click in the image to get the cursor ✣ with which you can move right, move left, look up and down. You can move to another view point each time the cursor turns to ⌂. This virtual visit requires QuickTime 5 or later to be installed on your computer. Free Windows and Mac OS downloads are available from www.apple.com/quicktime.
Have a nice visit!

(1) The ILL is usually a very busy place but, for technical reasons, as few people as possible were present during the shooting.

institut laue-langevin
6, rue jules-horowitz - bp 156 - 38042 grenoble cedex 9 france
http://www.ill.fr